

39  
NASA CR 66393

A SUPERSONIC COMBUSTION TEST PROGRAM  
UTILIZING GAS SAMPLING, OPTICAL AND PHOTOGRAPHIC  
MEASURING TECHNIQUES

by

Anthony Casaccio and Richard L. Rupp

Prepared under Contract No. NAS 1-6314 by  
FAIRCHILD HILLER  
Republic Aviation Division  
Farmingdale, Suffolk County, New York 11735

for

NATIONAL AERONAUTICS AND SPACE ADMINISTRATION

N67-34996

(ACCESSION NUMBER)

115  
(PAGES)

(THRU)

(CODE)

33

(CATEGORY)

(NASA CR OR TMX OR AD NUMBER)

A SUPERSONIC COMBUSTION TEST PROGRAM  
UTILIZING GAS SAMPLING, OPTICAL AND PHOTOGRAPHIC  
MEASURING TECHNIQUES

by

Anthony Casaccio and Richard L. Rupp

Distribution of this report is provided in the interest  
of information exchange. Responsibility for its contents  
resides in the author or organization that prepared it.

Prepared under Contract No. NAS 1-6314 by  
FAIRCHILD HILLER  
Republic Aviation Division  
Farmingdale, Suffolk County, New York 11735

for

NATIONAL AERONAUTICS AND SPACE ADMINISTRATION



# A SUPERSONIC COMBUSTION TEST PROGRAM UTILIZING OPTICAL AND PHOTOGRAPHIC MEASURING TECHNIQUES

by

Anthony Casaccio and Richard L. Rupp

## SUMMARY

An experimental study has been conducted to investigate the effects of certain parametric variations on the supersonic combustion of hydrogen in air. The test program was performed in a one-megawatt arc-jet facility at a Mach number of 2.35 and an air static pressure of 0.5 atm. Free-jet testing of single, three-point and peripheral (ring) injection geometries were conducted for controlled variations in air static temperature, fuel total temperature, fuel-to-air velocity ratio, fuel-air equivalence ratio and fuel-air spacing. In addition, two segmented combustor contours were tested for various air static temperatures (2100°R, 2700°R, 2900°R and 3100°R), fuel stagnation temperatures of 600°R and 1000°R and fuel-air equivalence ratios of 0.5 and 1.0.

Spectroscopic and photographic techniques were employed to measure combustion stream temperatures and to note general flame characteristics. Gas samples were extracted from the combustion stream for each of the test runs and analyzed in a gas chromatograph. Furthermore, wall pressures and temperatures were recorded for each of the segmented combustor test runs in the series.

The results of the program show that changes in air static temperature, equivalence ratio and fuel-air velocity ratio have, in general, a more pronounced effect on combustion characteristics than changes in fuel stagnation temperatures. Slight effects due to variation in fuel-air spacing were also noted. For the segmented combustor portion of the experimental program, the results indicate the importance of maintaining a pressure level above 0.5 atm. in the forward portion of the combustor and of properly contouring the region just downstream of the fuel injection station in order to avoid a large separated region there.

## CONTENTS

	PAGE
SYMBOLS	v
LIST OF ILLUSTRATIONS	viii
INTRODUCTION	1
DESIGN OF EXPERIMENTAL APPARATUS	2
Arc-Jet Nozzle Design	2
Fuel Injection Conditions and Design	3
Combustion Rig Design	4
Combustor Contour Design	5
Combustor Off-Design Study	6
DESCRIPTION OF ARC-JET FACILITY	6
INSTRUMENTATION	9
EXPERIMENTAL PROCEDURES	10
Arc-Jet Instrumentation	10
Photography	11
Spectrometry	13
Spectrometer Alignment and Wavelength Calibration Procedure	14
Optical System	16
Optical Alignment Procedure	17
Light Source Calibration Procedure	17
Temperature Measurement by Sodium Line Reversal Technique	18
Temperature Measurement by OH Radical Emission and Absorption Technique	20
Gas Analysis	21

## CONTENTS (Cont'd)

	PAGE
Analytical Technique	22
EXPERIMENTAL RESULTS AND DISCUSSION	25
Experimental Program	25
Point Injection Tests	26
Ring Injection Tests	32
Original Segmented Combustor Tests	37
Modified Segmented Combustor	41
CONCLUSIONS AND RECOMMENDATIONS	47
APPENDIX A	53
APPENDIX B	69
APPENDIX C	75
APPENDIX D	76
APPENDIX E	82
REFERENCES	86
APPENDIX F	192

## SYMBOLS

$A$	cross-sectional area
$A_s$	surface area
$C_f$	skin friction drag coefficient
$C_{D_{eff}}$	skin friction drag coefficient defined as $\frac{2D}{(\rho V^2)_{av}} A_s$
$C_p$	specific heat at constant pressure
$D$	skin friction drag
$f/a$	fuel-air ratio, $\frac{w_f}{w_a}$
$f'$	velocity ratio, $\frac{u}{u_a}$
$g$	stagnation enthalpy ratio, $\frac{H}{H_a}$
$g$	acceleration due to gravity
$h$	static enthalpy
$H$	total or stagnation enthalpy
$\frac{\delta}{\theta}^*$	form factor, $\frac{\delta}{\theta}^*$
$K_f$	incompressible form factor
$K_f$	forward reaction rate
$l_d$	ignition delay length
$l_r$	reaction length
$l_R$	total reaction length
$L$	combustor length
$M$	Mach number
$N_{St}$	Stanton number
$n$	exponent in Equation (B-9)
$n_i$	number of moles of $i^{th}$ species
$p, p_s$	static pressure
$p_i$	partial pressure

$P_r$	Prandtl number
$q$	local heat transfer rate
$Q$	total heat transfer
$Q_R$	total heat rejected from combustor
$r$	local cross-sectional radius
$R$	gas constant
$Re$	Reynolds number
$s$	density ratio, $\rho_a/\rho$
$t$	reaction time
$T$	static temperature
$T_b$	bulk temperature of fluid
$T_s$	saturation temperature
$T_c$	combustion temperature
$u$	streamwise velocity component
$V$	average streamwise velocity used in one-dimensional analysis
$w$	mass flow
$W$	molecular weight
$x$	streamwise coordinate
$X$	mole fraction
$y$	coordinate normal to streamwise direction
$y_*$	nozzle throat radius
$z_i$	ratio of mass fractions, $\frac{Y_i}{Y_{ia}}$
$\alpha$	exponent in Equation (B-8)
$\beta$	pressure gradient parameter (Appendix D)
$\epsilon$	turbulent exchange coefficient
$\eta$	cycle definition according to Equation (A-8)
$\eta_c$	combustion efficiency defined in Appendix A
$\kappa$	quantity defined in Equation (D-2)
$\lambda$	quantity defined in Equation (D-1)
$\mu$	coefficient of viscosity
$\rho$	density
$\tau_w$	wall shear stress
$Y_i$	mass fraction of $i^{\text{th}}$ species

$\tilde{Y}$	element mass fraction
$\varphi$	stagnation enthalpy parameter (Appendix D)
$\phi$	fuel-air equivalence ratio
$X$	similarity parameter defined in Reference 23
$\psi$	stream function

### Subscripts

a	refers to air values
c	refers to combustion values
e	refers to values outside the boundary layer
f	refers to fuel values
i	refers to the $i^{\text{th}}$ species and to initial values
k	refers to elements composing species (Appendix D)
m	refers to mixture values
o	refers to stagnation values
s	refers to flame sheet values in Appendix D and to static values elsewhere
w	refers to wall values
*	refers to reference values

## LIST OF ILLUSTRATIONS

FIGURE		PAGE
1	Variation of Fuel-Air Injection Parameters for an Air Mach Number of 2.3 and $p_a = p_f = 0.5$ atm.	101
2	Fuel Injector Configurations	102
3	Combustion Rig Layout Showing Original Combustor Contour	103
4	Sub-Cooled Pool Boiling Heat Fluxes	104
5	Displacement Thickness Distribution Inside Segmented Combustor (Design Case)	105
6	Skin Friction Drag Distribution Inside Segmented Combustor (Design Case)	106
7	Total Heat Transfer Distribution Inside Segmented Combustor (Design Case)	107
8	Transmission Curve of Perkin Elmer Spike Filter	108
9	Transmission Curve of Zeiss Ultraviolet Filter	109
10	Spectrometer Resolution of Mercury 3131.6A° Doublet	110
11	Optical Layout for Spectrometry	111
12	Transmission Curve of Rohm and Haas UVT Plexiglass	112
13	Pyrometer Calibration Curve	113
14	Lamp Calibration Curve (Secondary Standard)	114
15	Sodium Salt Injection System and Gas Sampling Probe	115
16	Schematic of Metco Type MP Powder Feed Unit	116
17	Typical Sodium Line Reversal Spectral Readout	117
18	Gas Sampling Tube-General Assembly	118
19	Gas Sampling Tube Tip	119
20	Gas Sampling Tube Tip Assembly	120
21	Gas Sampling and Pitot Probes	121

## LIST OF ILLUSTRATIONS (Cont'd)

FIGURE		PAGE
22	Gas Collection and Storage System	122
23	Schematic of Gas Sampling System	123
24	Gas Chromatographic Analysis System	124
25	Analytical Working Curve: Hydrogen in Supersonic Gas Streams	125
26	Analytical Working Curve: Oxygen in Supersonic Gas Streams	126
27	Analytical Working Curve: Nitrogen in Supersonic Gas Streams	127
28	Typical Gas Chromatograms	128
29	Definition of Pertinent Reaction Zone Lengths Read from UV Negatives	129
30	UV Photograph of a 2394°R, Single-Point Injection Test using Cold Hydrogen for $V_f/V_a = 0.4$ (0.108" Spacing)	130
31	UV Photograph of a 2772°R, Single Point Injection Test using Cold Hydrogen for $V_f/V_a = 0.4$ (0.108" Spacing)	131
32	UV Photograph of a Pitot Probe during 2646°R Test	132
33	Ignition Delay Lengths for Single-Point Injection Tests (Cold Hydrogen)	133
34	Reaction Lengths for Single-Point Injection Tests (Cold Hydrogen)	134
35	Ignition Delay Lengths for Single-Point Injection Tests (Heated Hydrogen)	135
36	Reaction Lengths for Single-Point Injection Tests (Heated Hydrogen)	136
37	Ignition Delay Lengths of Three-Point Injection Tests (Cold Hydrogen)	137
38	Reaction Lengths for Three-Point Injection Tests (Cold Hydrogen)	138



# LIST OF ILLUSTRATIONS (Cont'd)

FIGURE		PAGE
39	UV Photograph of a 2664°R, Cold Hydrogen Test Run Viewed from Beneath - $V_f/V_a = 0.4$ , (1.108" Spacing)	139
40	Densitometry Plot of Point Injection Run 41B (5 Second Exposure)	140
41	UV Photograph of the Gas Sampling Probe during a 2700°R, Cold Hydrogen Test	141
42	Local Equivalence Ratio vs $T_a$ for Single-Point Injection Tests (0.216" Spacing)	142
43	Ring-Injection Test Setup	143
44	UV Photograph of a 2124°R Ring-Injection Test for Cold Hydrogen and $\phi = 1.0$	144
45	Ignition Delay Lengths for Ring-Injection Tests	145
46	Reaction Lengths for Ring-Injection Tests	146
47	Total Reaction Zone Lengths for Ring-Injection Tests	147
48	Schematic Representation of Theoretical Model	148
49	UV Photograph of the Air Stream at 3078°R	149
50	UV Photograph of a 3132°R Ring-Injection Test for Cold Hydrogen and $\phi = 1.0$	150
51	UV Photograph of a 3240°R Ring-Injection Test for Cold Hydrogen and $\phi = 0.5$	151
52	Local Equivalence Ratio vs $T_a$ for First Series of Ring-Injection Tests	152
53	Local Equivalence Ratio vs $T_a$ for Second Series of Ring-Injection Tests	153
54	Experimental Static Enthalpy Values for First Series of Ring-Injection Tests	154
55	Experimental Static Enthalpy Values for Second Series of Ring-Injection Tests	155

# LIST OF ILLUSTRATIONS (Cont'd)

FIGURE		PAGE
56	Variation of $\phi_{\ell}/\phi_{\text{Eff}}$ with $T_a$ for Ring-Injection Tests	156
57	Variation of $\phi_{\ell}/\phi_{\text{Eff}}$ with Measured Temperatures for Ring-Injection Tests	157
58	Three-Combustor Segments	158
59	Three-Segment Combustor Configuration	159
60	Pressure Distribution Inside Segmented Combustor Air Temperature 2100°R (One Segment)	160
61	Pressure Distribution Inside Segmented Combustor Air Temperature 2700°R (One Segment)	161
62	Pressure Distribution Inside Segmented Combustor Air Temperature 2100°R (Two Segments)	162
63	Pressure Distribution Inside Segmented Combustor Air Temperature 2700°R (Three Segments)	163
64	Pressure Distribution Inside Segmented Combustor Air Temperature 2100°R (Three Segments)	164
65	Pressure Distribution Inside Segmented Combustor Air Temperature 2700°R (Three Segments)	165
66	UV Photographs of Exit Plane of the Combustor $T_a = 2106^\circ\text{R}$ -Cold Hydrogen - $\phi = 1.0$	166
67	UV Photographs of Exit Plane of the Combustor $T_a = 2700^\circ\text{R}$ -Cold Hydrogen - $\phi = 1.0$	167
68	Wall Temperature Distributions for First Combustor Test Series	168
69	1-Segment Combustor Heat Rejection Rates - First Combustor	169
70	2-Segment Combustor Heat Rejection Rates - First Combustor	170
71	3-Segment Combustor Heat Rejection Rates - First Combustor	171
72	Local Equivalence Ratio for the First Series of Combustor Tests	172

# LIST OF ILLUSTRATIONS (Cont'd)

FIGURE		PAGE
73	Experimental Static Enthalpies for the First Series of Combustor Tests	173
74	Comparison of Combustor Contours	174
75	Modified Combustor Contour	175
76	UV Photograph of the Exiting Combustion Zone $T_a = 3105^\circ\text{R}$ - Cold Hydrogen - $\phi = 1.0$	176
77	Pressure Distribution Inside Segmented Combustor - $\phi = 0.5$ Air Temperature = $2700^\circ\text{R}$ , (Modified Combustor)	177
78	Pressure Distribution Inside Segmented Combustor - $\phi = 1.0$ Air Temperature = $2700^\circ\text{R}$ (Modified Combustor)	178
79	Temperature Distribution in Segmented Combustor $2700^\circ\text{R}$ Air Runs	179
80	Temperature Distribution in Segmented Combustor Hydrogen Runs	180
81	Pressure Distribution Inside Segmented Combustor Air Temperature = $3100^\circ\text{R}$ (Modified Combustor)	181
82	Temperature Distribution in Segmented Combustor - $3100^\circ\text{R}$ Air Runs	182
83	Temperature Distribution in Segmented Combustor - Hydrogen Runs	183
84	Local Heat Rejection Distribution in Segmented Combustor - Second Combustor	184
85	Comparison of Pressure Data for the $2700^\circ\text{R}$ Modified Combustor Tests	185
86	Comparison of Pressure Data for the $2100^\circ\text{R}$ Modified Combustor Test (Cold Hydrogen)	186
87	Comparison of Pressure Data for the $3100^\circ\text{R}$ Modified Combustor Tests (Heated Hydrogen)	187
88	Comparison of Total Heat Transfer Data for a $T_a = 3100^\circ\text{R}$ , $\phi = 1.0$ , Cold Hydrogen Test Run	188

## LIST OF ILLUSTRATIONS (Cont'd)

FIGURE		PAGE
89	Displacement Thickness Distribution for the Same Test as in Figure 88	189
90	Total Skin Friction Drag for the Same Test as in Figure 88	190
91	Plot of Sodium Line Reversal Data for Temperature Determination	191

## LIST OF TABLES

TABLE I	BRIGHTNESS TEMPERATURE AT THE ARC STREAM AS A FUNCTION OF NEUTRAL FILTER DENSITY	19
TABLE II	POINT AND THREE-POINT INJECTION DATA (0.108" SPACING)	89
TABLE III	SINGLE-POINT INJECTION TEST DATA (0.216" SPACING)	90
TABLE IV	RING INJECTION TEST DATA	93
TABLE V	ORIGINAL COMBUSTOR DATA	98

## INTRODUCTION

One of the most important problem areas related to the development of a hypersonic air-breathing vehicle is that of the supersonic burning of hydrogen in air. Most of the earlier work in supersonic combustion dealt with the detonation type of combustion where premixed fuel and oxidizer entering the combustion chamber experience sufficient rise in static pressure and temperature, due to the wave pattern there, to initiate combustion. In this mode of combustion, the premixing of the fuel and oxidizer occurs upstream of the combustor in a region where the static pressure and temperature are sufficiently low to preclude the possibility of chemical reaction occurring.

Some of the earlier work in this field was carried out by Gross and Chinitz (Reference 1), Nicholls (Reference 2) and more recently Rhodes, et al (References 3 and 4). The outcome of these investigations have indicated certain difficulties which would exist in applying this scheme to an engine system; namely, the large total pressure losses incurred and the general high pressure and temperature level of operation required of the combustor.

In recent years, a great deal of interest has been generated into the possibility of utilizing deflagration or diffusion flames in supersonic combustion. For this mode of combustion, the mixing and burning mechanisms are intimately connected since the onset of combustion greatly enhances the rate of mixing. Particular applications of the low speed fuel jet concepts, introduced in Reference 5, to hypersonic air-breathing vehicles was first suggested by Ferri in Reference 6. The use of this mode of supersonic combustion exhibits several advantages over the detonation mode of burning. In diffusion burning, the flames are controlled by the mixing of the injected fuel with the oxidizer, while additional thrust is derived from the injected fuel without encountering the usual total head losses inherent in the detonation mode of burning.

The ideas and concepts introduced in Reference 6 were further developed in Reference 7 where the possibility of utilizing supersonic diffusion flames in hypersonic ramjet operation was investigated. Results of the investigation indicated that a ramjet, using hydrogen fuel, can produce large thrust per unit frontal area and can operate at a high specific impulse even at hypersonic speeds. Another investigation into the possibility

of using supersonic combustion diffusion flames in hypersonic ramjet operation is presented in Reference 8.

Since the fuel of greatest interest to the supersonic combustion concept of burning is hydrogen, a great deal of interest has been directed to the chemical kinetics of the hydrogen-air system. Various studies into the reactions and reaction rates composing the hydrogen-air system have been presented in References 9-11, while additional studies in supersonic combustion have been reported on in Reference 12-17.

In the present study, an experimental investigation was conducted to determine the effects of controlled variations in pertinent mixing and combustion parameters such as air static temperature, fuel total temperature, fuel-air equivalence ratio, fuel-to-air velocity ratio and the spacing between the fuel and air streams. Single point, three point and peripheral (ring) injection configurations were tested during the free-jet portion of the program in order to determine their relative effect on general combustion zone characteristics, such as ignition delay and reaction length. It was originally intended to use the free-jet peripheral injection data as an aid in designing the segmented combustor contour required for the Phase II portion of the program. Due to scheduling requirements, however, it became necessary to utilize ring injection data accumulated in a previous in-house experimental study whose results have been presented in Reference 18. The present study can be considered a continuation of the work of Reference 18 which showed conclusively the feasibility of shock-free supersonic combustion utilizing both optical and photographic measuring techniques.

The authors wish to acknowledge the assistance of Messrs. A. Cravero and W.B. Champney in carrying out the experimental test program.

## DESIGN OF EXPERIMENTAL APPARATUS

### Arc-Jet Nozzle Design

As part of the test program requirements, a Mach 2.3 arc-jet nozzle was designed for exit conditions of 0.5 atm., 2700°R and a one inch exit diameter. The calculation of the nozzle contour is based on the method of Reference 19 where the regions of the nozzle are calculated from a combination of the source flow equations and the method of characteristics. The computer program of the method, obtained from NASA-Langley, also considers the boundary layer displacement effect on the inviscid nozzle flow. Some modification to the boundary layer portion of the program was necessary since the original program only treats nitrogen as the working gas.

Since the nozzle program only yields the supersonic contour away from the throat region, a separate analysis was required to evaluate the contour in the subsonic and sonic portions of the nozzle. A smooth subsonic contour is required which possesses a zero slope at the throat and a radius of curvature there matching the supersonic contour supplied by the program. These conditions together with the specification of the coordinates of the last calculated point of the computer program,  $x_p$ ,  $y_p$ , are sufficient to define a cubic representation in the supersonic portion of the throat region in the form

$$y = (y_p - y_* - \frac{x_p^2}{2R_t}) \frac{x^3}{x_p^3} + \frac{x^2}{2R_t} + y_*$$

where the throat radius of curvature is given by

$$R_t = \frac{2}{y_* \left( \frac{d^2 \frac{A}{A^*}}{dM^2} \right)_{x=0} \left( \frac{dM}{dx} \right)^2_{x=0}}$$

For the subsonic section of the nozzle a cubic curve fit was employed to insure the proper entrance dimensions necessitated by the existing arc-jet hardware.

#### Fuel Injection Conditions and Design

A study of fuel injection conditions and related geometry was undertaken early in the program to determine a consistent range of values for the set of parameters selected to be varied in the experimental supersonic combustion study. Controlled variations in air static temperature, fuel total temperature, equivalence ratio and fuel-air velocity ratio were the primary considerations regulating the design of the fuel injection system. In order to maintain a shock free environment for combustion, parallel fuel injection at a fuel static pressure equal to that of the air stream was imposed on the analysis used to obtain corresponding test conditions for the fuel injection system. The nomograph shown in Figure 1 is the result of the aforementioned analysis for a static pressure of 0.5 atm. and a Mach number of 2.3.

Four different fuel injection configurations were utilized in the test program. These included two single-point injectors, with fuel-air separation distances of 0.108" and 0.216" respectively, one three hole injector with a separation distance of 0.108" and a twenty-four hole ring injector with a 0.108" separation distance. The single-

point and three-point injectors were designed for  $\frac{A_f}{A_a} = 0.1$ , whereas for the ring injector the fuel-air area ratio was 0.195. A photograph of the fuel injectors used in the experimental test program is shown in Figure 2.

### Combustion Rig Design

The overall layout of the combustion rig utilized in the experimental program is shown in Figure 3. Details of the instrumentation, fuel injection geometry, cooling systems for the nozzle and segmented combustor and related hardware are shown in this figure. The combustor contour shown here was designed for constant pressure combustion for the conditions of parallel fuel injection, an air static temperature of 2700°R and an equivalence ratio of unity. Combustion tube cooling was accomplished by means of subcooled pool boiling. The experimental data of Reference 20 was utilized in the analysis of the combustion rig cooling system since the conditions under which the data was taken were almost identical to those of the present study.

The solid lines in Figure 4 represent a reproduction of the fairings through the data of Reference 20 while the dashed line is a correlation for forced convection surface boiling which is also given in the same reference. Forced convection surface boiling has the characteristics of being independent of the degree of subcooling and of velocity and presumably would approach the data of Reference 20 which were taken at very low velocities. The figure shows that this correlation gives an average of the data which is useful in estimating wall temperature. The nearly horizontal line on Figure 4 is an estimate of the maximum heat flux expected in the combustor tube for the design conditions. The intersection of this line with the forced convection line shows that the maximum tube outer wall temperature can be expected to be 288°F while a heat balance of the inner surface results in an expected temperature of 447°F.

Burnout heat fluxes given in Figure 4 were calculated by means of the correlation of saturated pool boiling data that was developed by Rohsenow and Griffith (Reference 21) and the equation giving the ratio of subcooled to saturated pool boiling burnout heat fluxes that was developed by Kutateladze and given in Reference 22. The burnout heat flux at  $T_g - T_b = 173^\circ\text{F}$  corresponds to the conditions expected in the segmented combustor.



Fuel injector surface cooling in the test setup was accomplished by means of water circulation in the upstream half of the injector. The downstream half of the injector surface was cooled by conduction through the beryllium-copper wall. Water flow rates in the cooling passage were calculated assuming that the resistance to flow occurred in the inlet and outlet tubes welded to the injector section and the injector surface itself. For an inlet pressure of 300 psia, the water flow rate was calculated to be 2.3 gallons per minute with a cooling passage pressure of 259 psia. At the Mach 2.3 test conditions, it was calculated that the water flow rate would maintain the inner and outer walls of the upstream half of the injector at 288°F and 298°F, respectively. The calculation also indicated a maximum injector surface temperature of 635°F at the Mach 2.3 condition, occurring on the downstream end of the air nozzle exit plane.

### Combustor Contour Design

The contour of the segmented combustor shown in Figure 3 is the result of an analytical study utilizing in-house engine cycle, chemical kinetics and turbulent boundary layer programs. The engine cycle analysis assumes a one-dimensional inviscid flow with constant area mixing prior to chemical reaction while the chemical kinetics program utilizes the best available reaction rates in determining the amount of heat released during reaction. An iterative procedure was employed in using these separate analyses to ensure that the proper combustor drag coefficient and total heat rejected were used in the cycle and kinetics calculations. As previously mentioned, the analytical design of the combustion zone contour was calculated for a constant pressure of 0.5 atm., 2700°R air static temperature, 1000°R fuel total temperature and  $\phi = 1$ , accounting for the displacement effect of the boundary layer. The ultimate variations in displacement thickness, total drag and total heat rejected along the combustor surface for the design conditions are shown in Figures 5, 6 and 7. A detailed description of the pertinent programs utilized in the analytical design of the combustor contour are presented in Appendix A of this report.

The analytical model used in designing the combustor contour did not account for any physical material separating the fuel and air streams as is required in practical applications. In order to maintain parallel fuel injection, it was required to displace the analytical contour to allow for the structural material required between the fuel and arc-jet air streams and that required between the fuel injector and the combustor

surface to allow sufficient machining tolerance to ensure the proper matching and alignment of the combustor to the fuel injection hardware.

### Combustor Off-Design Study

An analytical study was initiated early in the program to determine, analytically, the off-design conditions expected during the segmented combustor tests. In order to arrive at a good estimate for the off-design cases, it is necessary to have a proper accounting of all losses experienced inside the combustor. In general, this entails a complex iteration procedure between the viscous and inviscid flow calculations. In an attempt to speed up this calculation process, an approximate analysis was developed utilizing one-dimensional cycle equations together with the turbulent boundary layer equations to arrive at consistent initial values of  $C_D$  and  $Q_R$  needed in the cycle and kinetics programs. A complete description of the analysis, which is based on the equilibrium behavior of the  $H_2$ -air combustion products, is presented in Appendix B.

### DESCRIPTION OF ARC-JET FACILITY

The experimental test program was conducted at the arc-jet facility now owned by the Farmingdale Corporation. The arc heater used to supply the high temperature air for these tests is of the vortex-stabilized type. The configuration consists of a thoriated tungsten tipped cathode and a tubular copper anode, both supported in a water cooled head. An anode with 1.125 inch inside diameter and 18.00 inches long was used. The electrode gap can be adjusted continuously during operation of the arc-jet in order to optimize the arc voltage. Nitrogen is introduced with a helical motion through the arc gap to insure uniform heating and to prevent oxidation of the electrodes. Sufficient oxygen is added downstream of the arc heater to simulate the required composition and weight flow of air.

A transition piece expands the hot nitrogen emerging from the anode into a plenum chamber which is 3.50 inch inside diameter by 4.00 inches long. Both pieces are cooled by back surface high velocity water flow. Oxygen is injected radially into the upstream end of the plenum in order to obtain good mixing with the hot nitrogen. The sodium carbonate used for the sodium line reversal temperature measurements was also injected radially into the plenum to insure a more uniform distribution. A static pressure tap measured the plenum pressure for the determination of the air static conditions.

For the testing required in the present program the downstream end of the plenum terminated in a contoured  $M = 2.30$  air nozzle with a 0.6366 inch diameter throat and an exit diameter of 1.0052 inches. Cooling for the nozzle is accomplished by a high velocity flow of water over its back surface. A static pressure tap 0.125 inches upstream of the nozzle exit was used in maintaining a close match between the exit air static pressure and the test chamber static pressure.

Power for the electric arc heater is supplied by eight silicon-junction rectifier units, each rated at 120 kw. The eight units are connected in series for all tests in order to give the highest voltage across the electrodes. For starting purposes a high frequency, high voltage charge is superimposed on the DC output of the rectifiers, ionizing the gas and initiating the arc. Once the arc has been started, the high frequency voltage is discontinued as the DC arc continues to ionize the gas.

The arc generator and the tunnel components are cooled by circulation of distilled water at a rate of up to 400 gpm through a water-to-water tube-type heat exchanger. The heat removed from the distilled water by the heat exchanger was finally dissipated in a single stack cooling tower.

The test chamber consists of an 8-1/2 feet diameter by 30 feet long vessel. The test model is mounted at the upstream end at the centerline of the chamber. Eleven 12 x 48 inch windows longitudinally encircle the chamber, five of which are on the side of the chamber with the door and the remainder on the opposite side. Special UV transmitting windows, required for the optical measurements, were installed in the region of the test. Instrumentation ports on each side of the tank provide for 54 channels of thermocouple data, 30 manometer outlets, and other electrical signals.

Evacuation of the test chamber is accomplished by combining the last stage of the normal five stage steam ejection system with a parallel arrangement of two auxiliary steam ejectors. This combination gives a through flow rate of 0.655 lb/sec. at 0.5 atm. The inflow to the chamber reached this value when low air temperature, fuel rich runs were made.

Nitrogen is supplied to the arc generator and to the various purge locations from a liquid to gaseous nitrogen conversion plant. A 2600 gallon liquid nitrogen storage tank replenishes the gaseous nitrogen stored in the 214 cubic foot, 2200 psig vessels.

The capacity of the system is such that continuous operation is possible.

Oxygen added to the hot nitrogen to simulate air is supplied from a bank of 22 bottles initially pressurized to 2200 psig. Flow rates up to 0.075 lb/sec. are available. The capacity of this system is sufficient for several hours of operation. A nitrogen purging system was added to the oxygen supply in order to purge the lines of oxygen following each test.

The hydrogen fuel supply consists of eight bottles initially at 2200 psig pressure. During the test program the pressure was regulated at 100 or 50 psig dependent upon fuel flow requirements. Flow rates up to 0.0075 lb/sec. were controlled remotely from the control console through the use of nitrogen pressurized operator valves. For safety purposes the hydrogen system, including all controls and pressure transducers are kept outside the facility. The hydrogen fuel is fed to the fuel plenum after flowing through an electric heater which is capable of raising the gas temperature 500°F.

The hydrogen heater consists of a twenty foot length of Inconel X tubing one half inch in diameter. Two welding generators, each capable of up to 12 kw output, supply current to the heater. One generator is connected to the upstream half of the heater and the other to the downstream half. With both generators in operation, the temperature of the hydrogen could be raised 500°F in less than one minute. Once the elevated hydrogen gas temperature is reached, it is maintained by reducing the output of the welding machines. A thermocouple strapped to the hot end of the heater tube monitored the metal temperature. A second thermocouple, mounted in the hot hydrogen stream, indicates the temperature of the hydrogen entering the fuel plenum.

In the interest of safety, several procedures were followed to minimize the risks involved in utilizing hydrogen as a combustion fuel. The test chamber was evacuated to as low a level as possible before starting the arc head. The test chamber static pressure level required for testing was obtained and maintained by bleeding in purging nitrogen. Following a test, the hydrogen system was purged with nitrogen and the test chamber again evacuated to a low level before admitting air at atmospheric pressures. A MSA combustible gas detector was kept in operation at all times. The interior of the test chamber was sampled before and after each evacuation while the area over the test chamber was sampled during all testing. All test personnel were kept clear of the test

chamber during the light-off phase of the operation. If ignition of the hydrogen fuel was not achieved within thirty seconds after start of flow, the hydrogen flow was immediately shut down.

### INSTRUMENTATION

The instrumentation facilities that were used in the course of the experimental studies were comprised of:-

- a. Arc jet instrumentation for the determination of (1) electrical power input, (2) gas pressures and flowrates and (3) coolant water flowrates and temperatures.
- b. Photographic equipment for the recording of the combustion process using the radiations emitted during combustion.
- c. A high speed spectrometric system with associated optical train for temperature determinations of the combustion stream using the sodium line reversal technique and by use of the vibrational-rotational spectra of the OH radical in emission or absorption.
- d. Gas sampling and analyses equipment for the determination of hydrogen, oxygen, nitrogen, water and nitrogen dioxide in the gas stream.

## EXPERIMENTAL PROCEDURES

### Arc Jet Instrumentation

The arc jet was instrumented for the determination of electrical power input, gas pressures and flowrates and coolant water flowrates and temperature rise. These measurements were used for the calculation of enthalpies and gas temperatures.

The electrical power input was measured by a D.C. ammeter and voltmeter on the power supply. These meters are accurate to  $\pm 2\%$ .

The nitrogen flowrate was determined using standard A.S.M.E., technique. This technique employs a Bourdon pressure guage on the inlet side of a tube section with a sharp edge orifice. A Bailey differential pressure gauge spans the orifice. The maximum nitrogen flowrate was 0.260 lbs./sec. measured with an accuracy of  $\pm 2\%$  or  $\pm 0.0052$  lbs./sec.

The oxygen flowrate was measured in a similar manner. The maximum oxygen flowrate was 0.07 lbs/sec. measured with an accuracy of  $\pm 3\%$  or  $\pm 0.002$  lbs./sec.

The technique for the hydrogen flowrate measurement was similar to the nitrogen and oxygen measurements but it differed in that the pressures were measured by calibrated pressure transducer systems. The maximum hydrogen flowrate was 0.006 lbs/sec. measured with an accuracy of  $\pm 3\%$  or  $\pm 0.0002$  lbs/sec.

The stagnation enthalpy (H) was determined by the use of two standard methods:

1. Heat Balance Method

At the exit of the arc-jet nozzle

$$H = \frac{\text{Volts} \times \text{Amperes} \times 0.05689 \left( \frac{\text{BTU}/\text{min}}{\text{watt}} \right) - \dot{w}_{\text{H}_2\text{O}} (\text{lbs}/\text{min}) \times (\Delta T_{\text{F}})}{\dot{w}_{\text{air}} (\text{lbs}/\text{min})}$$

For this method the error is estimated to be  $\pm 5\%$ .

## 2. Choked Nozzle Method

At the nozzle throat

$$\frac{1}{H} \approx \frac{\dot{w}_{\text{air}} \text{ lbs/min.}}{P_T A^*} \quad \text{where } P_T = \text{plenum pressure}$$

$A^* = \text{throat area}$

The error incurred for this method is also  $\pm 5\%$ .

The losses in the nozzle from the throat to the exit are subtracted from the choked nozzle value. The enthalpies obtained by both methods were then averaged. The uncertainty of this average enthalpy was estimated to be  $\pm 5\%$  of the test value.

### Photography

The camera system for the recording of combustion streams using the ultraviolet radiation of the OH radical at 3064 angstroms wavelength was comprised of a 4" x 5" Speed Graphic camera body fitted with special accessories. These accessories included a Graflex 120 Roll Holder back and a lens board fitted with an Ilex No. 2 Acme Synchro shutter and a Carl Zeiss Jena UV achromatic lens 4.5/120 6616896. The filters used with the lens were Zeiss 42 UV" mit 42 UV' 313 nm. and a 42 UV' 280-380nm. The lens and filters were purchased from the Ercona Corporation., N.Y.C., N.Y. Since the lens is a quartz-rock salt achromat, it was stored in a dessicator over anhydrous silica gel when not in use.

The film used in most of the ultraviolet photography was Kodak Tri-X. Exposures ranged from 5 second at f/4.5 for 2100°R air temperature combustion runs to 0.1 second for 3100°R air temperature combustion runs. Probe exposures were 1/25 second at f/4.5. The Tri-X film was developed using Acufine Industrial Film Developer manufactured by the Baumann Photo. Chemical Corporation 125 West Hubbard Street, Chicago 10, Illinois. The development procedure, 6 1/2 minutes at 68°F, increases the film speed to ASA 1200. Film fix and rinsing were done conventionally.

Color photographs were taken of each run with a Honeywell Pentax 35 mm. single lens reflex camera fitted with an Auto-Takumar lens 1:3.5/35 57262 made by the Asahi Optical Company Japan.

Kodak Ektachrome-X film was used with exposures of 1/8, 1/15, 1/30, 1/60 second for the combustion runs and 1/60 second for the probe runs. The lens was not stopped down. Film development was carried out in accordance with Kodak procedures.

Various changes in the photographic system were attempted in order (1) to improve the signal-to-noise ratio in the ultraviolet photography of the OH radical at 3064 angstroms wavelength, and (2) increase the speed of recording and processing the films (an attempt at "on spot" picture retrieval). A spike filter was purchased from the Perkin-Elmer Corporation, Norwalk, Conn. This filter had a narrow band-pass at 3064 Å and had good sideband rejection down to 2000 angstroms and up to 7000 angstroms. Since the arc jet combustion flame produces radiation from other species i.e., nitrogen oxide and atomic oxygen, the recording of the combustion stream using the radiation from the OH band at 3064 angstroms requires the severe filtering out of spurious radiation. This problem is magnified tremendously when one considers that photographic recording is an integrating device and background integration over a wavelength range of 5000 angstroms can easily nullify the effect of signal integration over a wavelength range of 100 angstroms. A curve showing the efficacy of the Perkin-Elmer spike filter is shown in Figure 8. This should be compared with the curve of the Zeiss ultraviolet filter shown in Figure 9. We were unable to get focused pictures when using the spike filter. Discussions were conducted with the Perkin-Elmer Corporation, fabricators of the spike filter and the Fish-Schurman Corporation, distributors of Schott glass filters, in order to resolve the poor image definition. The spike filter consists of two 3 mm. thick pieces of Schott UG-11 glass filters which sandwich a thin film layer. While conceding that a problem area exists, they would do nothing more than offer suggestions as to the possible cause. These possible cause(s) are:

1. the parallelity of the glass substrate may not be fine enough and the glass substrates may have some optical power.
2. the filter is translucent instead of transparent
3. the glass substrate (Schott UG -11) contains ultraviolet scattering centers.
4. the glue that binds the two glasses may be fluorescent in ultraviolet light.
5. the Schott UG-11 is susceptible to radiation damage by ultraviolet light forming a coating on the glass. This coating, either on the outside of the filter or in contact with the thin film may fluoresce or scatter the ultraviolet light.



The narrow band pass and the sideband rejection of this filter are such worthwhile characteristics for use in combustion studies that we feel it is worthwhile to isolate the cause of the poor image definition of the spike filter.

Early photographic work using the beam-splitting attachment for recording the combustion stream images in the ultraviolet and the infra-red using Polaroid film showed that details like weak shock wave structure was lost on this film. One needs to look at a negative in transmitted and reflected light in order to obtain the most information about the combustion stream. The Polaroid film, while photographically fast, did not satisfy this requirement and was therefore replaced with Kodak Tri-X. Ideally, combustion streams should be examined by multicolor laser holography. This new technique would provide three dimensional analyses of color (chemical species) in the combustion stream.

#### Spectrometry

Combustion temperatures are obtained by spectral measurements of various optically active species in the combustion stream. These measurements were accomplished by use of a spectrometer system and an optical train containing assorted optics. This system was designed for use with any one or combination of standard techniques of temperature measurement i.e., sodium line reversal, OH radical in emission or absorption.

The spectrometer system is comprised of a Jarrell-Ash 0.5 Meter Ebert Scanning Spectrometer model 82-000, an EMI 9526S photomultiplier detector and a Jarrell-Ash Model 82-110 Recording Electronic System.

The scanning spectrometer was fitted with an 30,000 line per inch diffraction grating blazed for a wavelength of 7500 angstroms in 1st order. The spectrometer specifications with this grating are as follows:

spectral range	2000-8000A° (1st order)
effective aperture ratio	f/8.6
reciprocal linear dispersion	16A°/min.
resolution	0.2A°
scan speed	2-500A°/min.

The detector used in this spectrometer is an EMI 9526 S photomultiplier whose specifications are:

spectral response	"S" (Q)
average sensitivity	50 Microamperes/Lumen
cathode-D1 volts	100
anode sensitivity	2000 Amperes/Lumen
gain	$40 \times 10^6$
dark current	$5 \times 10^{-9}$ Amperes
overall volts	1700

The voltage divider for the tube was constructed as follows:

1. cathode - D1 resistance 680 K ohms
2. D1 - D11 - ground 1 megohm
3. cathode negative high voltage
4. dynode D-11 through 1 megohm to ground positive high voltage
5. all resistors 1/4 watt

The recording system used with the spectrometer was a Jarrell-Ash Model 82-110 Recording Electronic System. This system consists of a stabilized high voltage, 400-2000 volt, d-c power supply for 9 and 13 stage photomultiplier tubes, a high gain stable electrometer amplifier and a Bristol Dynamaster Recorder for read-out.

#### Spectrometer Alignment and Wavelength Calibration Procedure

The maximum utilization of a spectrometer system for sensitivity and resolution is attained when the following conditions are satisfied:

1. the collimating mirror solid angle with the slit is filled with the light incident on the entrance slit.
2. the first diffraction pattern of this light is made to just fill the collimating mirror by closing the entrance slit.
3. the wavelength scan rate and the time constants of the detector circuit, amplifier and recorder are matched.
4. impedances of the amplifier output and recorder input are matched so that the signal is not attenuated by loading the amplifier.

5. the internal optics of the spectrometer are aligned so that the image of a point on the entrance slit is in the identical position on the exit slit and
6. the entrance slit, exit slit and diffraction grating lines are closely parallel with each other. In this spectrometer system, the slits are curved while the diffraction grating lines are straight, thereby making alignment more difficult.

Great care was placed on spectrometer internal alignment because of the resolution need in the recording of OH radical band spectra at 3064 angstroms wavelength.

Thin wires (0.005" diam.) were placed across the horizontal centers of the entrance and exit slits and the collimating mirror. The instrument was leveled and the instrument checked with a Pye cathetometer to see if all wires were in the same horizontal reference plane. With this accomplished, the room was darkened and the wire on the entrance slit illuminated, the position of the image of the wire on the exit slit was noted using the grating in zero order. The image traverse of the exit slit was also made. Grating tilt in the forward and backward positions was adjusted to bring the wire on the exit slit and the image of the wire from the entrance slit into correct juxtaposition. The wires were then removed and the entrance slit set at 50 microns and illuminated using a Gates Pen Ray Mercury Lamp. The traverse of the visible images of the mercury spectral lines across the exit slit was studied using the first and second order spectra on both sides of zero order. Grating tilt in the forward and backward direction was more finely adjusted while the coarse adjustment of sideways grating tilt was adjusted to bring the traverse loci on the horizontal plane. The fine sideways grating tilt was adjusted using the spectrometer scan and readout of the mercury doublet spectral lines at 3131.55 and 3131.83 angstroms wavelength in second order as shown in Figure 10. This latter adjustment is time consuming and has to be done with great care in order to bring about the best resolution of this doublet.

After alignment was completed, the grating was indexed and locked for zero wavelength with zero order filling the exit slit. A scan of the wavelengths of spectral lines from the mercury lamp was made as a function of wavelength readout on the grating drive counter. The readout was within 2 angstroms of the true wavelength.

## Optical System

The purpose of the optical train was to efficiently relay the radiations used for the determination of combustion stream temperature by sodium line reversal and OH radical spectra to the spectrometer system for analytical scan and readout.

The optical system (20 ft. long) consists of a standard light source, a relay imaging system for the stepwise attenuation of the standard light source by the use of a neutral density stepped filter, a second relay imaging system to pass the beam through the center of the arc stream followed by a quartz lens collection and imaging relay system to pass the attenuated beam to the readout spectrometer. This last collection and relay system is also used to pass the OH radical emission at 3100 angstroms wavelength to the spectrometer and therefore must be made of quartz lenses and front surface aluminum mirrors with high light collection efficiency. A detailed diagram of the system is shown in Figure 11.

The focal length of the lenses and the distances between optical elements are as follows:

<u>Lens</u>	<u>Focal Length</u>	<u>Effective Diameter</u>	<u>Remarks</u>
A	1"	1"	Glass
B	17"	2"	Quartz
C	17"	2"	Quartz
D	19"	2"	Quartz with variable stop at 1 1/8 diam.

<u>Optical Elements</u>	<u>Distance (Inches)</u>
lamp filament to lens A	3 1/2
lens A to stop (slit 1/2" x 1/8")	1 1/2
stop to lens B	19
lens B to relay mirror	29 1/2
relay mirror to stream center	58 1/2
stream center to lens C	17
lens C to relay mirror	41 1/2

relay mirror to lens D (stop 1-1/8" d)	34
lens D to spectrometer slit	19

### Optical Alignment Procedure

The arc jet chamber has two ten foot optical benches, one at each side of the chamber. The tank had two five foot Rohm & Haas UVT Plexiglas windows (1/4" thick). The windows and benches were situated at the nozzle end of the chamber. The benches were leveled to within 0.01 centimeters using a Pye cathetometer. The Plexiglas windows transmit the ultraviolet radiation; the transmission curve is shown in Figure 12. Lens and mirror positioning was accomplished by relaying a leveled collimated light beam through the center of the arc stream to the quartz collecting and relay system. The system was adjusted so that the focussed image of the standard lamp on the spectrometer slit did not move when the relay mirrors changed the light beam to all positions corresponding to the plane of the combustor tube ends. A small optical bench was mounted within the chamber and ruggedized. Quartz collection lenses were set on this bench on the optical axes corresponding to the plane of the combustor tube ends and set at their focal length ( $\sim 17$  inches) from the center of the arc stream. The focal length of the lenses was the minimum allowable because of the arc swing of the gas sampling probe. The optical image of the standard lamp did not move when the beam was moved through the various positions. An alternate alignment method made use of the Pye cathetometer and showed no discrepancy with the optical beam alignment. Essentially, alignment with the Pye cathetometer consists of leveling the telescope, determining the setting for the center of the nozzle, indexing both sides of the chamber for nozzle center, and finally the centering of all lenses, spectrometer slit, spectrometer collimating mirror and standard source filament.

Care was taken to assure that the positions for lens D was such that the ultraviolet image of the arc stream was focused on the spectrometer slit. This was done by maximizing spectrometer readout for the Hg. 3131.83 angstroms spectral line from the mercury lamp situated in the arc stream.

### Light Source Calibration Procedure

The light source used to supply a continuum of known brightness temperature for the sodium line reversal experiments consisted of a G.E. tungsten ribbon pyrometer lamp, serial no. 431-P-408, rated as 20 amperes, 6 volts. This lamp was

connected to the secondary of a 20 ampere Variac A.C. source which was monitored by a Weston Model 904 No. 5478 A.C. Ammeter U.S.A.F. No. 17111. The Plexiglas window on the spectrometer side of the arc jet chamber was removed so that a calibrated optical pyrometer would focus on the relayed image of the lamp filament focused at the center of the arc stream. The brightness of this image is calibrated at the exact position where the sodium line reversal measurements take place so that corrections for window and lens transmission and mirror reflection losses are not needed. The micro optical pyrometer model No. 95 serial No. M4461, manufactured by the Pyrometer Instrument Co., Inc. Bergenfield, N.J. was standardized against a certified National Bureau of Standards standard lamp. The pyrometer calibration curve is shown in Figure 13. The calibration curve of the lamp for the light source is shown in Figure 14. This curve was used to arrive at a constant current setting (17.9 amperes) for the lamp which would provide a brightness temperature of 4200°R at the arc stream without an attenuation filter in the optical path. The brightness temperature of the filament image is then successively decreased by the use of Kodak Wratten neutral density filters. This arrangement serves to expedite the temperature determination during the run by the judicious choice of filters for the temperature encountered. Table I shows brightness temperature at the arc stream as a function of filter density. The arc jet chamber window was replaced when calibration was completed. A second calibration of the standard lamp was done using a pyrometer calibrated at the National Bureau of Standards. Both calibrations were within 10°C of each other at 1800°C.

#### Temperature Measurement by Sodium Line Reversal Technique

The technique of sodium line reversal for temperature measurement is accomplished as follows: A sodium salt is continuously injected into a flame at a rate that (1) provides medium intensity sodium resonance lines at 5889.95 and 5895.92Å and (2) does not influence the flame temperature. Light from a continuum source, (a standard lamp) is then brought to a focus on the center of the flame. When the temperature of the continuum source is less than that of the flame, the sodium lines are read out in emission. When the temperature of the continuum source is greater than that of the flame, the sodium lines are read out in absorption. The temperature of the flame is equal to that of the source when the sodium lines match or are indistinguishable from the continuum or background.

TABLE I  
BRIGHTNESS TEMPERATURE AT THE ARC STREAM AS A FUNCTION OF  
NEUTRAL FILTER DENSITY

<u>Neutral Filter Density</u>	<u>Brightness Temperature (°R)</u>
0	4334
0.1	4150
0.2	4064
0.4	3795
0.7	3580
1.0	3290
2.0	2642
3.0	2291

The sodium salt injection system uses a Metco Type MP Powder Feed Unit manufactured by the Metallizing Engineering Co., Inc. Westbury, N. Y. and is shown in Figure 15. The unit consists of a pressurized hopper, a vortexing mixer and a vibrator and was previously used for plasma flame spray powder work. A schematic of the system is shown in Figure 16. This system was pressure tested to 160 psig. The sodium salt was finely powdered dry sodium bicarbonate. Injection into the plenum chamber was accomplished using dry nitrogen at a pressure of 10 psig above the plenum pressure (~ 90 psig).

The instrument settings for spectrometer readout were as follows:

photomultiplier voltage	1100 volts
electrometer amplifier range	$10^{-7}$ amperes
scale factor	$\times 10$
time constant	1
recorder chart speed	4 $\frac{1}{2}$ inches/min.
spectrometer slit width	20 microns
scan rate	20A°/min.

Typical readout for sodium line reversal measurement is shown in Figure 17. The temperature was determined to be 3520 °R. The calculations are shown in Appendix C. The brightness temperatures were varied during the run by the judicious selec-

tion of attenuation filters for the combustion stream temperatures encountered. It should be noted that this technique was the only one that could be used for the temperatures encountered in these experiments (3400 - 4200°R). In some instances, the spectral readout was winged showing various peaks and dips either side of where the spectral line position should have been. This indicates a multi-zone region where the temperatures in the inner and outer cones was markedly different. It was not possible to determine a temperature for this region.

#### Temperature Measurement by OH Radical Emission and Absorption Technique

Great care was taken with the spectrometer and optical systems to provide high sensitivity, good resolution and rapid scan rate for temperature determinations by OH radical emission in the  $R_2(0,0)$  band at 3064 Å wavelength. The spectrometer system had a sensitivity 50 times greater than previously used systems and a complete scan of the OH  $R_2(0,0)$  band could be done in fifteen seconds. We were unable to record OH spectra, using either emission or absorption techniques, in the combustion runs done in this study. To rule out equipment problems, a Bethlehem burner was set up at the point where the arc stream and optical train intersect. The OH radical  $R_2(0,0)$  band was read out from stoichiometric air-hydrogen and oxy-hydrogen flames. Temperatures for the air-hydrogen flame approximate 4300°R and for the oxy-hydrogen flame 5500°R. We have not been able to measure temperatures lower than 4200°R by OH radical emission or absorption.

It is apparent from the sodium line reversal temperatures determined in this study (range from 3400-4200°R) that combustion temperatures were too low to be measured by OH radical spectra. It should be remembered that an optical problem with the instrumentation did exist. During combustion runs, the heating of the arc chamber caused the focused image to move off the spectrometer entrance slit. Since the radiation from the combustion stream is very weak, this movement cannot be visually discerned and corrected unless the image of the standard lamp in the arc stream is relayed to the spectrometer. Correction of the image at the spectrometer was done by adjusting the relay mirror. The image moves in the opposite direction when the arc chamber is cooling. Apparently, the image shift is due to arc chamber expansion. We were unable to record OH spectra even with corrections for image shift.



## Gas Analysis

The gas sampling equipment consists of a gas sampling probe and gas collection and storage equipment. The gas sampling probe was fabricated according to the design of the Applied Physics Laboratory of Johns Hopkins University. The probe was scaled up a factor of two; detailed drawings are shown in Figures 18, 19, and 20. A photograph of the gas sampling probe is also shown in Figure 15. The probe was mounted on a pneumatically driven arm as shown in Figure 21. Probe position longitudinally and vertically in relation to the arc stream had to be pre-set prior to the run and could not be moved during the run. The probe arm swings into the stream at a shallow angle requiring the placement of spectrometer collector optics (3" diam. lens) at no less than 17 inches from the arc stream. The water coolant for the probe was vented into the tank atmosphere during the run. Ideally, the probe should be designed so that the water does not vent into the atmosphere and probe location can be changed from outside the chamber during a run.

Two gas collection and storage systems were fabricated. The first system consists of three 450 ml. gas bottles, each with its own electrical solenoid valve, shut-off valves, pressure gauge, capillary delivery tube and demountable stainless steel cold trap and is shown in Figure 22. A schematic of the system is shown in Figure 23. The second system is a single bottle system similar in construction to the first. The systems were checked for leaks by evacuating to 30 inches Hg. vacuum and closing the valve leading to the pump. The system was opened from the solenoid valve, through the cold trap, through the gauge and storage bottle to the pump valve. Each system held the vacuum for three days. The probe line from the probe tip to the collection and storage system was checked for leaks in a similar fashion.

The gas sampling was accomplished as follows: The gas collection and storage system was evacuated to 30 inches Hg. vacuum with valves in the following position:

- solenoid valve closed
- capillary delivery tube valve closed
- valve between trap and bottle opened
- valve between trap and solenoid valve opened

When the vacuum inside the system was 30 inches Hg, the valve to the vacuum pump was closed. Crushed dry ice was placed in a Dewar flask around the dry tared cold trap immediately prior to sampling. The probe with coolant water flowing was driven into the stream. The line from the probe to the gas sampling system was pumped with the vacuum pump for at least 20 seconds before the solenoid valve was tripped and a sample collected. Two methods were used in collecting samples, (1) the gas stream entering the probe was subjected to a vacuum in order to swallow the bow shock wave and to provide the pressure differential needed to fill the gas bottle, and (2) the gas stream was closed to vacuum through a valve after the sample header was purged. Under the first condition, the bottle pressure approaches the tank pressure which is approximately 0.5 atmospheres while for the second approach the bottle pressure registered 2 atmospheres, which is approximately the pitot pressure behind the detached bow shock wave. Since the chemical composition of the gas stream changes when passing through the bow shock wave, it was decided to use the first approach for gas sampling and to adapt the gas chromatograph analyses procedure for sample injection at reduced pressure. When sampling was completed, all valves were closed, the dry ice removed and the traps demounted and capped with numbered tared rubber stoppers. Each trap was numbered and had its own stoppers with which it was already tared.

#### Analytical Technique

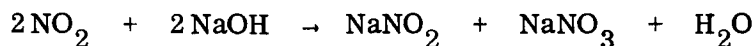
The analysis of the gases from the combustion stream consists of three separate procedures, (1) the analyses for water by weight differences in the tared cold trap, (2) the analyses of  $\text{NO}_2$  by titration of the contents of the cold trap with standardized dilute sodium hydroxide solution using phenolphthalein solution as the indicator and (3) the analyses of hydrogen, oxygen and nitrogen in the cylinder by gas chromatography.

The stoppered cold trap was warmed to room temperature and the outside of the trap dried. It was then weighed on a Christian Becker Analytical Balance Model AB-B Serial No. A-18441. Each cold trap was weighed to the nearest milligram. Balance capacity was two kilograms; the cold traps weighed in the vicinity of 200 grams and each trap was weighed to the nearest milligram. Each trap was emptied into a clean 25 ml. beaker and washed with 4 x 4 ml. distilled water. Three drops of phenolphthalein solution was added and the sample titrated with 0.0102 N. sodium hydroxide solution for the analysis of  $\text{NO}_2$ . The trap was rinsed with acetone, dried in an oven for 1/2

hour, reweighed with its own stopper. The differences in weight in the two readings was the water content in the sampled volume (470 ml.).

The procedure used to convert titration results into  $\text{NO}_2$  concentrations was as follows:-

The chemical equation for the reaction of  $\text{NO}_2$  with sodium hydroxide is



according to Prescott and Johnson's "Qualitative Chemical Analysis" p. 470, 1933. Since the number of milliequivalents of NaOH (milliequivalents = normality of base X the volume (ml.) required for neutralization) equals the number of milliequivalents of  $\text{NO}_2$ , this product (normality X volume (ml.)) is then multiplied by the milliequivalent weight of  $\text{NO}_2$  (0.046g) to give the weight of  $\text{NO}_2$  in the 470 ml. sample of gas.

The gas analysis was done by using a Burrell Kromo-tog gas chromatograph. The chromatograph is shown in Figure 24. The instrumental settings for the analysis of hydrogen, oxygen and nitrogen are as follows:

Column - 8 ft. long glass U tube

Absorbent - Molecular Sieve 5A° conditioned for 5 hrs. at 200°C in Argon -

Carrier Gas - Argon 75 ml./min.

Thermal Conductivity Detector - 160 ma.

Preheater Temperature - 20°C

Column Temperature - 20°C

Fractionator Temperature - 20°C

Detector Temperature - 20°C

Recorder Chart Speed - 1"/min.

Gas Injector Volume - 1 ml.

The gas injector has a loop which contains a standard volume (1 ml.). The injector was reworked so that it would not leak at reduced pressures. The injection procedure consisted of pulling 760 mm. Hg vacuum on the injector which had a mercury manometer and the sample bottle delivery tube attached to it. All tubing was 3/32" capillary to minimize dead volume and preserve sample gas. The gas from the sample bottle was used to backfill the injector system to a 500 mm. Hg vacuum. In some cases, backfill was done to 680 mm. Hg vacuum, depending upon the bottle pressure.

A series of primary gas standards was purchased from the Matheson Company, East Rutherford, New Jersey. Chromatograms were recorded and peak heights were plotted against the mole fraction of gas in the mixture. These working curves are shown in Figures 25, 26 and 27. The standards were run with each set of analyses to serve as indexing points for possible curve shifts. Typical chromatograms are shown in Figure 28.

The precision of the gas analyses for the determination of hydrogen, oxygen and nitrogen was  $\pm 1\%$ ,  $\pm 1.7\%$  and  $\pm 3.7\%$ , respectively. The nitrogen determinations were very much dependent upon the precise control of carrier gas flowrate. The precision of the analyses of  $\text{NO}_2$  and  $\text{H}_2\text{O}$  was estimated to be  $\pm 2\%$  and  $\pm 1.5\%$  respectively. It should be emphasized that gas standards were run prior to each set of analyses in order to compensate for working curve shifts and that a curve shift for one gas did not necessarily mean the curves shifted for the other gases. These day-to-day curve shifts are the reasons why the analytical values taken from the typical gas chromatograms do not check exactly with the values taken from the typical working curves.

The method used in the determination of the local equivalence ratio, based on the results of the gas analysis, is presented in Appendix E. The water collected in the cold trap did not match the water that should have been formed there due to oxygen and nitrogen mole fraction changes. This anomaly could be the results of a) water by-passing the probe due to local mass diffusion caused by concentration gradients, b) condensation in the cold trap is incomplete and c) the possibility of some nitrogen entrainment or oxygen depletion, in the free-jet cases, due to the mixing which occurs at the outer regions of the arc-jet stream.

During some of the earlier tests of the experimental program, a few gas samples of the arc-jet air stream were taken in checking out the operation of the gas sampling probe. The limited number of air samples collected were at sufficiently different downstream locations to adequately cover the range of interest. The pertinent data for these test runs are as follows:

Run No.	$\dot{w}_{\text{O}_2} \left( \frac{\text{lbs.}}{\text{min.}} \right)$	$\dot{w}_{\text{N}_2} \left( \frac{\text{lbs.}}{\text{min.}} \right)$	$T_a (^{\circ}\text{R})$	$X_{\text{O}_2}$	$X_{\text{N}_2}$	Sampling Location
26	3.51	10.9	2610	0.20(0.19)	0.80(0.79)	2" (on center)
31	3.00	10.85	2349	0.175(0.18)	0.825(0.83)	12" (on center)
43A	3.282	11.0	2727	0.20(0.10)	0.81(0.89)	17 5/8" (1/8" low)

The mole fractions in parentheses indicate the composition obtained from samples collected without the vacuum system operating. For some unexplainable reason it appears from the data that the probe bow shock was not swallowed in Runs 26 and 31 even where the vacuum was applied. As a consequence, the input ratio of nitrogen to oxygen could not be checked with the ratio obtained from the sample. The ratio of nitrogen mole fraction to oxygen mole fraction based on mass flows input to the arc-jet was 3.547 for Run 26 and 4.131 for Run 31 while the gas analyses yielded 4.0 and 4.71 respectively. This constitutes an 11.3% deviation due to the unstart condition of the gas sampling probe for Run 26 and 12.3% for Run 31. Accordingly, it can be argued from the data that the contribution of arc-jet air mixing with the ambient nitrogen can not be more than a few percent at the 12" position. The initial conditions for these two tests were sufficiently similar (261°R variation in air temp) to justify the comparison. In Run 43A, as in the remainder of the test runs, the data indicated the proper operation of the gas sampling probe under vacuum conditions. For this case the ratio of nitrogen to oxygen introduced into the system was 3.828 by mole while that obtained from the gas analysis was 4.05. The 5.48% deviation between these two values at the 17 5/8" location is most likely due to an combination of nitrogen entrainment and oxygen depletion as caused by the interchange which occurs at the interface between the arc-jet air stream and the ambient nitrogen.

Based on this somewhat limited test data it would appear that the effect of the mixing of the air stream with the surrounding nitrogen in the arc-jet test chamber is relatively small (at most 5 to 6%). The percent error incurred by neglecting its effect on the results of the gas analyses is within the experimental accuracy of the measurements recorded. It is felt that a larger error would be introduced into the gas analysis calculation if some theoretical correction were attempted since no solution exists for the turbulent mixing of two gas streams separated by a combustion zone (as in the case at hand). Consequently, it was considered justifiable to neglect possible outside effects in determining the stream concentrations from the gas sampling data.

## EXPERIMENTAL RESULTS AND DISCUSSION

### Experimental Program

The experimental program, designed to investigate the various aspects of supersonic combustion of hydrogen in air, was divided into two phases. The first phase

(Phase I) of the testing was devoted to the free-jet testing of the single and three-point injection configurations under controlled parametric variations for an air static pressure of 0.5 atms. For the single-point injection tests, the effects of varying air static temperature, fuel total temperature, fuel-to-air velocity ratio and the spacing between the fuel and air streams were investigated. Only variation in air static temperature, however, was considered for the three-point injection tests conducted in Phase I of the study.

The second phase (Phase II) of the testing investigated, 1) the free-jet characteristics of the 24 hole ring injection configuration for controlled variations in air static temperature, fuel total temperature and fuel-air equivalence ratio; and 2) the combustion characteristics of a three-segment combustor configuration for the same parametric variations. For the confined flow portion of the testing, a one, two and three segment combustor configuration was tested.

Data recording during each of the test runs included an optical measurement of the combustion stream temperature, gas sampling at the same location, and UV and color photographs of the entire reaction zone. For the combustor runs, additional data were recorded in the form of surface pressure distribution, surface temperature distribution, and combustor coolant inlet and outlet temperature and flow rate.

Prior to the start of the combustion program, several arc-jet nozzle shake down runs were made to determine the air flow characteristics. The indicated Mach number from these tests and from subsequent tests during the program was 2.35. The air flow exiting the contoured nozzle appeared to be uniform and free of Mach waves and shock diamonds when operating at the design pressure level of 0.5 atmospheres.

#### Point Injection Tests

The main purpose of the point-injection combustion tests was to study the effects of varying certain pertinent parameters on the ignition delay and reaction lengths. Originally, it was proposed to run this series of tests at air static temperatures of 1900°R, 2300°R and 2700°R. The 1900°R case, however, was observed to yield irregular and highly unstable ignition. The flame repeatedly formed and then broke away downstream. It appeared that the mixture temperature for this case was too low to sustain a stable combustion zone. This test was repeated several times with the same result. Higher

settings were then tried until a stable combustion zone was observed. This occurred at around the 2000°R to 2100°R level.

Total fuel temperatures of 600°R and 1000°R as well as fuel-to-air velocity ratios of 0.4 and 0.65 and fuel-air spacings of 0.108" and 0.216" were also considered during this portion of the test program. The range of fuel-air velocity ratios considered correspond to equivalence ratios in the range of 0.4 to 0.97.

UV and color photographs were taken of the combustion zone at various film exposures. The main purpose of the different exposures was to determine the proper UV exposure for each of the air static temperatures considered for the free-jet portion of the experimental test program. The ultraviolet exposures using Tri-X film at a stop number of f/4.5 were (1) 5 seconds for an air static temperature of 2100°R, (2) 1 second for an air static temperature of 2700°R and (3) 0.1 seconds for an air static temperature of 3100°R. During combustion, and at various fuel-to-air ratios, two or more exposures were made spanning each nominal exposure. Generally, an increase in exposure decreases delay length but does not increase reaction length. Delay lengths were taken from exposures when the background from the arc was not visible. The integration of arc background by the emulsion can lead to erroneous delay lengths due to the fogging off of the toe of the H&D emulsion sensitivity curve and sensitization of the emulsion to lower light levels.

Gas samples were extracted from the combustion stream at various locations in an attempt to locate the main reaction zone. Optical combustion temperature measurements were also attempted at the same stream location, using the OH emission technique discussed in this report. These attempts at temperature measurements from OH emission spectra proved unsuccessful for all of the 0.108" fuel-air spacing tests. A densitometer study was made of several of the UV negatives of the series in order to locate the main zone of OH radiation. Use of this information in positioning the optics also proved unsuccessful in realizing a useful OH spectra. All the information gathered seemed to indicate that the combustion temperature was too low to yield a distinctive OH spectra for the range of parameters considered. Temperature data was recorded for the 0.216" fuel-air spacing single-point injection tests by the sodium-line reversal technique.

Previous work done on supersonic combustion at Republic Aviation Corporation showed that the combustion temperatures were in the range of 4600 - 4800°R, as determined by OH spectra. The lowest temperature at which OH spectra can be recorded in the laboratory is 4200°R and this is from a stoichiometric air-hydrogen mixture burned in a Bethlehem burner. All attempts to record OH spectra in this study were unsuccessful, therefore, the combustion temperatures must be less than 4200°R. The difficulties encountered in these temperature measurements were detailed in progress reports of the present study, i. e., References 23 and 24.

Ignition delay and reaction lengths were measured directly from the UV negatives. Figure 29 shows a sketch of the lengths as read from the negatives. Both the arc-jet nozzle exit diameter and the gas sampling probe position were used to determine the scale factor required to measure the pertinent combustion zone lengths. Typical UV photographs are shown in Figures 30 and 31 for the 0.108' fuel-air spacing with cold hydrogen,  $V_f/V_a = 0.4$  and both 2394°R and 2772°R air static temperatures, respectively. The exposure time for these photographs, as determined from the aforementioned UV film exposure study, were 5 sec. for the 2394°R test run and 1 sec. for the 2772°R case. Clearly visible in these UV photographs is the OH radiation zone, characteristic of the  $H_2$ -air reaction. The supersonic nature of the flow in the combustion region is clearly established in Figure 32 which is a UV photograph of a probe during a 2646°R - three-point injection test showing the combustion zone and the detached shock wave in front of the probe. The pitot probe for this test run was located 9 inches downstream, in line with the arc-jet nozzle center line.

The increase in fuel total temperature from 600°R to 1000°R did not show any appreciable difference in the overall characteristics of the combustion zone in the UV photographs. Only slight changes in measured ignition delay and reaction lengths were noted for this variation in fuel total temperature.

Ignition delay and reaction lengths, as measured from the UV negatives, are plotted versus air static temperature in Figures 33 and 34 for the cold hydrogen tests and in Figures 35 and 36 for the heated hydrogen test runs in this series. In general, the ignition delay and reaction lengths read from the UV negative exhibited the proper trend as to variations in static air temperature and fuel-air velocity ratio. An increase of  $V_f/V_a$  from 0.4 to 0.65 shows an increase in ignition delay and reaction



length. Conversely, an increase in air static temperature resulted in lower ignition delay lengths and almost constant reaction lengths (a slight decrease, if anything). These effects appear to be less pronounced for the 0.216 spacing.

The absence of an expected slight increase in  $\ell_d$  for the 0.216' spacing tests must be attributed to difficulties connected with reading the UV negatives. For some unexplainable reason the resolution of the negatives was not as good as those previously obtained in the 0.108" point injection tests.

Theoretical curves for both the ignition delay and reaction length are also presented in Figures 33 through 36. The method of Schott and Kinsey presented in Reference 11 was used to determine the theoretical behavior of the ignition delay times while the method of Reference 25 was utilized for the theoretical reaction lengths. In applying the method of Reference 11 to the test cases at hand it was assumed that an initial gas mixture of  $O_2$ ,  $N_2$  and  $H_2$  (based on input values) existed at condition of temperature and pressure equal to the arc-jet air values. The ignition delay length is taken as the product of the delay time computed for these conditions and the calculated arc-jet exit velocity. These assumption are felt to be justified since the theoretical ignition delay curves presented here are to indicate the general trend of the data. A direct comparison is not truly justified since the definition of ignition delay time as presented in Reference 11 differs from the experimental definition of the present study. Schott and Kinsey in Reference 11 define their ignition delay time as the time required for the OH concentration to reach  $1 \times 10^{-6}$  moles per liter. On the other hand, the delay times for the experiments depend on ignition delay lengths read directly from the UV negatives. Accordingly, it is difficult to truly assess theory versus experiment for this case since the concentration of OH corresponding to the amount of OH radiation emitted and recorded on the UV negatives is not easily determined.

The theoretical approach developed in Reference 25 is applicable to two-dimensional turbulent mixing and burning zones for either frozen or equilibrium chemistry. The analysis utilizes a flame sheet approximation to the equilibrium flow case which yields the slope of the combustion zone under stoichiometric conditions. Application of this method to the experimental situation at hand is felt justified to obtain an engineering approximation to the actual behavior. Owing to the relative sizes of the fuel and air streams considered, the flow locally behaves quasi-two-dimensionally for some ten to twenty air-jet diameters downstream. Details of the theoretical analysis

for the determination of reaction lengths are given in Appendix D. It should be noted that the analysis neglects any effect of possible nitrogen entrainment or oxygen and hydrogen depletion due to mixing of the fuel and air streams with the nitrogen atmosphere of the arc-jet chamber. In addition to the theoretical difficulties involved in such an analysis (of which no solution exists according to the authors knowledge), experimental data already discussed has shown these effects to be small enough to be neglected in an engineering calculation of the type considered here.

The theoretical curves for the reaction length have been determined using the value of  $x$  evaluated from Equation (D-34) (Appendix D) for  $y_s$  equal to the diameter of the air nozzle. This represents the downstream length required for the flame sheet to traverse the air stream. In lieu of the above discussion, the reaction lengths presented must be considered an upper bound to the actual values and are included in this study to indicate the general trend of the data.

In Figures 37 and 38, ignition delay and reaction lengths are presented for the three-point injection test runs. Discrepancies existing between the theoretical curves and the experimental points for this case are attributed to the same reasons as those outlined for the single-point injection test data.

In Figure 39 a UV photograph of a point-injection test run at  $2664^\circ\text{R}$  and  $V_f/V_a = 0.4$  is shown as viewed from beneath the fuel injection port. For this test run the fuel injector section was rotated  $90^\circ$  from its original position. The film from a similar run (Figure 31) in which the ultraviolet pictures were taken with the hydrogen inlet at the bottom of the nozzle (side view) was densitometered in order to locate the main OH radiation zone. A plot of the isotransmissivity lines as a function of position is shown in Figure 40. The lateral scale was magnified by a factor of two over the longitudinal scale in order to clarify the plot. The main OH radiation zone is shown at 10.4 inches from the plane of the nozzle and directly in front of the hydrogen inlet. Numerous attempts to record OH spectra from this zone were unsuccessful.

The operation of the gas sampling probe during a  $2700^\circ\text{R}$ , cold hydrogen test is shown in Figure 41. Clearly evident from this UV photograph is the proper operation of the probe with the probe bow shock swallowed. The nose of the probe is clearly visible upstream of the envelope formed by the exiting probe cooling water. This

photograph was taken at 1/10 of a second exposure in an attempt to minimize the intensive radiation reflected from the cooling water exiting the probe. The combustion zone in this photograph is not clearly defined due to the fast exposure time used and due to the high intensity radiation from the cooling water which tends to wash out the less intense area.

As mentioned previously, gas samples for the 0.108" fuel-air spacing, point and three point injection tests were taken at various locations in the combustion stream in an attempt to locate the main OH radiation zone. As a result it becomes exceedingly difficult to draw any conclusions as to the chemical behavior of the combustion zone during the variation of some of the pertinent parameters. The lack of temperature measurements for these runs also made it difficult to determine the combustion efficiency at the measuring station. For completeness, measured and calculated values of pertinent parameters, for this series of tests, are presented in Table II. Details of the method used to determine the local equivalence ratio is presented in Appendix E.

For the point-injection tests with 0.216" fuel-air spacing, combustion zone temperatures were measured optically by use of the sodium line reversal technique discussed in a previous section of the report. The majority of the temperature measurements and gas samples were taken at the 18 inch downstream position, 5/8 inch below the centerline of the arc-jet nozzle towards the fuel port. The pertinent data for these test runs are presented in Table III.

The temperature measurements recorded and those which were attempted indicate a highly nonuniform distribution within the combustion zone. Winged spectra were noted in a number of test runs indicating the existence of more than one main temperature zone. Winged spectra are characterized by a peak or valley occurring on either or both sides of the sodium line in absorption or emission. From the data of this series of tests an increase in reaction length or combustion zone length was noted with an increase in initial equivalence ratio (which indicates the amount of fuel introduced into the system). Accordingly, for each set of initial conditions the reaction zone length changed whereas the probe and temperature measuring station was fixed at 18 inches. Consequently, different portions of the flame were sampled. Under these conditions, different measured temperatures and gas sampling data can be expected due to the

nonuniformity of the combustion zone.

In Figure 42 the variation of  $\phi_l$  vs  $T_a$  is shown for this series of data. In all but one case the local equivalence ratio exceeded the initial value. This result is expected, however, due to the position of the gas sampling probe. Consequently, for this particular case, the local equivalence ratio is not truly an indicator of the mixing attained. The data presented is insufficient to establish a trend with probe position.

The parameter  $\eta$  as listed in Table III is defined as the ratio of the mole fraction of water to the sum of the mole fractions of hydrogen and water at the gas sampling station of the combustion stream. This parameter can be considered a form of combustion efficiency based on gas sampling data. In addition, experimental values of the local static enthalpy are presented in Table III consistent with the measured temperature and species concentrations.

It is evident from the data that more intensive measurements are required in order to properly assess the combustion process. An optical scanning system and a rake of gas sampling probes would be required to determine profiles of combustion temperature and species concentrations. Distributions of this type at three or four downstream stations for the same initial conditions would be highly desirable in the assessment of the supersonic combustion characteristics of the hydrogen-air system.

### Ring-Injection Tests

The initial testing in the second phase of the experimental study was devoted to the ring injection of hydrogen through 24 injection ports for the  $\phi = 1$  case and 12 injection ports for the  $\phi = 0.5$  case. A photograph of the test set-up is presented in Figure 43 showing the full 24 hole configuration and the gas sampling probe activated into position. In this series of tests air static temperatures in the 2100°R and 2700°R range were considered for equivalence ratios of 0.5 and 1.0 and fuel total temperatures of 600°R and 1000°R. A second series of ring injection tests were performed later in the second phase of the program. For this series the range of air static temperature values was extended to 3100°R and the full 24 holes were utilized for the  $\phi = 0.5$  tests. Instead of changing  $A_f/A_a$  as in the first series of tests, an equivalence ratio of 0.5 was achieved by decreasing the hydrogen mass flow.

A study of the UV negatives for this series of tests indicated shorter and much narrower reaction zones for the  $\phi = 0.5$  test cases than those of the  $\phi = 1$  test cases. The  $\phi = 1.0$  cases exhibited the same billowing of the combustion zone as was noted in the point injection tests. It appears that once ignition has occurred a more sudden heat release occurs for the stoichiometric case. A typical UV photograph of the combustion zone for the ring injection case is presented in Figure 44.

As in the previously reported point and three-point injection tests, difficulty was experienced in obtaining stable combustion at either 1900°R or 2000°R. Combustion at these air static temperature settings was observed to be erratic in nature. As a consequence, it was decided to conduct this phase of the program at 2100°R rather than at the originally intended value of 1900°R. Gas samples and combustion temperature measurements were taken for this series of tests at each of three downstream stations, i. e., at 6, 12, and 18 inches corresponding to the exit plane of each of the combustor segments. At the six inch location no indication of a temperature rise was obtained from the sodium line reversal data. Unfortunately, a water leak in the arc-jet system invalidated the gas samples extracted at this location.

Some difficulty was experienced with the UV negatives due to the sodium bicarbonate tracer which was injected into the air stream for the sodium line reversal temperature measurements. The combustion zone in most cases, however, was distinguishable, making it possible to determine the ignition delay and reaction lengths. Most of the difficulty was encountered in the  $\phi = 1.0$  cases. Figures 45 and 46 show the variation in ignition delay and reaction lengths, with air static temperature, respectively, for equivalence ratios of 0.5 and 1.0. The theoretical curves for ignition delay shown in Figure 45 are based on the theory of Schott and Kinsey (Reference 11). The method of calculating ignition delay lengths used for this series of tests is the same as that used for the single point cases. Both the data and the theoretical curves show an increase in ignition delay length for increasing values of the fuel-air equivalence ratio, and a decrease in ignition delay length with increasing air static temperature. Little effect is noted due to fuel total temperature variations. The ignition delay data from the single and three point injector runs plotted in Figures 33, 35 and 37 give a reasonable scatter band when plotted together. However, the ring injection data from Figure 45 fall below this scatter band. An explanation for this behavior lies in the film response to radiation. The photographic film records

the three dimensional combustion stream as a two dimensional image. The radiation from the depth of the stream is recorded (integrated) on the film plane. When this occurs, the background (from the depth) fogs off the toe on the H&D emulsion sensitivity curve making the film more responsive to low light levels. This increase in response causes the ignition delay lengths to appear shorter. This effect can be corrected in future experiments by using films which have been prefogged before use to the linear response portion of the H&D emulsion sensitivity curve.

The reaction length data shown in Figure 46 indicates a decrease in reaction length with an increase in air static temperature. In addition, an increase in reaction length is noted for increasing fuel-air equivalence ratio. The theoretical curves shown in Figure 46, as in the point injection case, are based on the turbulent mixing and burning theory of Reference 25 outlined in Appendix D. The application of this two-dimensional theory to the axisymmetric case at hand is justifiable since it is a well established fact that the flow of an axisymmetric jet is initially quasi-two-dimensional. Data exists in the literature (Reference 26) which indicates that the initial behavior of an axisymmetric mixing zone is two-dimensional for downstream distances of approximately 30 times the air nozzle exit radius. As in the point injection case, the possible effects due to mixing of the ambient fluid and the fuel and air stream was not considered in this analysis.

Even though the theoretical method utilized is valid for only stoichiometric proportions of fuel and air, it has been applied here to the  $\phi = 0.5$  test cases to represent an engineering approximation for these cases. It is interesting to note that the theoretical curves in this case show a much more pronounced effect due to fuel total temperature variations. The scatter existing in the data (especially for the  $\phi = 1.0$  cases) must in part be attributed to the partial obscurement of the reaction zone by the sodium bicarbonate tracer required for the optical measurement of combustion temperature. Furthermore, the discrepancy which exists between the theory and the experiments is directly attributable to the deviation of the combustion stream from equilibrium behavior. The better agreement noted at the higher temperature levels substantiates this conclusion since a decrease in reaction time results with increasing temperature, i.e., the reaction proceeds to completion at a much quicker rate.

In Figure 47 the total reaction length, as determined from the data, (i. e., ignition delay plus reaction length) is plotted versus air static temperature. The theoretical curves shown in this figure have been computed by the turbulent mixing theory of Reference 25 using the sum of both the unreacted mixing length (Figure 48) and the previously discussed reaction length,  $l_r$ . Good agreement is noted between theory and experiment for this parameter. The significance of this comparison is that an engineering estimate of the total length of the reaction zone can be obtained by use of the theoretical predictions for the unreacted mixing length based on the frozen flow assumption and that for the reaction zone length based on the flame sheet approximation. In Figure 47 as in Figure 46 the value selected to represent the distance traversed by the flame sheet, prior to intersection at the center of the stream, is the sum of the fuel-air spacing and the radius of the arc-jet air nozzle. Selection of this characteristic dimension has a certain amount of arbitrariness connected with it since the theory does not account for the thickness of the metal separating the fuel and air at the fuel injection plane.

The contribution of the sodium bicarbonate tracer to the UV photographs can be seen in Figure 49 which is an air blank of a 3078°R air static temperature test run at one second exposure. All other air stream UV photographs without the sodium bicarbonate tracer were completely blank for the same exposure. In Figure 50 a typical  $\phi = 1.0$  UV photograph is shown which indicates the partial obscurement of the reaction zone due to the presence of sodium. A comparison of Figures 49 and 50 shows the end of visible emission for both the air run with sodium and the fuel injection case to occur at approximately the same location. This observation is partially connected with the usual quenching action of the external environment on any free-jet type test and with the fact that the superposition of the sodium emission does influence the end location of the emission zone.

The UV photographs shown thus far were taken with the use of the Zeiss filter whose characteristics have already been discussed in a previous section of the report. During the ring injection test runs, however, some of the UV photographs were recorded with the use of the Perkin-Elmer spike filter also discussed in an earlier section. A typical photograph of the OH radiation zone with this filter is shown in Figure 51 for a 3240°R air static temperature at an equivalence ratio of 0.5. The use of the spike filter, which was employed to insure the proper elimination of any extraneous

sources of radiation, proved to be unsuccessful because of the fuzzy combustion zone image that it recorded on the UV film. The cause of the fuzzy glow surrounding the reaction zone has in part been attributed to the possibility that the filter is translucent but not transparent.

The specie concentrations obtained from the gas sampling analysis, the optically measured combustion temperatures and other pertinent data calculated for the ring injection series of tests are presented in Table IV. Careful examination of the test data indicates an apparent decrease in sodium line reversal temperature for increasing air static temperature. Accordingly, the sodium line reversal temperatures show a decreasing trend with decreasing reaction length. The significance of this fact is that for a stationary optical measuring position (say at either the 12 inch or 18 inch position) a decrease in the length of the reaction zone results in temperature measurements at different downstream locations of the combustion region. As a consequence, the data shows a quenching of the reaction zone which causes a fall-off in temperature toward the tail end of the flame. It is thus evident that the maximum combustion temperature is attained somewhere towards the latter part of the combustion zone; probably at the point where the billowing of the reaction zone occurs.

The color photographs taken in this series of tests support the above results. A study of the yellow sodium radiation zone in these photographs indicates the same behavior as noted in the UV pictures of the combustion stream.

It is also of interest to note that the further the penetration of the gas sampling probe into the combustion stream, as caused by the reaction length variations cited above, the higher the concentration of unreacted hydrogen. Along with the decrease in reaction length noted for increasing air static temperatures, a decrease in unreacted hydrogen concentration was also noted. The formation of water, on the other hand, seems to peak at around the 2500°R to 2700°R temperature level. Consistent with the apparent motion of the focal point of the optics and the gas sampling probe location due to variations in reaction zone length, it is noted that the maximum (or peak value) concentration of water occurs towards the end of the reaction zone.

In Figures 52 and 53 local equivalence ratio data is presented for both the first and second series of ring injection tests. It is of interest to note the improved mixing (increasing  $\phi_{\ell}$ ) with downstream gas sampling probe location indicated in Figure 52.



The data appears well behaved especially for the second series of tests.

Experimental static enthalpy values based on the optical temperature measurements and gas sampling data are shown in Figures 54 and 55 plotted versus air static temperature for the first and second series of ring injection tests, respectively. The trend of the sodium line reversal temperature measurements with increasing air static temperatures, discussed previously, is evident in these figures.

In Figures 56 and 57 variations in the parameter  $\bar{\eta}$  with air static temperature and measured sodium line reversal combustion temperature, respectively, are presented. The trend of the data shown in these figures is consistent with other data from this series of test runs; namely that an increase in air static temperature results in a more efficient system, whereas for increasing optically measured temperature a decrease in efficiency is noted. The latter result is in keeping with the apparent movement of the optical focal point with changes in reaction zone geometry as caused by variations in test conditions.

In addition, it is evident from Figure 56 that better efficiencies result at lower air static temperatures for the 12 inch position while little effect was noted due to probe position at the higher air static temperatures. The data shown in Figure 57, on the other hand, indicates an almost constant efficiency up to a measured combustion temperature of 3500°R independent of position changes from 12 inches to 18 inches and a fall-off in efficiency beyond 3500°R for the 16.5 and 18 inch positions.

Included in the data presented in Table IV is an effective equivalence ratio,  $\phi_{\text{eff}}$ , defined as being that value of the equivalence ratio which with complete combustion would produce the required measured conditions. Accordingly, equilibrium thermodynamic data based on experimental static pressure and enthalpy (obtained from optically measured temperature and gas sampling data) values were used to determine  $\phi_{\text{eff}}$ .

#### Original Segmented Combustor Tests

Testing of the original segmented combustor, designed for constant pressure operation at 2700°R air static temperature, 1000°R fuel total temperature and an equivalence ratio of unity, comprised the major portion of the Phase II experimental

program. A photograph of the three segments composing the combustor is shown in Figure 58. Visible in the photograph is the inner surface tube of the combustor with its related pressure and thermocouple leads. The completely assembled combustor is shown in Figure 59. The pressure taps inside the combustor (ten in each segment) were connected to a mercury manometer which was photographed during each of the test runs of the series. Surface temperature histories from thermocouples (also ten in each segment) located on the alternate side of the combustor from the pressure taps, were automatically recorded by the facilities ATAR data acquisition system during the course of each test. The overall combustor test rig showing the initial combustor contour and the pressure and thermocouple locations has already been presented in Figure 3.

For the first series of combustor test runs each of one, two and finally three segments of the combustor were tested for the same set of flow property variations considered in the free-jet ring-injection series of tests. Pressure and wall temperature data were recorded in addition to the gas sampling and optical temperature data, measured in the center of the exit plane of the end segment in each of the configurations tested. Pressure distribution data is presented in Figures 60 and 61 for the one segment configuration at 2100°R and 2700°R, respectively; Figures 62 and 63 for the two segment configurations at 2100°R and 2700°R, and in Figures 64 and 65 for the complete combustor at the same air static temperatures.

From these recorded pressure distributions it is evident that the overall pressure level inside each of the combustor configurations was much lower than that expected. The low pressures recorded were obtained initially as a result of the sudden increase in area caused by the step formed by the parallel fuel injectors and the combustor wall. The large flow separation region formed at the step in the absence of fuel injection (during stabilization of the arc-jet air conditions) greatly decreased the pressure there. Once established, it becomes very difficult to remove the separated region with fuel flows of the magnitude used in these tests. In addition, because of the resulting low pressures and temperatures downstream of the step, combustion did not occur at the beginning of the designed constant pressure contour which also served to decrease the local values of the static pressure and temperature. Lack of combustion at this location caused a gas flow expansion in the absence of the pressure rise expected there due to burning. It is clear from Figures 60 - 65 that the general low pressure level and the reflections of the reattachment shock wave

downstream of the step caused the boundary layer to separate near the end of the combustor. It is also evident from the pressure data that the onset of combustion occurred in the region of flow separation near the end of each combustor configuration tested.

Typical UV photographs of the combustion stream exiting the combustor for this series of tests are shown in Figure 66 for a three segment combustor and in Figure 67 for a one segment combustor. The arc-jet chamber pressure for Figure 66 was 0.326 atm. while that for Figure 67 was 0.5 atm. A lambda shock wave pattern is discernible in each of these photographs which is similar to that encountered in over expanded supersonic nozzle flows of  $p_{\text{exit}}/p_{\text{tank}}$  in the range of 0.4 to 0.6.

Wall temperature distribution data for these combustor runs were recorded as being very erratic. Typical distributions for the complete combustor are shown in Figure 68. The random nature of the wall temperature measurements shown in this figure is attributed to widespread cracking and breaking away of the ceramic cement insulating the bare wire between the thermocouple sheaths and junctions. The consequence of this occurrence resulted in unpredictable and random thermocouple heat conduction errors. The nonuniform cracking and breaking from station to station resulted in a different heat loss environment for each thermocouple. For this reason, the bulk of the surface temperature distributions recorded for this combustor contour has been omitted from this report. Attempts at calculating local heat transfer rates from these thermocouple data also proved unsuccessful.

The total overall heat rejection rates for this series of combustor tests were obtained by measuring the total cooling water flow rate and temperature rise. These results are plotted in Figures 69, 70 and 71 in terms of heat rejection rate ( $Q$ ) divided by the air stream total temperature ( $T_{o1}$ ) upstream of the hydrogen injection station. This parameter was chosen in order to eliminate air temperature as a variable and thereby isolate the effect of fuel-air equivalence ratio, hydrogen temperature, and arc-jet chamber pressure on heat rejection rates. The total temperature of the air stream was determined from real gas thermodynamic tables utilizing the measured total pressure (arc-jet plenum pressure) and the total enthalpy resulting from a careful heat balance of the entire arc-jet system. Figures 69, 70 and 71 reveal the following points.

- 1) There is little effect of arc-jet chamber pressure on heat rejection for tests where  $\phi = 0$  (air alone).
- 2) There is no discernible effect of air temperature on  $Q/T_{o_1}$  for tests where  $\phi = 0$ .
- 3) In tests where hydrogen was injected, the higher air temperature results in lower values of  $Q/T_{o_1}$ .
- 4) The higher hydrogen temperatures result in only slightly higher values of heat rejection for the three-segment combustor and seem to give a larger spread of heat rejection in the case of the two-segment combustor. This is to be expected since in the three-segment combustor there is a greater heat release than in the two-segment combustor and this tends to obscure the differences in initial energy level.
- 5) In tests where hydrogen is injected, the arc-jet chamber pressure has a strong effect on heat rejection: higher pressures result in higher heat rejection. This occurs because velocities in the combustor decrease as back-pressure increases, and consequently, combustion efficiencies increase.
- 6) Heat rejection in tests where  $\phi = 0.5$  was approximately equal to that in tests made at the same pressure and  $\phi = 1.0$ .

Gas sampling data, sodium line reversal temperatures and other calculated data for the first series of combustion test runs are presented in Table V.

Local equivalence ratio data is presented in Figure 72 for both the two- and three-segment combustor. No set pattern can be established from the data. If anything there appears to be an increase in  $\phi_L$  with air static temperature for the two-segment combustor configuration and an opposite trend for the three-segment combustor. This reversal in trend is also noted in the experimental static enthalpies presented in Figure 73. Owing to the extremely complicated nature of the internal flow noted during the test runs in this series, it is difficult to pin-point the causes contributing to the difference in behavior noted for the two- and three-segment combustors. The flow pattern inside the first two segments, when operating as a complete combustor, is vastly different than when operating as part of the full three-segment combustor. This behavior contributes greatly to any discrepancy noted in measured values. Differences in

wave pattern, boundary layer growth and location of the separated region noted towards the end of each combustor configuration are apparent from the data. The pressure distributions shown in Figures 62 - 65 clearly indicates this fact.

### Modified Segmented Combustor

In an attempt to remedy the low pressure environment which resulted in the original segmented combustor and to improve its overall performance, it was decided to modify the existing combustor contour to a shape designed to maintain a high pressure environment for the fuel and air stream. The accomplishment of this objective required the relaxation of the parallel fuel injection condition originally specified. A converging contour (approximately  $10^\circ$ ) just downstream of the fuel injector hardware was selected to decrease the original area back to the design value. This contouring of the step region was instated to minimize the pressure drop in the separated region occurring thereby by fixing the length-to-step height below the critical value required for the flow to span the separated region (Reference 27). In addition to the above changes, the constant area mixing region was extended beyond its original location. Based on the experimental data of the original combustor it was evident that a longer constant area mixing region was required to help maintain a higher pressure level for a longer time so that ignition could occur prior to the contoured section designed to maintain constant pressure supersonic combustion. A comparison between the original, modified and the analytically designed constant pressure combustion contour is shown in Figure 74. The location  $x = 0$  in the figure corresponds to the end of the constant area section.

A complete layout of the modified contour which comprises the inner combustor tube is shown in Figure 75, along with the new instrumentation setup. Owing to the difficulties experienced with the first set of thermocouples, it was decided to change to a more positive system. Stainless steel sheathed thermocouples,  $1/16$  of an inch in diameter were purchased from the Conax Corporation. These thermocouples were used to measure both the inner and outer wall temperatures. The thermocouples which measured inner wall temperature were pressed into blind holes in the combustor wall to within 0.015 inches of the inner surface and silver soldered at the outer surface. The thermocouples which measured outer wall temperatures were simply silver soldered to that surface. At stations where temperature measurements were made, the inner and outer surface thermocouples were placed in the same cross sectional plane and within  $15^\circ$  of each other.

In order to avoid the separated region which occurred toward the end of the original combustor, it was decided to operate the arc-jet chamber at as low a pressure level as possible. For this series of test runs the chamber was kept at a pressure of 0.22 atmospheres. A typical UV photograph of the combustion stream exiting the 18 inch combustor is shown in Figure 76. The lambda shock wave pattern discussed earlier is also present in this photograph. Two distinct combustion zones (a peripheral type burning) are also visible in this photograph.

Pressure distributions inside the modified combustor are shown in Figures 77 and 78 for the 2700°R air static temperature tests at equivalence ratios of 0.5 and 1.0, respectively. It is clearly indicated by this data that no appreciable combustion could have occurred within the three-segment combustor. Lack of a pressure rise for either of the two equivalence ratio cases with both cold and heated hydrogen clearly indicates this fact. From visible observations of the tests it appeared that combustion occurred near the exit plane of the last segment of the combustor. It should be noted that the pressure tap at the 11.7 inch station was leaking during the test runs.

The corresponding wall temperature distributions shown in Figures 79 and 80 also confirm the absence of combustion inside the combustor since no rise in inner wall temperature was observed. This apparent lack of combustion was further confirmed by the gas samples taken at the exit plane which showed no free hydrogen or water, and oxygen and nitrogen in their original proportions. Furthermore, no meaningful data were recorded by means of the optical sodium line reversal temperature set-up focused at the center of the combustion exit plane.

It should be pointed out that the pressure data shown in Figures 77 and 78 does indicate the effectiveness of the recontouring in the vicinity of the fuel injection station. The separated region encountered there during the original combustor test series was drastically reduced in the absence of fuel injection and eliminated completely for the fuel injection cases. All indications appear to confirm that the gas stream in that vicinity behaved according to design. In addition, the flow separation experienced in the aft portion of the original combustor configurations (one, two or three-segments) was also eliminated.

It appears that complete mixing did not occur in the higher pressure level region just downstream of the fuel injection station. Apparently, a longer mixing length is required by the fuel and air streams at the pressure level encountered in the constant area section of the burner. A delayed ignition due to inadequate mixing would further be delayed due to the pressure fall off experienced by the mixture stream upon entering the contoured portion of the segmented burner designed for constant pressure supersonic burning. Indications are that any loss in static pressure (at least for the air static temperature range considered here) to a value below 0.5 atmospheres greatly hinders the auto-ignition characteristics of hydrogen-air combustion system.

On the basis of these combustor test results, it was decided to test the modified combustor at higher air static temperatures. In Figure 81, wall static pressure distributions are shown for a series of test runs conducted at 3100°R air static temperature for cold and heated hydrogen. A significant pressure rise is noted beginning near the start of the constant pressure contour section. The pressure level in this section is noted to increase from 0.15 atms. to 0.25 atms. for the cold hydrogen case and to 0.3 atms. for the heated hydrogen test.

Wall temperature distributions for the higher air static temperature tests are shown in Figures 82 and 83 for cases without hydrogen injection and with hydrogen injection, respectively. Substantial increases in wall temperatures are noted, which tend to confirm the attainment of combustion as indicated by the pressure data.

Unfortunately, during the 3100°R air static temperature test runs, several water leaks were incurred at the silver solder joints of the flanges used to support the inner combustion tube to the outer water jacket. The extent of the damage was severe enough to warrant completely new silver soldering of the flange joints which constituted a major repair effort to the model. This unfortunate situation caused a curtailment to the combustor test program at a point where significant results were being obtained.

Local heat transfer rates were computed from the wall temperature histories recorded by means of a one-dimensional heat conduction analysis. The validity of the one-dimensional approach utilized here is substantiated by the experimental data of Reference 28. In this reference, which reported test data on a nozzle of approximately

the same wall thickness as that of the modified combustor, it is shown that axial conduction effects are negligible. The thermocouple installation for the nozzle used in Reference 28 was the same as that for the modified combustor contour.

The one-dimensional heat conduction equation used in obtaining local heat transfer rates was derived as follows:

$$\dot{q} = -kA \frac{dT}{dr}$$

where

$$A = 2 \pi rL$$

and

$$k = k_o [ 1 + a (T - T_o) ]$$

As a result

$$\dot{q} \left( \frac{dr}{2 \pi rL} \right) = -k_o [ 1 + a (T - T_o) ] dT$$

which when integrated yields

$$\frac{\dot{q}}{A_1} = \frac{k_o}{r_i \ln \left( \frac{r_o}{r_o - \Delta r} \right)} \left\{ 1 + a \left( \frac{T_e + T_i}{2} - T_o \right) \right\} (T_i - T_e)$$

where

$\frac{\dot{q}}{A_1}$  - is the local heat rejection per unit area.

$k_o$  - is the thermal conductivity of the wall at  $T_o$ .

$T_o$  - is a reference temperature (picked to be 212°F for the present case).

$r_i$  - is the local inner surface radius.

$r_o$  - is the local outer surface radius.

$\Delta_r$  - is the radial separation between the inner and outer wall thermocouples.

$T_e$  - is the outer wall temperature.



$T_i$  - is the inner wall temperature.

The local heat transfer rates calculated by means of the derived equation are presented in Figure 84 for air, cold hydrogen injection and heated hydrogen injection for an equivalence ratio of unity. It is of interest to note from this figure and from Figures 82 and 83 the effect of hydrogen injection on wall cooling. The temperature and heat transfer data shows an effective cooling length of 4 to 5 inches which would tend to indicate poor mixing and penetration in this area. Since the constant pressure burning contour starts at the 3 inch station, it is evident from the data that the hydrogen is still close to the wall in this region. The pressure distributions of Figure 81 also bear out this conclusion since ignition is shown to occur in the vicinity of the 5 inch downstream location. This apparent poor mixing and penetration of the fuel into the air stream is quite surprising since the modified contour in the injection region forms an injection angle of approximately  $10^\circ$ . It would seem that the higher pressures just downstream of the fuel injection station causes the hydrogen to adhere to the surface there. Furthermore, the loss in pressure experienced downstream of this station and the resulting lack of combustion also contributes to the poor mixing and penetration noted in this test series.

Gas sampling data and sodium line reversal temperature measurements taken at the center-line of the combustor one-half inch from the exit plane didn't show any indications of burning there. The species concentrations recorded there indicated air in essentially the same proportions as inputted to the arc-jet system. Optical temperature observations during the course of the tests proved unsuccessful since the results showed that two high temperature zones existed on either side of the focus point of the optics. The "winged" temperature spectra, together with the absence of free hydrogen or oxygen depletion in the gas samples, indicate peripheral burning close to the surface of the combustor. These results appear to tie in with the delayed mixing and penetration observed from the wall pressure and temperature histories previously discussed.

In Figures 85, 86 and 87 theoretical pressure distributions are compared with the experimental values recorded during the abbreviated modified combustor test program. Figure 85 shows the largest discrepancy between the one-dimensional cycle analysis and experiment since no apparent burning occurred in the  $2700^\circ\text{R}$  air static

temperature test runs for either cold or heated hydrogen injection. Better agreement is noted in the 3100°R air static temperature cases shown in Figures 86 and 87.

The theoretical curves presented in these figures were calculated by an iterative matching procedure utilizing the cycle and kinetics programs discussed in Appendix A. Use was also made of the off-design analysis presented in Appendix B and the experimental values of the total heat transferred to the combustor walls. The use of the proper experimental total heat rejected and the resultant skin friction coefficient obtained from the off-design analysis, resulted in lower theoretical combustion efficiencies for the 3100°R air static temperature runs. The lower combustion efficiencies, in turn, yielded lower pressures inside the combustor since less heat is being released there. This trend in theoretical behavior is shown to compare quite well with the experimental pressures in Figures 86 and 87. It should be noted that the results of any one-dimensional analysis can at best only be considered an engineering approximation to the actual flow behavior inside the combustor. The highly non-uniform nature of the flow properties inside the combustor invalidate the one-dimensional approach except to indicate general trends and average engine cycle performance as required in vehicle integration studies.

A comparison of the measured and theoretical predictions for the total heat rejected from the combustor for one of the 3100°R test runs is shown in Figure 88. The theoretical curve has been calculated in accordance with the modified turbulent boundary layer approach of Reference 29 which is discussed in Appendix A. The inviscid outer conditions required for the boundary layer calculation were taken to be those predicted by the one-dimensional cycle analysis discussed above. The maximum discrepancy appears to occur in the middle portion of the combustor which can be attributed to previously noted discrepancy in wall pressure there. Corresponding theoretical variations in displacement thickness and internal drag are presented in Figures 89 and 90.

## CONCLUSIONS AND RECOMMENDATIONS

The various phases of supersonic combustion studied in this experimental program have indicated certain effects of varying some of the more pertinent mixing and combustion parameters. Within the range of values considered, more pronounced effects on combustion were noted due to air static temperature, equivalence ratio and fuel-air velocity ratio variations than due to fuel total temperature and fuel-air spacing changes. In general, only slight variations in measured quantities were attributed to changes in fuel total temperature from 600°R to 1000°R or in fuel-air spacing from 0.108" to 0.216".

Temperature measurements by both OH emission and absorption were attempted numerous times during the experimental program. The inability to obtain the OH spectra required for temperature determination is attributed to combustion temperatures being below the 4200°R level.

The sodium line reversal technique proved to be quite useful during this test program. It was the only, simple, rapid remote temperature sensing technique available for the combustion temperatures encountered (3400-4200°R). It should be noted that all optical measuring techniques average the temperature over some stream volume, which in the present optical setup consisted of two wedges joined together at their apices. The reliability of these methods suffer from stream inhomogeneities, i. e., non-uniformity, shock waves, etc. The remote temperature sensing technique with their attendant drawbacks are preferred over temperature probes which unduly disturb the stream. The introduction of sodium into the stream by the powder feed method was far superior to its introduction by salt solution methods. The only adverse effect due to the sodium bicarbonate tracer in the stream was a slight obscurement of the combustion zone in the UV photographs. This effect did not cause any serious difficulties. Future work with sodium line reversal techniques for combustion temperature determination should utilize ganged, fiber optic probes aligned on either side of the combustion stream utilizing a common image of a standard lamp as the continuum source. This method eliminates critical alignments, moveable optics and results in the temperature sampling of small collimated cylindrical stream volumes. One spectrometer could be used to readout simultaneously spectral data from ten different probes. The fiber optics transmitting light from the flame would terminate on a

Hartman slide mounted on the spectrometer slit. The Hartman slide would have ten holes along the slit length. Using a stigmatic spectrometer, where a point on the entrance slit is imaged as a point on the exit slit, all channels are scanned simultaneously. The exit slit is constructed in a similar fashion to the entrance slit. Light from the exit slit is transmitted to the photomultipliers by fiber optics. Each channel in the system must have its own separate photomultiplier, amplifier and recorder.

The theoretically determined ignition delay and reaction lengths, calculated for the 0.5 atmospheres pressure level of the experiments, yielded approximate results whose general trend compared favorably with the experimental values read directly from the UV negatives. Best agreement for the reaction lengths was noted for the free-jet ring injection test cases since the theoretical model for these cases represents a better engineering approximation to the actual model in the absence of any nitrogen entrainment or oxygen depletion due to mixing of the air stream with the surrounding nitrogen. In particular it was shown that the overall reaction length (measured from the fuel injection station to the end of the combustion zone) can be predicted quite well utilizing the method of Reference 25 as presented in Appendix D.

Although good results were obtained for the free-jet portion of the test program (for point, three point and ring injection) it becomes evident from the data that more intensive measurements are required to properly analyze the particular combustion process. Transverse distributions of combustion temperature, specie concentrations, and stream total enthalpy (or stream velocity), measured at several downstream locations, would contribute greatly to the assessment of combustion characteristics and the uniformity of the reaction zone. Traverse systems similar to those used in wind tunnel boundary layer probing can be used to achieve the above suggested increase in combustion zone measurements. Knowledge of stream total enthalpy, as obtained by a total enthalpy probe, would simplify the determination of combustion efficiency.

It is clear from the results of the present study that experimental data obtained from free-jet tests contributes very little to the design of a combustor using a similar fuel injection system. The presence of the combustor wall alters the local behavior of the flow sufficiently to invalidate the fuel-air mixing and general ignition characteristics as predicted by the free-jet data. The contribution of the surrounding environment to the downstream combustion reaction quenching and the absence of wall effects (which

is the most important factor) also render the free-jet reaction length data inadequate for combustor length determination. It should be emphasized that any theoretical approximation as to fuel-air mixing, ignition and reaction lengths required for a particular combustor must consider the mixing and burning processes in the presence of a cooled surface. Only in this manner can theoretical prediction be considered adequate for combustor design.

In the original combustor tested during the second phase of the test program the main emphasis was placed on parallel fuel injection at a matched static pressure value of 0.5 atms. between the hydrogen and the air stream. The results of the testing clearly indicate the need to maintain as high a pressure level in the beginning of the combustor as possible. The loss of pressure caused by the rapid area change produced by the fuel injection plate and the combustor wall, was never recovered. Once established (during stabilization of the arc-jet air conditions), the separated region formed at the step could not be removed even when the hydrogen was injected there. This factor together with the final separation of the flow near the end of the combustor caused by the reflections of the strong reattachment shock wave downstream of the step contributed greatly to the poor performance of the original combustor.

It is clear from the data recorded during this series of tests that loss of pressure below the 0.5 atms. level greatly hinders the auto-ignition characteristic of the hydrogen-air system. Lack of combustion prior to the contoured portion of the combustor further hindered the mixing and general pressure level. It is felt that future supersonic combustion testing should be conducted at pressure levels of one atmosphere. The higher initial pressure would be beneficial to ignition which in turn would help the mixing between the hydrogen and the air.

Modification of the original combustor contour minimized the initial separated region during the arc-jet air stabilization period of the test and removed it completely when hydrogen was injected. The pressure drop in the step region was minimized by fixing the length-to-step height of the contour there below the critical value required for the flow to span the separated region. In addition to the higher pressure level achieved in the forward portion of the combustor, the modification also contributed to the elimination of the flow separation noted towards the end of each of the original combustor configuration (one, two or three segments) by the removal of the reflections of

the strong reattachment shock wave which existed downstream of the step region in the original combustor.

The lack of burning noted inside the modified combustor for the 2700°R air static temperature test runs must be ascribed to mixture pressures and temperatures in the constant area portion of the combustor below those of the free-jet ring injection tests at 2700°R which resulted in ignition delay lengths of less than 2 inches. Since the wall pressures recorded in this region for the 2700°R test runs (Figure 85) indicate a level between 0.45 and 0.5 atms. (at the design point just prior to the contoured section) the absence of ignition must be mainly due to a mixture static temperature well below the estimated value of 2100°R for the cold hydrogen test and 2200°R for the heated hydrogen case. These mixture temperatures were calculated on the basis of a one-dimensional adiabatic, constant area mixing calculations. The slightly lower pressure recorded at the one inch position is due to a slight flow expansion caused by the apparent fuel injection angle (less than 10°) at that station. In general, it appears that the effect of combustor wall cooling is sufficient to decrease the mixture temperature below the values cited above which are required for ignition. The condition existing in the constant area section was further aggravated by the flow expansion which occurred in the designed constant pressure contour in the absence of burning. The combined effects resulted in a pressure level below 0.2 atms., a level which requires very long ignition delay lengths. It should be noted here, however, that the apparent poor mixing indicated by the data was one of the major factors contributing to the lack of combustion previously cited.

An increase in air static temperature to 3100°R did induce combustion inside the modified burner. For these off-design cases the pressure level in the constant area section of the burner (Figures 86 and 87) was essentially the same as that for the 2700°R tests while the mixture temperatures were estimated at 2500°R for the cold hydrogen test and 2600°R for the heated hydrogen case. The higher mixture temperatures were sufficient to induce combustion just prior to the contoured section designed for constant pressure burning. The theoretical off-design analysis for the 3100°R test cases, using the experimental values of  $Q_R$  (total heat rejected), showed a corresponding decrease in skin friction coefficient. Both these effects tend to decrease the combustion efficiency which results in lower pressures inside the burner since the amount of heat being released there is decreased. This off-design behavior

predicted by theory is substantiated by the experimental wall pressure values.

Although brief, the modified combustor tests did indicate certain pertinent factors which should be considered in combustor design.

1. A great deal of care must be exercised in designing the contour in the fuel injection region. The data from the tests show that the existence of a separated region caused by a rapid area increase in the fuel-injection region is highly undesirable especially at the lower entrance pressures (0.5 atmosphere). If the separated region is desired there to act as a flame holder, care must be taken to design the contour there (as in the modified combustor contour) so that its effect on the local pressure level is minimized.

2. The constant area section (used as a mixing region) prior to the contour designed for constant pressure burning should be sufficiently long to insure proper mixing and ignition there. Indications from all the combustor test runs are that it is very important to avoid the increasing area region of the constant pressure contour before the onset of combustion since the resultant flow expansion there in the absence of combustion results in an appreciable loss in pressure. The heat release noted for the lower pressure level of these tests appears to occur gradually. As a result a longer constant area section could be utilized without danger of thermal choking (at the pressure levels of the subject tests).

3. The effectiveness of annular injection (essentially  $10^\circ$  for the modified combustor) on the mixing and penetration characteristics of the hydrogen is greatly impaired if ignition is delayed due to static pressure or temperature deficiencies. Beneficial results can only be expected if the mixture pressure and temperature is maintained at a level consistent with its free-jet counterpart whose results as to ignition delay length should be utilized in the design of the combustor.

On the basis of the present experimental program, it is recommended that future combustor test programs be conducted at higher pressure levels (at about one atmosphere). It is clear from the data that strong adverse effects are encountered at the lower pressure levels (below 0.5 atms.) in the presence of combustor wall cooling. Since the effect noted here due to wall cooling would not exist for a full scale vehicle using regenerative cooling of the combustor surfaces, higher entrance temperatures should also be utilized in future testing. In a regenerative cooling system the heat

loss to the surface coolant shows up as an increase in fuel temperature so that the overall mixture temperature is not affected. Accordingly, the effect of wall cooling should be eliminated from the mixture temperature by increasing the initial air static temperature or the fuel temperature.



# APPENDIX A

## DESCRIPTION OF COMPUTER PROGRAMS USED FOR COMBUSTOR CONTOUR DESIGN

### Combustion Cycle Analysis

The existing Republic Aviation Division combustion cycle analysis program is based on the solution of the classical one-dimensional conservation equations. The program considers Station 2 to be the entrance to the combustor, Station 3 to be the end of the mixing zone and Station 4 to be the exit of the combustor.

Fuel is introduced into the system at Station 2. The calculation of fuel injection characteristics is based upon a shockless injection process in which the static pressure at the exit of the injector is equal to the local air static pressure, and in which the fuel velocity vector is axial and directed downstream. Fuel flow properties are calculated from input values of fuel total temperature, total to static pressure ratio, the assumption of an isentropic expansion process, and the use of hydrogen tables.

The calculation from Station 2 to Station 3 assumes a shockless, non-reactive, constant area, adiabatic, dragless mixing process. The gas mixture leaving Station 3 is assumed to be homogeneous and its thermodynamic state is determined through an iterative calculation of the static pressure and temperature there using the following one-dimensional conservation equations and hydrogen-air thermodynamic tables. From continuity

$$\frac{p_{s3}}{p_{s2}} = \left( \frac{RT_s}{V} \right)_3 \frac{1}{\alpha_2} \quad (A-1)$$

momentum

$$\frac{p_{s3}}{p_{s2}} = \frac{\beta_2}{\left[ g + \left( \frac{V^2}{RT_s} \right)_3 \right]} \quad (A-2)$$

energy

$$H_3 = H_{2a} + H_{2f} = h_3 + \frac{V_3^2}{2gJ} \quad (A-3)$$

or

$$h_3 = \left[ h_{3a} + h_{3f} \left( \frac{f}{a} \right) \right] \frac{1}{1+f/a} \quad (A-4)$$

Combining Equations (A-1) and (A-2) there results the working equation

$$T_{s3} = \frac{V_3 (\alpha_2 \beta_2 - V_3)}{g R_3} \quad (A-5)$$

where

$$\alpha_2 = \sum_{k=1}^4 \left( \frac{RT_{s3}}{V} \right)_k \left( \frac{w_k}{w_{2a}} \right) \left( \frac{1}{1+f/a} \right) \quad (A-6)$$

$$\beta_2 = g + \sum_{k=1}^4 \left( \frac{V^2}{RT_{s3}} \right)_k \left( \frac{A_k}{A_2} \right) \quad (A-7)$$

and where  $k$  is used here to represent the possibility of considering four separate gases entering the mixing zone. The iteration procedure utilized in this portion of the program is initiated by inputting estimates of the answers required.

The calculation from Station 3 to 4 is based upon a one-dimensional shockless, heat addition process. The effects of combustion efficiency, internal drag, and heat rejection are accounted for. The gas leaving Station 4 is assumed to be homogeneous and in an equilibrium state. As used in this analysis, the combustion efficiency defines the percent of the ideal heating value added to the total enthalpy of the system.

Two supersonic combustion cycles were utilized in the present study: The general process in which the pressure-area relationship is defined by the equation

$$p^{\eta-1} A^{\eta} = \text{constant}$$

and the special case of a constant pressure cycle. In the general case,

- $\eta = 1.0$ , constant area cycle
- $\eta > 0$ , increasing pressure cycle
- $\eta = 0$ , constant pressure cycle (indeterminate in this format)
- $\eta < 1$ , decreasing pressure cycle

For the  $\eta$ -cycle, the governing one-dimensional conservation equations and the equation of state results in the following set of working equations.

From cycle definition

$$p^{\eta-1} A^{\eta} = \text{constant} \quad (\text{A-8})$$

continuity,

$$\frac{p_{s4}}{p_{s3}} = \left[ \left( \frac{RT_s}{V} \right)_4 \frac{1}{\alpha_3} \right]^{\eta} \quad (\text{A-9})$$

momentum,

$$\frac{p_{s4}}{p_{s3}} = \left[ \frac{\beta_3}{\eta g + \left( \frac{V^2}{RT_s} \right)_4} \right]^{\eta} \quad (\text{A-10})$$

and energy,

$$H_4 = H_3 + \Delta Q_A - \Delta Q_R = h_4 + \frac{V_4^2}{2gJ} \quad (\text{A-11})$$

Combining Equations (A-8) and (A-9) yields

$$T_{s4} = \frac{V_4 (\alpha_3 \beta_3 - V_4)}{\eta R_4 g} \quad (\text{A-12})$$

where Equation (A-8) can be re-stated according to

$$\frac{A_4}{A_3} = \left( \frac{p_{s3}}{p_{s4}} \right)^{\frac{\eta-1}{\eta}} \quad (\text{A-13})$$

and where

$$\alpha_3 = \left( \frac{RT}{V} \right)_3 \quad (\text{A-14})$$

$$\beta_3 = \eta g + \left( \frac{V^2}{RT_s} \right)_3 - \Gamma \quad (\text{A-15})$$

$$\Gamma = \left( \frac{C_D}{2} \right) \left( \frac{A_s}{A_3} \right) \frac{(\rho V^2)_{av.}}{p_{s_3}} = \frac{D A_3 g}{p_{s_3}} \quad (\text{A-16})$$

$$\begin{aligned} \Delta Q_A &= \frac{\eta_c H_f \phi (f/a)_{st}}{[1 + \phi (f/a)_{st}]} \quad (\text{for } \phi \leq 1.0) \\ &= \frac{(\eta_c + \phi - 1.0) H_f (f/a)_{st}}{[1 + \phi (f/a)_{st}]} \quad (\text{for } \phi > 1.0) \end{aligned} \quad (\text{A-17})$$

$\Delta Q_R$  in the analysis refers to the heat rejected from the combustor which in an engine system is partially accounted for in the fuel total enthalpy when the system is regeneratively cooled. The combustion process for this cycle is solved for a given  $\eta$  by iterative calculations of the combustor exit static pressure and temperature in conjunction with the appropriate hydrogen-air equilibrium thermodynamic tables.

For the constant pressure portion of the computer program, the governing equations are as follows

$$p_{s_4} = p_{s_3} \quad (\text{cycle definition}) \quad (\text{A-18})$$

$$D = w_3 \frac{(V_3 - V_4)}{g} \quad (\text{momentum}) \quad (\text{A-19})$$

or

$$D = \left( \frac{C_D}{2} \right) \left( \frac{A_s}{A_3} \right) \frac{A_3 V_3^2 \rho_{av.}}{g} \quad (\text{A-20})$$

and

$$H_4 = H_3 + \Delta Q_A - \Delta Q_R = h_4 + \frac{V_4^2}{2gJ} \quad (\text{energy}) \quad (\text{A-21})$$

Combining Equations (A-19) and (A-20) yields the working equation

$$V_4 = V_3 \left\{ 1 - \left( \frac{C_D}{4} \right) \left( \frac{A_s}{A_3} \right) \left[ 1 + \frac{(RT_s)_3^3}{(RT_s)_4^3} \right] \right\} \quad (\text{A-22})$$

For this combustion process variations in fluid properties inside the combustor are obtained by iteration of the exit static temperature.

The computed area ratio,  $A_4/A_3$ , varies with the input cycle parameter  $\eta$  as well as the other input parameters. To maintain a fixed geometry combustor area ratio with the present program, it is necessary to parametrically calculate area ratio versus  $\eta$ . The matched value of  $\eta$  is then used for the final calculation.

The initial input value of combustion efficiency,  $\eta_c$ , is usually estimated from experience. A manual procedure was developed to calculate the actual combustion efficiency for a given combustor length, area ratio, and equivalence ratio once the combustor entrance and exit conditions are known. This procedure entails the use of the cycle analysis program in which the  $\eta$ -cycle values are varied through a reasonable range at 100 percent combustion efficiency. The resultant combustor inlet and exit conditions are then input into a chemical kinetics computer program which calculates species concentrations and combustion efficiency as a function of length for each value of the cycle  $\eta$ . Cross plots of the cycle and chemical kinetic data produce the matched combination of combustion efficiency and cycle  $\eta$  for the given combustor length and area ratio.

The internal drag coefficient used as the initial input value must be re-evaluated following the initial cycle calculation. This is usually accomplished by a separate internal drag calculation for the combustor model using the initial combustor inlet and exit conditions and the specified fuel injection method and combustor model. The revised drag coefficient is calculated using Equations (A-16) - (A-20) and re-inserted into the cycle analysis program.

The drag coefficient is referenced to the combustor entrance and exit thermodynamic and flow properties as indicated in Equation (A-16). For the cases where film cooling is applied, an effective drag coefficient is manually calculated in which the properties of the hydrogen film are included. The approximation is of the form

$$C_{D_{eff.}} = C_D \left(1 - \frac{L_f}{L}\right) + C_{D_f} \left(\frac{L_f}{L}\right) \frac{(\rho V^2)_f}{(\rho V^2)_{av.}}$$

where  $L_f/L$  = the hydrogen film to total surface length ratio

For the case at hand an iterative procedure was utilized using the cycle, kinetics, and turbulent boundary layer programs to arrive at a matched system where the  $C_{D_{eff.}}$  and  $\Delta Q_R$  used in the cycle analysis was verified by the boundary layer calculation.

#### Chemical Kinetic Analysis

A general chemical kinetic program is available at Republic Aviation Division which yields thermodynamic and specie data for the hydrogen-air combustion system. The program permits

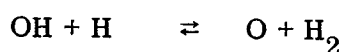
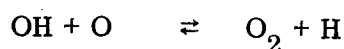
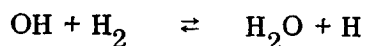
I) the calculation of the equilibrium composition of an arbitrary mixture of hydrogen and air (3.773 moles of nitrogen per mole of oxygen) as a function of static temperature and pressure. The outputs are the partial pressures of nine components ( $H_2$ ,  $O_2$ ,  $H_2O$ ,  $H$ ,  $O$ ,  $OH$ ,  $N_2$ ,  $NO$ ,  $N$ ) as a function of temperature.

II) the calculation of properties as in I for low temperatures where the formation or destruction of  $NO$  might be slow compared with other reactions of the hydrogen-air system. The ratio of  $NO$  to  $N_2$  is specified and the partial pressure is assumed to be zero.

III) the calculation of properties by inputting the molecular weight in addition to the inputs of II. For this program option the assumption is made that only shuffling reactions, involving no change in mole number between hydrogen and oxygen compounds, are in equilibrium. In addition, the substantial derivative

of the inverse molecular weight is calculated from a kinetic equation given in the following paragraph. The derivative is then integrated to give the total Eulerian reaction time.

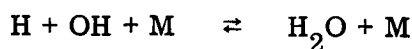
It has been shown both theoretically (Reference 9) and experimentally (References 11 and 30) that at elevated temperatures above the ignition point, the rapid shuffling reactions



are equilibrated at the end of the ignition delay period and remain in equilibrium throughout the reaction zone. Heat is released as the molecular weight gradually increases as a result of several recombination reactions occurring in parallel. The third option listed above considers the recombination reactions no longer in equilibrium; instead, the chemical equations must satisfy the boundary condition pressure, temperature, and inverse molecular weight. The substantial derivative  $D(1/W)/Dt$  is calculated and the substantial time necessary to reach the  $r$ th station is given by

$$t = \left( \frac{1}{W_r} - \frac{1}{W_{r-1}} \right) \left[ \frac{D(1/W)}{Dt} \right]_r \quad (\text{sec.})$$

To calculate  $(D(1/W)/Dt)$ , the following recombination reactions are considered:



in which M is the third body. Details of the program are contained in References 31 and 32. The reaction rates applicable to the above reactions are taken

from survey data presented in Reference 33 which represents the latest test data concerning hydrogen-oxygen reactions. The reaction rates that have been used in the above equations are listed in Table A-1.

TABLE A-1 - RECOMBINATION RATE DATA

Reaction	M	$K_f$ (cm <sup>3</sup> /g mole) °K sec <sup>-1</sup>
H + OH $\rightleftharpoons$ H <sub>2</sub> O + M	H <sub>2</sub> O	$1.8 \times 10^{22} T^{-1.5}$
	All Others	$0.45 \times 10^{22} T^{-1.5}$
H + H + M $\rightleftharpoons$ H <sub>2</sub> + M	H <sub>2</sub>	$5.0 \times 10^{18} T^{-1}$
	H <sub>2</sub> O	$1.5 \times 10^{19} T^{-1}$
	H	$2.0 \times 10^{19} T^{-1}$
H + O + M $\rightleftharpoons$ OH + M	All	$6 \times 10^{14}$
O + O + M $\rightleftharpoons$ O <sub>2</sub> + M	O <sub>2</sub>	$2.0 \times 10^{14}$
	O	$5.5 \times 10^{14}$

#### Real-Gas Turbulent Boundary Layer

The turbulent boundary layer analysis used to calculate the integral properties for real-gas conditions is a modification of the Reshotko-Tucker method presented in Reference 29. This modified method has been programmed for digital computation on the IBM 7090 and affords several improvements over the original method of Reference 29. These improvements can be summarized as follows:



- 1) The removal of some serious objections which could justifiably be leveled against the manner by which several integrals of enthalpy distributions were approximated. This was accomplished by utilizing the Crocco enthalpy-velocity relation, as a curve fit, in evaluating these integrals.
- 2) No approximations are made concerning the viscosity-temperature relation, and the relation between density and temperature at the reference enthalpy state.
- 3) The calculation of boundary-layer momentum thickness is made using the result obtained by transforming back to the physical plane thereby removing the troublesome necessity of having to evaluate stagnation values of certain properties.
- 4) Removal of perfect gas assumption and the utilization of existing equilibrium air or hydrogen air combustion products tables to evaluate the thermodynamic properties within the boundary layer.

The proposed method utilizes a transformation of the independent variables of the form

$$X = \int_{x_0}^x \frac{\rho^*}{\rho_0} \left( \frac{\mu^*}{\mu_0} \right)^{0.268} \left( \frac{h_e}{h_0} \right)^{1/2} dx \quad (A-23)$$

$$Y = \left( \frac{h_e}{h_0} \right)^{1/2} \int_0^y \frac{\rho}{\rho_0} dy \quad (A-24)$$

with the velocities in the physical and transformed planes related according to  $U = (h_0/h_e)^{1/2} u$ . As a result the governing differential equations expressed in terms of the physical longitudinal distance for the transformed momentum thickness,  $\theta_{tr}$ , and the form factor  $\mathcal{H}_i$  which result are given by

$$\frac{d\theta_{tr}}{dx} + \frac{\theta_{tr}}{U_e} \frac{dU_e}{dx} \left[ 2 + \frac{h_w}{H_e} \right] + \frac{\theta_{tr}}{r} \frac{dr}{dx} =$$

$$0.23 \left( \frac{h_e}{h_o} \right)^{1/2} \frac{\rho^*}{\rho_o} \left( \frac{\mu^*}{\mu_o} \right)^{0.268} \left( \frac{U_e \theta_{tr}}{\nu_o} \right)^{-0.268} \quad (A-25)$$

and

$$\frac{d\mathcal{H}_i}{dx} = -\frac{1}{U_o} \left[ \frac{\mathcal{H}_i (\mathcal{H}_i + 1)^2 (\mathcal{H}_i - 1)}{2} \right] \left[ 1 - \left( 1 - \frac{h_w}{H_e} \right) \left( \frac{2\mathcal{H}_i}{\mathcal{H}_i + 1} - \frac{\mathcal{H}_i + 1}{\mathcal{H}_i + 3} \right) \right] \frac{dU_e}{dx}$$

$$- 0.03 (0.123) \left( \frac{h_e}{h_o} \right)^{1/2} \frac{\rho^*}{\rho_o} \left( \frac{\mu^*}{\mu_o} \right)^{0.268} \left( \frac{U_e \theta_{tr}}{\nu_o} \right)^{-0.268} \frac{\mathcal{H}_i (\mathcal{H}_i^2 - 1)}{\theta_{tr}} e^{-1.561 \mathcal{H}_i} \quad (A-26)$$

where

$$\theta_{tr} = \frac{\rho_e}{\rho_o} \left( \frac{h_e}{h_o} \right)^{1/2} \theta \quad (\text{transformed momentum thickness})$$

$$\theta = \int_0^\infty \frac{\rho u}{\rho_e u_e} \left( 1 - \frac{u}{u_e} \right) dy \quad (\text{physical momentum thickness})$$

$$\nu_o = \frac{\mu_o}{\rho_o}$$

$$\mathcal{H} = \frac{\delta^*}{\theta}$$

$H$  = Stagnation enthalpy

$r = r(x)$  = local radius of body cross-section

and where

$( )_e$  = denotes local conditions external to boundary layer

$( )_o$  = denotes stagnation conditions external to boundary layer

$( )^*$  = denotes conditions corresponding to reference enthalpy state

$( )_w$  = denotes wall values

These equations are the counterparts of Equations (12) and (13) of the Reshotko-Tucker analysis of Reference 29. The program outlined below computes the physical momentum thickness obtained by transforming back into the physical plane the solution to Equation (A-25) and is utilized to compute various mass-flow averaged properties such as velocity and enthalpy, as well as friction coefficient and drag. An option is provided in the program to allow for a perfect-gas type calculation of the turbulent boundary layer.

At specified values of the independent variable,  $x/L$ , values of the following quantities (which vary with  $x/L$ ) are inputted:

- $u_e$  = velocity, feet/second
- $p_e$  = static pressure, pounds/sq ft
- $T_e$  = static temperature, degrees rankine
- $r$  = body radius, feet

In addition, the following quantities, which are constants, are specified:

- $L$  = wetted surface length, feet
- $T_w$  = static wall temperature, °R
- $H_e$  = total (stagnation) enthalpy at outer edge of boundary  
ft<sup>2</sup>/sec<sup>2</sup>
- $\mu_o$  = coefficient of absolute viscosity, evaluated at stagnation conditions,  $\frac{\text{lb/sec}}{\text{ft}^2}$

together with the initial values (values at  $x/L = x_i/L$ ) of the following quantities:

$$\begin{array}{l} \text{initial values} \\ \text{at} \\ \frac{x}{L} = \frac{x_i}{L} \end{array} \left\{ \begin{array}{l} u_{e_i} \cdot p_{e_i} \cdot T_{e_i} \cdot r \\ \theta_i = \text{momentum thickness, feet} \\ (\rho_i) = \text{incompressible form factor} \end{array} \right.$$

For the real-gas option of the program, at each of the specified values of  $x/L$ , the quantities

$$\begin{aligned}\rho_e &= \text{density, lb sec}^2/\text{ft}^4 \\ \mu_e &= \text{coefficient of absolute viscosity, } \frac{\text{lb sec}}{\text{ft}^2} \\ h_e &= \text{static enthalpy, ft}^2/\text{sec}^2,\end{aligned}$$

corresponding to the given values of  $p_e$  and  $T_e$ , are read out (via a table look-up scheme) from the tables of thermodynamic properties of air, or, if specified, from the table of properties for hydrogen-air combustion products. The following quantity (reference enthalpy) is next computed at each of the specified values of  $x/L$ :

$$h^* = 0.50 (h_e + h_w) + 0.0980 u_e^2 \text{ (ft}^2/\text{sec}^2\text{)}$$

Reference state values of density and coefficient of absolute viscosity, namely  $\rho^*$  and  $\mu^*$ , corresponding to reference enthalpy  $h^*$  at a pressure  $p_e$ , are looked up from equilibrium tables at each of the specified values of  $x/L$ .

For the perfect gas option on the other hand, at each of the specified values of  $x/L$ , the quantities  $\rho_e$  and  $h_e$  corresponding to the given values of  $p_e$  and  $T_e$  are calculated using the perfect gas law assumptions, namely

$$\begin{aligned}\rho_e &= \frac{p_e}{RT_e} \\ h_e &= C_p T_e\end{aligned}$$

The reference enthalpy is computed, as before, from  $h^* = 0.50 (h_e + h_w) + 0.0980 u_e^2$

The corresponding reference temperature is obtained from

$$T^* = \frac{h^*}{C_p}$$

and is used to calculate the quantity

$$\rho^* = \frac{p_e}{RT^*}$$

The quantities  $\mu^*$  and  $\mu_e$  are calculated at each of the specified values of  $x/L$  using the Sutherland formula

$$\mu = 2.270 \left( \frac{T^{3/2} \times 10^{-8}}{T + 198.6} \right) \left( \frac{\text{lb sec}}{\text{ft}^2} \right)$$

and by correlation formulae of the form:

$$\frac{\rho \mu}{p} = C_1 h^{c_2}$$

for other gas mixtures.

At this point the two fundamental boundary-layer quantities, the momentum thickness,  $\theta$ , and the so-called incompressible form factor,  $\mathcal{H}_i$ , can be computed.

The value of the momentum thickness,  $\theta$ , at any specified value of  $x/L$  is obtained from the following relation:

$$\theta^{1.2155} = \frac{\rho_{e_o}^{1.2155} \left( \frac{u_{e_o}}{h_{e_o}^{1/2}} \right)^B h_{e_o}^{1/2} u_{e_o}^{0.2155} \theta_o^{1.2155} \left( \frac{r_o}{L} \right)^{1.2155j}}{\rho_e^{1.2155} \left( \frac{u_e}{h_e^{1/2}} \right)^B h_e^{1/2} u_e^{0.2155} \left( \frac{r}{L} \right)^{1.2155j}} + \frac{0.01773 \mu^{-0.0525} L \int_{X_o/L}^{X/L} \rho^* \mu^{*0.268} \left( \frac{r}{L} \right)^{1.2155j} \left( \frac{u_e}{h_e^{1/2}} \right)^B h_e^{1/2} d\left( \frac{X}{L} \right)}{\rho_e^{1.2155} \left( \frac{u_e}{h_e^{1/2}} \right)^B h_e^{1/2} u_e^{0.2155} \left( \frac{r}{L} \right)^{1.2155j}}$$

where:

$$j = 0, \text{ for the 2-dimensional case}$$

$$j = 1, \text{ for the axisymmetric case}$$

$$B = 2.62 + 1.58 \frac{h_w}{h_{s_e}}$$

The incompressible form factor,  $\mathcal{H}_i$ , is obtained from the following transcendental relation:

$$\frac{f(\mathcal{H}_i)}{f(\mathcal{H}_i)_i} = \frac{\left(\frac{u_e}{h_e}\right)^{1/2}}{\left(\frac{u_e}{h_e}\right)_i^{1/2}}$$

where:

$$f(\mathcal{H}_i) = \left(\frac{\mathcal{H}_i}{a-b\mathcal{H}_i}\right)^{2/a} \frac{a-b\mathcal{H}_i}{(\mathcal{H}_i+1)} \frac{3a+5b}{2(a+b)^2} \frac{a-b\mathcal{H}_i}{(\mathcal{H}_i-1)} \frac{1}{2(a-b)} \frac{1}{(a+b)(\mathcal{H}_i+1)} e^{c(x)}$$

and where

$$a = 1 - 0.40 \left(1 - \frac{h_w}{H_e}\right)$$

$$b = 0.16 \left(1 - \frac{h_w}{H_e}\right)$$

$$c(x) = -0.193 \int_{x_0}^x \frac{c_f}{\theta} \frac{(\mathcal{H}_i - 1.3)(\mathcal{H}_i + 7.25)}{(\mathcal{H}_i - 1)(2.45 - \mathcal{H}_i)(a - b\mathcal{H}_i)} dx$$

and

$$f(\mathcal{H}_i)_i = \left(\frac{\mathcal{H}_i}{a-b\mathcal{H}_i}\right)^{2/a} \frac{a-b\mathcal{H}_i}{(\mathcal{H}_i+1)} \frac{3a+5b}{2(a+b)^2} \frac{a-b\mathcal{H}_i}{(\mathcal{H}_i-1)} \frac{1}{2(a-b)} \frac{1}{(a+b)(\mathcal{H}_i+1)}_i$$

The remaining quantities of interest, again at specified values of  $x/L$ , i.e.,

$$\mathcal{H} = \mathcal{H}_i \frac{h_w}{H_e} + \frac{1}{2} \frac{u_e^2}{h_e} \left[1 + \frac{h_w}{H_e} \mathcal{H}_i\right]$$

$$\delta^* = \frac{2}{3} \theta$$

Displacement thickness (feet)

$$\frac{\dot{w}}{\rho_e u_e} = \frac{2 \frac{2}{3} \theta}{\frac{2}{3} \theta_i - 1}$$

Average mass flow in the boundary layer

$$\delta = \delta^* + \frac{\dot{w}}{\rho_e u_e}$$

Boundary Layer thickness, feet

$$\frac{\bar{u}}{u_e} = \frac{\frac{2}{3} \theta_i + 1}{2 \frac{2}{3} \theta_i}$$

Average velocity

$$\frac{\bar{u}^2}{u_e^2} = \frac{\frac{2}{3} \theta_i + 1}{3 \frac{2}{3} \theta_i - 1}$$

Average squared velocity

$$\frac{H_{a_v}}{H_e} = \frac{h_w}{H_e} + \frac{(\frac{2}{3} \theta_i + 1)}{2 \frac{2}{3} \theta_i} (1 - \frac{h_w}{H_e})$$

Average stagnation enthalpy

$$Re_\theta = \frac{\rho_e u_e \theta}{\mu_e}$$

Reynolds number based on momentum thickness

$$C_f = \frac{2 \tau_w}{\rho_e u_e^2} = 0.246 e^{-1.56 \frac{2}{3} \theta_i} \frac{\rho^*}{\rho_e} \left( \frac{\mu^*}{\mu_e} \right)^{0.268} \left( \frac{\rho_e u_e \theta}{\mu_e} \right)^{-0.268}$$

$$\tau_w = \frac{\rho_e u_e^2}{2} C_f$$

and

$$D = (2\pi)^j L \int_{(x/L)_0}^{x/L} r^j \left( 1 + \left( \frac{dr}{dx} \right)^2 \right)^{1/2} \tau_w \cos(\arctan(\frac{dr}{dx})) d(x/L)$$

can now be calculated. The local heat transfer rate can be obtained using the Colburn form of the Reynolds analogy for turbulent flow given by:

$$N_{St} = \frac{C_f}{2} Pr^{*-2/3}$$

whence

$$-\dot{q}_w = \rho_e u_e (h_r - h_w) \frac{C_f}{2} \text{Pr}^*^{-2/3}$$

$$Q = (2\pi)^j L \int_{(x/L)_0}^{x/L} r^j \left(1 + \left(\frac{dr}{dx}\right)^2\right)^{1/2} \dot{q}_w d(x/L)$$

where the recovery enthalpy is given by

$$h_r = h_e + \sqrt[3]{\text{Pr}^*} \frac{u_e^2}{2}$$



APPENDIX B  
APPROXIMATE ANALYSIS OF COMBUSTION PROPERTIES  
AT OFF-DESIGN CONDITIONS

In an attempt to speed up the iterative procedure required by the existing cycle program to arrive at off-design conditions, an approximate analysis was developed utilizing both cycle and boundary layer equations to arrive at consistent initial values of  $C_D$  and  $\Delta Q$ . The analysis is based on the equilibrium behavior of the  $H_2$ -air combustion products assuming a constant pressure turbulent boundary layer.

From one-dimensional consideration of the combustion cycle, it is possible to express the governing equations as

continuity:

$$\frac{w}{g} = \rho AV \quad (B-1)$$

momentum:

$$Adp + \tau_w dA_s = - \frac{w}{g} dV \quad (B-2)$$

energy:

$$\Delta H = H_4 - H_3 = \frac{109.5}{1 + 0.02917\phi} + \frac{(51373\eta_c + 8936)(0.02917\phi)}{1 + 0.02917\phi} - \frac{Q_R}{w_m} \quad (B-3)$$

It should be noted that Equation (B-3) has been re-arranged to suit the existing combustion cycle and kinetics digital computer programs where Station 2 refers to the combustor entrance, Station 3 to the end of the constant area mixing, and Station 4 to the end of the combustor. If in general the cycle is defined according to

$$p^{\eta-1} A^{\eta} = \text{const.} \quad (B-4)$$

then integration of Equation (B-2) between Stations 3 and 4 results in

$$D = \frac{w}{g} (V_3 - V_4) - \eta (p_4 A_4 - p_3 A_3) \quad (B-5)$$

From constant pressure turbulent boundary layer considerations it can be shown that an adequate representation of the skin friction and heat transfer coefficients is

$$C_f = \frac{\tau_w}{\frac{1}{2} \rho_e V_e^2} = \frac{0.029}{R_{e_x}^{1/5}} \left( \frac{\mu_*}{\mu_e} \right)^{1/5} \left( \frac{\rho_*}{\rho_e} \right)^{4/5} \quad (B-6)$$

and

$$- \dot{q}_w = \frac{C_f \rho_e V_e (h_r - h_w)}{2 P_{r_*}^{2/3}} \quad (B-7)$$

where  $( )_r$  refer to recovery values,  $( )_e$  to external values and  $( )_*$  to reference conditions (like the Eckert reference enthalpy values).

If an equation of state is defined in the form

$$\rho \mu = K \frac{p}{h^\alpha} \quad (B-8)$$

with

$$\mu = C h^n \quad (B-9)$$

then the reference conditions required in Equation (B-6) can be obtained from

$$p = p_* = p_e$$

and

$$h_* = \frac{1}{2} \left[ H_e + h_w - (1 - 0.44 \sqrt[3]{P_{r_*}}) \frac{V_e^2}{2} \right] \quad (B-10)$$

the Eckert reference enthalpy. The values of  $K$ ,  $C$ ,  $\alpha$  and  $n$  are evaluated by curve fitting the equilibrium values of the  $H_2$ -air combustion products over the pressure, temperature and equivalence ratio ranges of interest to the present study. Utilizing these results it is possible to express Equations (B-6) and (B-7) as

$$\tau_w = 0.0145 \frac{K^{4/5}}{C^{3/5}} \frac{p_e^{4/5} V_e^{9/5}}{x^{1/5}} h_*^{-\frac{4\alpha + 3n}{5}} \quad (B-11)$$

$$-\dot{q}_w = \frac{\left[ H_e - h_w - (1 - \sqrt[3]{P_{r*}}) \frac{V_e^2}{2} \right]}{P_{r*}^{2/3}} \frac{\tau_w}{V_e} \quad (B-12)$$

Integration of Equations (B-11) and (B-12) over an equivalent cylindrical surface area and assuming average external fluid properties (local flat plate or cylinder) results in

$$D = \frac{0.01813 K^{4/5} p_e^{4/5} V_e^{9/5} A_s}{C^{3/5} L^{1/5} h_* \frac{4\alpha + 3n}{5}} \quad (B-13)$$

$$Q_R = \frac{\left[ H_e - h_w - (1 - \sqrt[3]{P_{r*}}) \frac{V_e^2}{2} \right]}{V_e P_{r*}^{2/3}} D \quad (B-14)$$

Consistent with the existing cycle and kinetics digital computer programs, an effective drag coefficient is defined according to

$$C_{D_{eff}} = \frac{D}{\frac{1}{2} (\rho V^2)_{av.} A_s} \quad (B-15)$$

where

$$(\rho V^2)_{av.} = \frac{(\rho V^2)_3 + (\rho V^2)_4}{2}$$

and

$$V_{av.} = \frac{V_3}{2} \left( 1 + \frac{V_4}{V_3} \right) \quad (B-16)$$

Consequently, it is possible to arrive at certain pertinent relationships which satisfy both the cycle and boundary layer requirements, i. e., 1) from combustion cycle Equations (B-1) and (B-5)

$$\frac{V_4}{V_3} = \frac{1 - \frac{A_s}{4A_3} C_{D_{eff}} + \Omega_o}{1 + \frac{A_s}{4A_4} C_{D_{eff}}} \quad (B-17)$$

$$\Omega_o = \frac{p_3}{\rho_3 V_3^2} \eta \left[ 1 - \left( \frac{A_4}{A_3} \right)^{-\frac{1}{\eta-1}} \right] \quad (B-18)$$

2) from boundary layer Equations (B-13) and (B-14)

$$C_{D_{eff}} = \Omega_1 \frac{(1 + \frac{V_4}{V_3})^{1/5}}{(1 + \frac{A_3}{A_4} \frac{V_4}{V_3})^{1/5}} \quad (B-19)$$

where

$$\Omega_1 = \frac{0.03625 C^{1/5}}{L^{1/5} (\rho_3 V_3)^{1/5}} \frac{\left\{ \frac{1}{2} \left[ \Delta H + 2H_3 - \frac{V_3^2}{4} \left( 1 + \frac{V_4}{V_3} \right)^2 \right] \right\}^{\frac{4(\alpha+n)}{5}}}{\left\{ \frac{1}{4} \left[ \Delta H + 2(H_3 + h_w) - (1 - 0.44 \sqrt[3]{P_{r_*}}) \frac{V_3^2}{4} \left( 1 + \frac{V_4}{V_3} \right)^2 \right] \right\}^{\frac{4\alpha+3n}{5}}} \quad (B-20)$$

and

$$\frac{Q_R}{w} = \Omega_2 \frac{(1 + \frac{A_3}{A_4} \frac{V_4}{V_3})^{4/5}}{(1 + \frac{V_4}{V_3})^{4/5}} \quad (B-21)$$

where

$$\Omega_2 = \frac{\Omega_1}{2P_{r_*}^{2/3}} \frac{A_s}{A_3} \left\{ \frac{1}{2} \left[ \Delta H + 2(H_3 - h_w) - (1 - \sqrt[3]{P_{r_*}}) \frac{V_3^2}{4} \left( 1 + \frac{V_4}{V_3} \right)^2 \right] \right\} \quad (B-22)$$

3) from cycle Equation (B-3)

$$\Delta H + \frac{Q_R}{w_m} = Q_o \quad (B-23)$$

where

$$Q_o = \frac{1}{(1 + 0.02917 \phi)} \left[ 109.5 + (51373 \eta_c + 8936)(0.02917 \phi) \right] \quad (B-24)$$

4) from the requirements that  $(C_{D_{eff}})_{cycle} = (C_{D_{eff}})_{b.1.}$ ,

$$4\Omega_o = \Omega_1 \frac{A_s}{A_3} \left(1 + \frac{V_4}{V_3}\right)^{1/5} \left(1 + \frac{A_3}{A_4} \frac{V_4}{V_3}\right)^{4/5} - 4\left(1 - \frac{V_4}{V_3}\right) \quad (B-25)$$

and 5) from the requirement that  $\left(\frac{Q_R}{w_m}\right)_{cycle} = \left(\frac{Q_R}{w_m}\right)_{b.1.}$

$$Q_o = \Delta H + \Omega_2 \frac{\left(1 + \frac{A_3}{A_4} \frac{V_4}{V_3}\right)^{4/5}}{\left(1 + \frac{V_4}{V_3}\right)} \quad (B-26)$$

Equations (B-21), (B-22), (B-23), (B-24) and (B-26) can be used to construct a nomograph which can be used to obtain  $\Delta H$ ,  $\frac{Q_R}{w_m}$ ,  $\frac{V_4}{V_3}$  and  $\Omega_2$  for a given  $\phi$  for the  $\frac{A_3}{A_4}$  of the designed combustor. It should be noted here that conditions at Station 3 are required for the calculation. These can be obtained in accordance with the calculation procedure from Station 2 to Station 3 outlined in Appendix A. Once  $\Delta H$ ,  $\frac{Q_R}{w_m}$ ,  $\frac{V_4}{V_3}$  and  $\Omega_2$  are determined Equations (B-18), (B-19), (B-20) and (B-25) are used to calculate the remaining parameters, i.e.,  $\Omega_1$ ,  $\Omega_o$ ,  $C_{D_{eff}}$ , and  $\eta$ .

A separate study of the thermodynamic behavior of the hydrogen-air combustion products yielded approximate values for the coefficient of Equations (B-8) and (B-9) of

$$n = 0.6296$$

$$\alpha = 0.3247$$

$$K = 4.61453 \times 10^{-6} \left[ \left( \frac{BTU}{lb.} \right)^\alpha \frac{lb.^2}{atm. ft^4-sec} \right]$$

$$C = 0.4501 \times 10^{-6} \left[ \frac{lb.}{ft-sec \left( \frac{BTU}{lb.} \right)^n} \right]$$

for  $\phi = 0.5$ , and

$$n = 0.6392$$

$$\alpha = 0.3228$$

$$K = 4.42474 \times 10^{-6} \left[ \left( \frac{\text{BTU}}{\text{lb.}} \right)^{\alpha} \frac{\text{lb.}^2}{\text{atm. ft}^4\text{-sec}} \right]$$

$$C = 0.36851 \times 10^{-6} \left[ \frac{\text{lb.}}{\text{ft-sec} \left( \frac{\text{BTU}}{\text{lb.}} \right)^n} \right]$$

for  $\phi = 1.0$ .

These results together with Equations (B-8) and (B-9) represent good approximations to the behavior of the gas mixture considered over the ranges  $(0.5 \text{ atm.} \leq p \leq 1.0 \text{ atm.})$  and  $(2000^{\circ}\text{R} \leq T \leq 4500^{\circ}\text{R})$ .

## APPENDIX C

### CALCULATION OF COMBUSTION STREAM TEMPERATURES FROM SODIUM LINE REVERSAL DATA

The method used for the calculation of combustion stream temperatures employs a plot of line intensity (peak height in mm.) against brightness temperature ( $^{\circ}\text{R}$ ) of the lamp image at the arc stream on rectangular coordinate graph paper to determine the temperature at which the spectral line goes from emission to absorption. The data taken from Figure 17 are as follows:

Continuum Temperature ( $^{\circ}\text{R}$ )	Intensity (Peak Height in mm.)	
4334	-56	
4064	-25	
3795	-12	
3290	+ 4-1/2	
3290	+42	Scale factor x 10
3000	+60.5	Scale factor x 10
2642	+67.5	Scale factor x 10

This data is plotted in Figure 91. The temperature at zero intensity is  $3500^{\circ}\text{R}$ .

# APPENDIX D DETERMINATION OF THEORETICAL REACTION LENGTH

The method of analysis utilized to establish theoretical reaction lengths follows the turbulent mixing analysis of Reference 25. The governing equations as determined in that reference are

$$\lambda = \frac{g_f - f_f'^2}{1 - f_f'^2} \quad (D-1)$$

$$\kappa = \frac{s_* - f_*'^2}{\phi_* - f_*'^2} \quad (D-2)$$

where

$$\frac{\tilde{\rho}_a}{\tilde{\rho}} \approx \frac{\tilde{h}}{\tilde{h}_a} \approx \frac{\tilde{H}}{\tilde{H}_a} = \phi(\chi), \quad s = \frac{\rho_a}{\rho} \quad (D-3)$$

$$g = \frac{H}{H_a} = \lambda + (1-\lambda)\phi \quad (D-4)$$

and where ( )<sub>\*</sub> conditions refer to reference values. Furthermore

$$\tilde{u}_a = \alpha_1 \tilde{x}^m, \quad \tilde{\rho}_*^2 \tilde{\epsilon}_* = \alpha_2 \tilde{x}^n \quad (D-5)$$

$$\tilde{x} = \left[ \frac{2\sigma^2 \phi_*}{k H_a^{1/2}} \int_{x_i}^x \frac{\rho_*^2 \epsilon_*}{\tilde{\rho}_a^2} \left( \frac{u_a}{\sqrt{H_a}} \right)^{1-2\kappa} dx' \right]^{1/2} \quad (D-6)$$

$$\tilde{y} = \sigma \left( \frac{u_a}{\sqrt{H_a}} \right)^{1-\kappa} \int_0^y \frac{\rho}{\tilde{\rho}} dy' \quad (D-7)$$

$$s = \kappa \phi + (1-\kappa) f'^2 \quad (D-8)$$



$$y = \left( \frac{\beta k}{m \phi_*} \right)^{1/2} \frac{\tilde{\rho}_a}{\rho_a} \left( \frac{u_a}{\sqrt{H_a}} \right)^{\chi-1} \frac{\tilde{x}}{\sigma} \int_0^{\chi} s \, d\chi' \quad (D-9)$$

where

$$\beta = \frac{2m}{1+n+m}, \quad \sigma = \frac{\tilde{\psi}}{\psi} \quad (D-10)$$

Consistent with the analysis, it is assumed that the turbulent exchange coefficients are expressible as

$$\tilde{\rho}^2 \tilde{\epsilon} = \frac{k \tilde{\rho}_a^2 \tilde{u}_a \tilde{x}}{\phi_*} \quad (D-11)$$

in the transformed plane and

$$\rho^2 \epsilon = \frac{k \rho_a^2 u_a x}{s_*} \quad (D-12)$$

in the physical plane. From recent work reported in Reference 34, it was found that for the low speed-variable density case that

$$\frac{\tilde{\rho} \tilde{\epsilon}}{\tilde{\rho}_f \tilde{u}_f} = k_2 \tilde{x} \left[ \frac{\tilde{\rho}_a \tilde{u}_a}{\tilde{\rho}_f \tilde{u}_f} - 1 \right] \quad (D-13)$$

where  $k_2 = 0.00075$ . As a result

$$\tilde{\rho} \tilde{\epsilon} = k \tilde{\rho}_a \tilde{u}_a \tilde{x} = k_2 \left( 1 - \frac{f'_f}{\phi_f} \right) \tilde{\rho}_a \tilde{u}_a \tilde{x} \quad (D-14)$$

or

$$k = 0.00075 \left( 1 - \frac{f'_f}{\phi_f} \right) \quad (D-15)$$

making Equation (D-6)

$$\tilde{x} = \left[ \frac{2 \phi_*}{s_*} \int_{x_i}^x \frac{\rho_a^2}{\tilde{\rho}_a^2} \left( \frac{u_a}{\sqrt{H_a}} \right)^{2(1-\chi)} x' \, dx' \right]^{1/2} \quad (D-16)$$

In the application of the method to the free-jet tests performed in the experimental program certain simplifications result. Since the tank pressure was maintained constant during the testing,  $p_a = \text{constant}$ ; and  $u_a = \text{constant}$  from momentum which results in  $h_a = \text{constant}$  and  $\rho_a = \text{constant}$ . As a consequence,  $\tilde{u}_a = \text{constant}$ ,  $\tilde{\rho}_a = \text{constant}$ ,  $m = 0$ , and  $n = 1$ . Furthermore  $\chi = 1$  which results in  $\phi = s$  in the expressions for  $\tilde{x}$ ,  $\tilde{y}$ ,  $y$  and  $k$ . Utilizing these results

$$\tilde{x} = \frac{\rho_a}{\tilde{\rho}_a} x \quad (x_i = 0) \quad (\text{D-17})$$

and

$$\frac{y}{x} = \sqrt{\frac{0.00075}{s_*} \left(1 - \frac{f'_f}{s_f}\right)} \int_0^x s d\chi' \quad (\text{D-18})$$

### Flame Sheet Analytical Model

It has been demonstrated in the literature that a suitable approximation to the quasi-equilibrium behavior of a combustion zone for temperatures of interest in supersonic combustion can be realized by the assumption of a flame sheet model. This combustion model is based on the low-speed flow diffusion flame concept applied to high-speed flow. The assumptions made are that the reaction zone is of zero thickness and that the reacting species burn instantaneously upon reaching the sheet. The first assumption reduces the reaction zone to a surface which acts as a sink for reacting species, and as a source for the combustion products. The second approximation implies that the concentrations of the reactants at the sheet must be zero. This requires that the reactants diffuse towards the sheet in the stoichiometric ratio so that no species can diffuse across the sheet to react with those on the other side. These simplifications are justified provided the reaction rates are very large compared to the diffusion velocities of the species toward the sheet.

If one considers the species  $i = 1, 2, 3$ , and 4 to indicate molecular oxygen, hydrogen, water in gaseous form, and nitrogen, respectively, then the mass fractions are related according to

$$\begin{aligned} Y_{1s} &= Y_{2s} = 0 \\ Y_{3s} + Y_{4s} &= 1 \end{aligned} \quad (\text{D-19})$$

at the flame sheet. The chemical reaction considered in this combustion model is



where in general the element mass fractions are related to the species mass fractions by

$$\tilde{Y}_k = \sum_i a_{i_k} \frac{\tilde{W}_k}{W_i} Y_i \quad (k = 1, 2, \dots, e) \quad (\text{D-21})$$

where  $e$  represents the number of elements in the system.

From the mixing analysis of Reference 25, the species concentrations are determined from

$$z_i = \frac{1}{(1 - f'_f)} \left[ z_{i_f} - f'_f + (1 - z_{i_f}) f'_f \right] \quad (\text{D-22})$$

Where

$$z_i = \frac{Y_i}{Y_{ia}} \quad (\text{for frozen flow case})$$

$$z_i = \frac{\tilde{Y}_k}{\tilde{Y}_{ka}} \quad (\text{for the equilibrium flow case})$$

Consequently, at the flame sheet

$$\tilde{Y}_{1s} = \frac{W_1}{2W_3} Y_{3s} = \frac{\tilde{Y}_{1f} - \tilde{Y}_{1a} f'_f + (\tilde{Y}_{1a} - \tilde{Y}_{1f}) f'_s}{(1 - f'_f)} \quad (\text{D-23})$$

$$\tilde{Y}_{2s} = \frac{W_2}{W_3} Y_{3s} = \frac{\tilde{Y}_{2f} - \tilde{Y}_{2a} f'_f + (\tilde{Y}_{2a} - \tilde{Y}_{2f}) f'_s}{(1 - f'_f)} \quad (\text{D-24})$$

which reduce to

$$\frac{W_1}{2W_3} Y_{3s} = Y_{1a} \frac{(f'_s - f'_f)}{(1 - f'_f)} \quad (\text{D-25})$$

$$\frac{W_2}{W_3} Y_{3s} = \frac{(1 - f'_s)}{(1 - f'_f)} \quad (D-26)$$

when utilizing relations

$$\tilde{Y}_{1f} = 0, \quad \tilde{Y}_{1a} = Y_{1a}, \quad Y_{2a} = 0, \quad \tilde{Y}_{2f} = Y_{2f} = 1$$

Equating Equations (D-25) and (D-26) and utilizing the latter of Equations (D-19) there results

$$f'_s = \frac{1 + \frac{2W_2}{W_1} Y_{1a} f'_f}{1 + \frac{2W_2}{W_1} Y_{1a}} \quad (D-27)$$

$$Y_{3s} = \frac{2W_3}{W_1} \left( \frac{Y_{1a}}{1 + \frac{2W_2}{W_1} Y_{1a}} \right) \quad (D-28)$$

and

$$Y_{4s} = \frac{Y_{4a}}{1 + \frac{2W_2}{W_1} Y_{1a}} \quad (D-29)$$

Once  $f'_s$  has been evaluated from Equation (D-27),  $\chi_s$  is determined from the  $f'(\chi)$  vs  $\chi$  tables of Reference 35 for the  $\beta$  ( $\beta = 0$  for the present application) and  $f'_f$ . Accordingly the shape of the flame sheet is given by

$$\frac{y_s}{x} = \sqrt{\frac{0.00075}{s_*} \left( 1 - \frac{f'_f}{s_f} \right)} \int_0^{\chi_s} s d\chi' \quad (D-30)$$

For the constant pressure case the density ratio,  $s$ , can be calculated from

$$s = \frac{g - \lambda}{1 - \lambda} = \frac{1}{1 - \lambda} \left\{ \frac{1}{(1 - f'_f)} \left[ g_f - f'_f + (1 - g_f) f' \right] - \lambda \right\} \quad (D-31)$$

which together with the definition of  $\lambda$  results in

$$s = \frac{1}{(1 - f'_f)} \left\{ s_f - f'_f + (1 - s_f) f' \right\} \quad (D-32)$$

Consistent with these results the corresponding static enthalpy is given by

$$h = H_a \left[ \lambda + (1 - \lambda) s - f'^2 \left( \frac{u_a^2}{2H_a} \right) \right] \quad (D-33)$$

The theoretical reaction length is calculated from Equation (D-30) according to

$$x = \frac{y_s}{\sqrt{\frac{0.00075}{s_*} \left( 1 - \frac{f'_f}{s_f} \right) \int_0^{X_s} s \, d\chi'}} \quad (D-34)$$

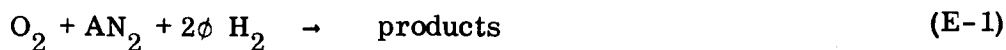
utilizing a characteristic value of  $y_s$ . For the single-point and three-point injection cases  $y_s$  was taken to be the diameter of the arc-jet nozzle. Accordingly, the reaction length represents the distance required for the flame sheet (across which no oxygen remains) to traverse the air stream. As indicated in the text the theoretical curve of  $\ell_r$  represents an engineering approximation to the actual behavior since the actual flow model is three dimensional in nature.

For the ring injection tests  $y_s$  was selected as the centerline value. In this manner the reaction length calculated represents the axial distance required for the flame sheets (emanating from both sides due to symmetry) to meet at the centerline of the arc-jet air stream. The schematics shown in Figure 48 indicate the various models utilized in both the asymmetric and symmetric cases considered.

The analysis presented here to determine Equation (D-34) represents an application of the method presented in Reference 25 utilizing a specific model of the eddy viscosity as determined in Reference 34.

# APPENDIX E DETERMINATION OF THE LOCAL EQUIVALENCE RATIO

In defining the equivalence ratio it is convenient to assume an initial state of the gas mixture where the species composing the mixture exist in their molecular states as unreacted fuel and undissociated air. The initial concentrations of molecular oxygen, molecular hydrogen and molecular nitrogen are conveniently expressed in terms of the equivalence ratio which is defined in accordance with the chemical equation



where

$$A = \left( \frac{X_{\text{N}_2}}{X_{\text{O}_2}} \right)_i$$

and

$$2\phi = \left( \frac{X_{\text{H}_2}}{X_{\text{O}_2}} \right)_i$$

In terms of  $\phi$  the initial concentrations are given by

$$Y_{\text{H}_2} = X_{\text{H}_2} \frac{W_{\text{H}_2}}{W} = \frac{4.032\phi X_{\text{O}_2}}{W} \quad (\text{E-2})$$

$$Y_{\text{O}_2} = X_{\text{O}_2} \frac{W_{\text{O}_2}}{W} = \frac{32 X_{\text{O}_2}}{W} \quad (\text{E-3})$$

$$Y_{\text{N}_2} = X_{\text{N}_2} \frac{W_{\text{N}_2}}{W} = \frac{28.016A X_{\text{O}_2}}{W} \quad (\text{E-4})$$

Accordingly,

$$\frac{w_{H_2}}{w_{mix}} = \frac{f/a}{1 + f/a} = Y_{H_2} = \frac{4.032\phi X_{O_2}}{W}$$

or

$$f/a = \frac{W_{H_2} X_{H_2}}{W - W_{H_2} X_{H_2}} = \frac{4.032\phi}{(32 + 28.016A)} \quad (E-5)$$

In obtaining Equation (E-5) use was made of the definition

$$W = \sum_k X_k W_k \quad (E-6)$$

From Equation (E-5) it is evident that

$$(f/a)_{st.} = \frac{4.032}{[32 + 28.016A]} \quad (E-7)$$

A mass balance of the chemical reaction required to go from initial concentrations to final conditions in the gas sampling bottle after water removal yields

$$(n_{O_2})_i = \left(\frac{1}{2} n_{H_2O} + n_{NO_2}\right)_B + (n_{O_2})_A \quad (E-8)$$

$$(n_{N_2})_i = (n_{N_2})_A + \frac{1}{2} (n_{NO_2})_B \quad (E-9)$$

$$(n_{H_2})_i = (n_{H_2})_A + (n_{H_2O})_B \quad (E-10)$$

where subscript B refers to stream values prior to the cold trap and subscript A refers to values in the gas sampling bottle after removal of condensable species in the cold trap. Using the known initial proportions of nitrogen and oxygen it is possible with the use of Equations (E-8) and (E-9) to determine the amount of water that was removed from the system.

Accordingly

$$\left[ \frac{n_{O_2}}{n_{N_2}} \right]_i = \frac{1}{A} = \frac{(\frac{1}{2} n_{H_2O} + n_{NO_2})_B + (n_{O_2})_A}{(n_{N_2})_A + \frac{1}{2} (n_{NO_2})_B} \quad (E-11)$$

which results in

$$(n_{H_2O})_B = \frac{2}{A} \left[ (n_{N_2} - A n_{O_2})_A - (A - \frac{1}{2}) (n_{NO_2})_B \right] \quad (E-12)$$

Since the number of moles of  $N_2$  and  $O_2$  are unchanged in passing through the cold trap the subscript A in equation (E-12) can be replaced by the subscript B.

From Equations (E-5), (E-8), (E-9) and (E-10) it is possible to express the fuel-air ratio as

$$(f/a)_\ell = \frac{W_{H_2} \left[ (n_{H_2O})_B + (n_{H_2})_A \right]}{W_{O_2} \left[ (\frac{1}{2} n_{H_2O} + n_{NO_2})_B + (n_{O_2})_A \right] + W_{N_2} \left[ (n_{N_2})_A + \frac{1}{2} (n_{NO_2})_B \right]}$$

which with the use of Equation (E-12) becomes

$$\left[ \frac{f}{a} \right]_\ell = \left[ \frac{W_{H_2}}{W_{N_2} + \frac{W_{O_2}}{A}} \right] \left\{ \frac{\frac{2}{A} (n_{N_2})_A + (n_{H_2})_A - 2 (n_{O_2})_A - (2 - \frac{1}{A}) (n_{NO_2})_B}{(n_{N_2})_A + \frac{1}{2} (n_{NO_2})_B} \right\} \quad (E-13)$$

Using the stoichiometric fuel-air ratio given in Equation (E-7) together with Equation (E-13) it is possible to obtain

$$\phi_\ell = \frac{A}{2} \left\{ \frac{\frac{2}{A} (n_{N_2})_A + (n_{H_2})_A - 2 (n_{O_2})_A - (2 - \frac{1}{A}) (n_{NO_2})_B}{(n_{N_2})_A + \frac{1}{2} (n_{NO_2})_B} \right\} \quad (E-14)$$

which is the local equivalence ratio based on measured quantities. It should be noted that the A subscripts in Equation (E-14) can also be replaced by the subscript B.



The total number of moles required to obtain mole fractions of the constituents prior to the cold trap is given by

$$(n_{\tau})_B = (1 + \frac{2}{A}) (n_{N_2})_A + (n_{H_2})_A - (n_{O_2})_A - (1 - \frac{1}{A}) (n_{NO_2})_B \quad (E-15)$$

The value of A used in the calculations was determined from actual arc-jet input values of  $N_2$  and  $O_2$  according to

$$A = \frac{W_{O_2}}{W_{N_2}} \left[ \frac{\dot{w}_{N_2}}{\dot{w}_{O_2}} \right]_i \quad (E-16)$$

## REFERENCES

1. Gross, R.A. and Chinitz, W., "A Study of Supersonic Combustion", J. Aero Sci., Vol. 27, No. 7, pp. 517-524, July 1960.
2. Nicholls, J.A., "Stabilized Gaseous Detonation Waves", ARS J. Vol. 29, No. 8, pp. 607-608, August 1959.
3. Rhodes, R.D. and Chriss, D.E., "A Preliminary Study of Stationary Shock Induced Combustion with Hydrogen-Air Mixture" AEDC TN 61-36, July 1961.
4. Rhodes, R.D., Rubins, P.M., and Chriss, D.E., "The Effect of Heat Release on the Flow Parameters in Shock Induced Combustion", AEDC TDR 62-78, May 1962.
5. Burke, S.P. and Schumann, T.E.W., "Diffusion Flames", Ind. Eng. Chem., Vol. 20, pp. 998-1004, 1928.
6. Ferri, A., "Possible Directions of Future Research in Air-Breathing Engines", AGARD Combustion and Propulsion Colloquium Pergamon Press Ltd., London, England, pp. 3-15, 1960.
7. Nucci, L.M. and Zipkin, M.Z., "Composite Air-Breathing Systems", Fourth AGARD Combustion and Propulsion Colloquium, Pergamon Press Ltd., London, England, pp. 16-36, 1961.
8. Dugger, G.L., "Combustion of Hypersonic Ramjet Engines with Subsonic and Supersonic Combustion", Fourth AGARD Combustion and Propulsion Colloquium, Pergamon Press Ltd., London, England, pp. 84-119, 1961.
9. Duff, R.W., "Calculation of Reaction Profiles Behind Steady State Shock Waves", I. Application to Detonation Waves, J. Chem. Phys., Vol. 28, No. 6, pp. 1193-1197, June 1958.
10. Schott, G.L., "Kinetic Studies of Hydroxyl Radicals in Shock Waves", III. The OH Concentration Maximum in the Hydrogen-Oxygen Reaction, J. Chem. Phys. Vol. 32, No. 2, pp. 710-716, March 1960.
11. Schott, G.L. and Kinsey, J.L., "Kinetic Studies of Hydroxyl Radicals in Shock Waves", II. Induction Times in the Hydrogen-Oxygen Reactions, J. Chem. Phys., Vol. 29, No. 5, pp. 1177-1182, November 1958.
12. Yates, C.L., Billig, F.S. and Dugger, G.L., "Experimental Results and Data Analysis Techniques of a Hydrogen-Filled Supersonic Combustor", APL Rept. Issued under NASA contract SC-R-76/21-09-001.
13. Libby, P.A., Pergament, H., and Bloom, M.H., "A Theoretical Investigation of Hydrogen-Air Reactions", Part I - Behavior with Elaborate Chemistry, G.A.S.L. TR 250, AFOSR 1378, August 1962.
14. Momtchiloff, I.N., Taback, E.D. and Buswell, R.F., "An Analytical Method of Computing Reaction Rates for Hydrogen-Air Mixtures", Presented at Ninth International Symposium on Combustion, Cornell Univ., Ithaca, New York, August 1962.
15. Westenberg, A.A., "Hydrogen-Air Chemical Kinetic Calculations in Supersonic Flow", Johns Hopkins University A.P.L. Report CM-1028, Dec. 1962.

## REFERENCES (Cont'd)

16. Pergament, H., "A Theoretical Analysis of Non-Equilibrium Hydrogen-Air Reactions in Flow Systems, Presented at AIAA-ASME Hypersonic Ramjet Conference, NOL, White Oak, Maryland, April 23-25, 1963.
17. Ferri, A., Libby, P. A., and Zakkay, V., "Theoretical and Experimental Investigation of Supersonic Combustion, ARL 62-467, September 1962.
18. Bar-Gadda, et al "Supersonic Combustion" Republic Aviation Corporation Report No. 2493, Dec. 1964.
19. Johnson, C.B., Boney, L.R., Ellison, J.C. and Erickson, W.D., "Real-Gas Effects on Hypersonic Nozzle Contours with a Method of Calculation", NASA TND-1622, April 1963.
20. Bergles, A.E. and Rohsenow, W.M., "The Determination of Forced Convection Surface Boiling Heat Transfer", Journal of Heat Transfer, Vol. 86, No. 3, August 1964, pp. 365-372.
21. Rohsenow, W.M. and Choi, H. Y., "Heat, Mass and Momentum Transfer", Prentice-Hall, Inc., Englewood Cliffs, N.J., 1961.
22. Gambill, W.R., "Generalized Prediction of Burnout Heat Flux for Flowing, Subcooled, Wetting Liquids", Chem. Eng. Progress Symposium Series, No. 41, Vol. 59, A.I.Ch.E., N.Y., 1963.
23. Progress Report No. 5 of Contract NAS 1-6314
24. Progress Report No. 7 of Contract NAS 1-6314
25. Casaccio, A., "Turbulent Mixing of Reactive Gases", AIAA Journal, Vol. 3, No. 6, pp. 1160-1162, June 1965.
26. Libby, P. A., "Theoretical Analysis of Turbulent Mixing of Reactive Gases With Application to Supersonic Combustion of Hydrogen", ARS Journal Vol. 32, No. 3, March 1962, pp 388-396.
27. Charwat, A. F., Roos, J. N., Dewey, F. C. and Hitz, J. A., "An Investigation of Separated Flows - Part I: Pressure Field", Journal of the Aerospace Sciences, Vol. 28, No. 6, June 1961
28. Librizzi, J. and Cresci, R.J., "Transpiration Cooling of A Turbulent Boundary Layer in an Axisymmetric Nozzle", ARL 63-103, June 1963.
29. Roshotko, E. and Tucker, M., "Approximate Calculation of the Compressible Turbulent Boundary Layer with Heat Transfer and Arbitrary Pressure Gradient", NACA TN 4154, 1957.
30. Bulewicz, E.M., and Sugden, T.M., "Studies of Oxygen Atoms at High Temperatures", Chemical Society (London), Special Publication No. 9, LXXXI, 1958.
31. Romano, M.A. and Zinman, W.G., "A Simplified Kinetic Method for Multi-Component Mixtures", Second Conference In Kinetics, Combustion Institute, Los Angeles, April 1962.

#### REFERENCES (Cont'd)

32. Romano, M.A. and Zinman, W.G., "IBM 7090 Computer Program 64D007 for Calculating Thermodynamic and Kinetic Properties of Hydrogen-Air Mixture", RDAPM-106, August 1962.
33. Kaskan, W.E. and Brown, W.G., "Kinetics of  $H_2/CO/O_2$  System MSD/GE Report No. R64SD37, May 1964.
34. Kleinstein, G., "On the Mixing of Laminar and Turbulent Axially Symmetric Compressible Flows", ARL 63-108, June 1963.
35. Casaccio, A., "Similar Solutions for the Turbulent Compressible Mixing of Two Streams with Streamwise Pressure Gradient", Republic Aviation Rept. RAC-822A, March 1963.

TABLE II

POINT AND THREE-POINT INJECTION DATA (0.108" SPACING)

Run No.	$T_a$ °R	$T_{of}$ °R	$V_f/V_a$	$\phi_i$	$\phi_t$	Gas Sampling and Temp. Mea. Sta. (inches)
39A	2646	610	0.40	0.5998	0.4980	9.0
42B	2673	595	0.65	0.9517	0.2672	17-5/8 *
42C	2322	595	0.65	0.70786	0.5824	17-5/8 *
44B	3222	610	0.65	0.96833	0.6100	17-5/8 *
45B	2700	580	0.65	0.96516	0.7091	12" on H <sub>2</sub> hole
49	2763	1020	0.40	0.32624	0.0700	10-1/2 **
50B	2763	990	0.65	0.56651	0.3454	10-1/2 **
52A	2322	975	0.65	0.4806	0.5761	10-1/2" interface
Run No.	$X_{O_2}$	$X_{N_2}$	$X_{H_2}$	$X_{H_2O}$	$X_{NO_2}$	Injection Configuration
39A	0.1050	0.6866	-	0.2084	-	3 Point
42B	0.1564	0.7296	-	0.1140	-	Single Point
42C	0.0872	0.6895	0.0143	0.2090	-	
44B	0.0697	0.7124	-	0.2180	-	
45B	0.0728	0.6772	0.0431	0.2069	-	
49	0.2008	0.7690	-	0.0302	-	
50B	0.1252	0.7427	-	0.1321	-	
52A	0.0958	0.6961	0.0385	0.1696	-	

\* 1/8" below centerline of the tunnel

\*\* at interface between the air and hydrogen

TABLE III

## SINGLE-POINT INJECTION TEST DATA (0.216" SPACING)

Run No.	$T_a \sim ^\circ R$	$T_{of} \sim ^\circ R$	$V_f/V_a$	$\phi_i$	$\phi_t$	Gas Sampling and Temp. Mea. Sta. (inches)
190	2556	560	0.40	0.517	0.7398	9.0 *
191	2592	1090	0.40	0.329	0.8154	9.0 *
192	2628	1000	0.65	0.584	0.9489	9.0 *
195	2205	580	0.65	0.832	0.7050	18.0 *
196	2322	610	0.40	0.439	0.8101	
197	2484	600	0.40	0.519	0.7553	
198	2385	1060	0.40	0.347	0.7079	
199	2592	1010	0.65	0.587	0.7287	
200	2196	1070	0.40	0.256	0.4428	
201	2205	990	0.65	0.469	0.7059	
204	1998	575	0.40	0.363	0.5858	
205	2025	580	0.65	0.574	0.7941	
206	2025	1060	0.40	0.239	0.6216	

\* 5/8" below the centerline of the tunnel

TABLE III (cont'd)

Run No.	X <sub>O<sub>2</sub></sub>	X <sub>N<sub>2</sub></sub>	X <sub>H<sub>2</sub></sub>	X <sub>H<sub>2</sub>O</sub>	X <sub>NO<sub>2</sub></sub>
190	0.0992	0.6408	0.1078	0.1518	0.0004
191	0.0672	0.6387	0.0840	0.2096	0.0004
192	0.0530	0.6224	0.0891	0.2352	0.0003
195	0.0918	0.6635	0.0835	0.1603	0.0009
196	0.0753	0.6461	0.0866	0.1915	0.0005
197	0.0660	0.6580	0.0437	0.2319	0.0005
198	0.0692	0.6632	0.0285	0.2390	0.0003
199	0.0552	0.6878	0.0158	0.2408	0.0004
200	0.1193	0.7157	0.0319	0.1328	0.0003
201	0.0781	0.6737	0.0534	0.1945	0.0003
204	0.0956	0.6893	0.0398	0.1748	0.0003
205	0.0723	0.6526	0.0737	0.2012	0.0002
206	0.0869	0.6860	0.0363	0.1904	0.0003

TABLE III (cont'd)

Run No.	$T_{Exp} \sim R$	$\bar{\eta}$	$h_{Exp} \sim BTU/LB$
190	-	0.5848	-
191	3680	0.7138	1951
192	3860	0.7252	2111
195	-	0.6577	-
196	-	0.6887	-
197	3230	0.8414	1550
198	3340	0.8935	1506
199	3340	0.9385	1433
200	-	0.8062	-
201	-	0.7846	-
204	-	0.8144	-
205	-	0.7318	-
206	-	0.8397	-



TABLE IV

## RING INJECTION TEST DATA

Run No.	$T_a \sim ^\circ R$	$T_{of} \sim ^\circ R$	$V_f/V_a$	$\phi_i$	$\phi_\ell$	Gas Sampling and Temp. Mea. Sta. (inches)
56	1944	1055	0.8426	1.0	0.3695	12
102	2214	990	0.7261	1.0	0.4845	12
104B	2232	1020	0.7445	0.5	0.4644	12
105A	3240	660	0.3471	0.5	0.3430	12
105B	3258	1010	0.5220	0.5	0.3084	12
106B	2502	590	0.3935	0.5	0.6813	16.5
108	2700	1010	0.6446	0.5	0.2022	16.5
114A	2664	595	0.3818	0.5	0.5338	16.5
114B	2592	1045	0.6536	0.5	0.4846	16.5
115A	2160	620	0.4850	0.5	0.5428	16.5
115B	2304	1020	0.7541	0.5	0.5890	16.5
117A	2115	590	0.4614	0.5	0.5344	12
117B	2070	1030	0.8034	0.5	0.5675	16.5
118B	2700	630	0.3956	0.5	0.5529	16.5
118C	2646	1040	0.6448	0.5	0.5531	16.5
226	2124	570	0.4508	1.0	0.7891	18.5
227	2070	960	0.7228	1.0	0.7392	18.5
229	2592	600	0.3744	1.0	0.6510	18.5

TABLE IV (cont'd)

Run No.	$T_a \sim ^\circ R$	$T_{of} \sim ^\circ R$	$V_f/V_a$	$\phi_l$	$\phi_l$	Gas Sampling and Temp. Mea. Sta. (inches)
230	2619	990	0.6229	1.0	0.7186	18.5
232	3132	610	0.3312	1.0	0.6332	18.5
233	3132	990	0.5087	1.0	0.6156	18.5
235	3123	570	0.3272	0.5	0.6215	18.5
236	3105	1060	0.6136	0.5	0.6235	18.5
238	2700	610	0.4115	0.5	0.6488	18.5
239	2619	1030	0.7073	0.5	0.6260	18.5
241	2142	640	0.5521	0.5	0.6392	18.5
242	2160	960	0.8207	0.5	0.6343	18.5

Run No.	$X_{O_2}$	$X_{N_2}$	$X_{H_2}$	$X_{H_2O}$	$X_{NO_2}$
56	0.1194	0.7407	-	0.1399	-
102	0.0959	0.7216	-	0.1818	0.00077
104B	0.0966	0.7351	-	0.1681	0.00030
105A	0.1235	0.7454	-	0.1301	0.00110
105B	0.1302	0.7517	-	0.1171	0.00103
106B	0.0621	0.6723	-	0.2656	-
108	0.1464	0.7794	-	0.0742	-

TABLE IV (cont'd)

Run No.	$X_{O_2}$	$X_{N_2}$	$X_{H_2}$	$X_{H_2O}$	$X_{NO_2}$
114A	0.0938	0.6974	0.0082	0.1996	0.00101
114B	0.1040	0.7033	0.0050	0.1871	0.00060
115A	0.1145	0.6829	0.0594	0.1429	0.00035
115B	0.1026	0.6784	0.0546	0.1635	0.00086
117A	0.1129	0.6862	0.0521	0.1483	0.00045
117B	0.1045	0.6879	0.0522	0.1548	0.00054
118B	0.0845	0.7049	-	0.2101	0.00050
118C	0.0842	0.7054	-	0.2099	0.00062
226	0.0655	0.6593	0.0578	0.2172	0.00013
227	0.0617	0.6751	0.0309	0.2322	0.00013
229	0.0657	0.6872	-	0.2467	0.00042
230	0.0518	0.6806	-	0.2671	0.00051
232	0.0659	0.7053	-	0.2285	0.00031
233	0.0683	0.7099	-	0.2210	0.00040
235	0.0705	0.6971	-	0.2322	0.00024
236	0.0692	0.7001	-	0.2303	0.00029
238	0.0663	0.6915	0.0023	0.2396	0.00030
239	0.0690	0.6979	-	0.2326	0.00047
241	0.0773	0.6884	0.0232	0.2108	0.00029
242	0.0835	0.6858	0.0341	0.1966	0.00030

TABLE IV (cont'd)

Run No.	$T_{Exp} \sim ^\circ R$	$\bar{\eta}$	$h_{Exp} \sim BTU/LB$	$\phi_{Eff}$	Number of Injection Ports
56	-	1.0	-	-	24
102	2560	1.0	986	0.474	24
104B	2910	1.0	1086	0.430	12
105A	2760	1.0	988	0.330	12
105B	2380	1.0	852	0.298	12
106B	-	1.0	-	-	12
108	3920	1.0	1289	0.125	12
114A	3780	0.9607	1478	0.570	12
114B	3645	0.9740	1453	0.625	12
115A	3675	0.7064	1660	0.996	12
115B	3625	0.7495	1648	1.015	12
117A	4040	0.7399	1754	0.853	12
117B	4030	0.7476	1765	0.877	12
118B	3390	1.0	1309	0.54	12
118C	3375	1.0	1251	0.425	12
226	3700	0.7897	1794	1.235	24
227	3730	0.8827	1657	0.950	24
229	3700	1.0	1477	0.627	24

TABLE IV (cont'd)

Run No.	$T_{Exp} \sim R$	$\overline{\eta}$	$h_{Exp} \sim BTU/LB$	$\phi_{Eff}$	Number of Injection Ports
230	3580	1.0	1467	0.703	24
232	3240	1.0	1284	0.605	24
233	3075	1.0	1215	0.585	24
235	3180	1.0	1267	0.617	12
236	3070	1.0	1226	0.613	12
238	3290	0.9129	1331	0.66	12
239	3160	1.0	1261	0.620	12
241	3730	0.9008	1571	0.783	12
242	3590	0.8522	1564	0.890	12

TABLE V  
ORIGINAL COMBUSTOR TEST DATA

Run No.	No. of Segments	$T_a \sim R$	$T_{of} \sim R$	$\phi_L^*$	$\phi_L$	Gas Sampling and Temp. Mea. Sta. (inches)
123	3	2169	560	0.5	0.1206	0.5
124	3	2160	1040	0.5	0.1449	0.5
126	3	2709	570	0.5	0.0887	0.5
127	3	2664	1080	0.5	0.1148	0.5
132	2	2142	620	0.5	0.2929	0.5
136	3	2142	560	1.0	0.3804	0.5
137	3	2133	980	1.0	0.3596	0.5
140	3	2718	990	1.0	0.1899	0.5
142	2	2070	580	1.0	0.1436	0.5
147	2	2700	990	1.0	1.000	0.5
149	2	2137	590	0.5	0.4599	0.5
150	2	2115	985	0.5	0.5474	0.5
152	2	2754	630	0.5	0.6954	0.5
153	2	2718	1000	0.5	0.7975	0.5
167	3	2106	585	1.0	0.4100	0.5
171	3	2070	990	1.0	0.0980	0.5
173	3	2730	628	1.0	0.1879	0.5
174	3	2170	1010	1.0	0.2307	0.5

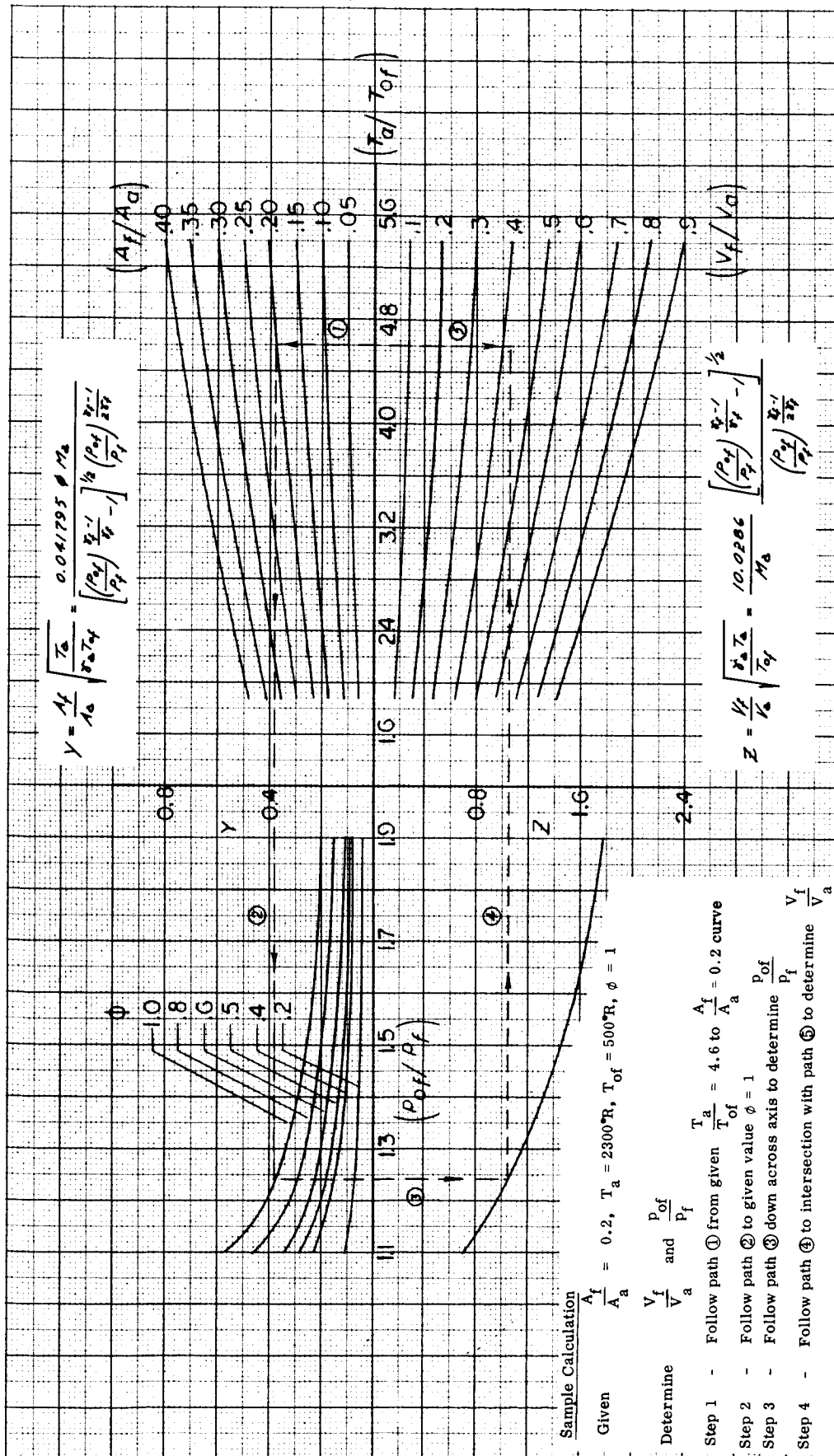


Figure 1. Variation of Fuel-Air Injection Parameters for an Air Mach Number 2.3 and  $p_a = p_f = 0.5 \text{ atm}$ .

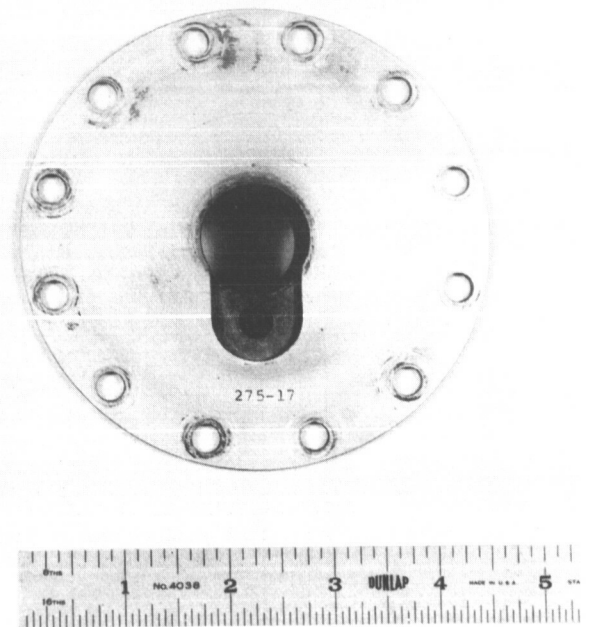
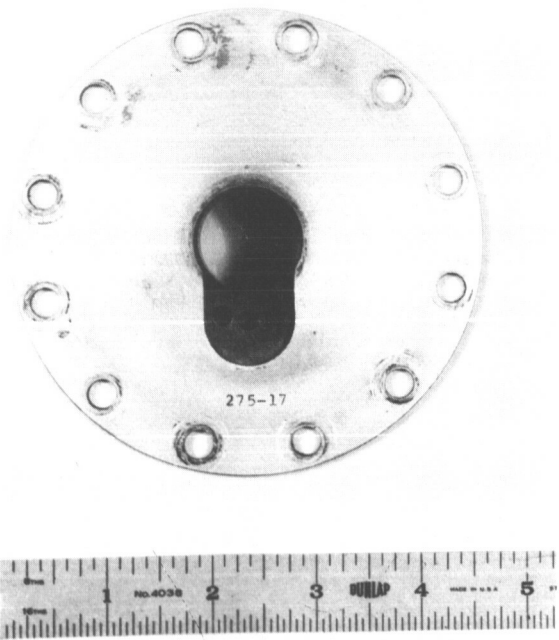
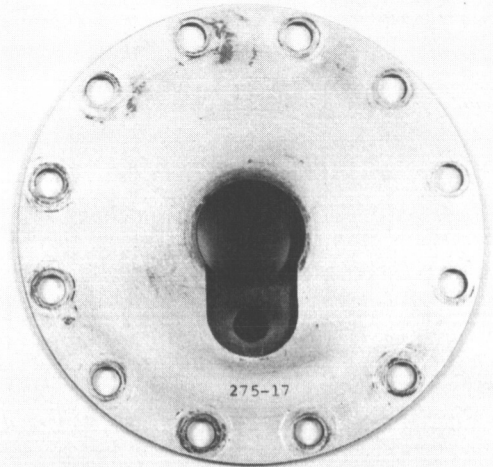
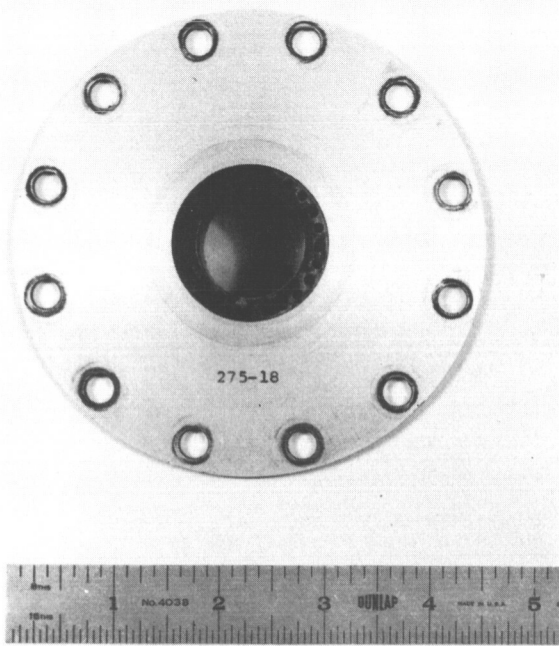


Figure 2. Fuel Injection Configurations





**Figure 3. Combustion Rig Layout Showing Original Combustor Contour**

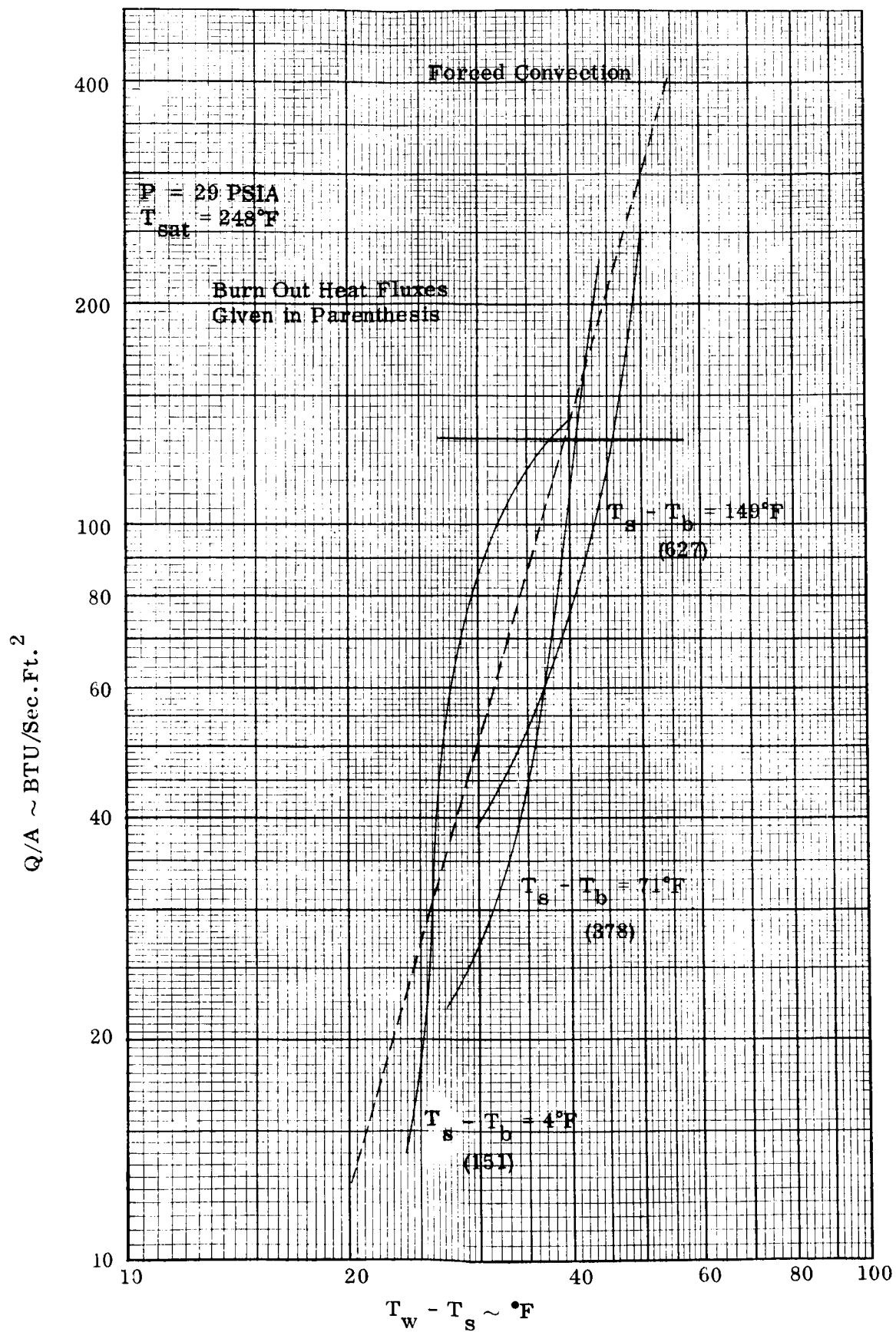


Figure 4. Subcooled Pool Boiling Heat Fluxes

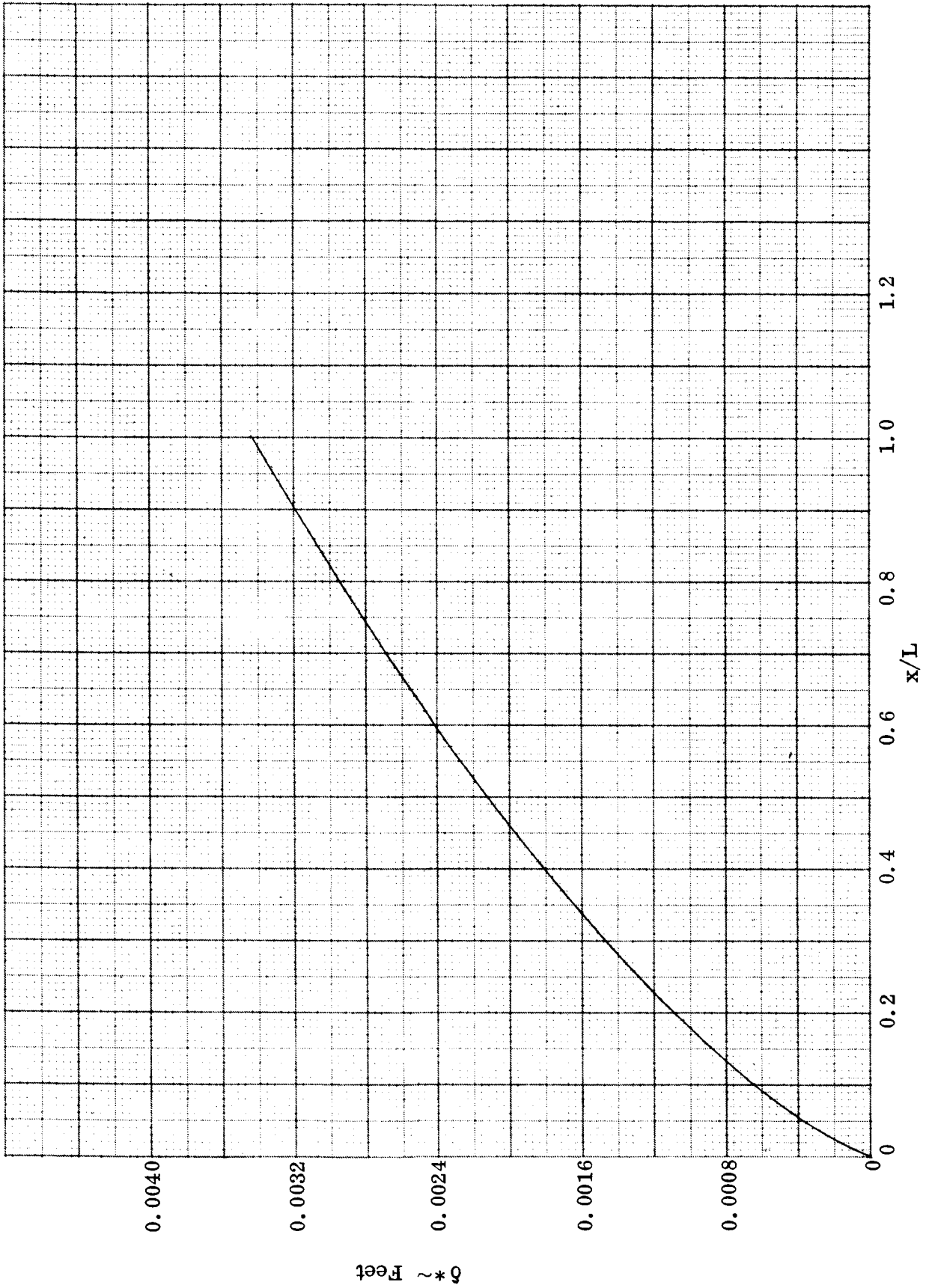


Figure 5. Displacement Thickness Distribution Inside Segmented Combustor (Design Case)

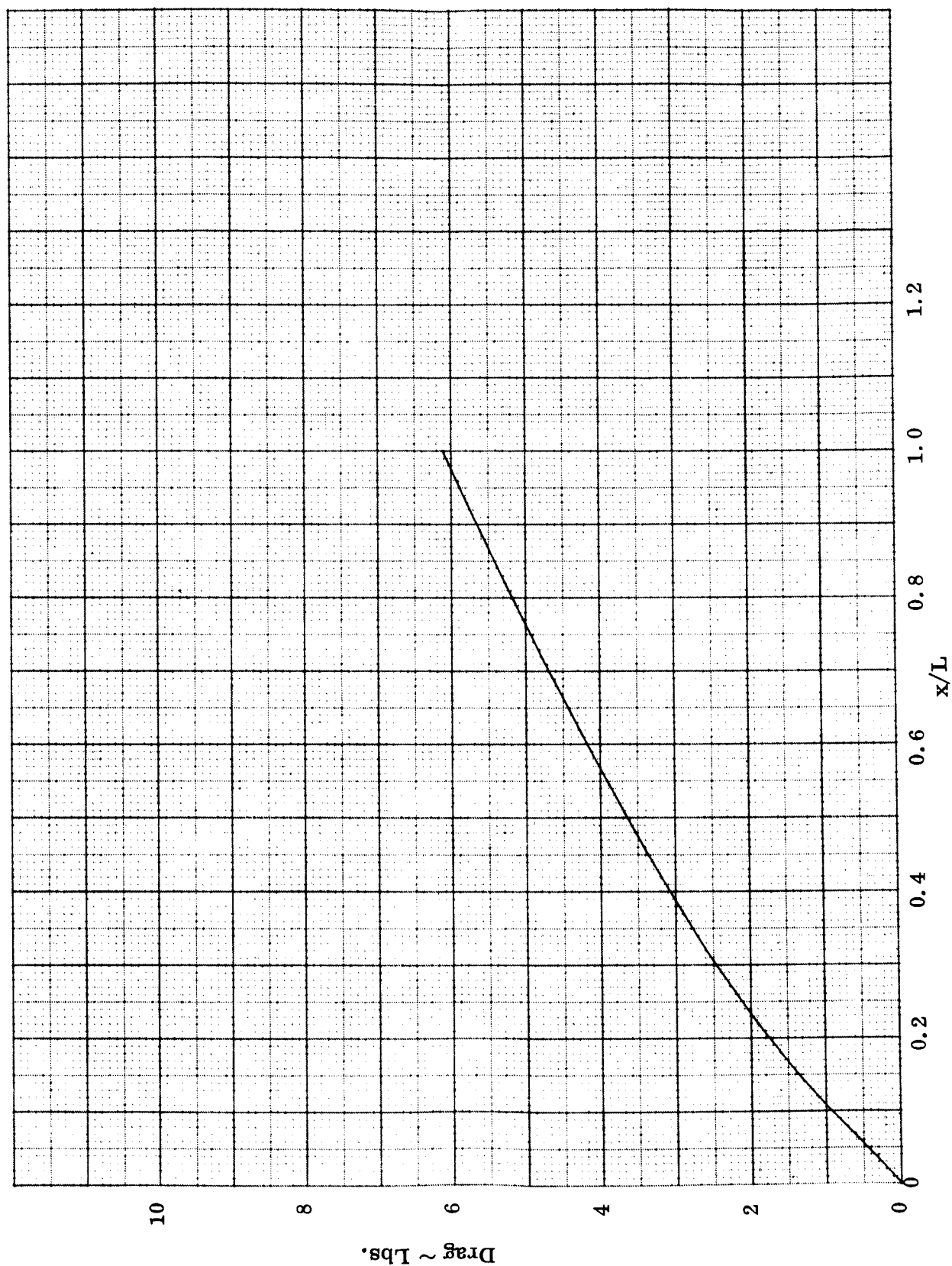


Figure 6. Skin Friction Drag Distribution Inside Segmented Combustor (Design Case)

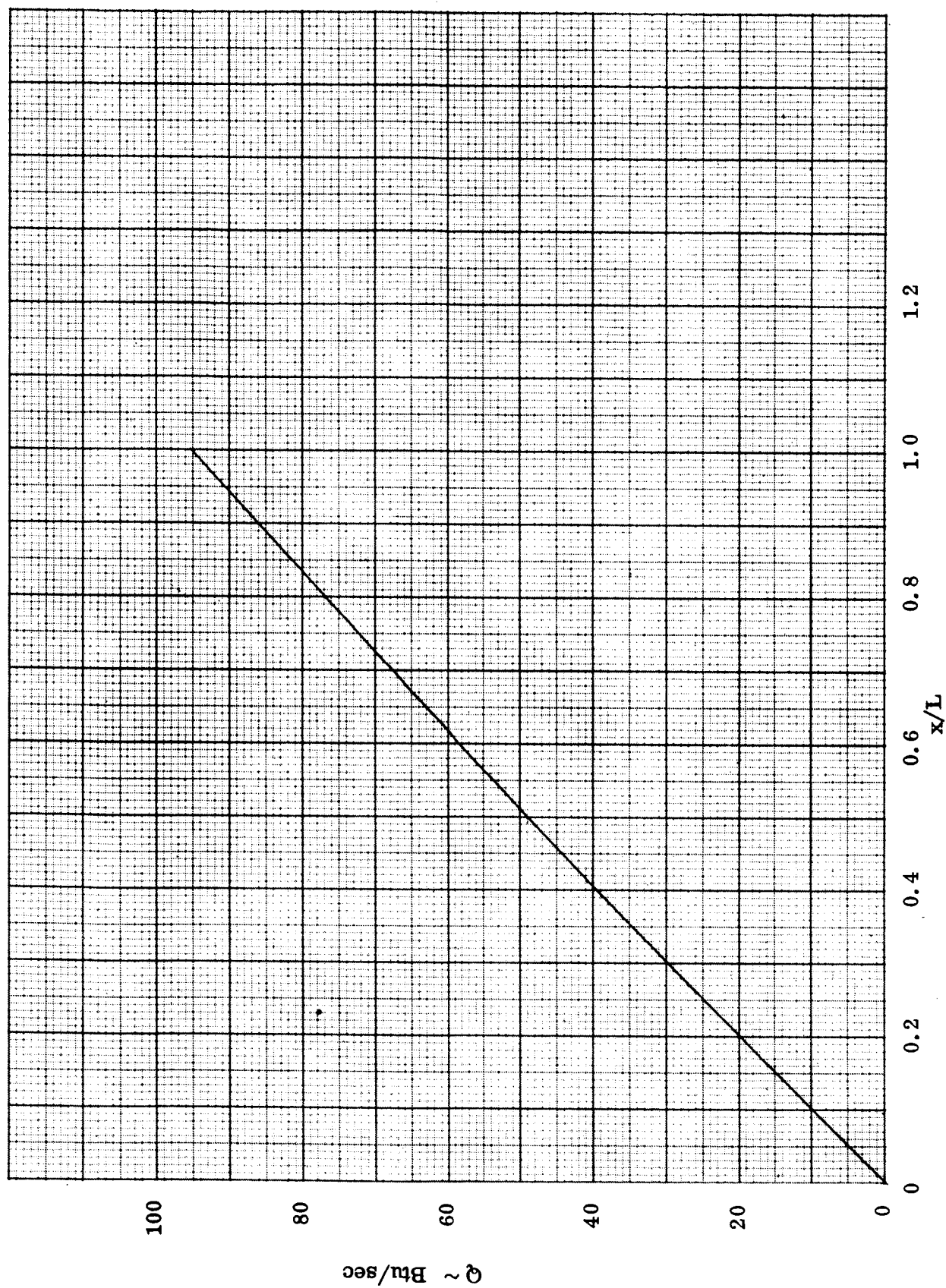


Figure 7. Total Heat Transfer Distribution Inside Segmented Combustor (Design Case)

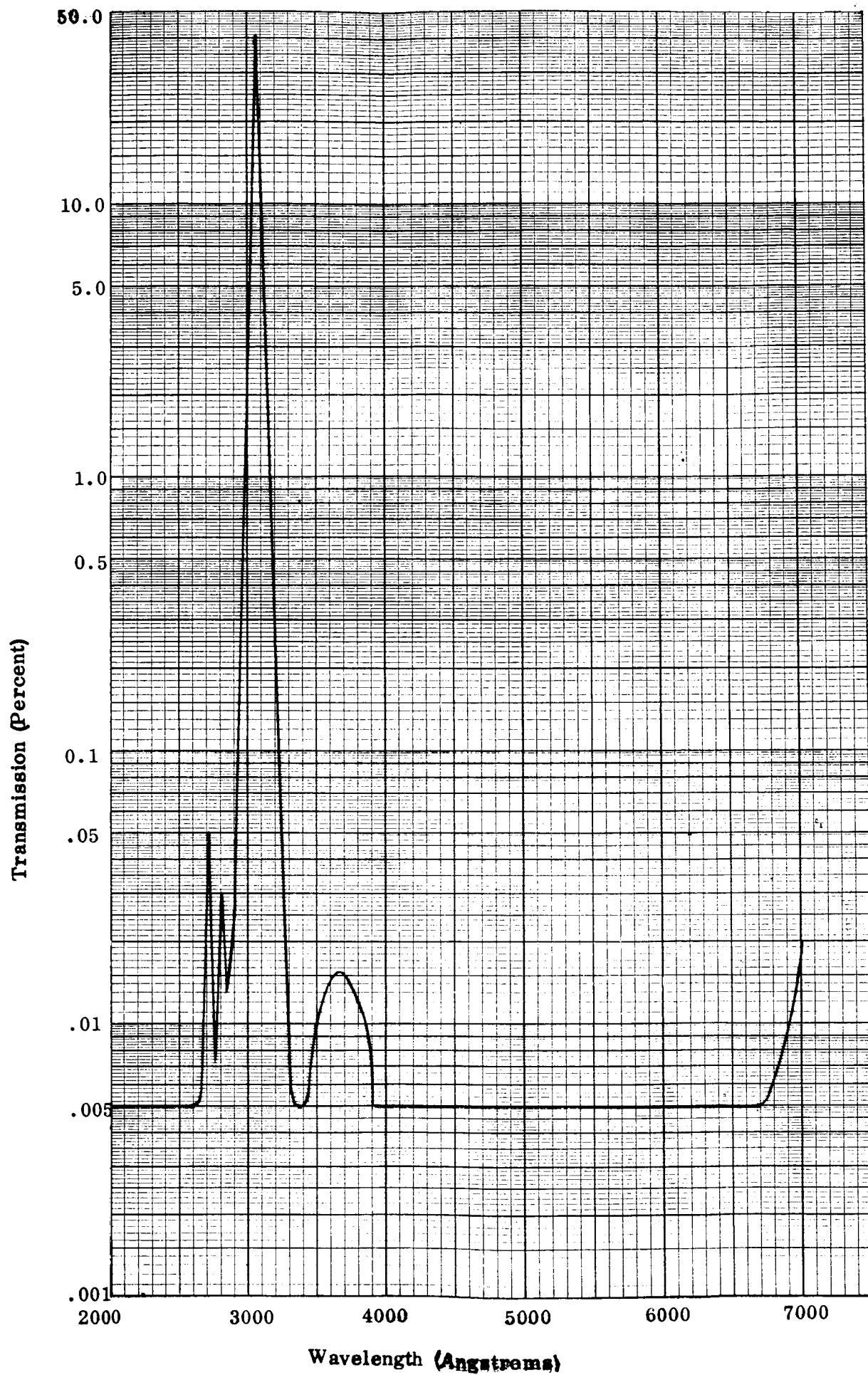


Figure 8.. Transmission Curve of Perkin-Elmer Spike Filter

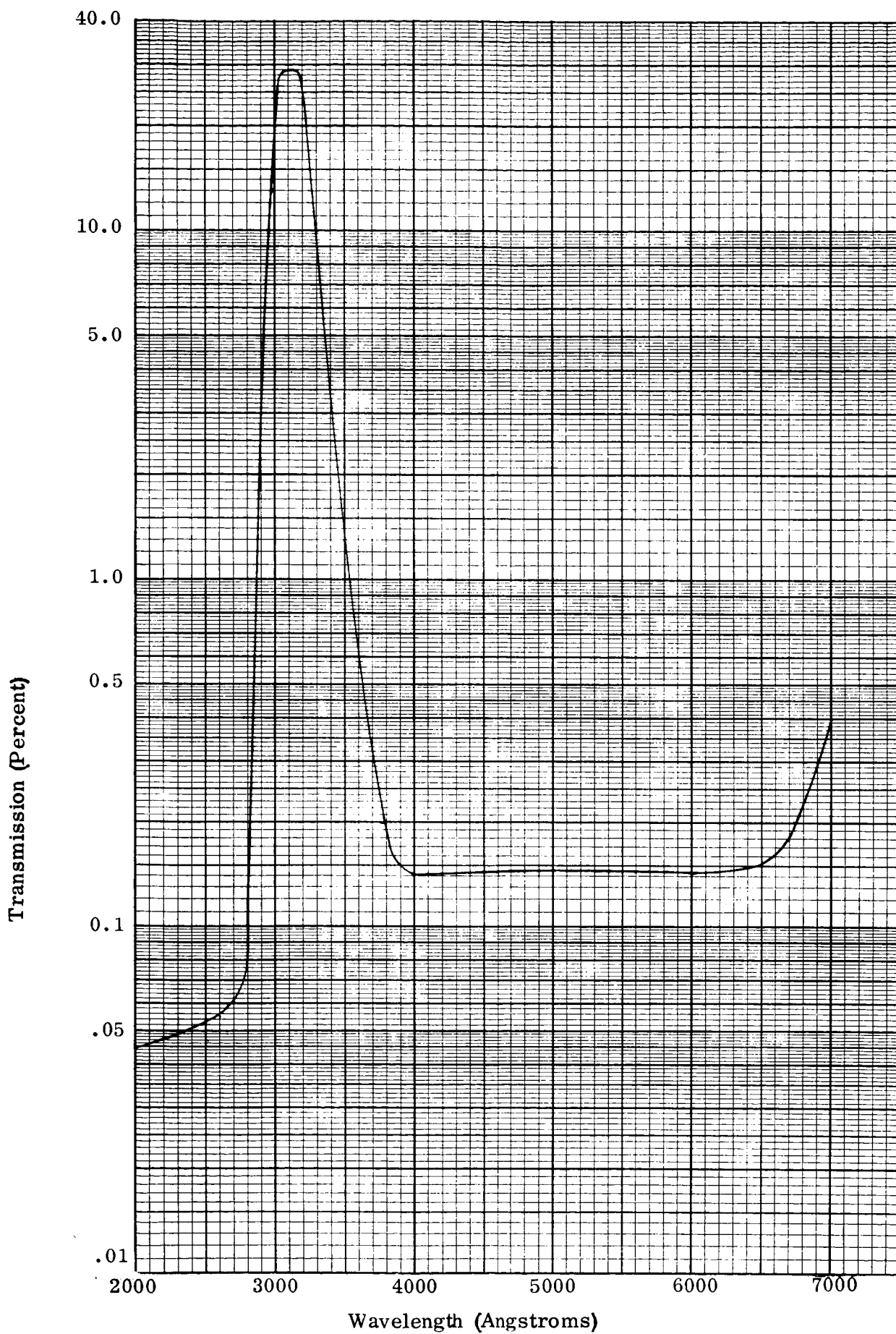


Figure 9. Transmission Curve of Zeiss Ultraviolet Filter

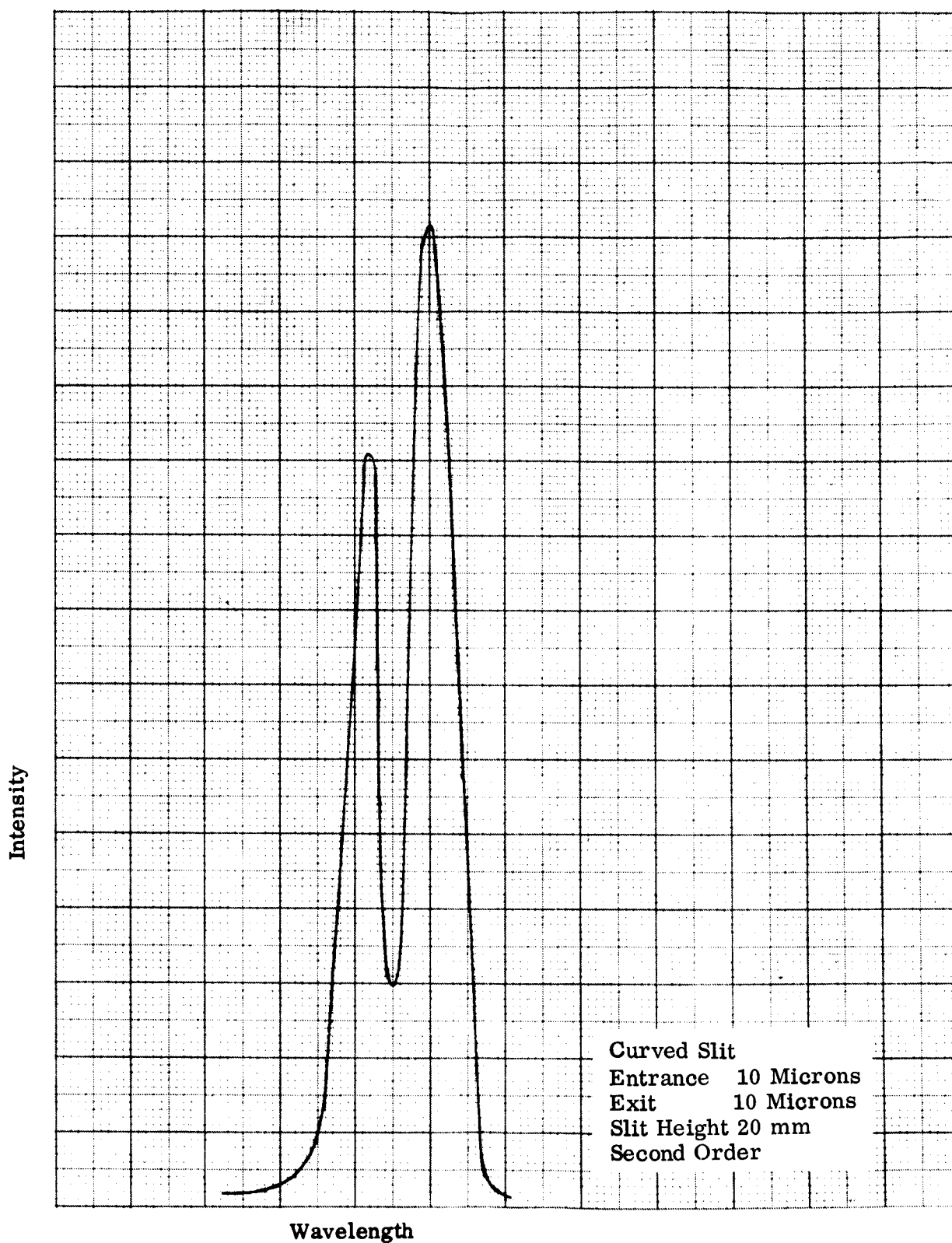


Figure 10.. Spectrometer Resolution of Mercury 3131.6A<sup>°</sup> Doublet



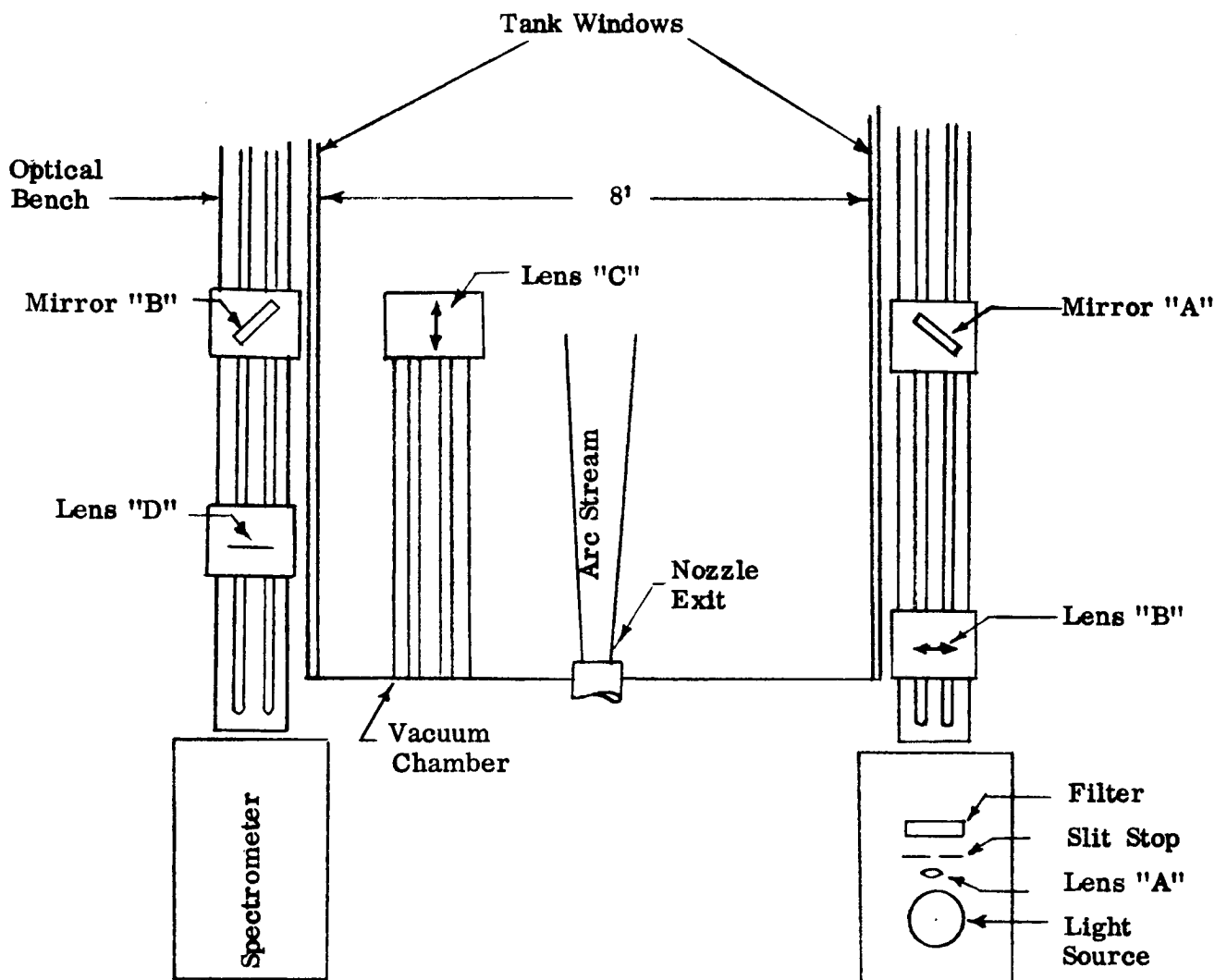


Figure 11.. Optical Layout for Spectrometry

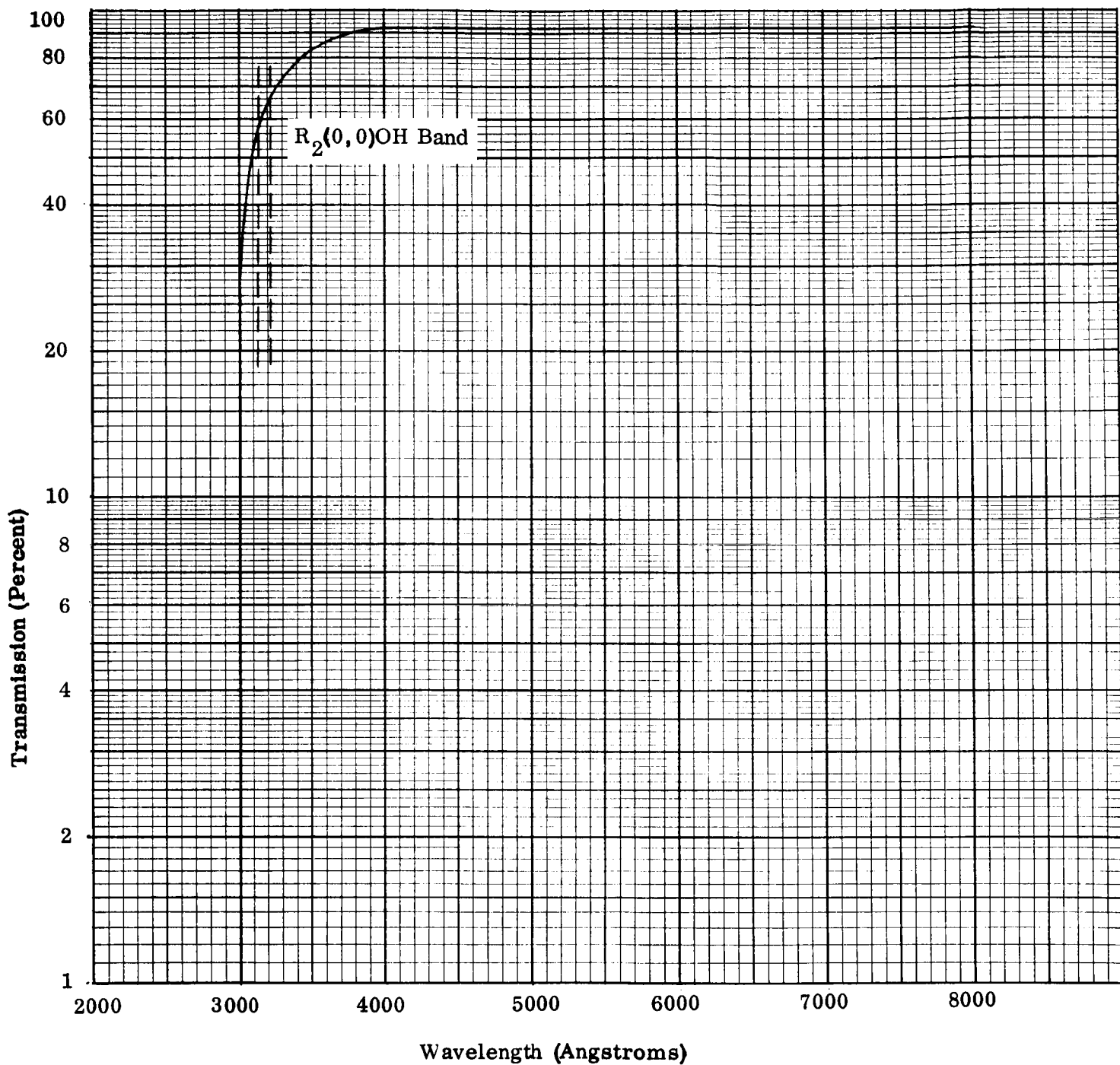


Figure 12. Transmission Curve of Rohm and Haas UVT Plexiglass

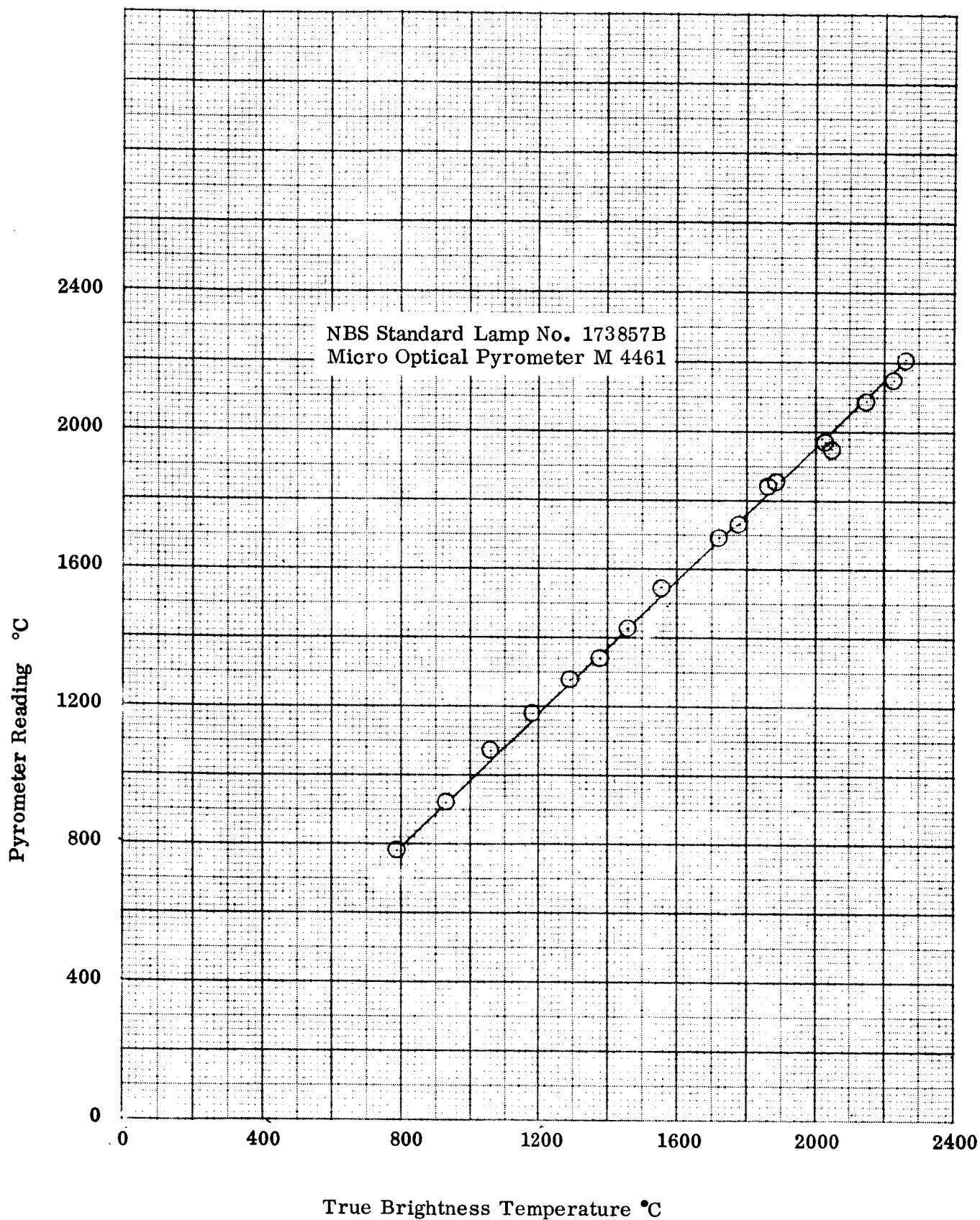


Figure 13.- Pyrometer Calibration Curve

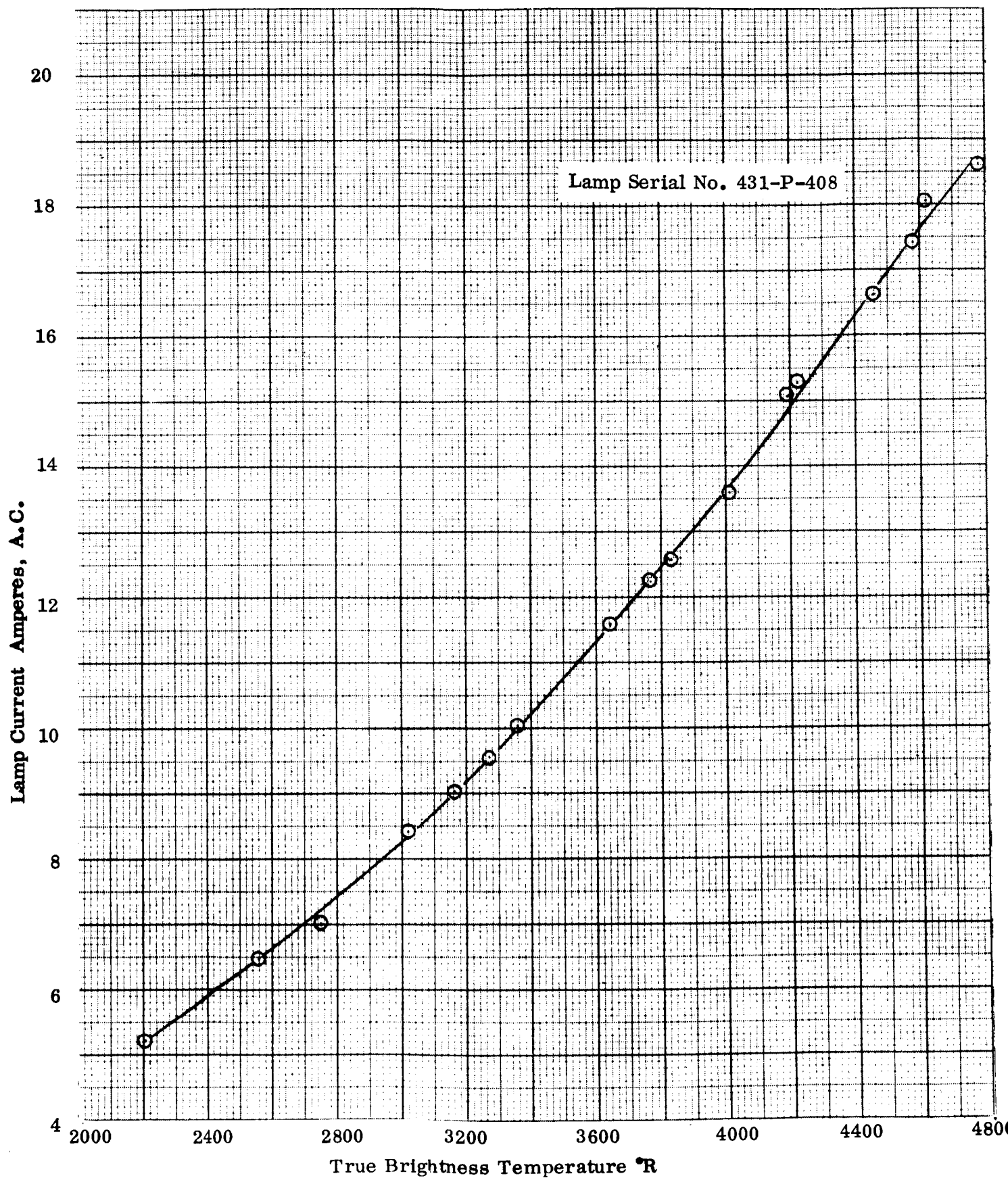


Figure 14. Lamp Calibration Curve (Secondary Standard)

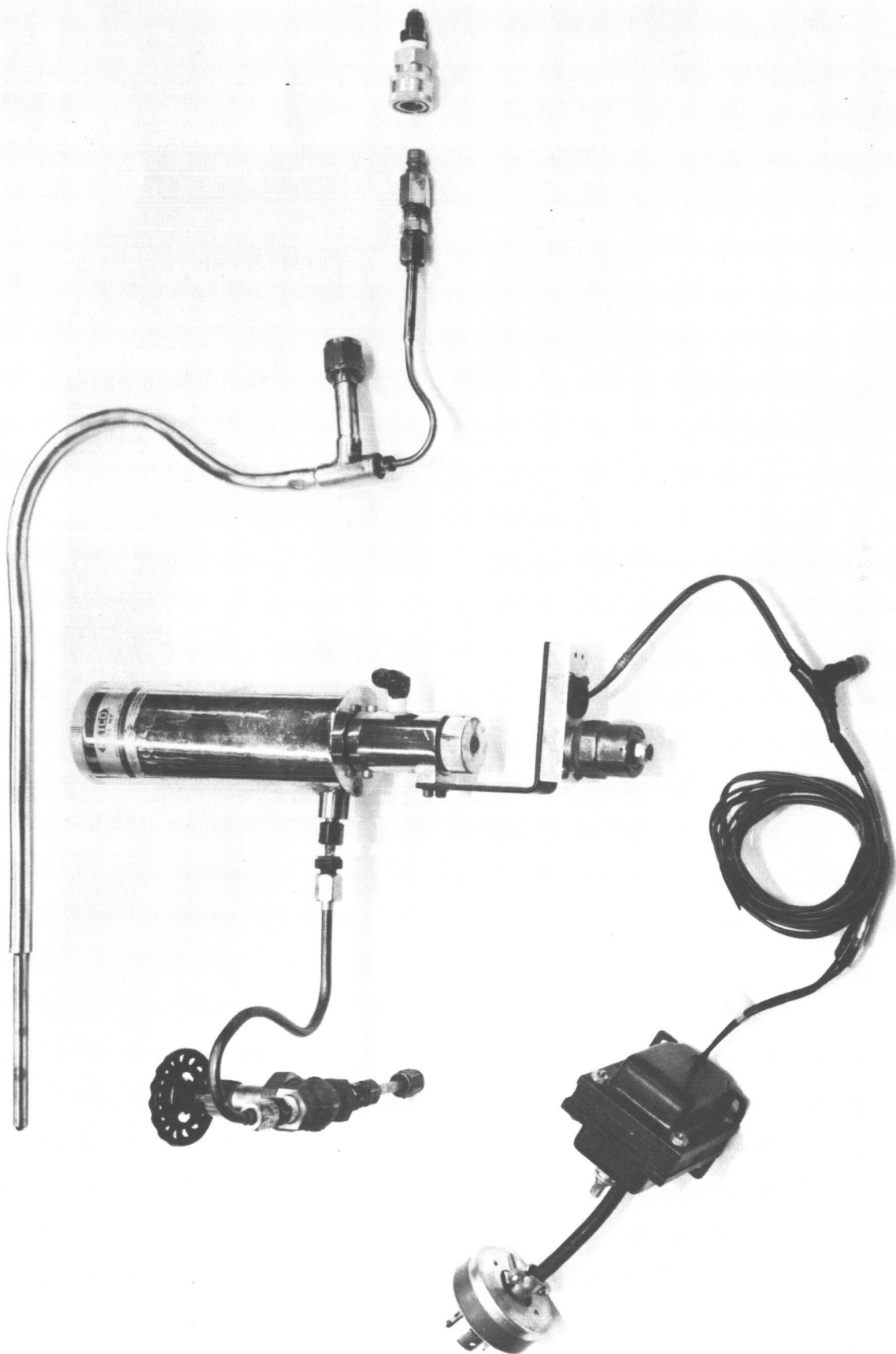


Figure 15. Sodium Salt Injection System and Gas Sampling Probe

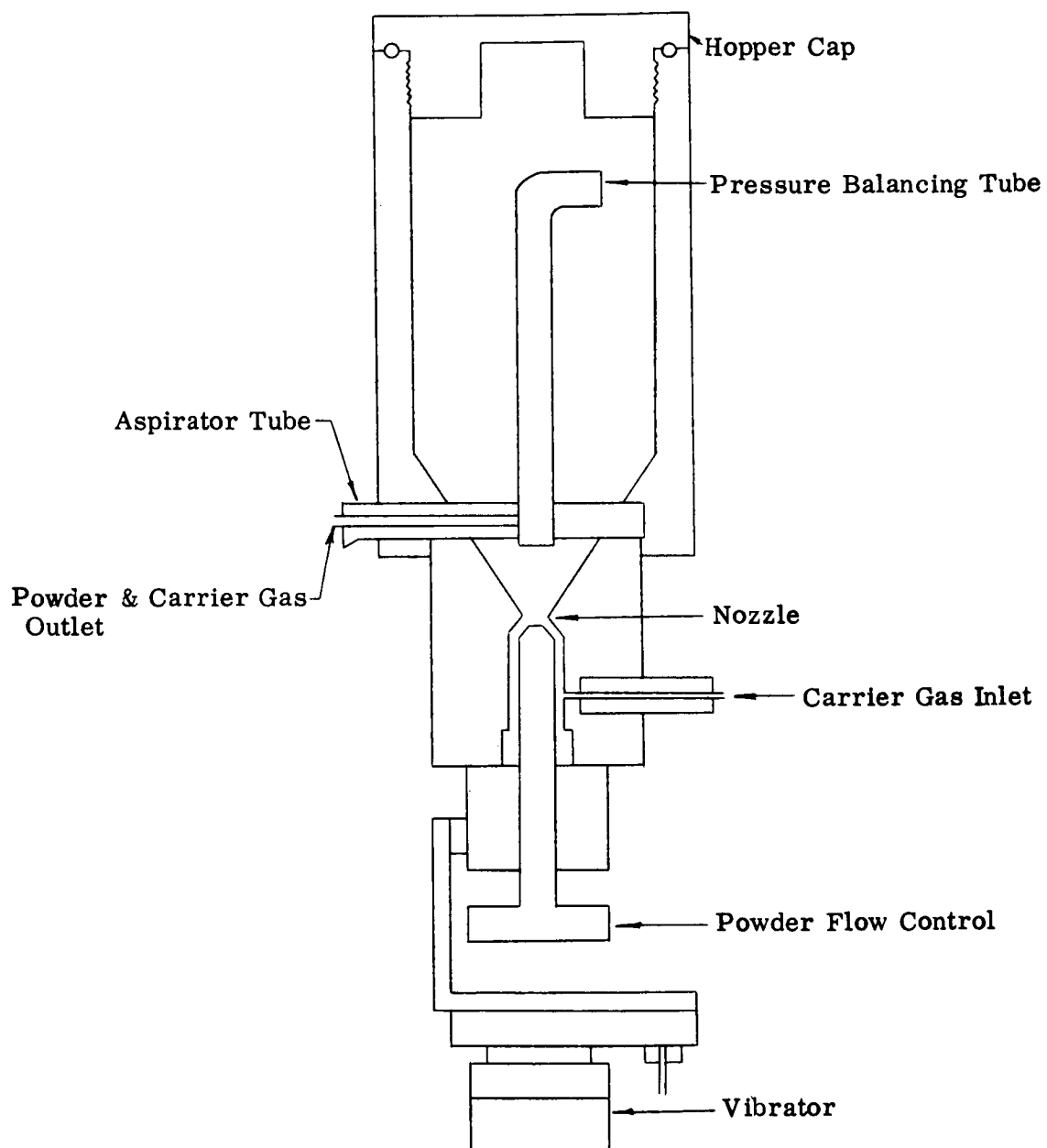


Figure 16. Schematic of Metco Type MP Powder Feed Unit

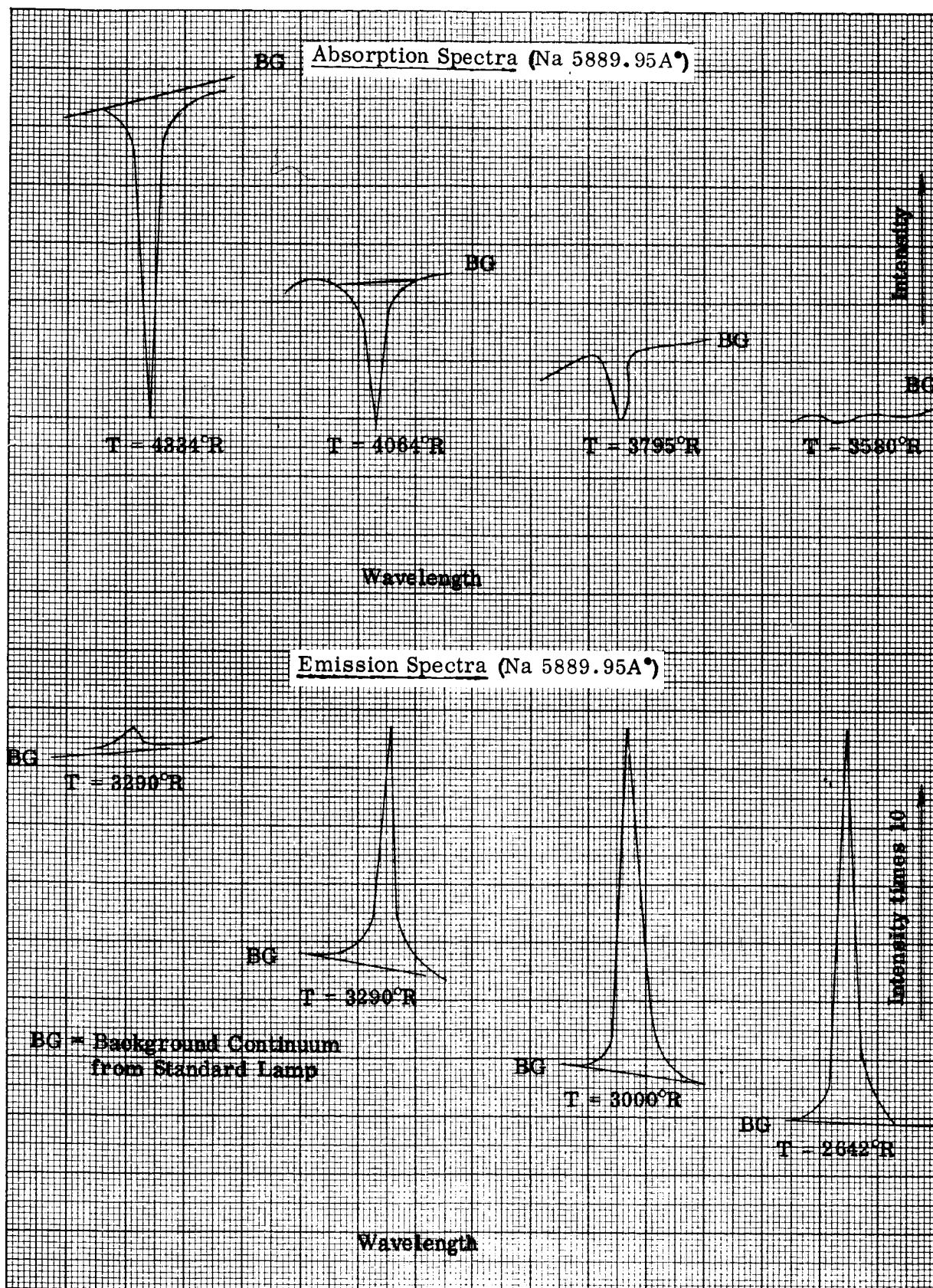
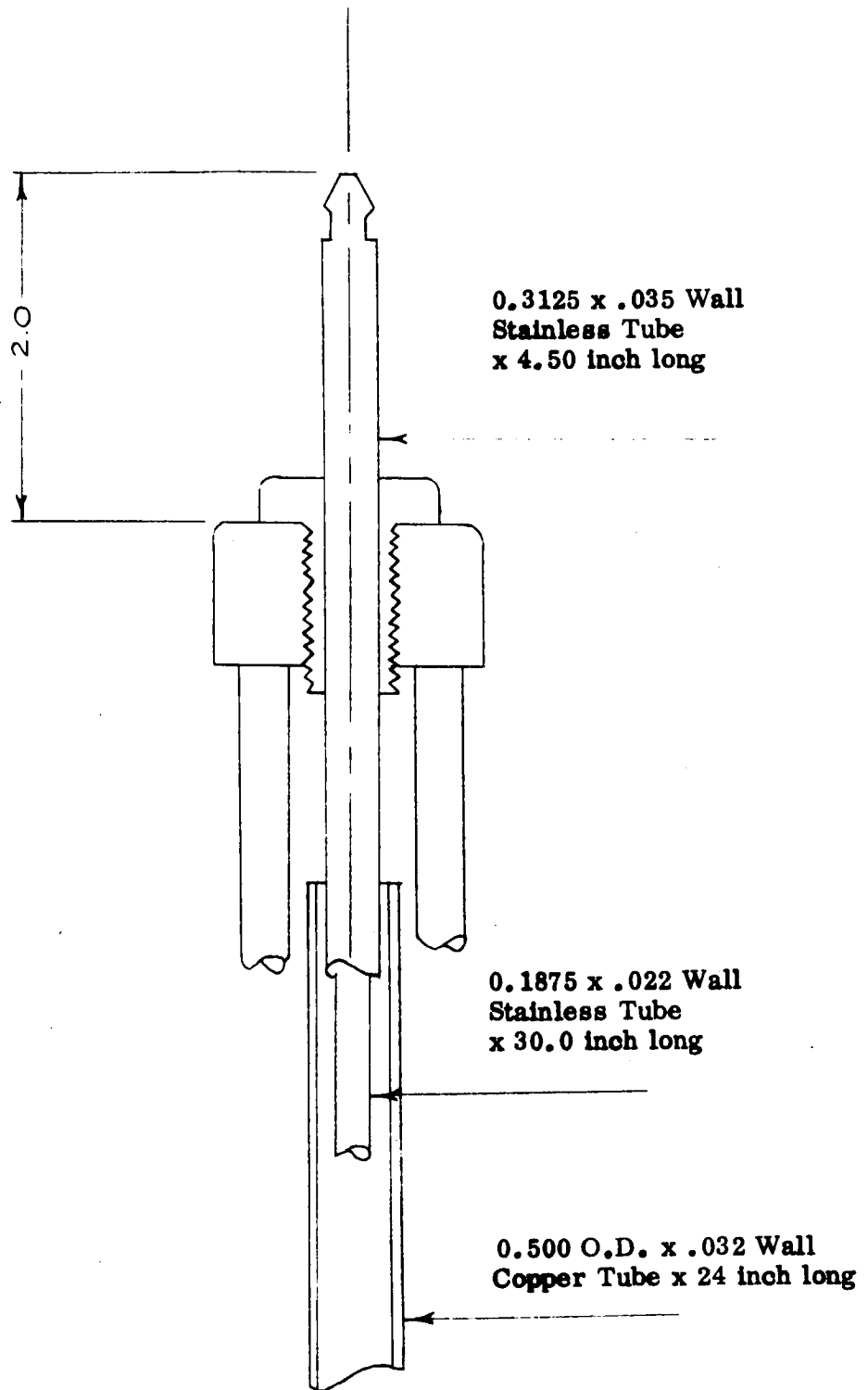


Figure 17. Typical Sodium Line Reversal Spectral Readout



**Figure 18.. Gas Sampling Tube**  
**General Assembly**



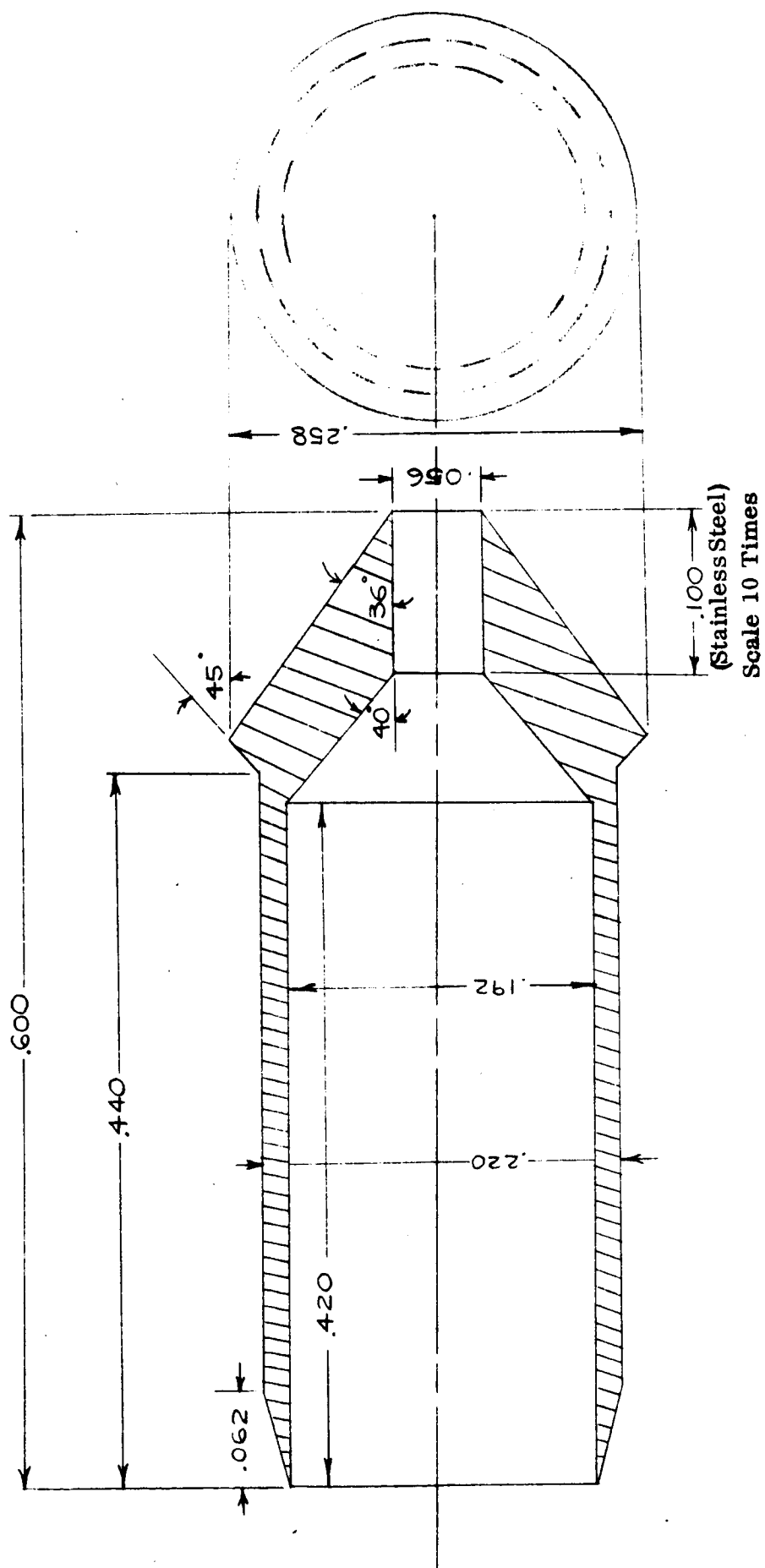


Figure 19. Gas Sampling Tube Tip

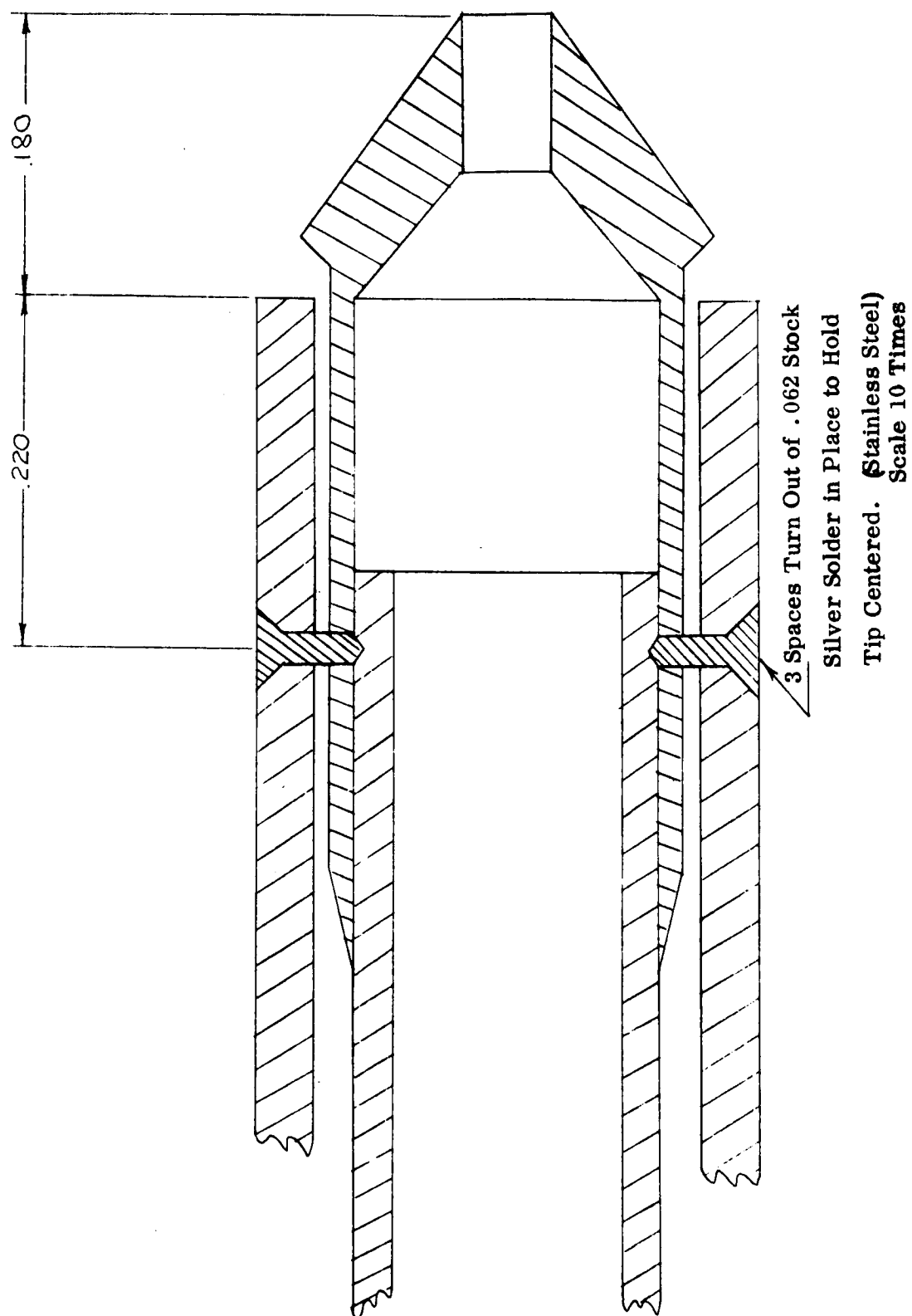


Figure 20. Gas Sampling Tube Tip Assembly

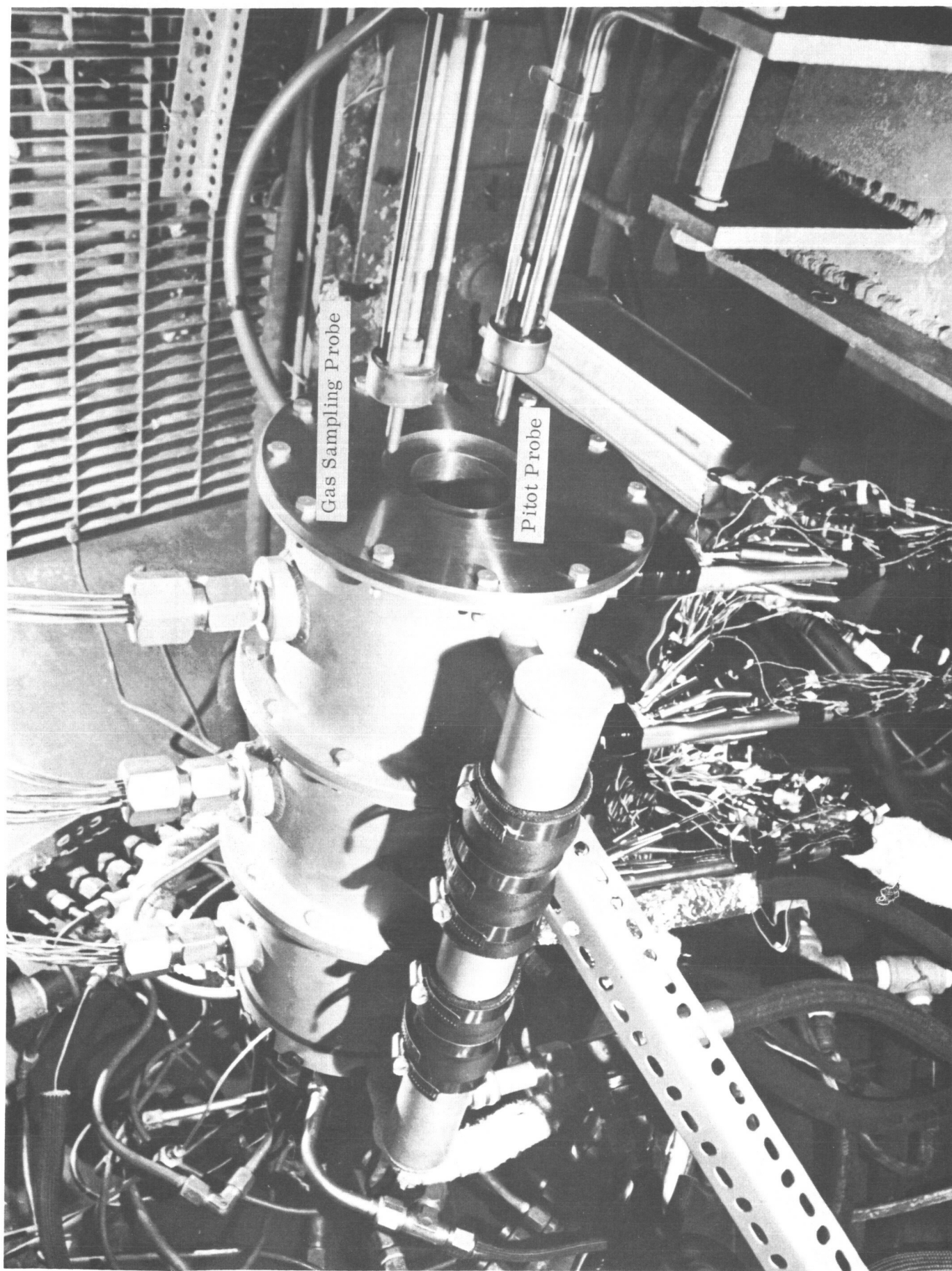
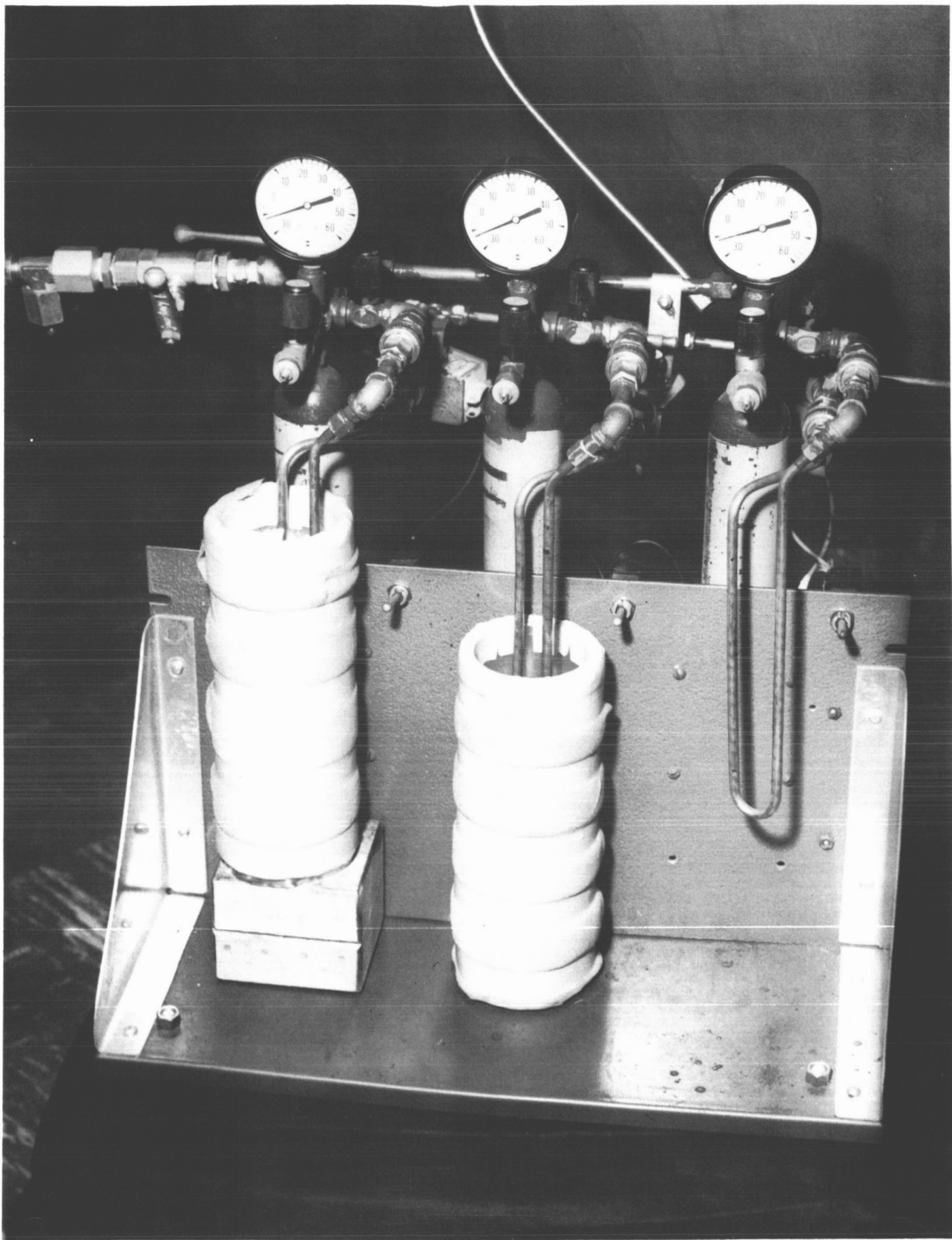


Figure 21. Gas Sampling and Pitot Probes



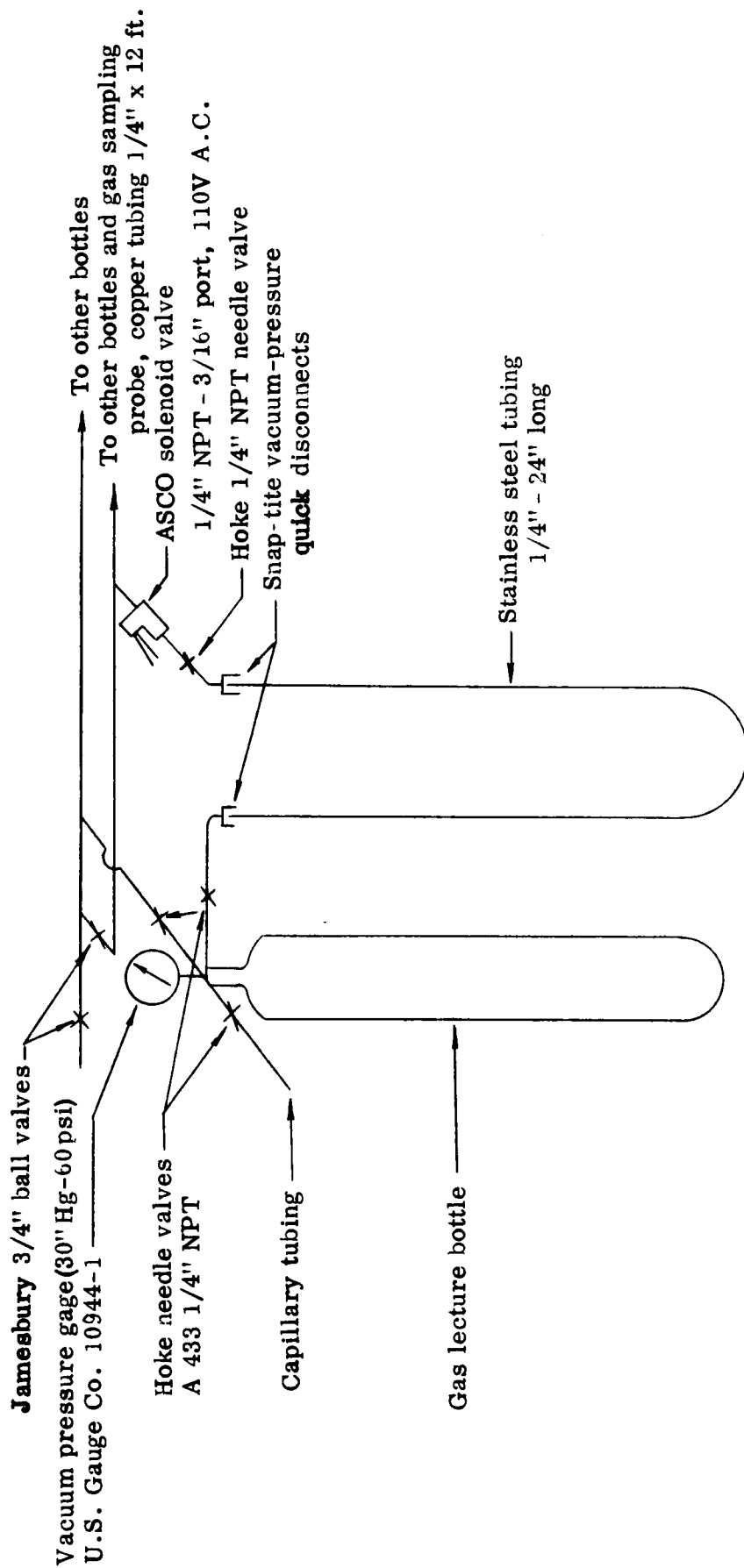


Figure 23. Schematic of Gas Sampling System



Figure 24. Gas Chromatographic Analysis System



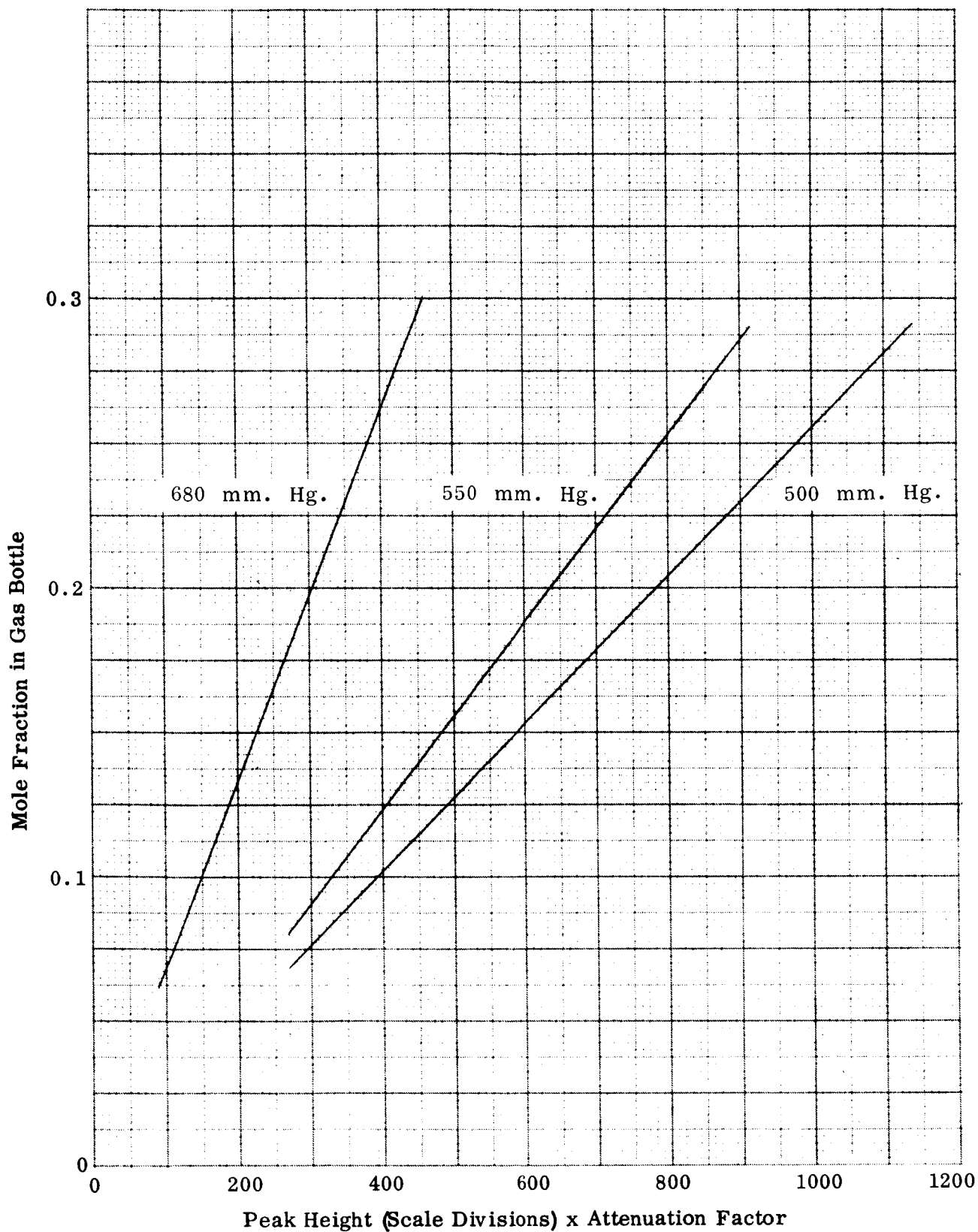


Figure 25. Analytical Working Curve: Hydrogen in Supersonic Gas Streams



Mole Fraction in Gas Bottle

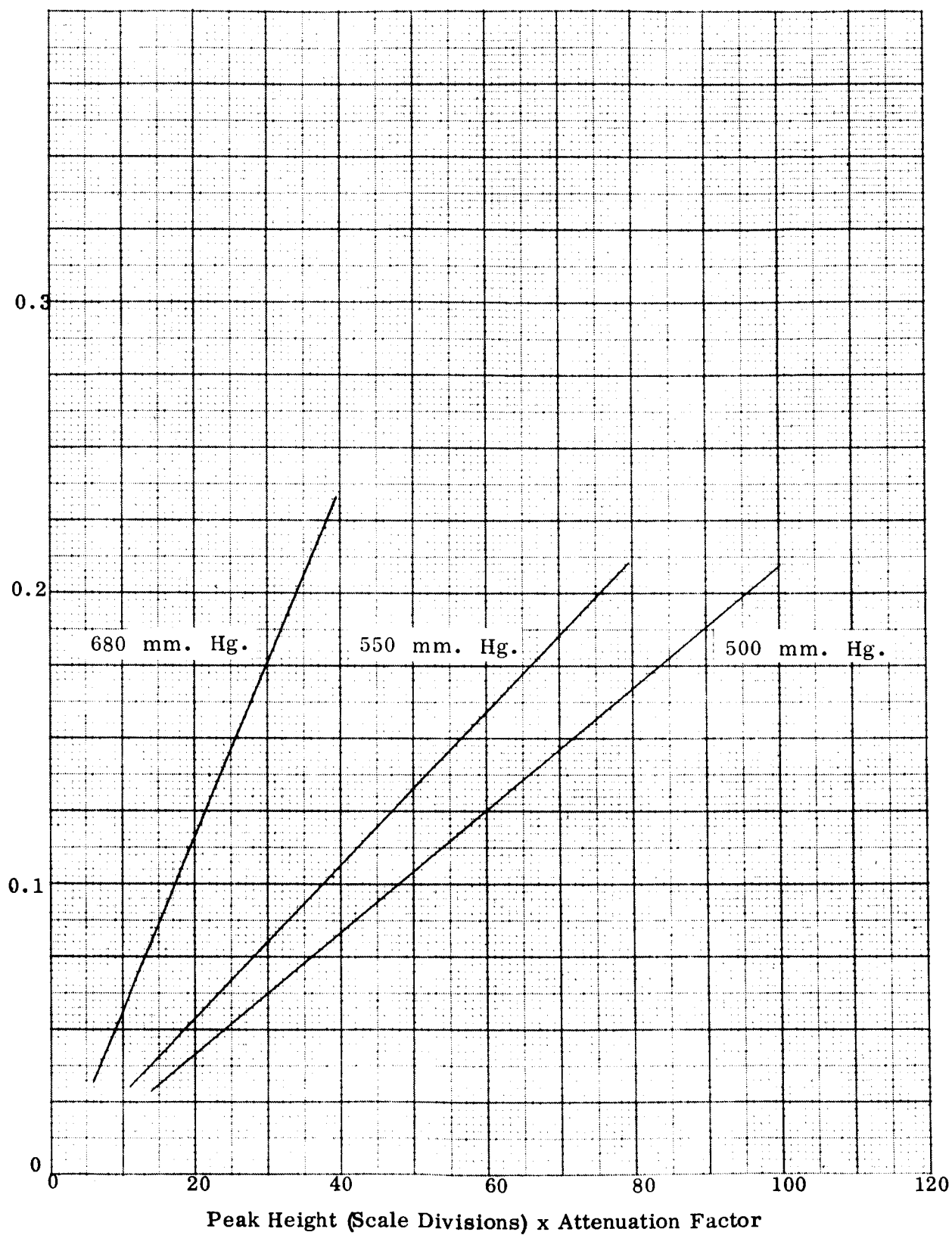


Figure 26. Analytical Working Curve: Oxygen in Supersonic Gas Streams



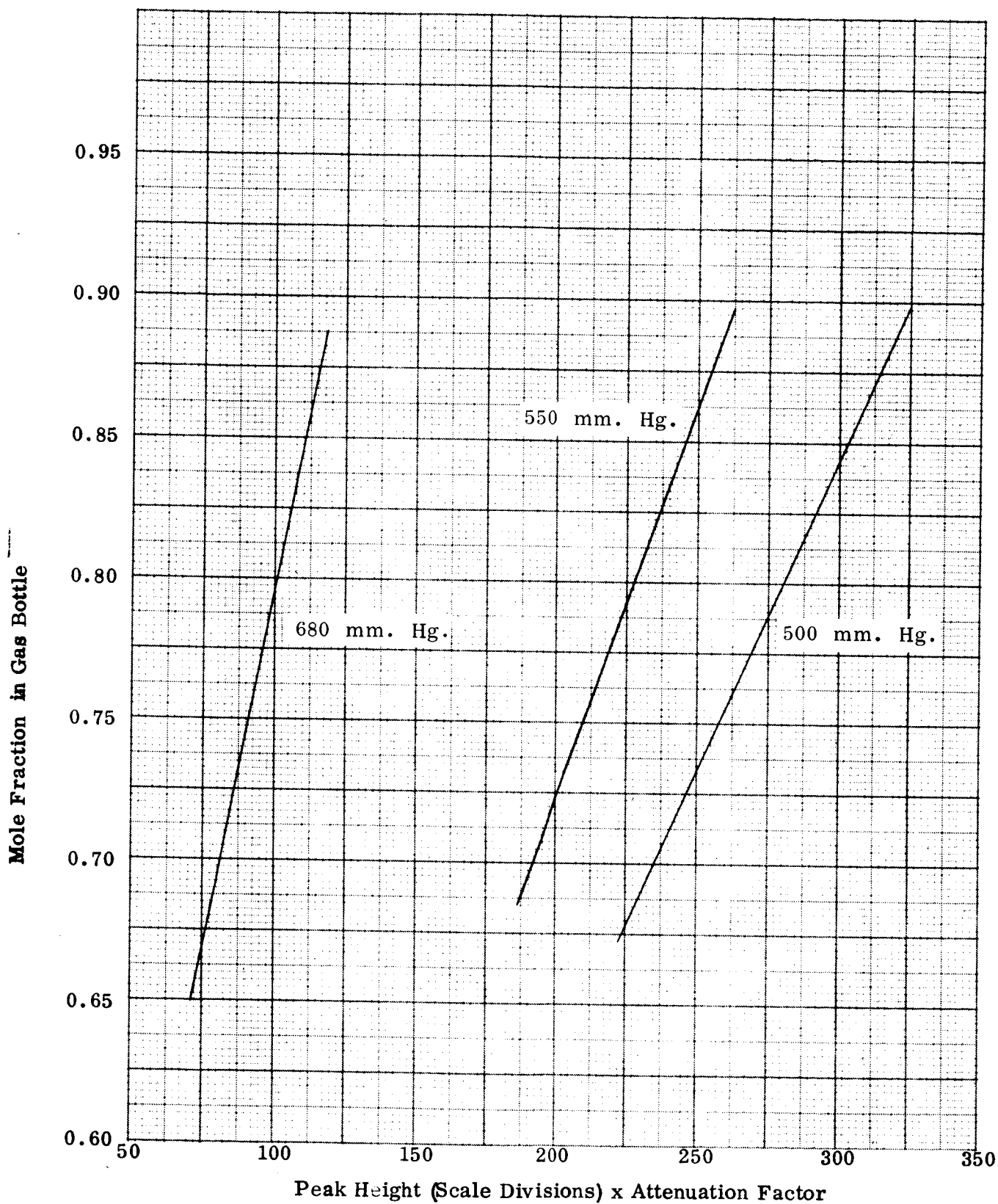


Figure 27. Analytical Working Curve: Nitrogen in Supersonic Gas Streams

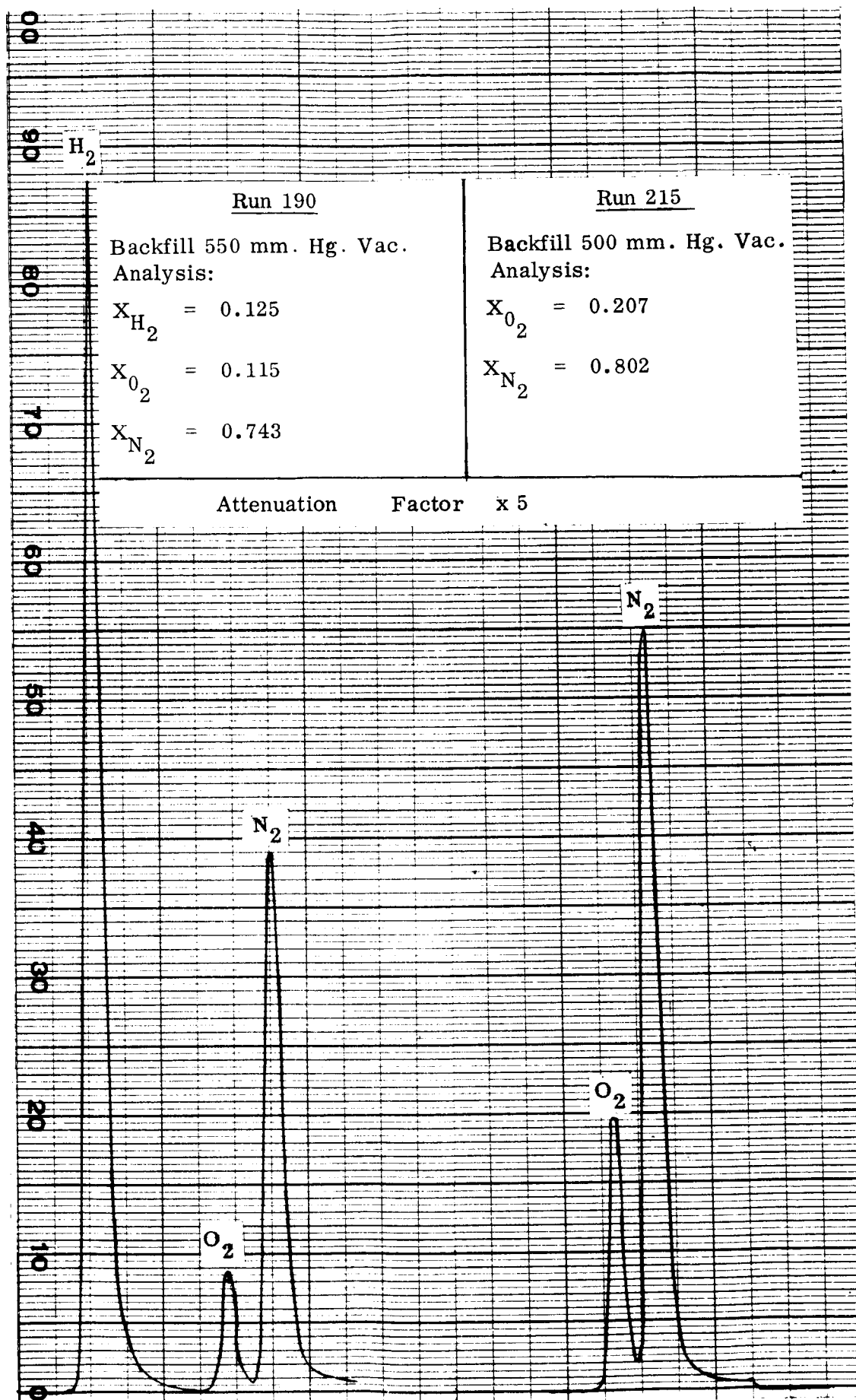


Figure 28.. Typical Gas Chromatograms

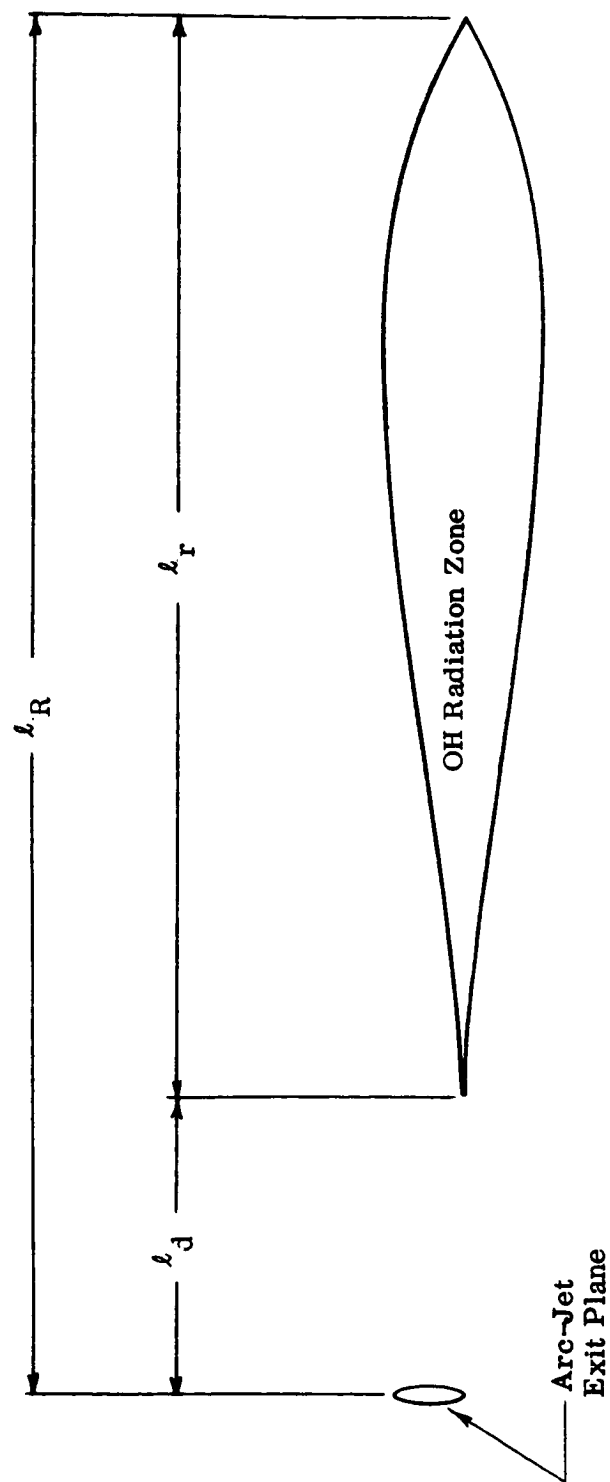


Figure 29. Definition of Pertinent Reaction Zone Lengths Read from UV Negatives

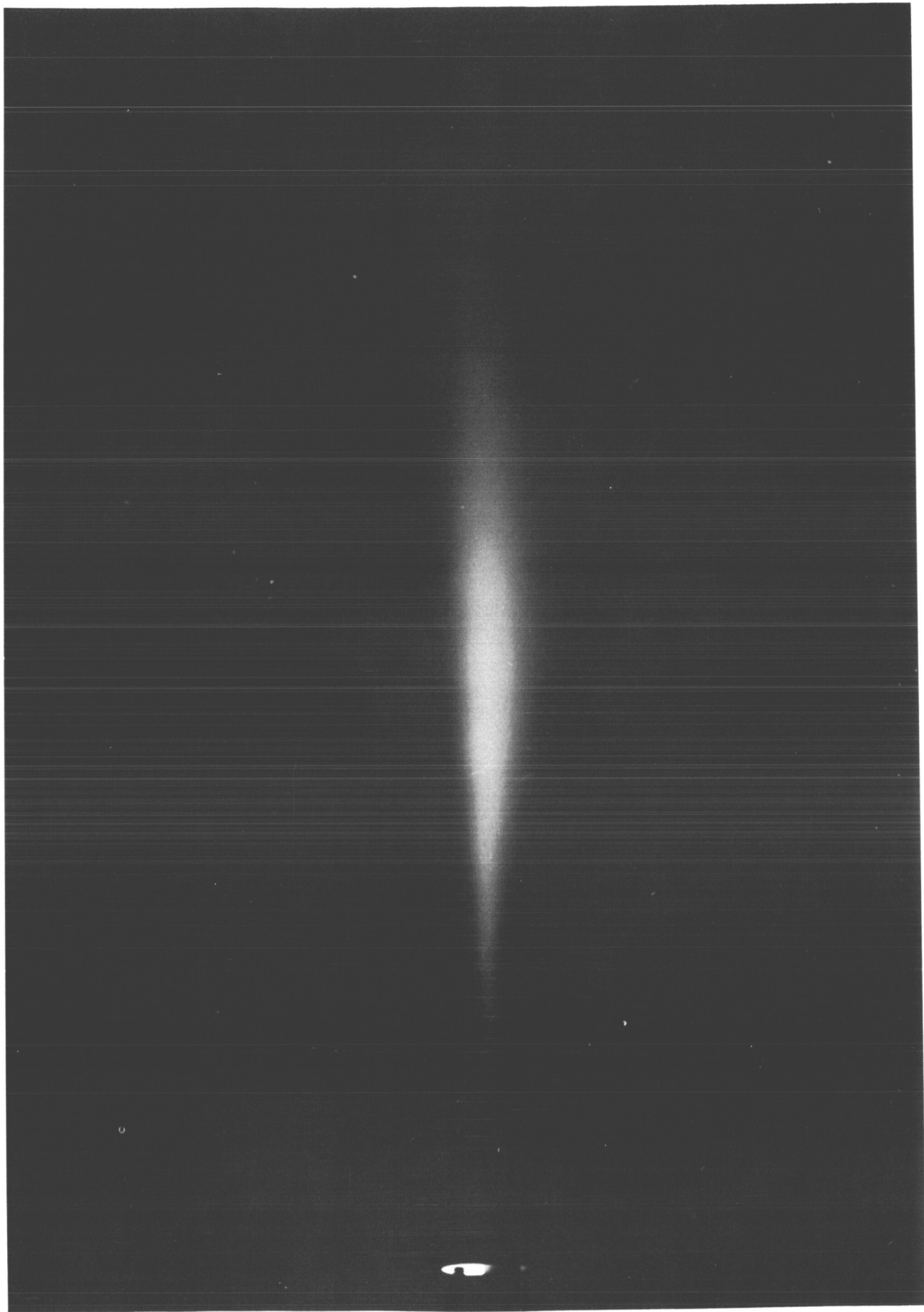


Figure 30. UV Photograph of a 2394°R, Single-Point Injection Test  
Using Cold Hydrogen for  $V_f/V_a = 0.4$  (0.108" Spacing)

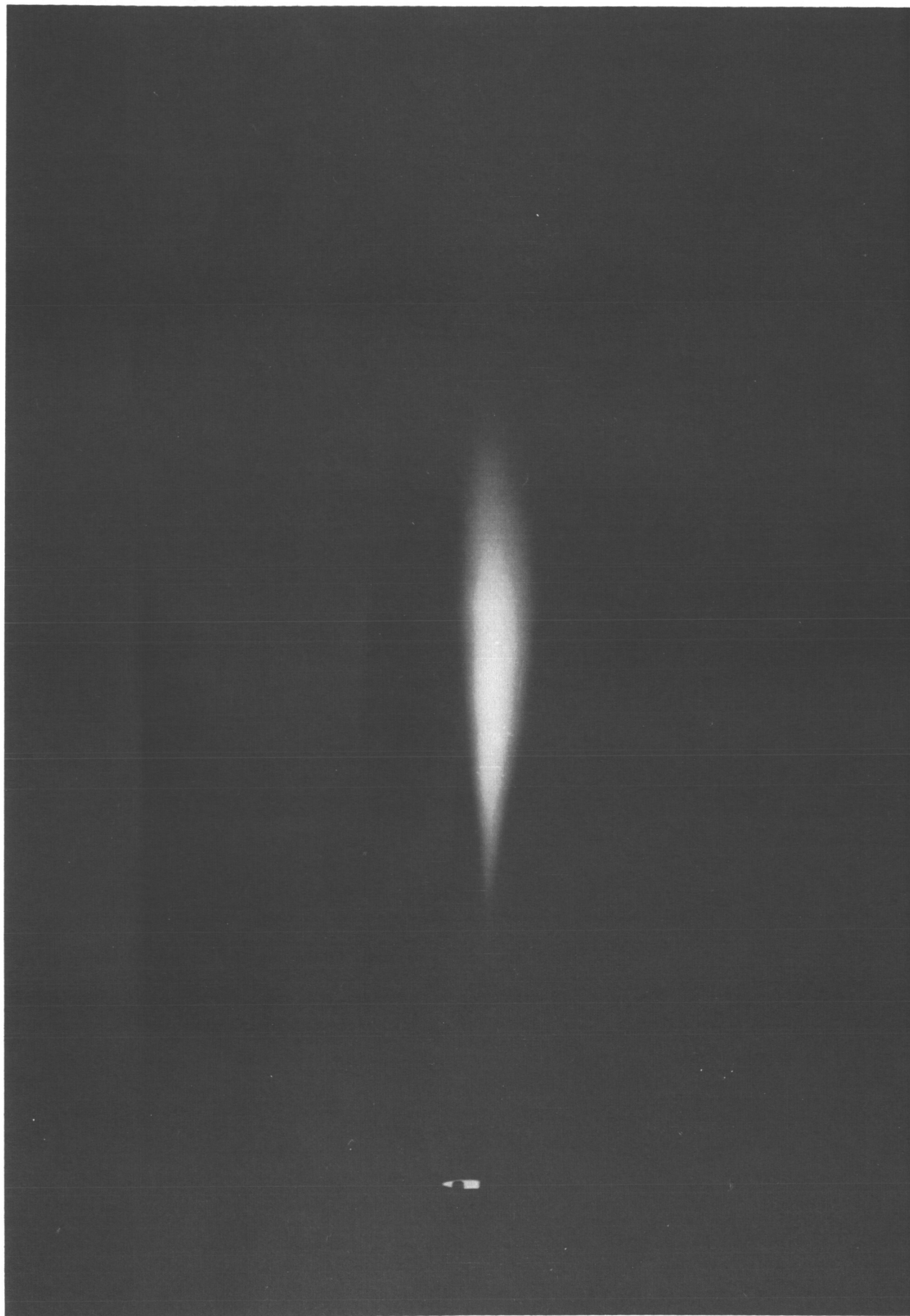


Figure 31. UV Photograph of a 2772°R, Single-Point Injection Test  
Using Cold Hydrogen for  $V_f/V_a = 0.4$  (0.108" Spacing)



Figure 32. UV Photograph of a Pitot Probe During 2646R Test

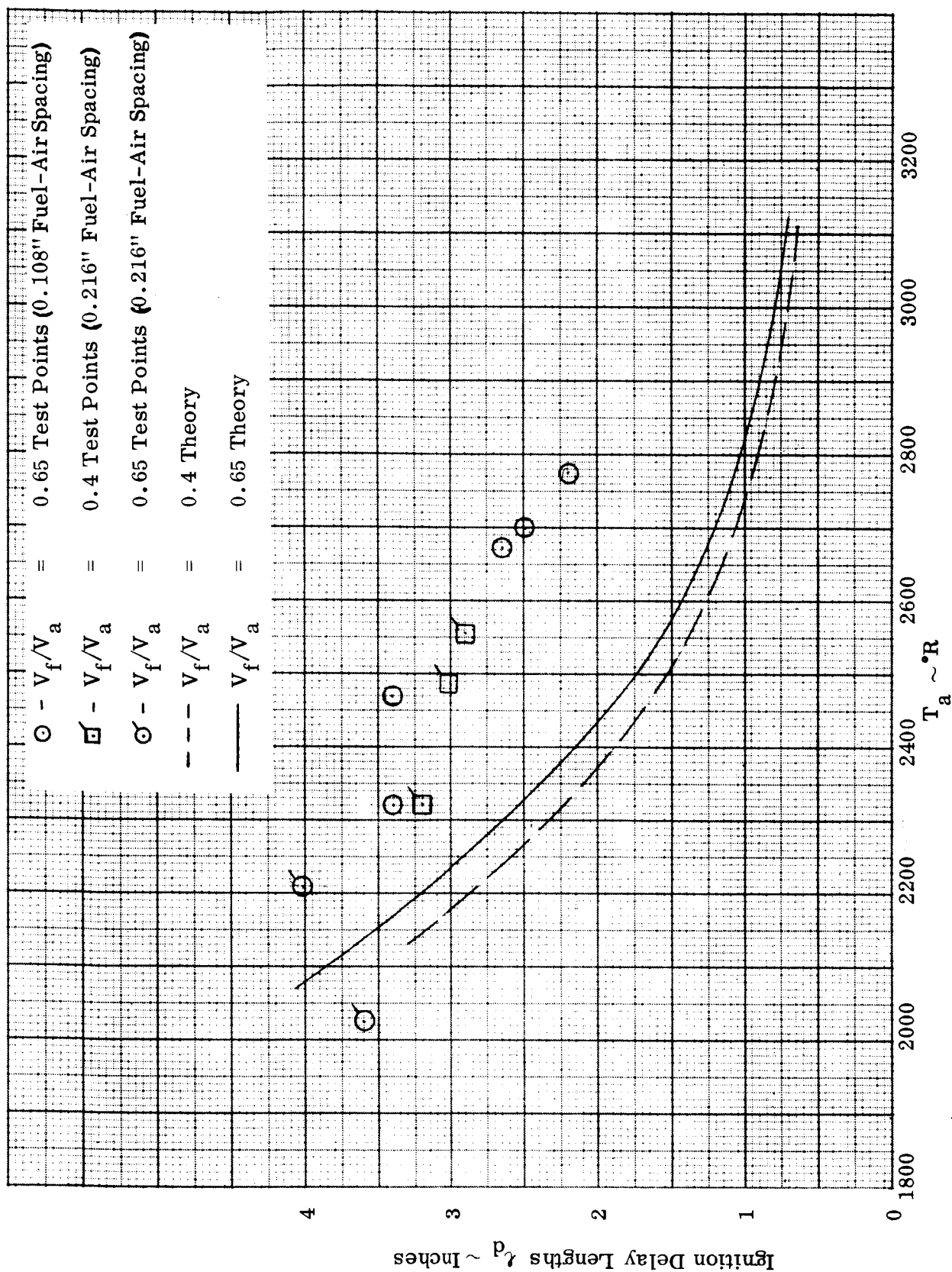


Figure 33. Ignition Delay Lengths for Single-Point Injection Tests (Cold Hydrogen)

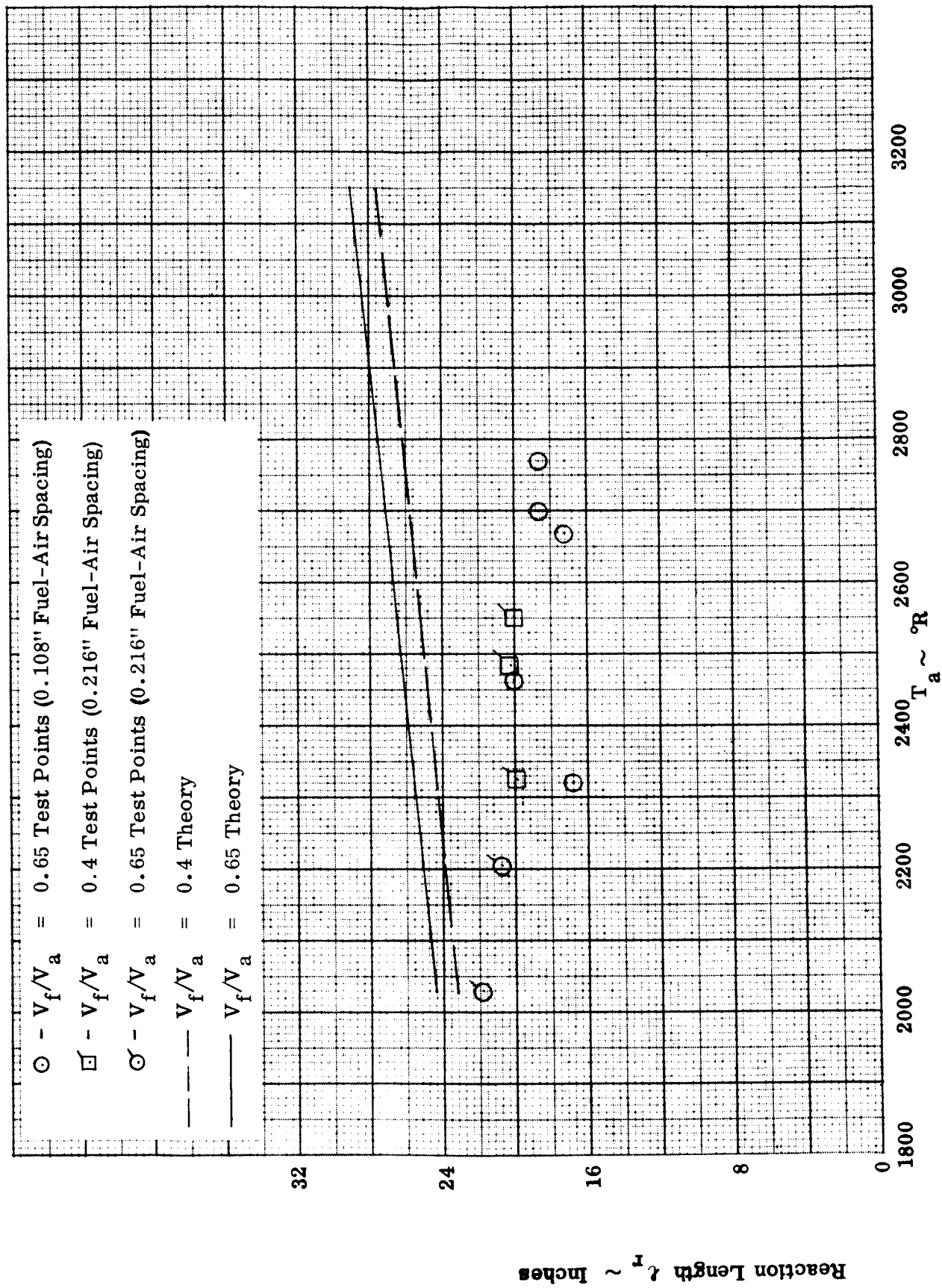


Figure 34. Reaction Lengths for Single-Point Injection Tests (Cold Hydrogen)



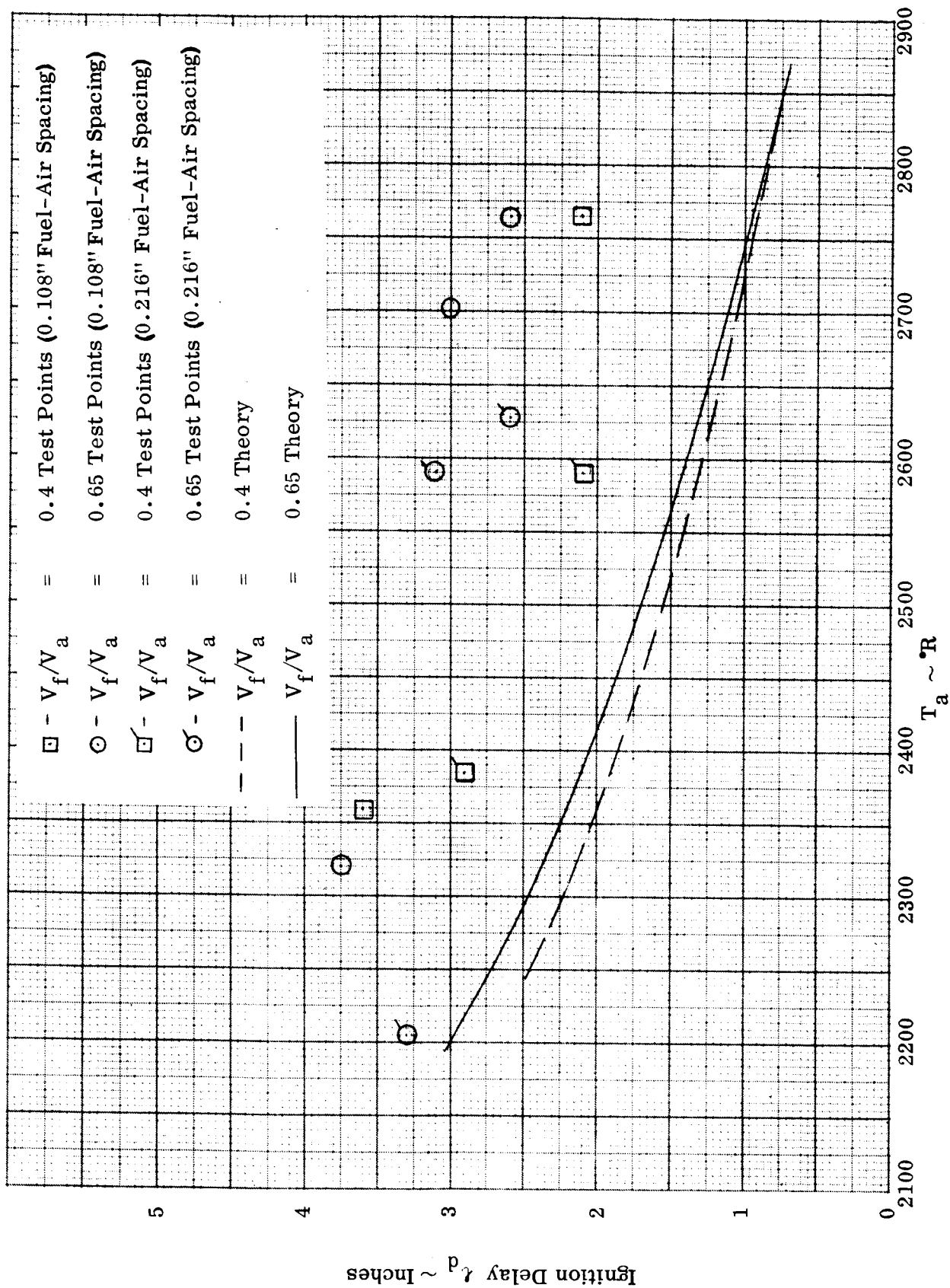


Figure 35. Ignition Delay Lengths for Single-Point Injection Tests (Heated Hydrogen)

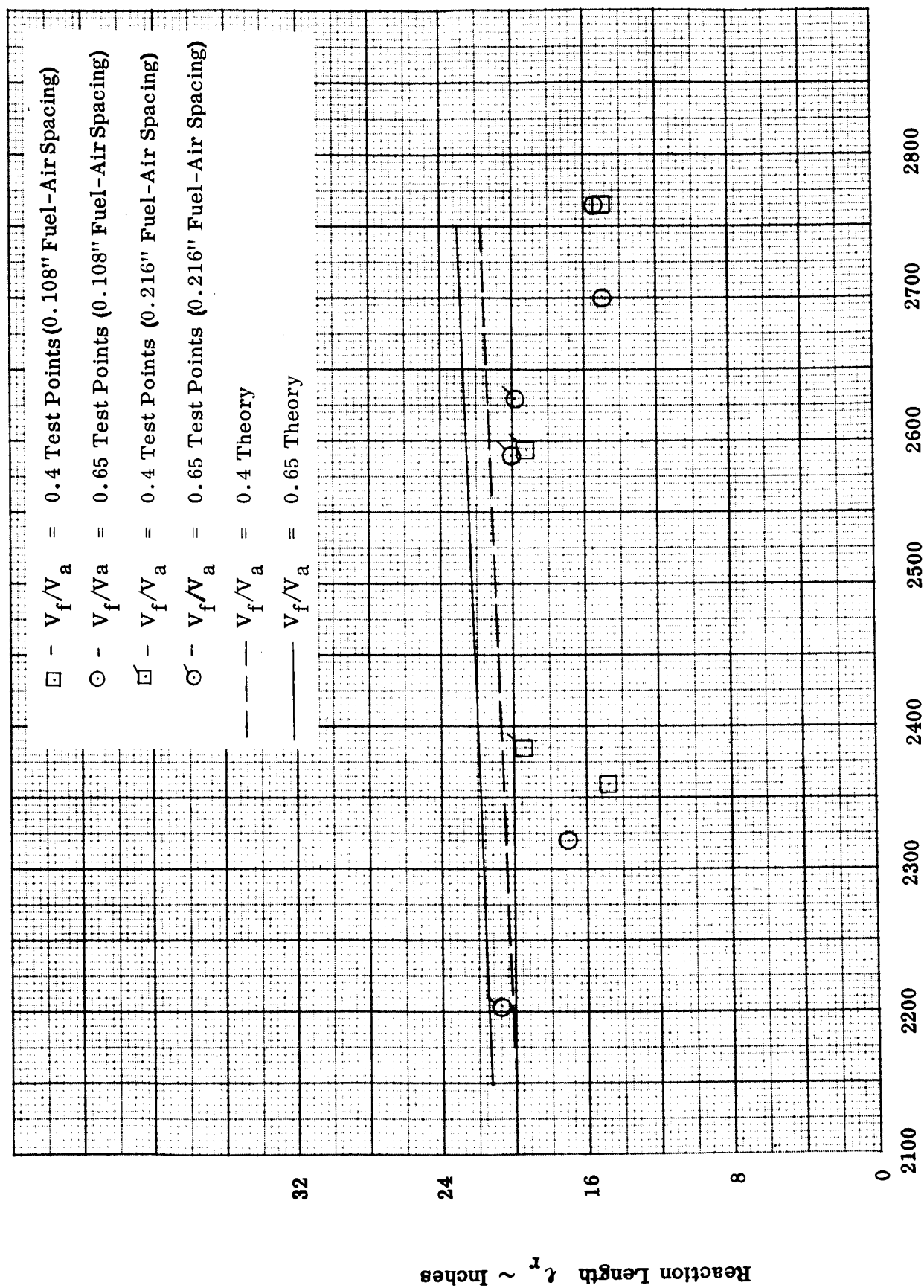


Figure 36. Reaction Lengths for Single-Point Injection Tests (Heated Hydrogen)

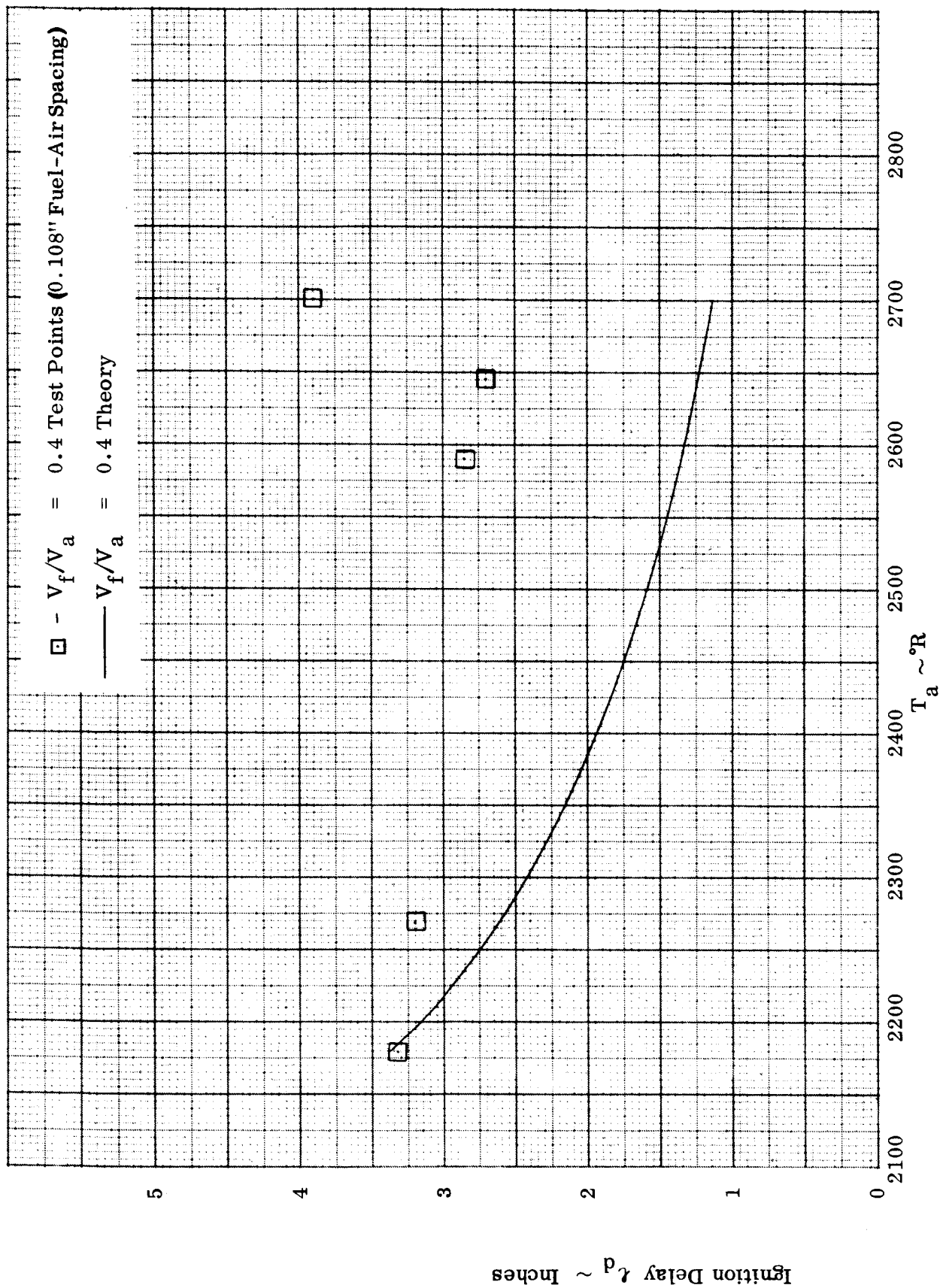


Figure 37.. Ignition Delay Lengths for Three-Point Injection Tests (Cold Hydrogen)

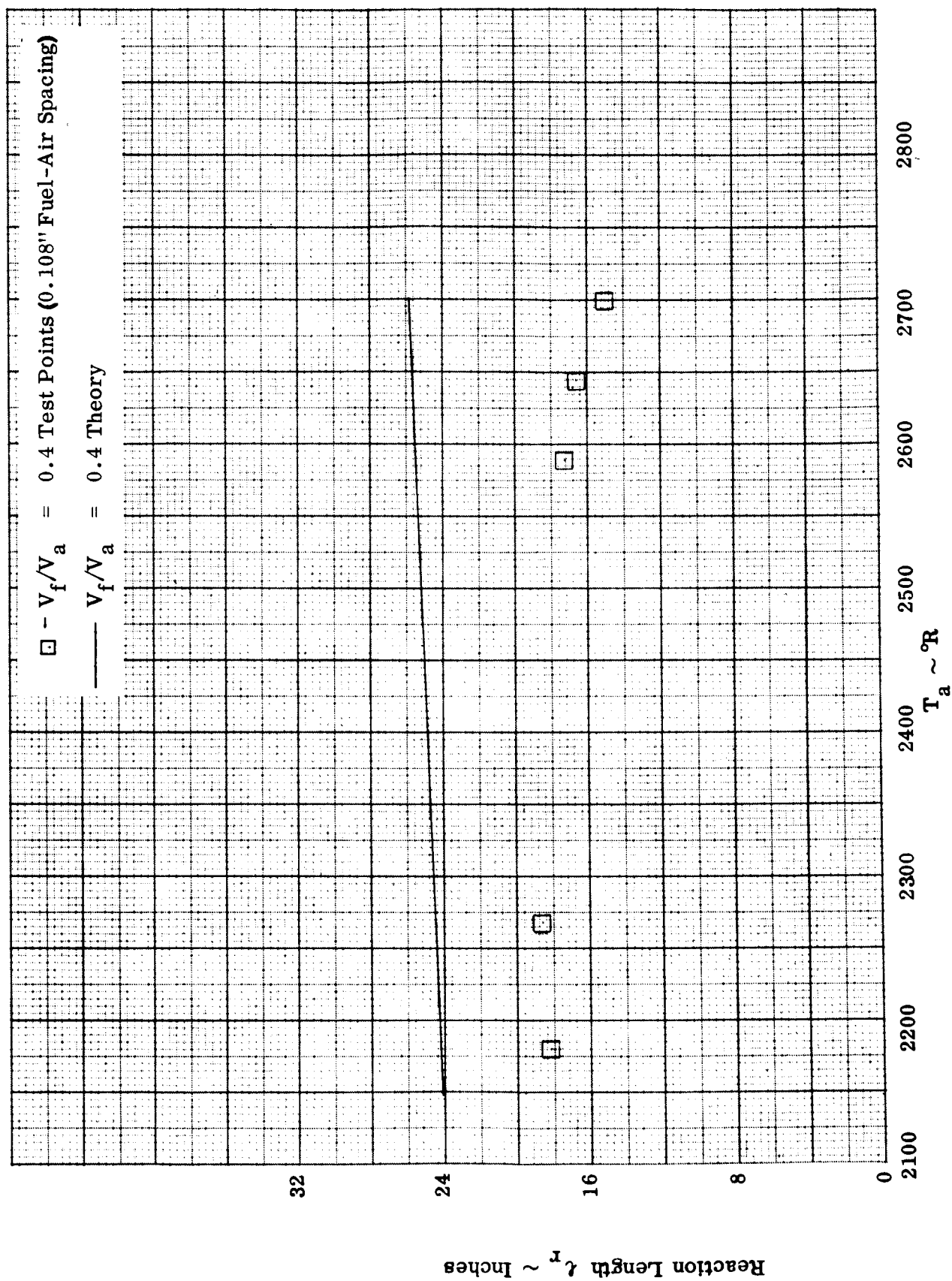


Figure 38. Reaction Lengths for Three-Point Injection Tests (Cold Hydrogen)

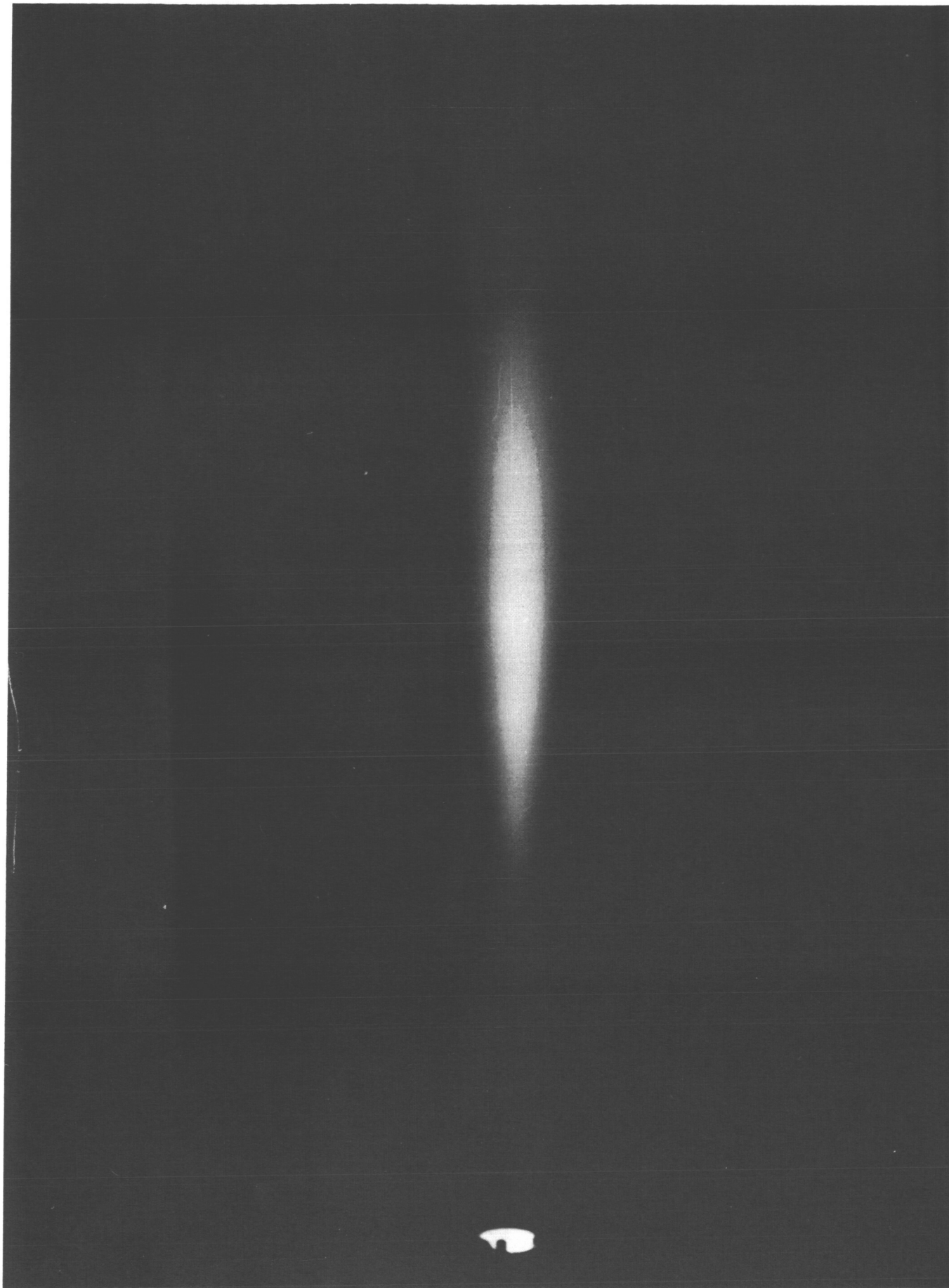


Figure 39. UV Photograph of a 2664•R Cold Hydrogen Test Run Viewed from  
Beneath  $V_f / V_a = 0.4$  (0.108" Spacing)

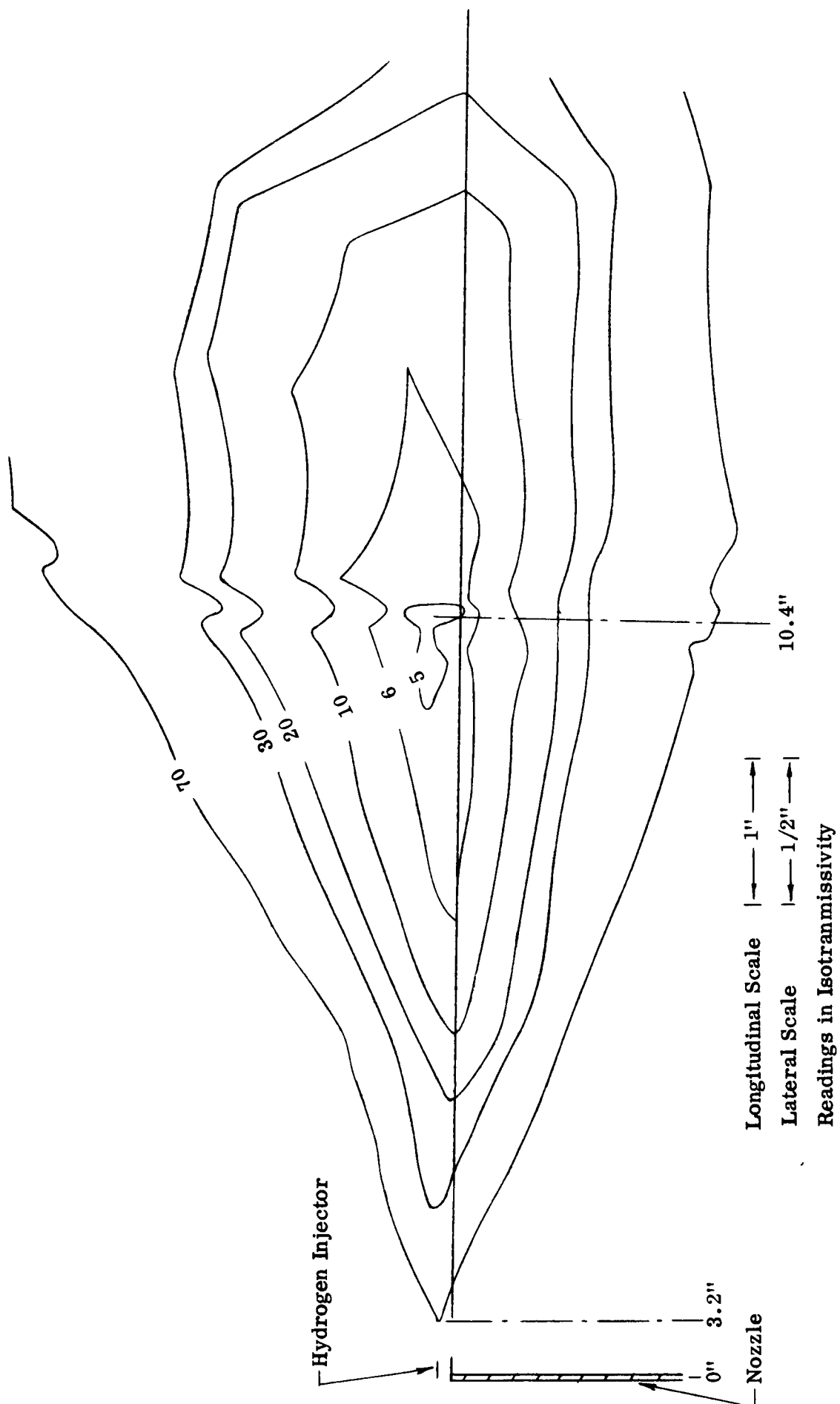


Figure 40. Densitometry Plot of Point Injection Run 41B (5 Second Exposure)

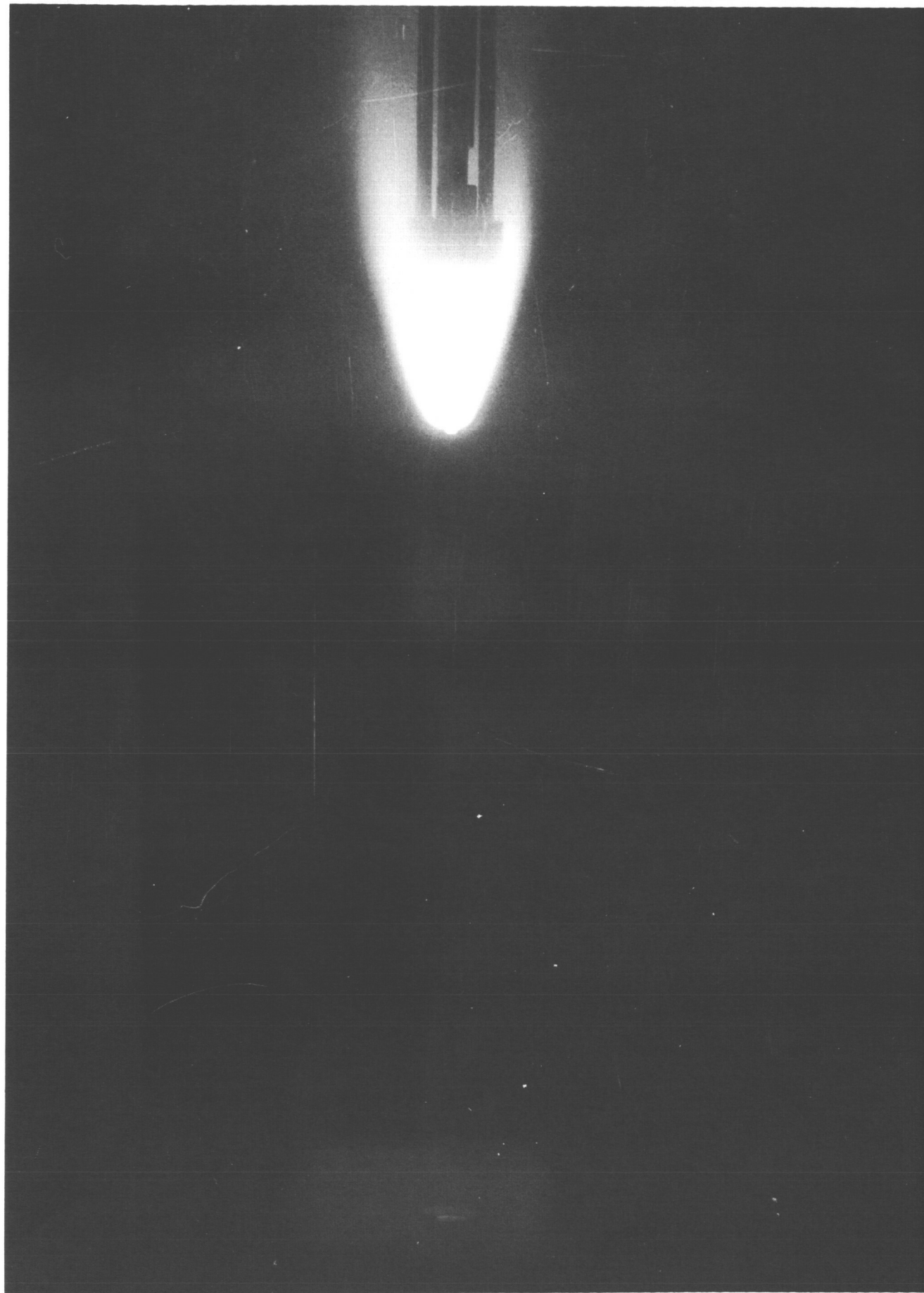


Figure 41. UV Photograph of the Gas Sampling Probe During a 2700°R,  
Cold Hydrogen Test



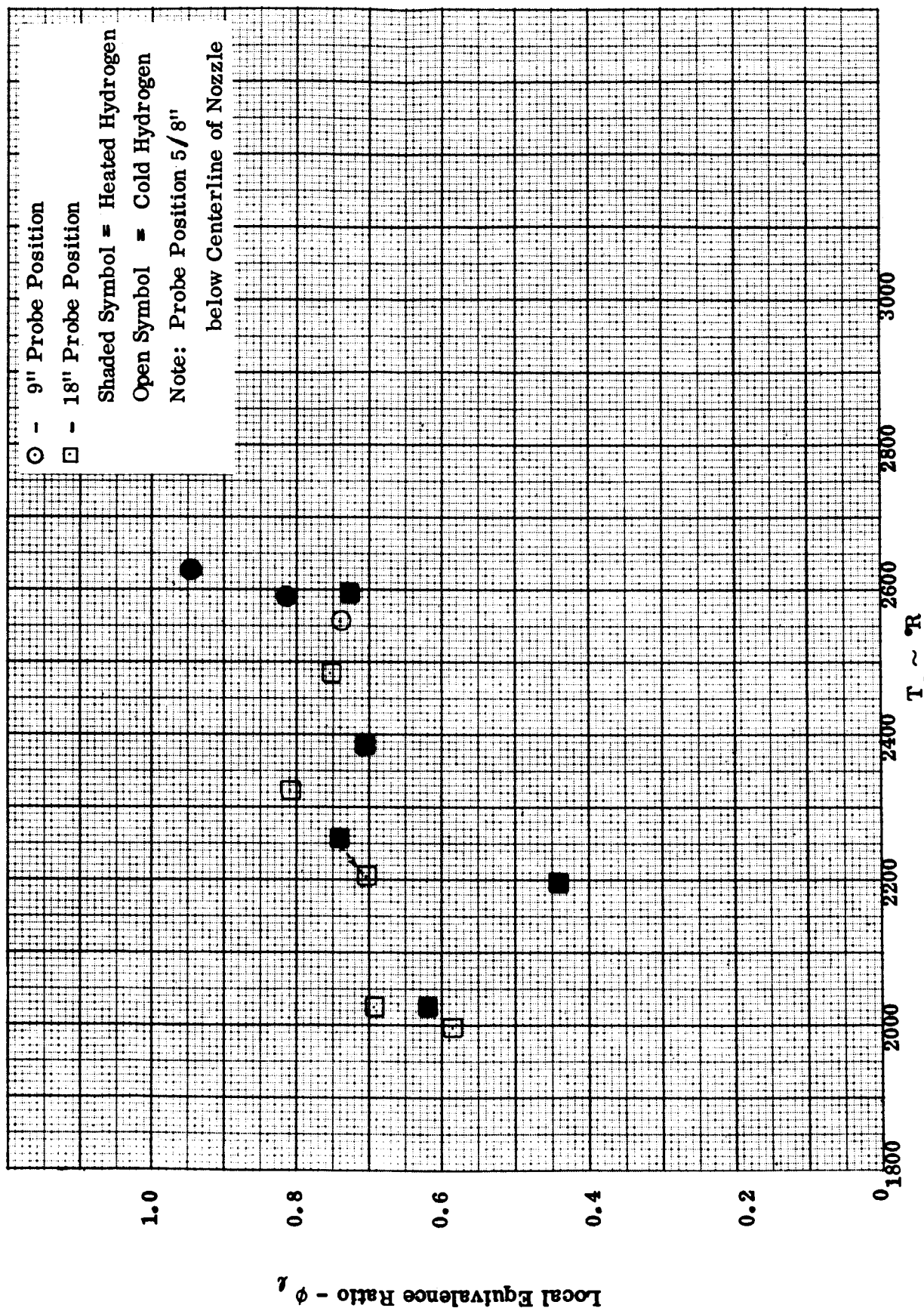


Figure 42. Local Equivalence Ratio vs  $T_a$  for Single Point Injection Tests (0.216" Spacing)



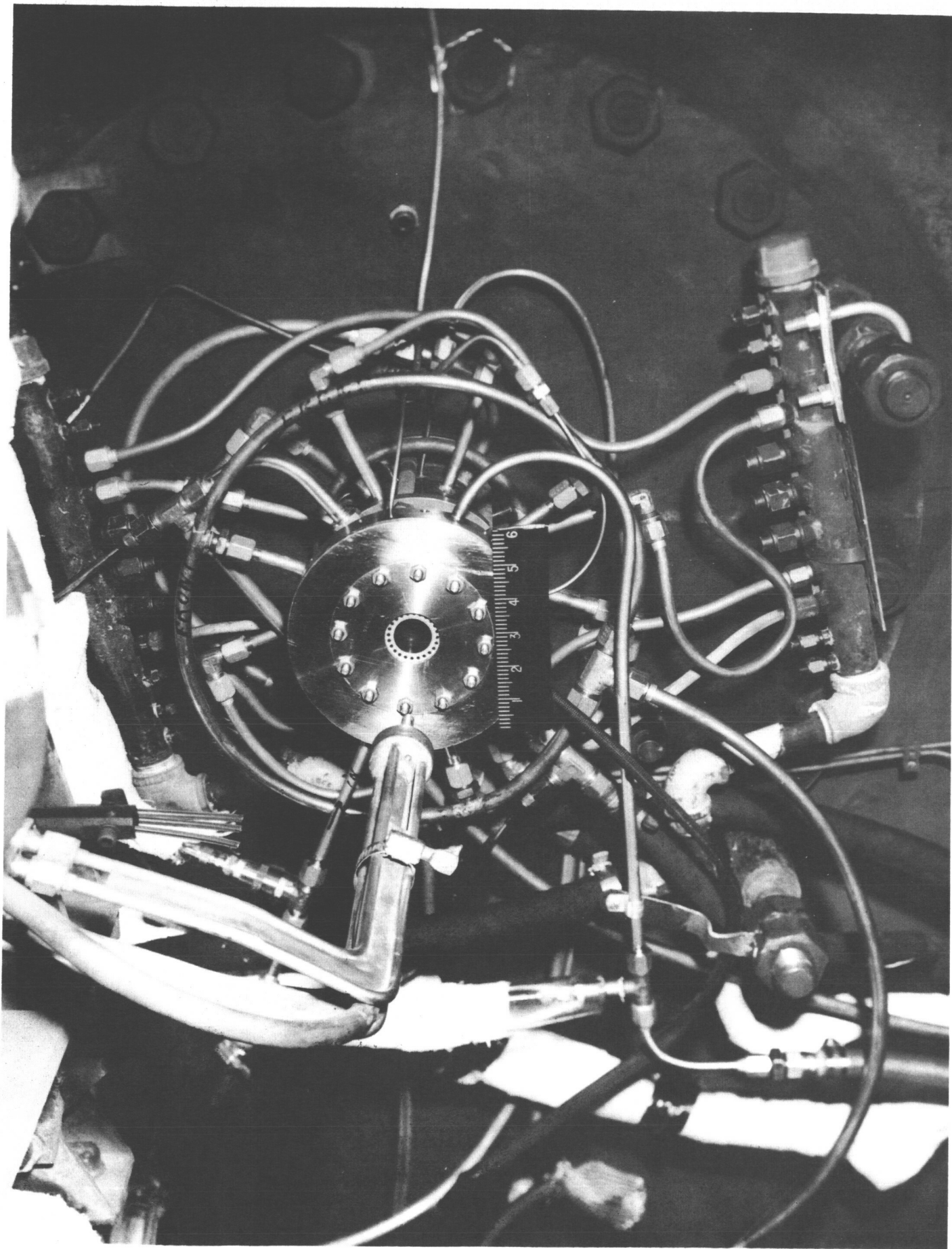


Figure 43. Ring-Injection Test Setup



Figure 44. UV Photograph of a  $2124^{\circ}\text{R}$  Ring-Injection Test  
for Cold Hydrogen and  $\phi = 1.0$

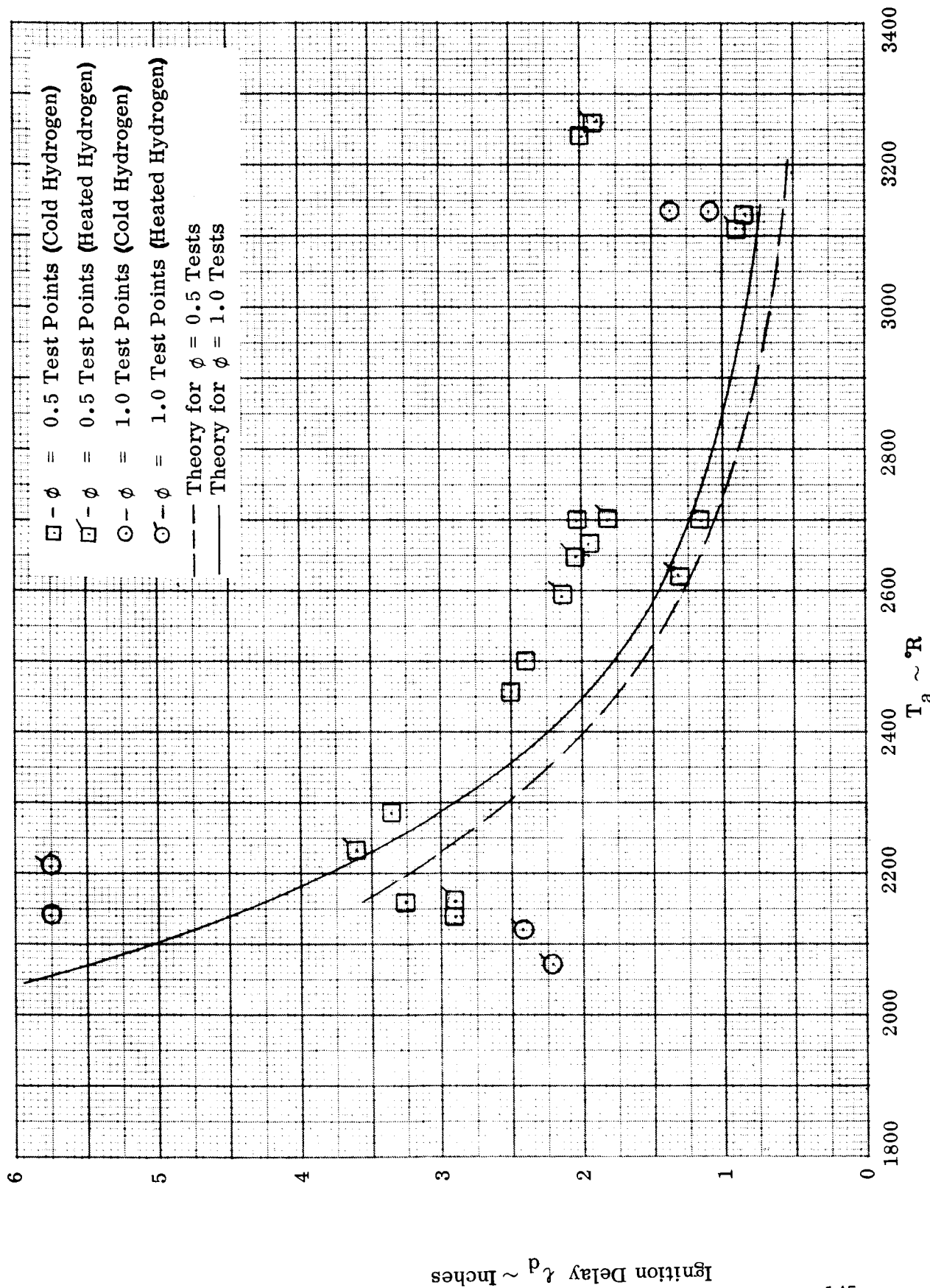


Figure 45.. Ignition Delay Lengths for Ring Injection Tests

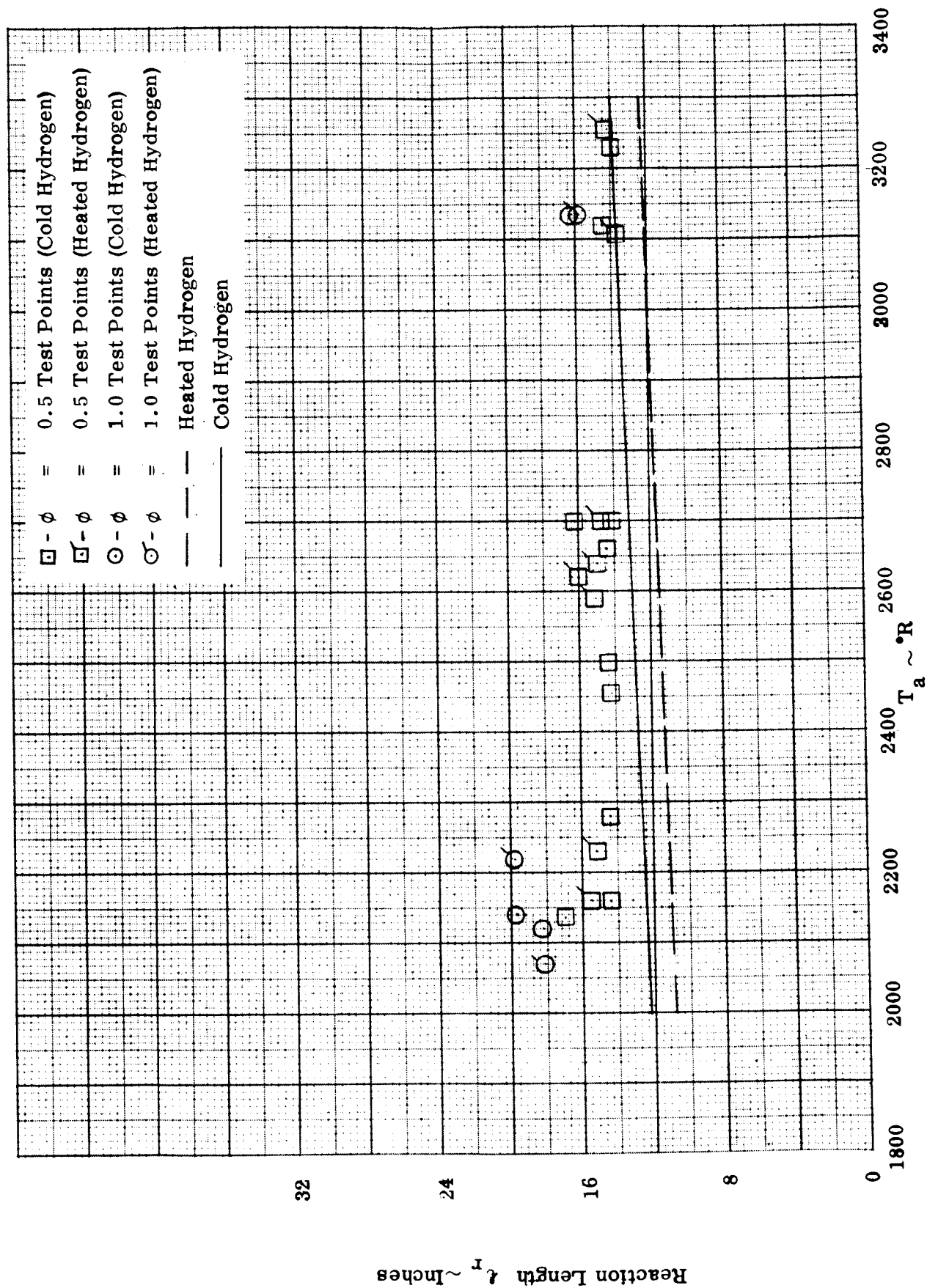


Figure 46. Reaction Lengths for Ring Injection Tests

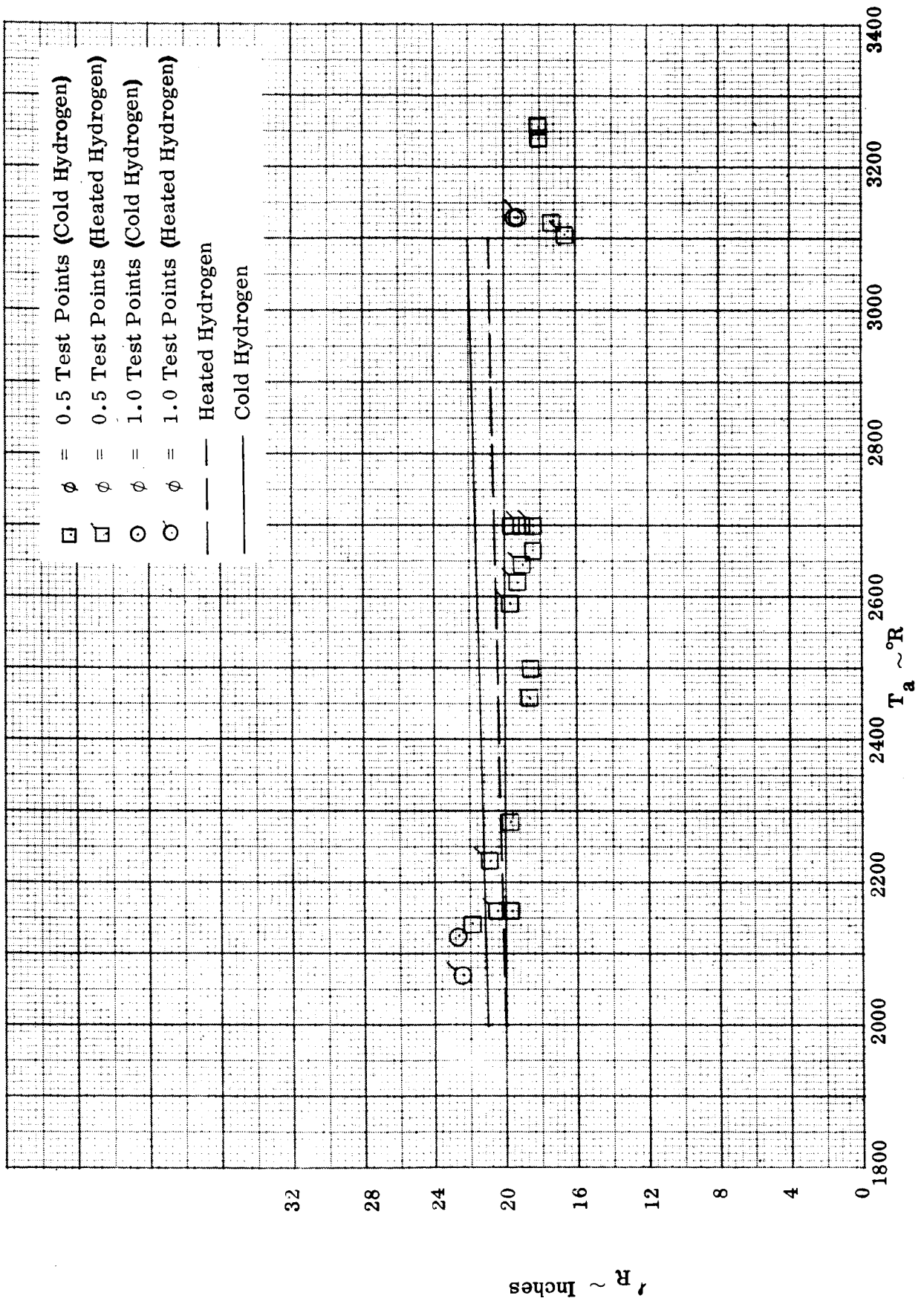


Figure 47. Total Reaction Zone Lengths for Ring Injection Tests

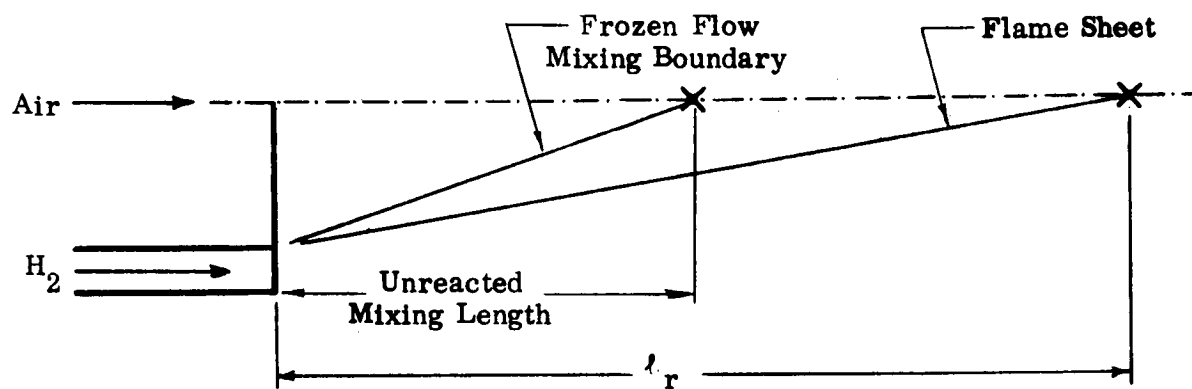
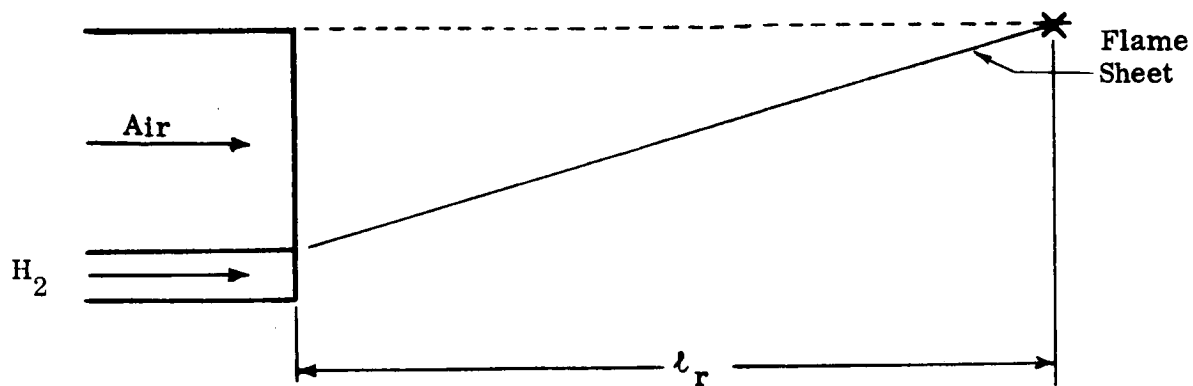


Figure 48. Schematic Representation of Theoretical Model



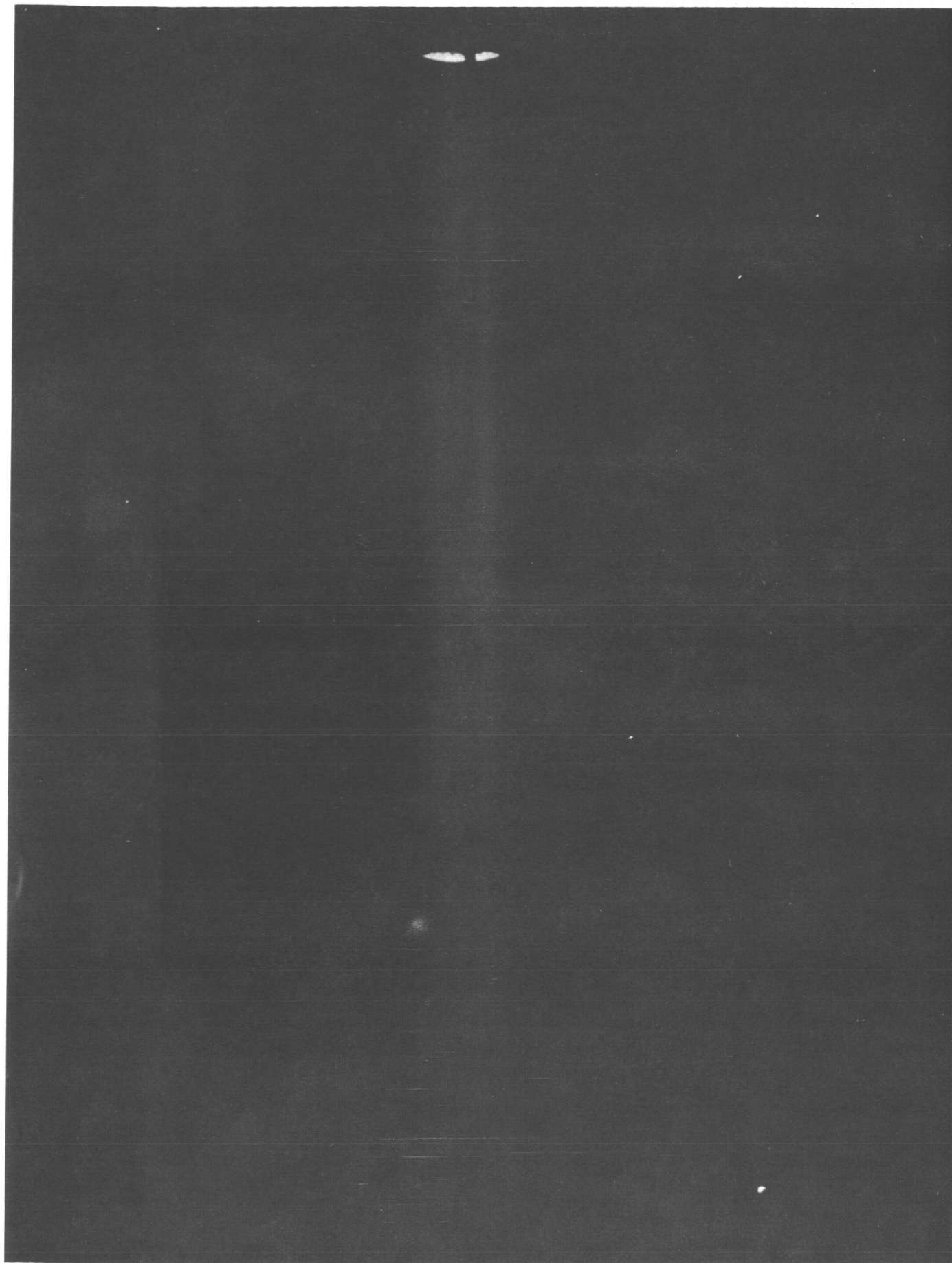


Figure 49. UV Photograph of the Air Stream at 3078°R

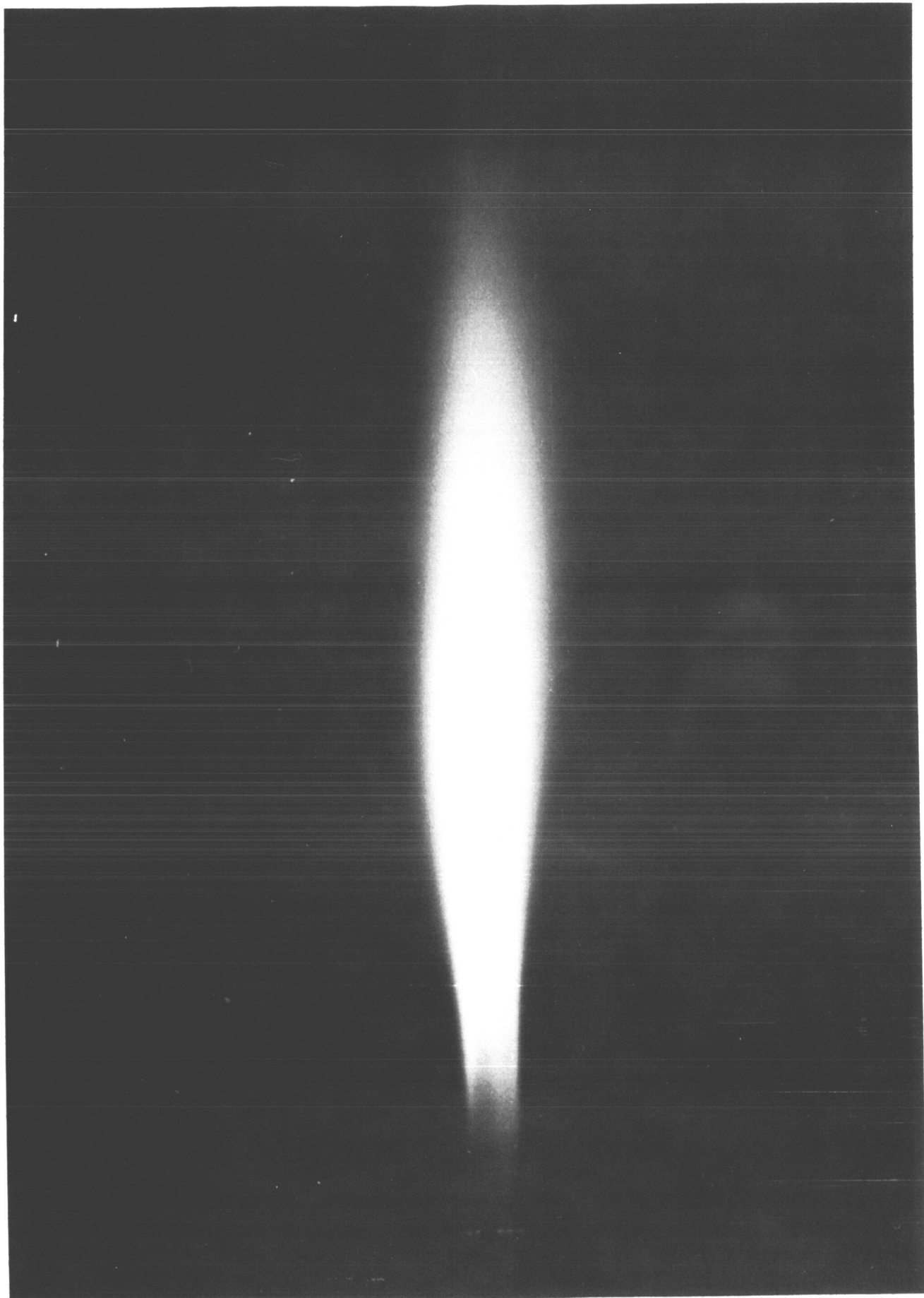


Figure 50. UV Photograph of a 3132<sup>2</sup>R Ring-Injection Test  
for Cold Hydrogen and  $\phi = 1.0$





Figure 51. UV Photograph of a 3240°R Ring-Injection Test  
for Cold Hydrogen and  $\phi = 0.5$

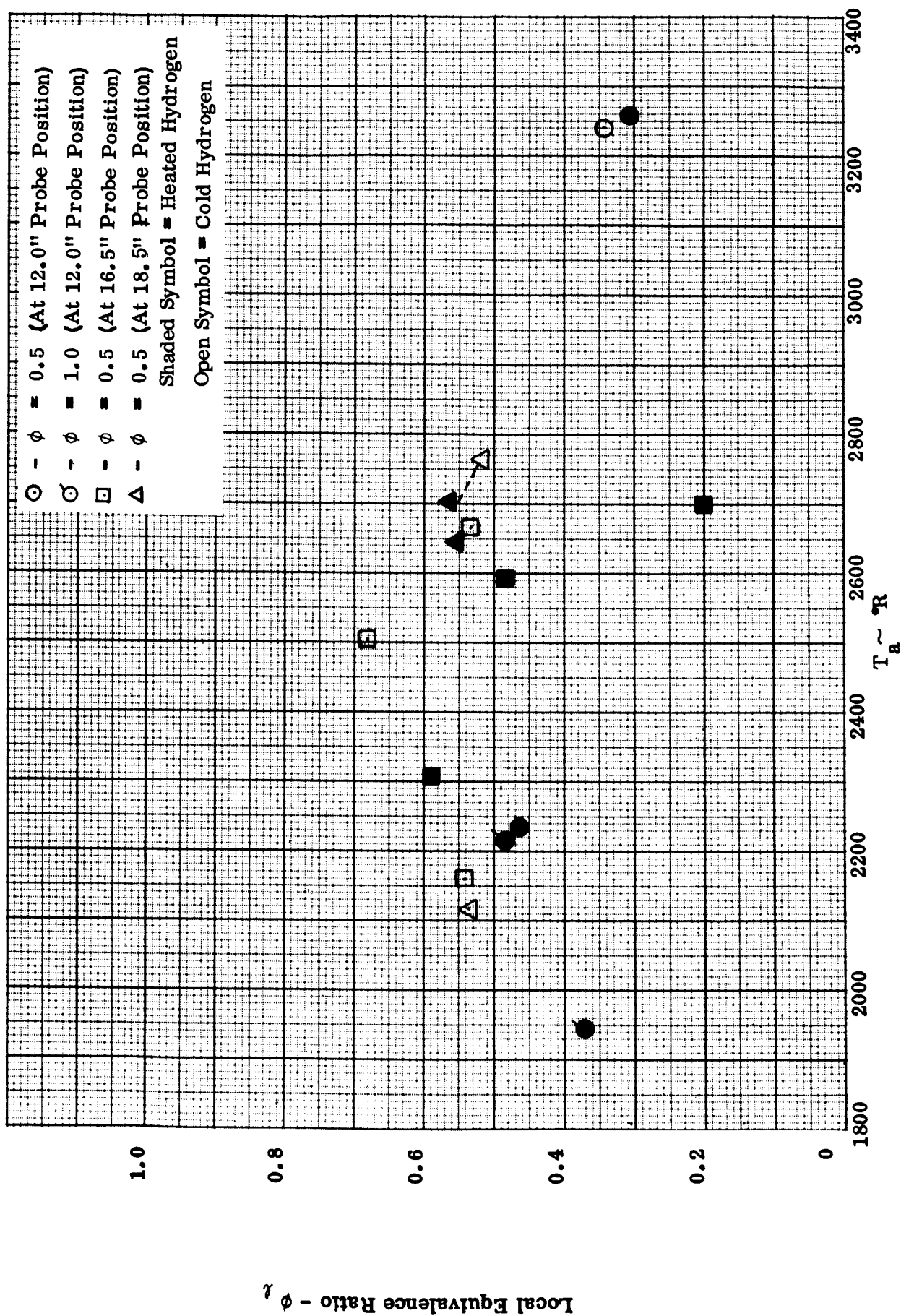


Figure 52. Local Equivalence Ratio vs  $T_a$  for First Series of Ring-Injection Tests

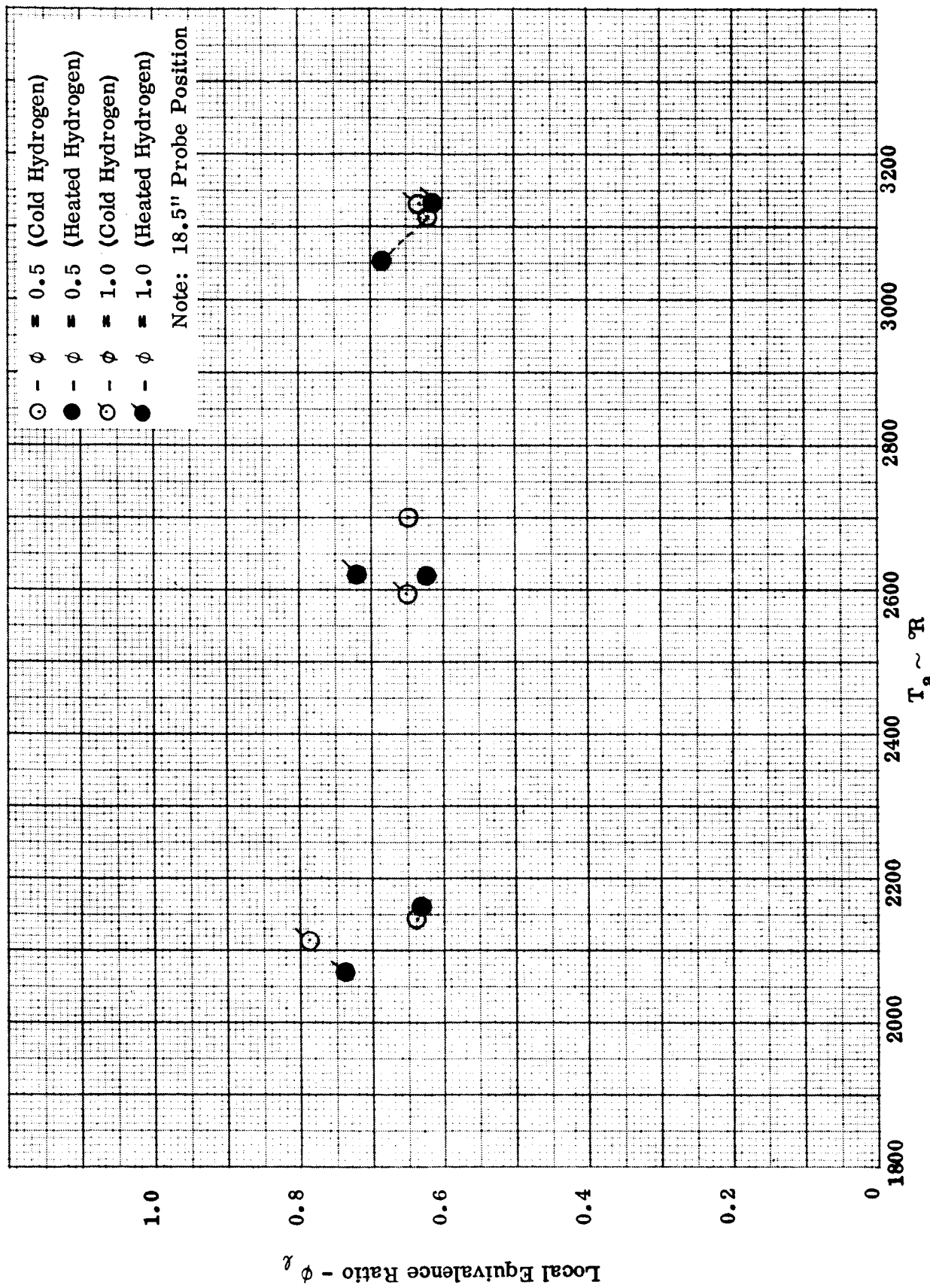


Figure 53. Local Equivalence Ratio vs  $T_a$  for Second Series of Ring-Injection Tests

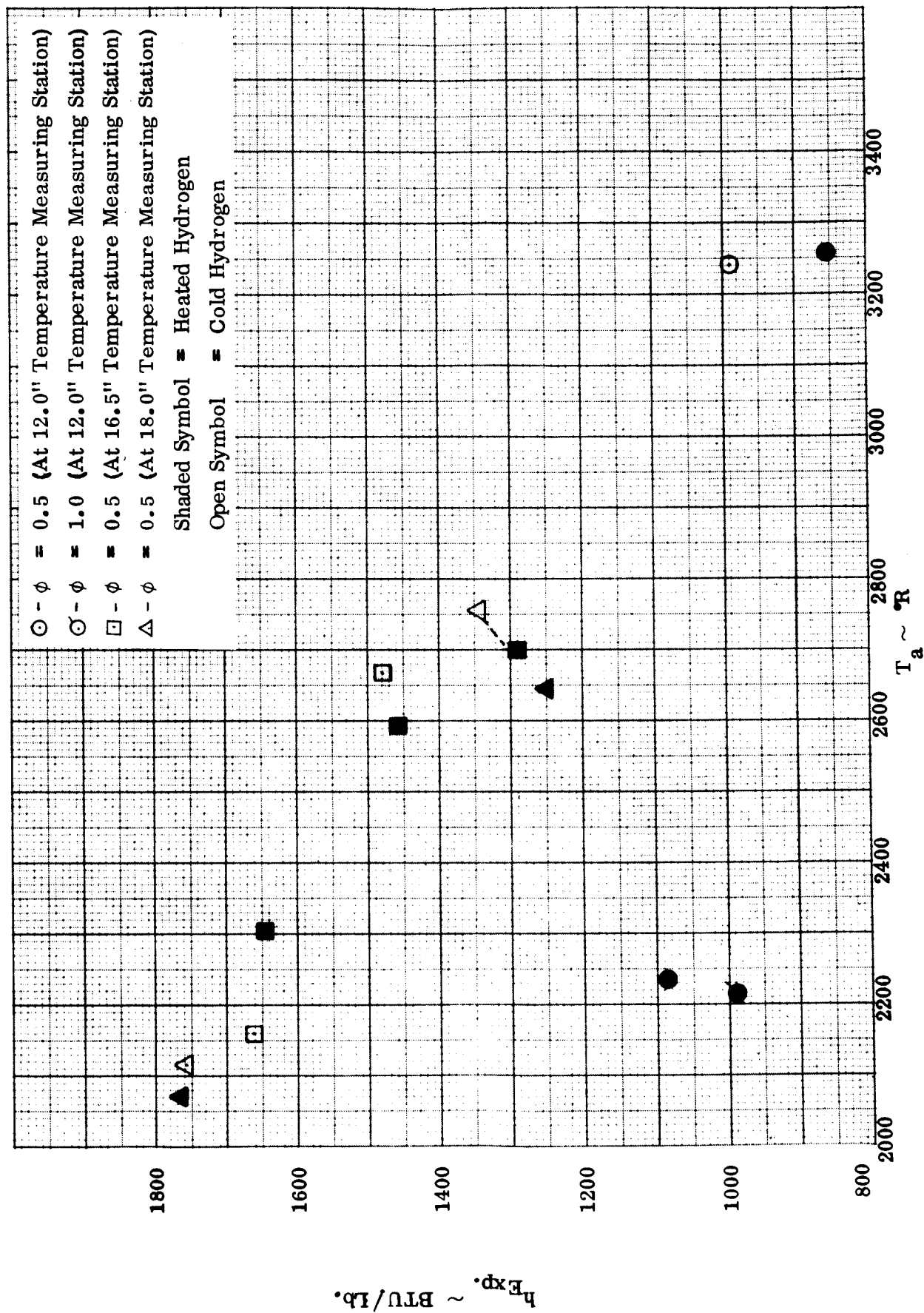


Figure 54 Experimental Static Enthalpy Values for First Series of Ring Injection Tests

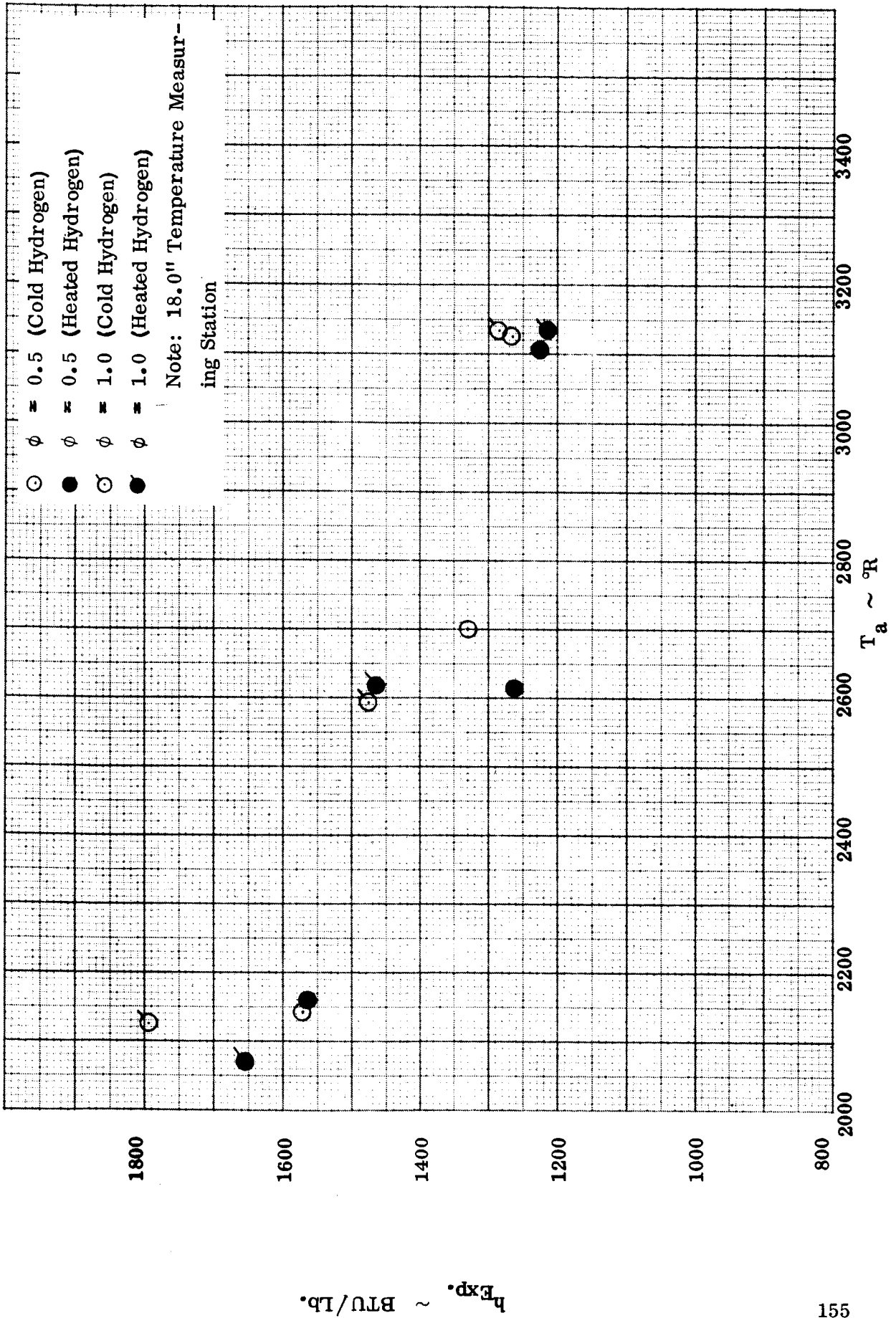
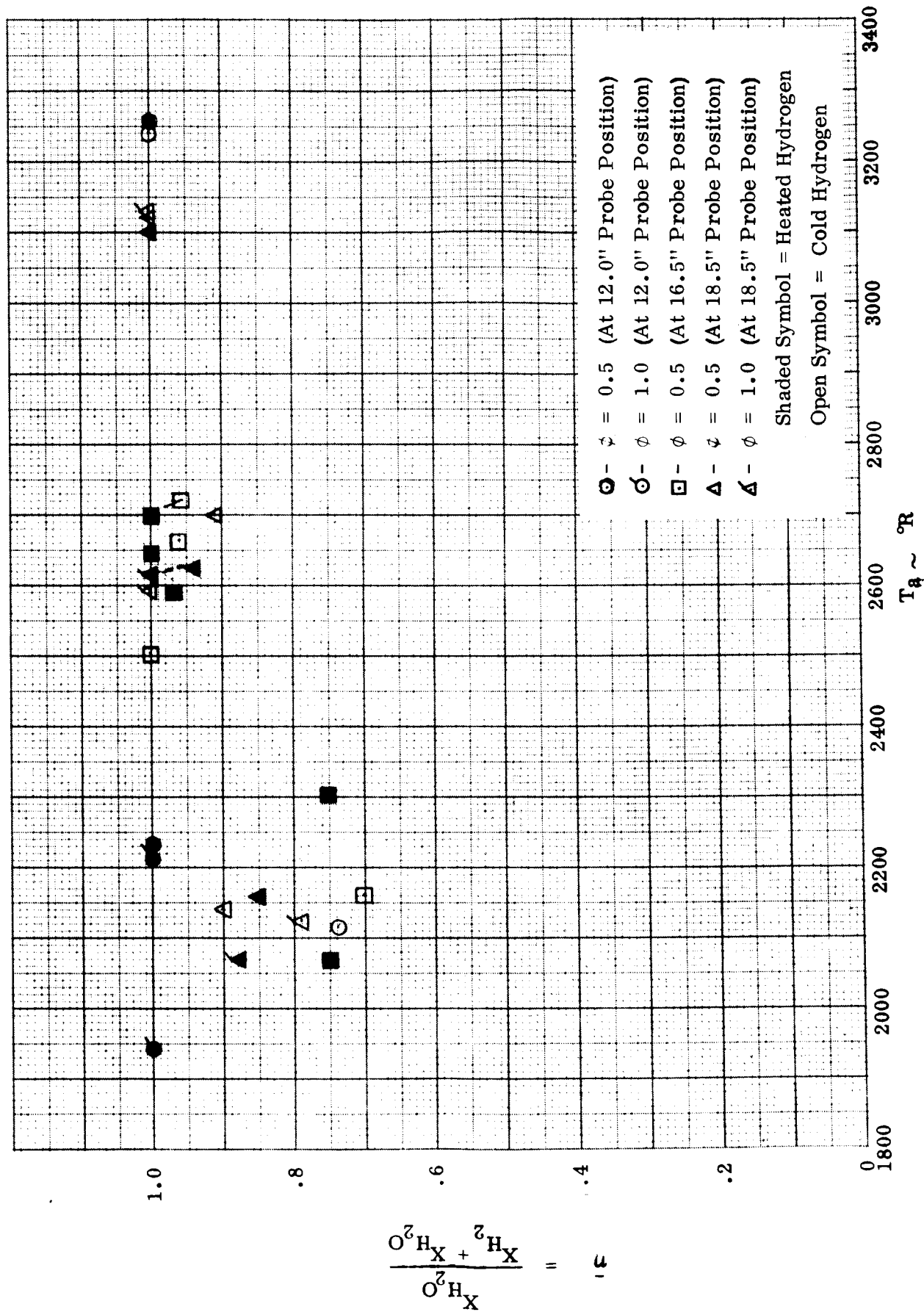


Figure 55. Experimental Static Enthalpy Values for Second Series of Ring Injection Tests

Figure 56. Variation of  $\bar{\eta}$  with  $T_a$  for Ring Injection Tests



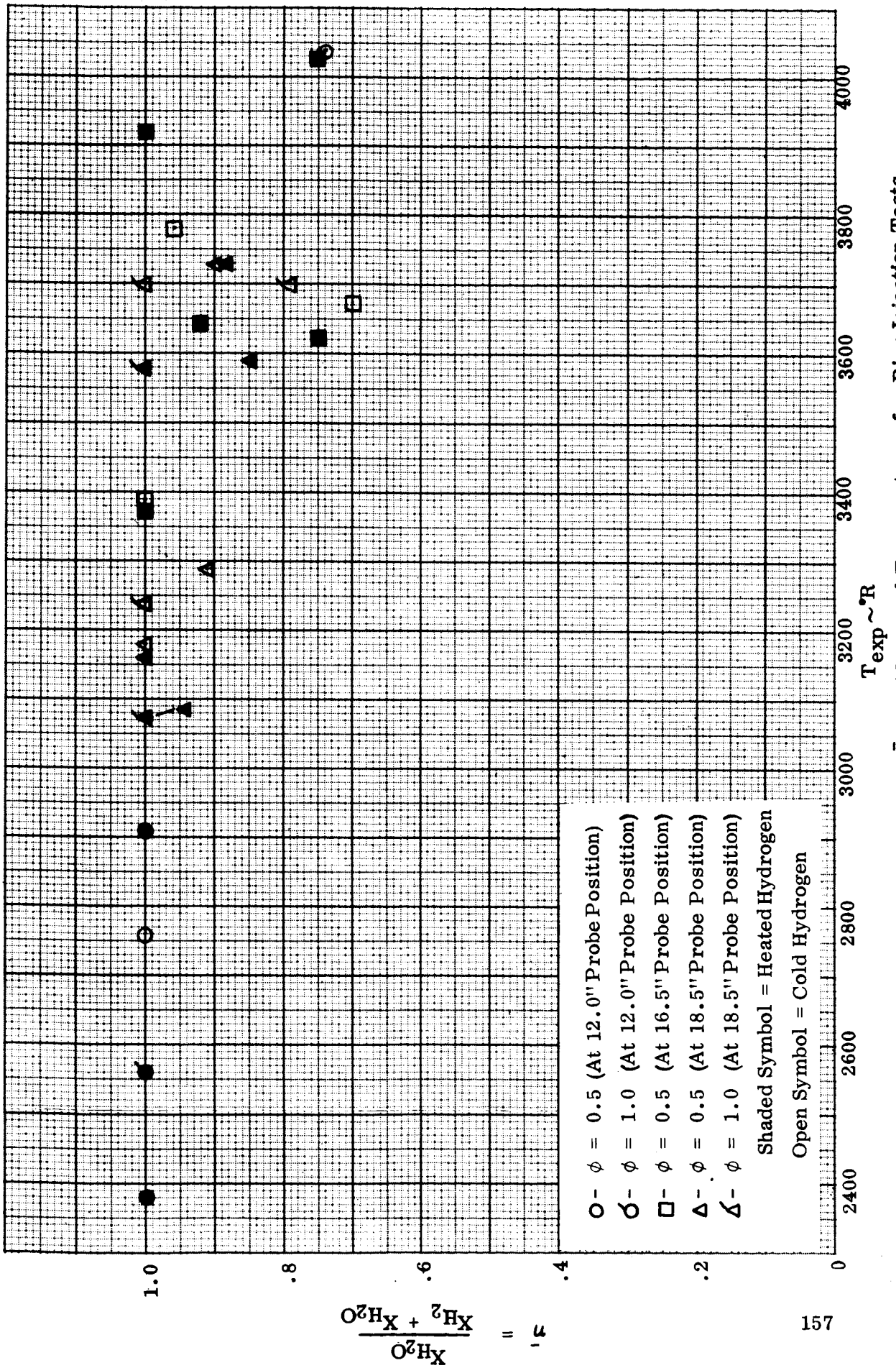


Figure 57. Variation of  $\bar{\eta}$  with Measured Temperatures for Ring Injection Tests

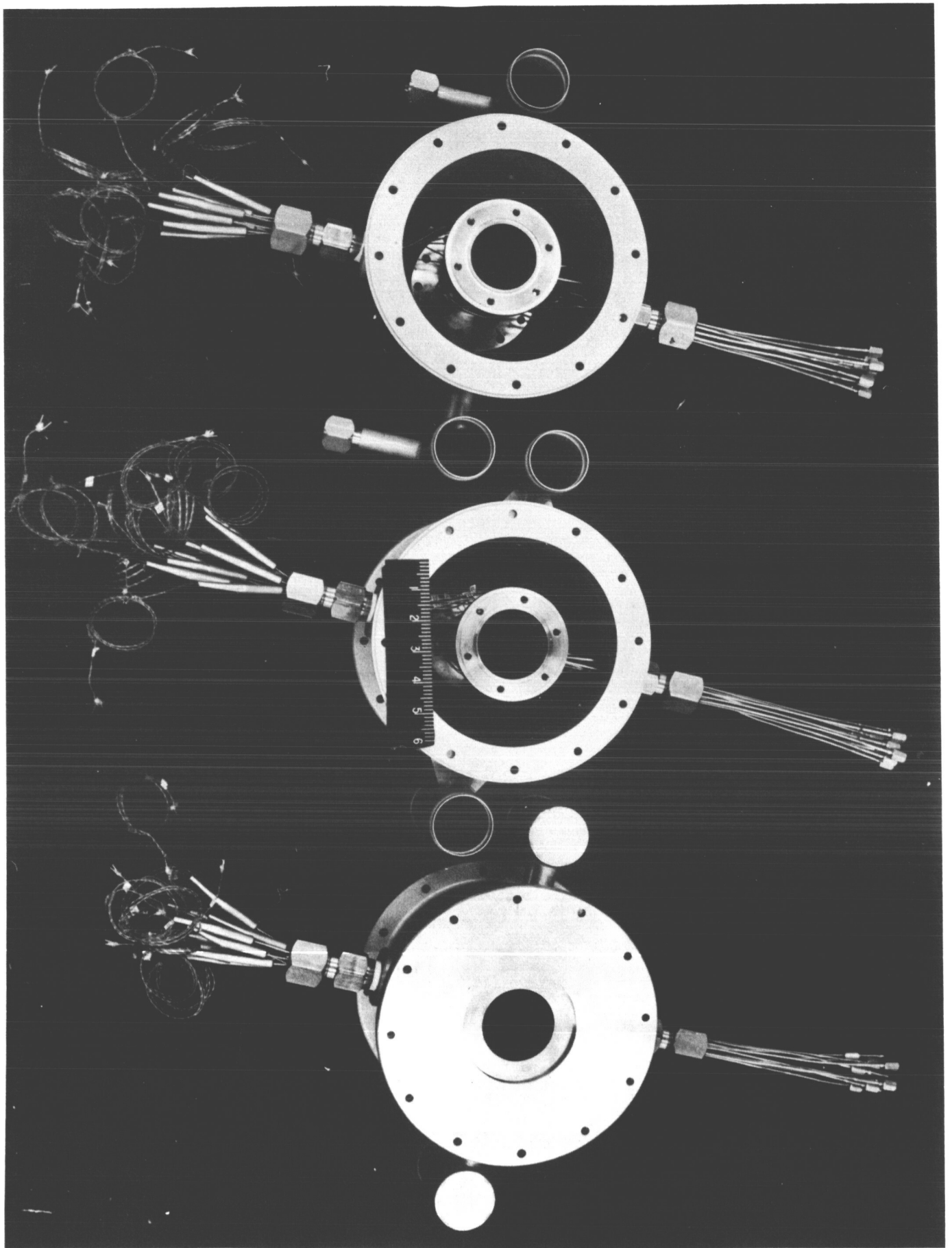


Figure 58. Three-Combustor Segments



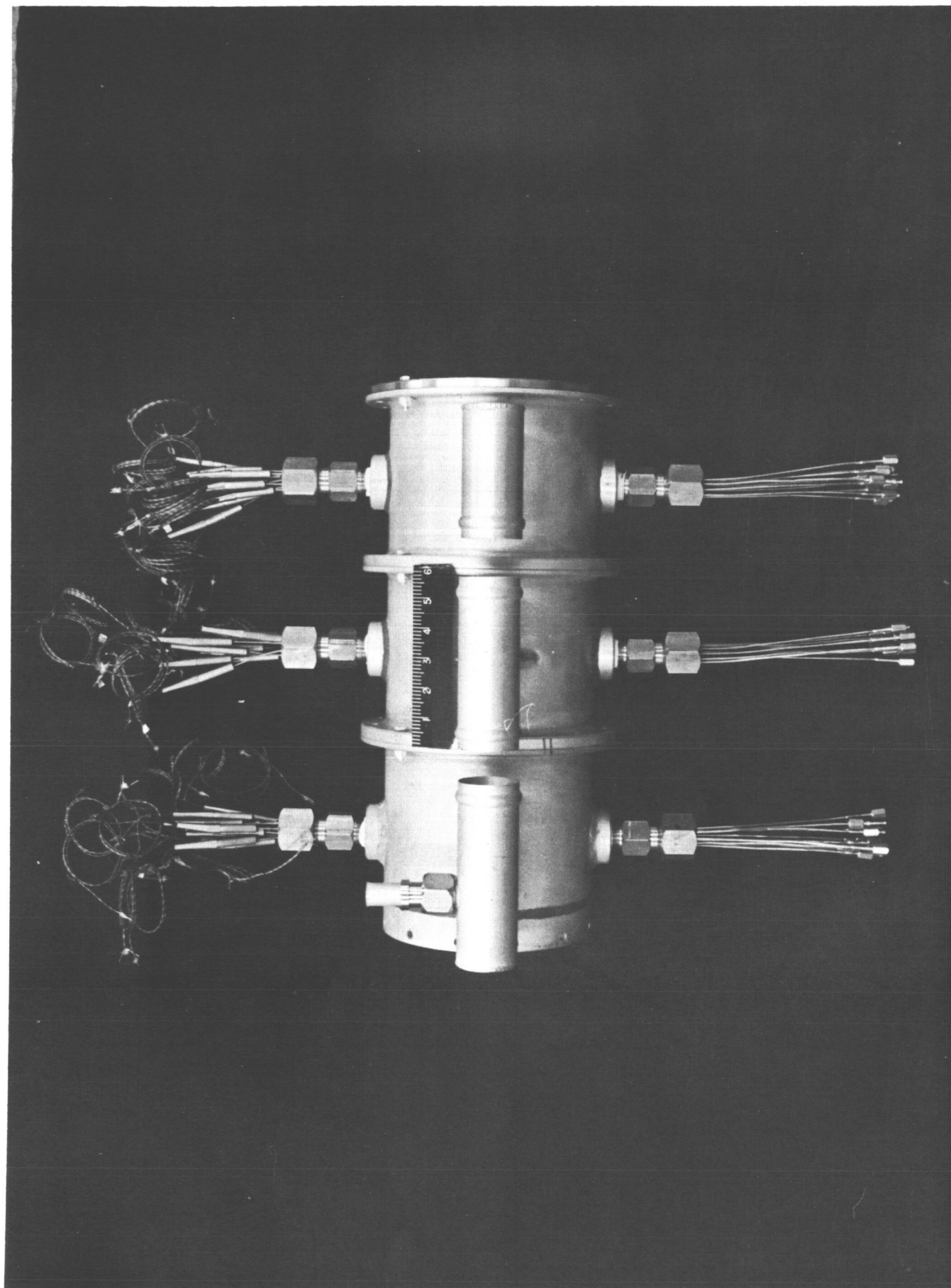


Figure 59. Three-Segment Combustor Configuration

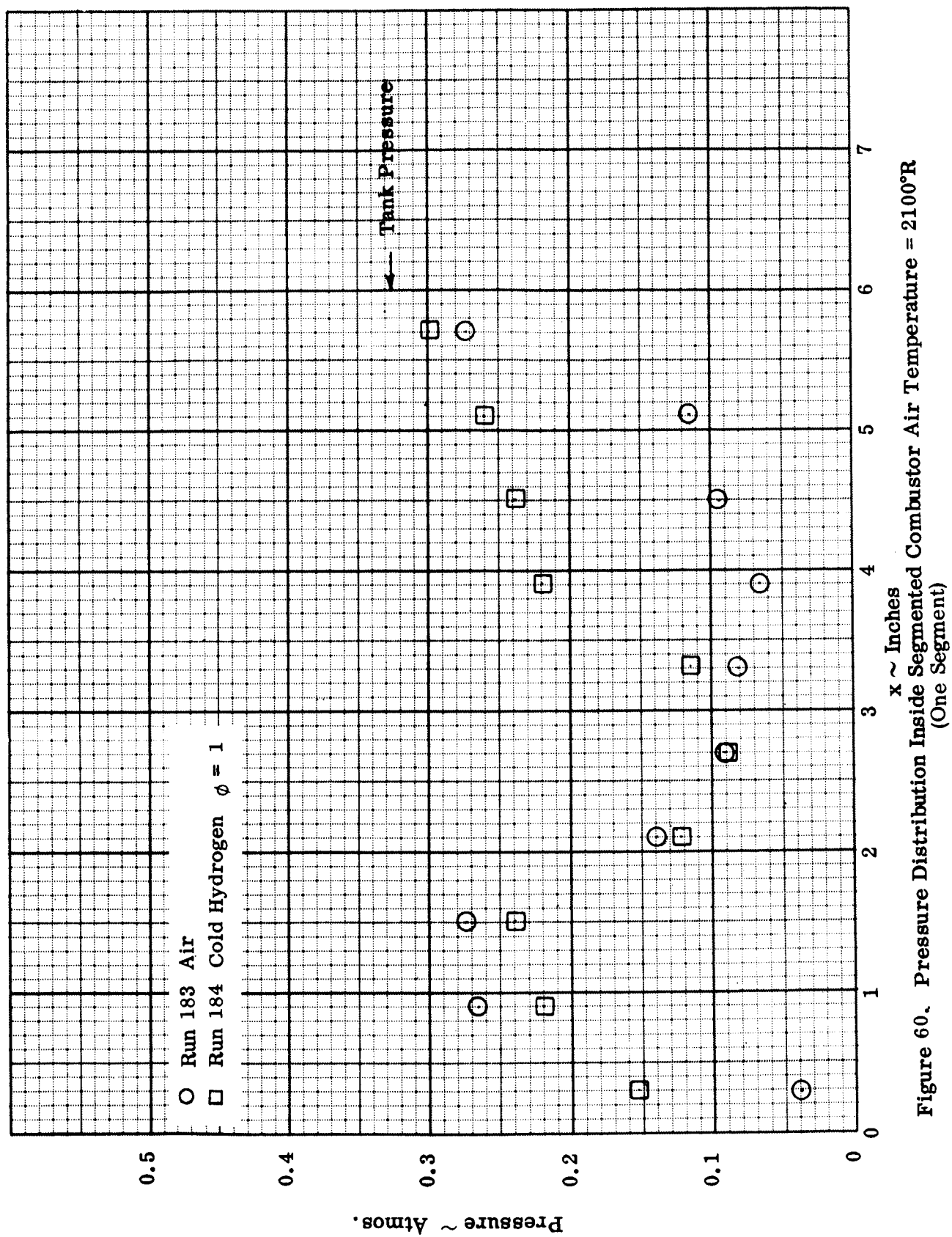


Figure 60. Pressure Distribution Inside Segmented Combustor Air Temperature = 2100°R  
(One Segment)

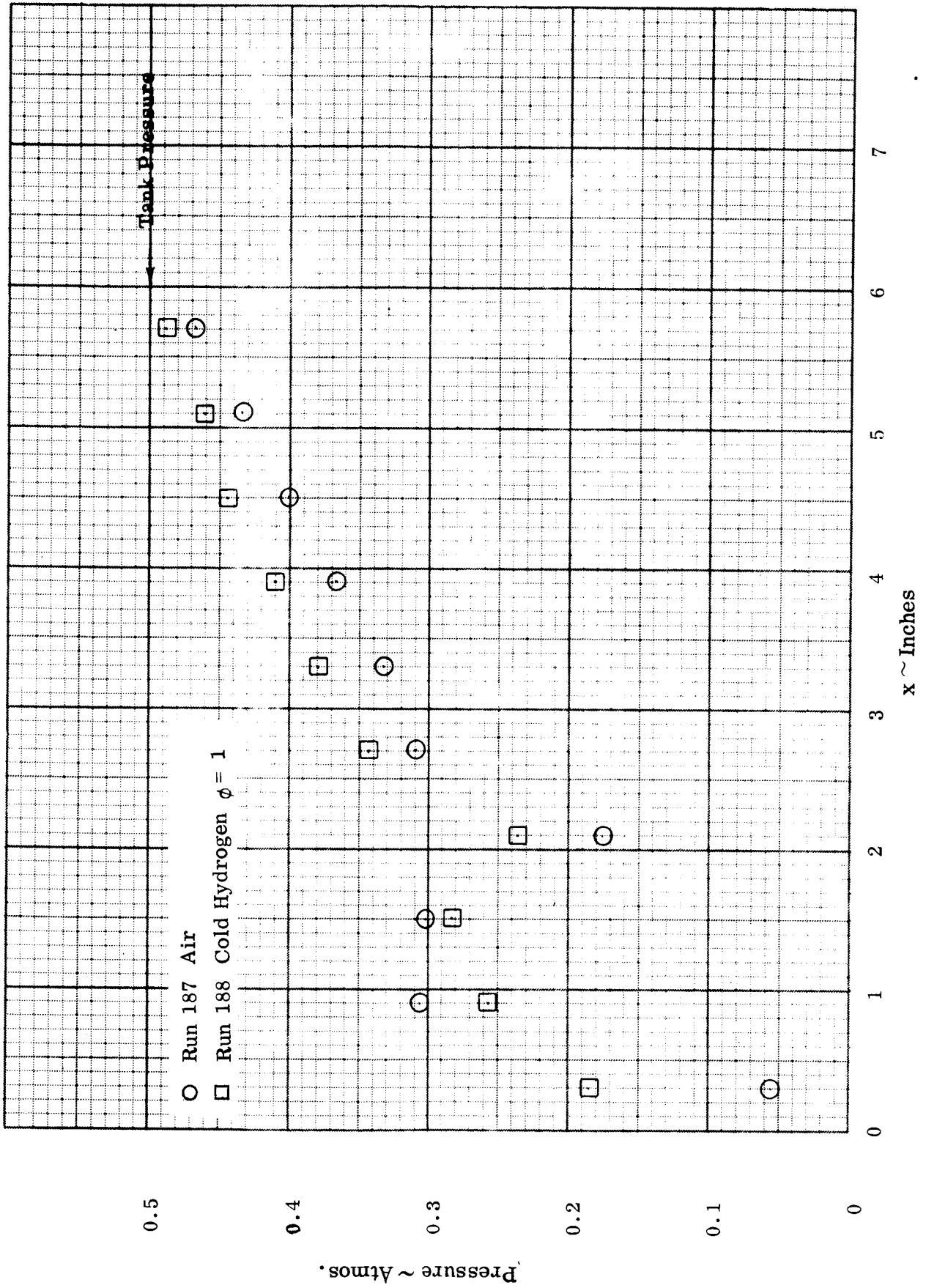
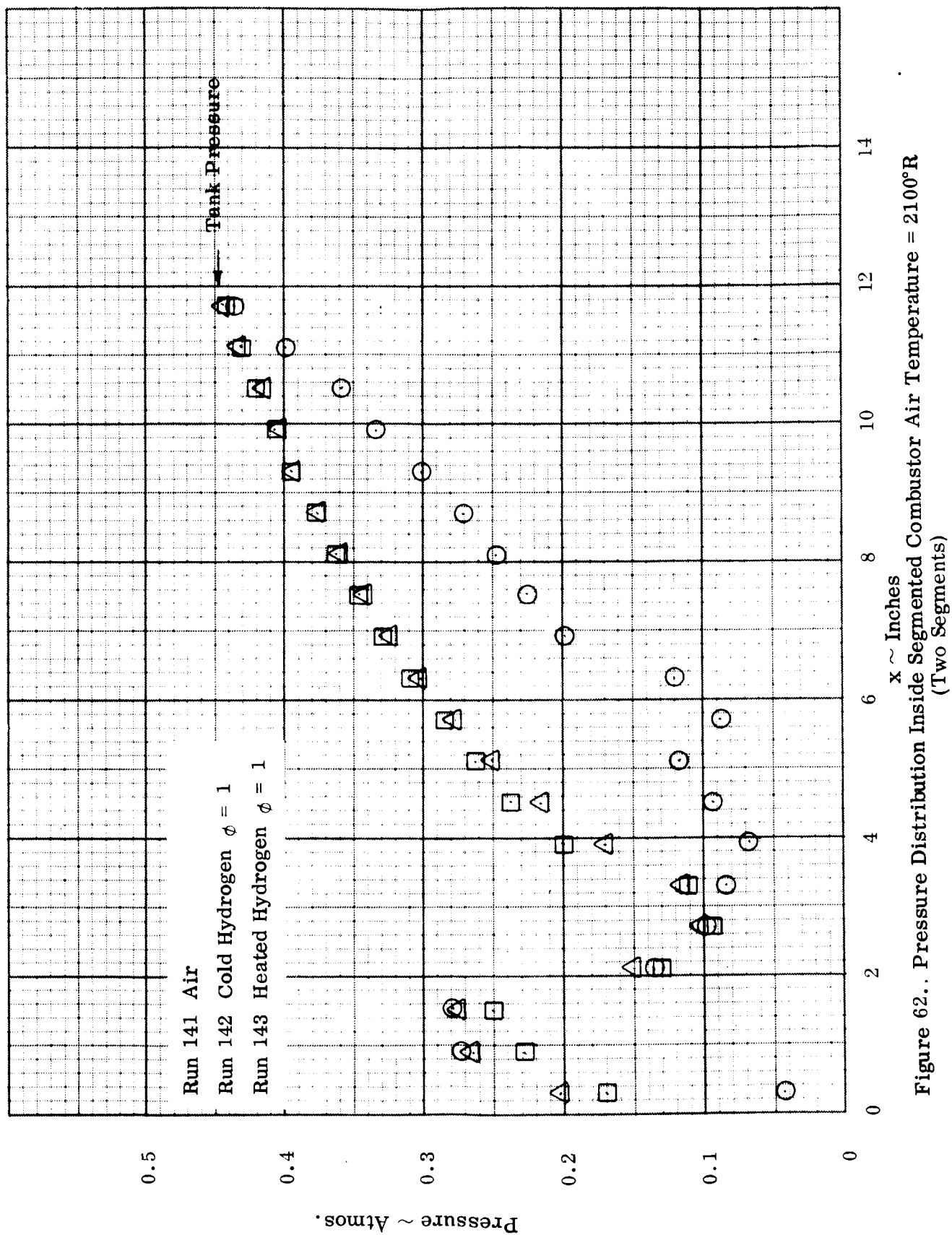


Figure 61. Pressure Distribution Inside Segmented Combustor Air Temperature = 2700°R  
(One Segment)



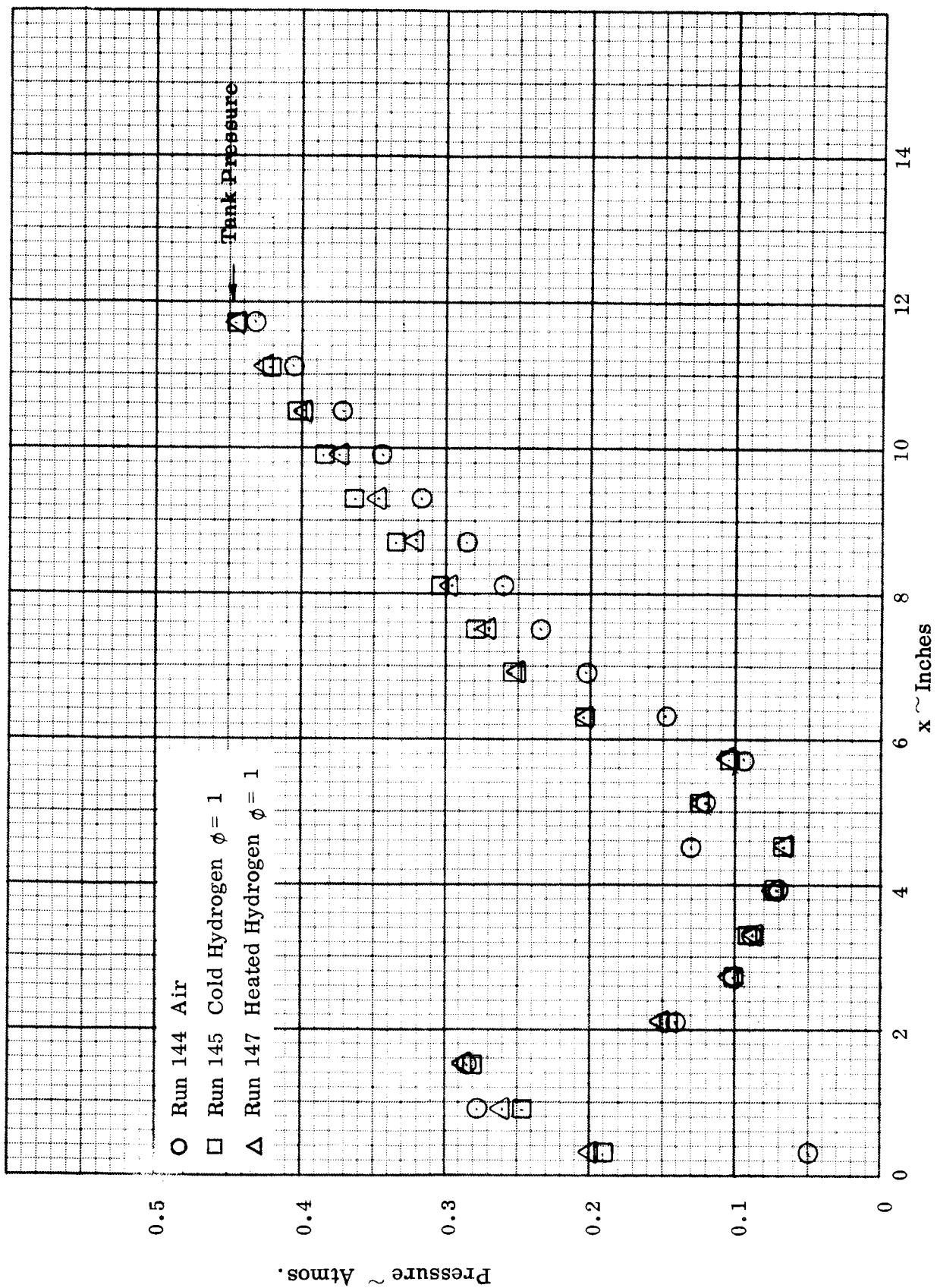


Figure 63. Pressure Distribution Inside Segmented Combustor Air Temperature = 2700°R  
 (Two Segments)

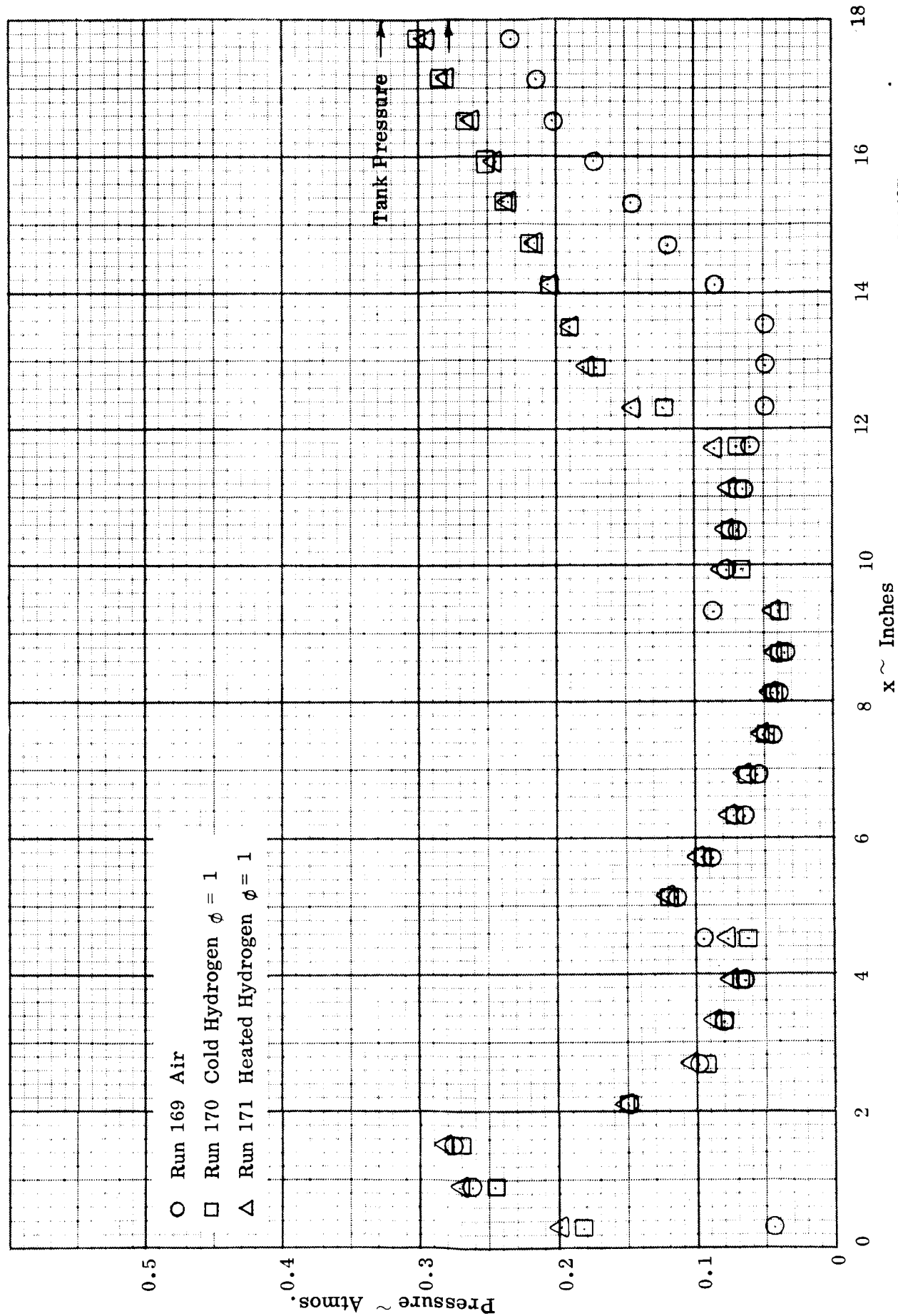


Figure 64.. Pressure Distribution Inside Segmented Combustor Air Temperature = 2100°R  
(Three Segments)

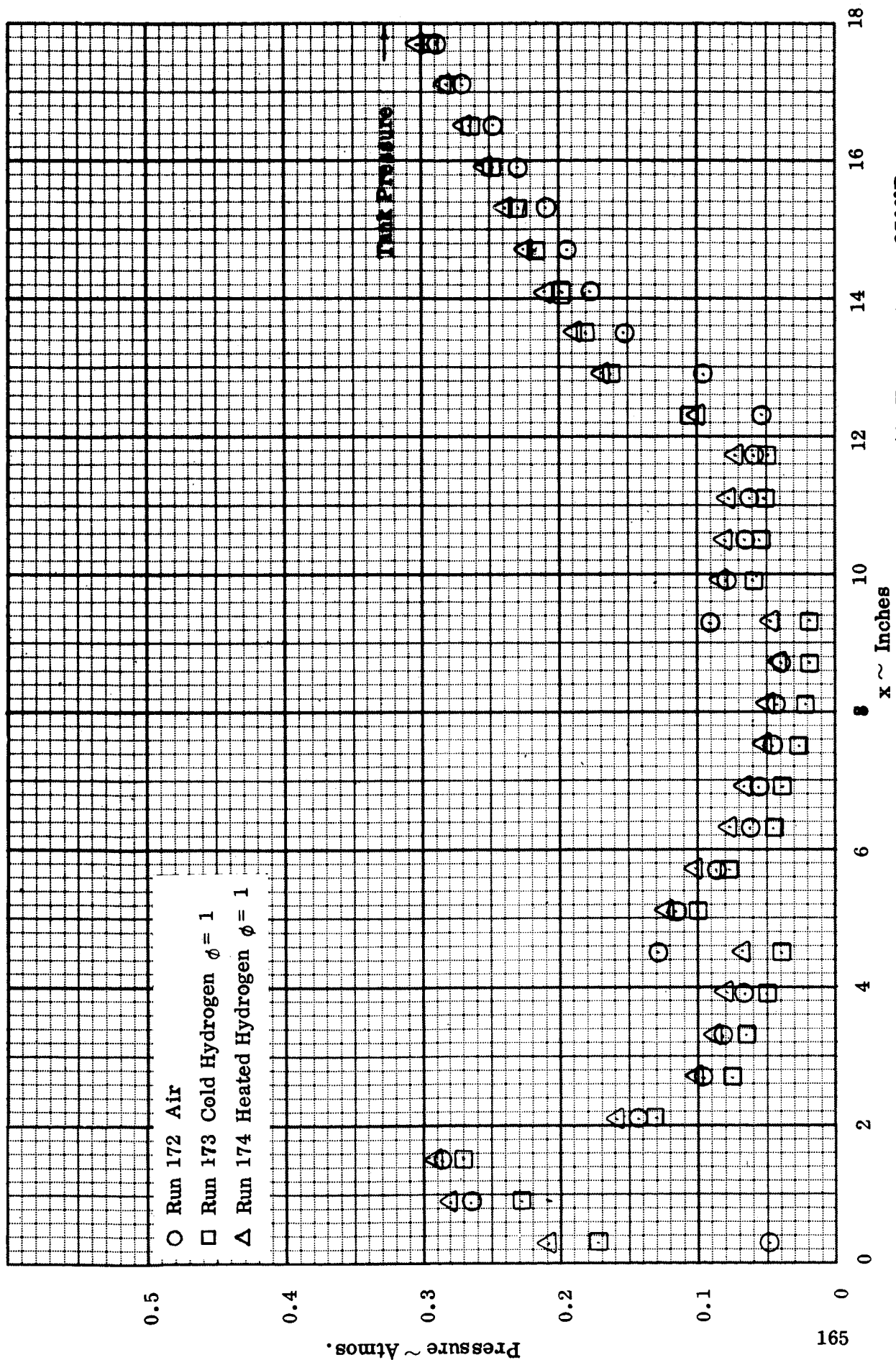


Figure 65.. Pressure Distribution Inside Segmented Combustor Air Temperature = 2700°R  
(Three Segments)



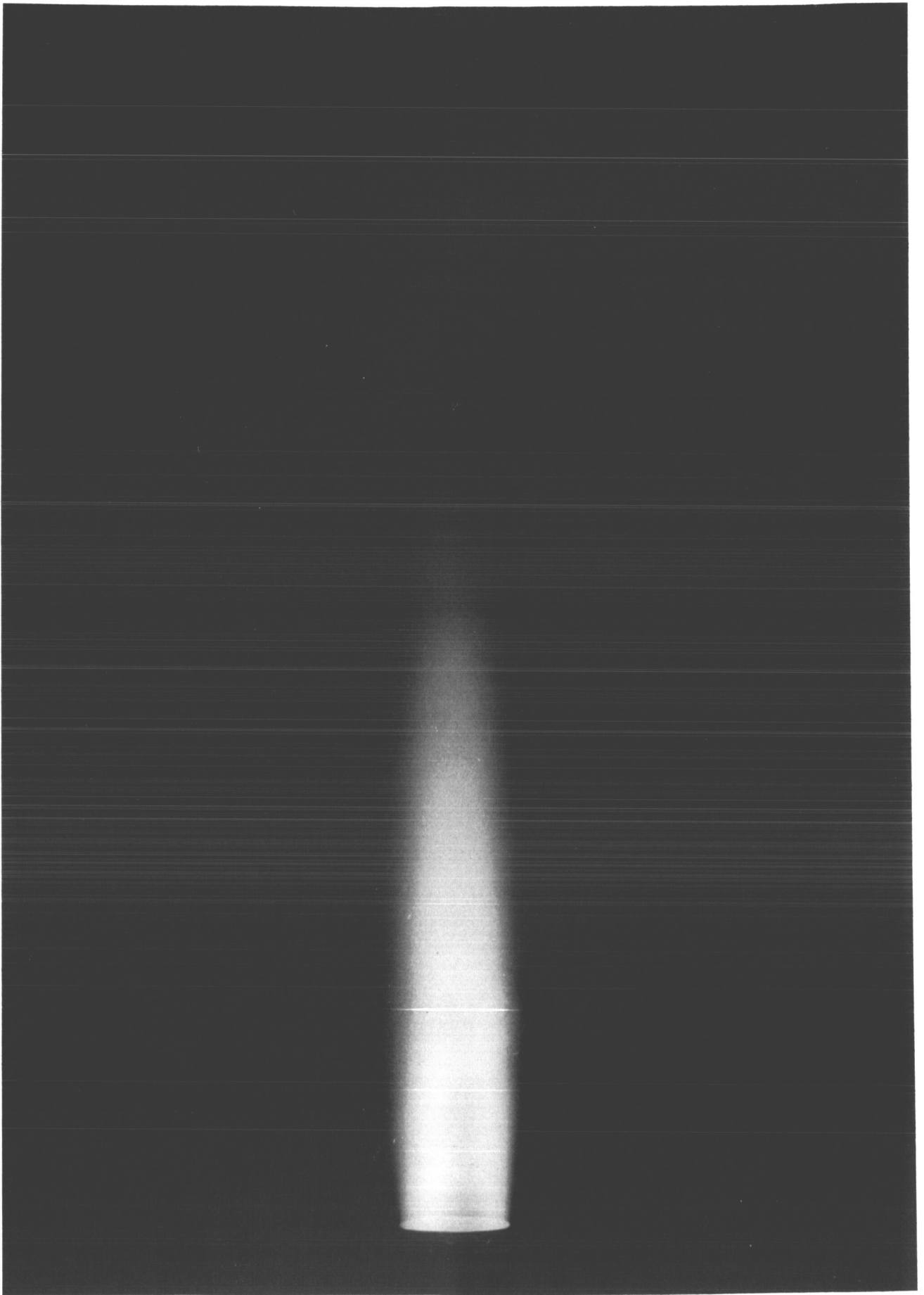


Figure 66. UV Photograph of Exit Plane of the Combustor  
 $T_a = 2106^\circ\text{R}$  - Cold Hydrogen -  $\phi = 1.0$



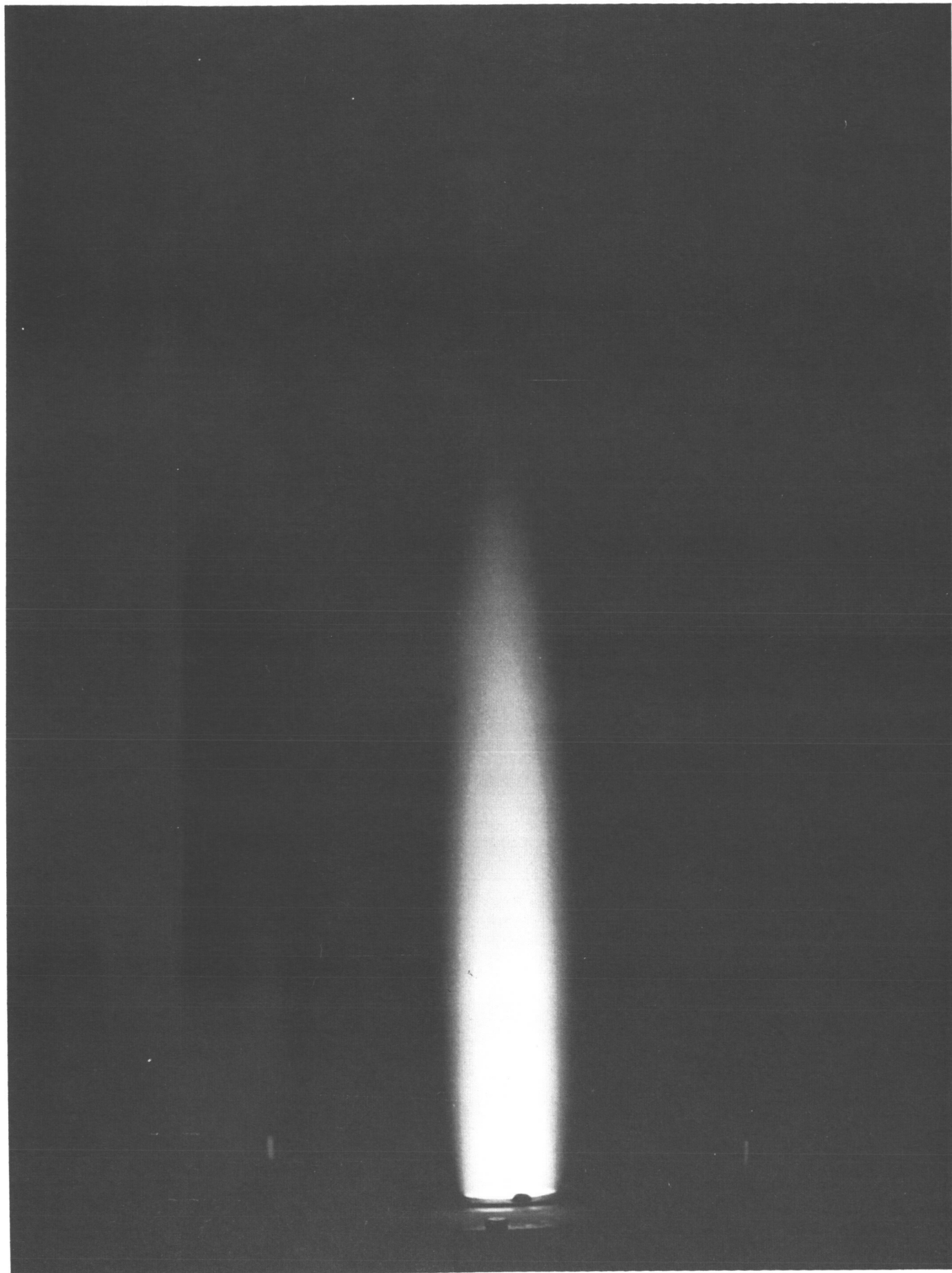


Figure 67. UV Photograph of Exit Plane of the Combustor  
 $T_a = 2700^\circ\text{R}$  - Cold Hydrogen -  $\phi = 1.0$

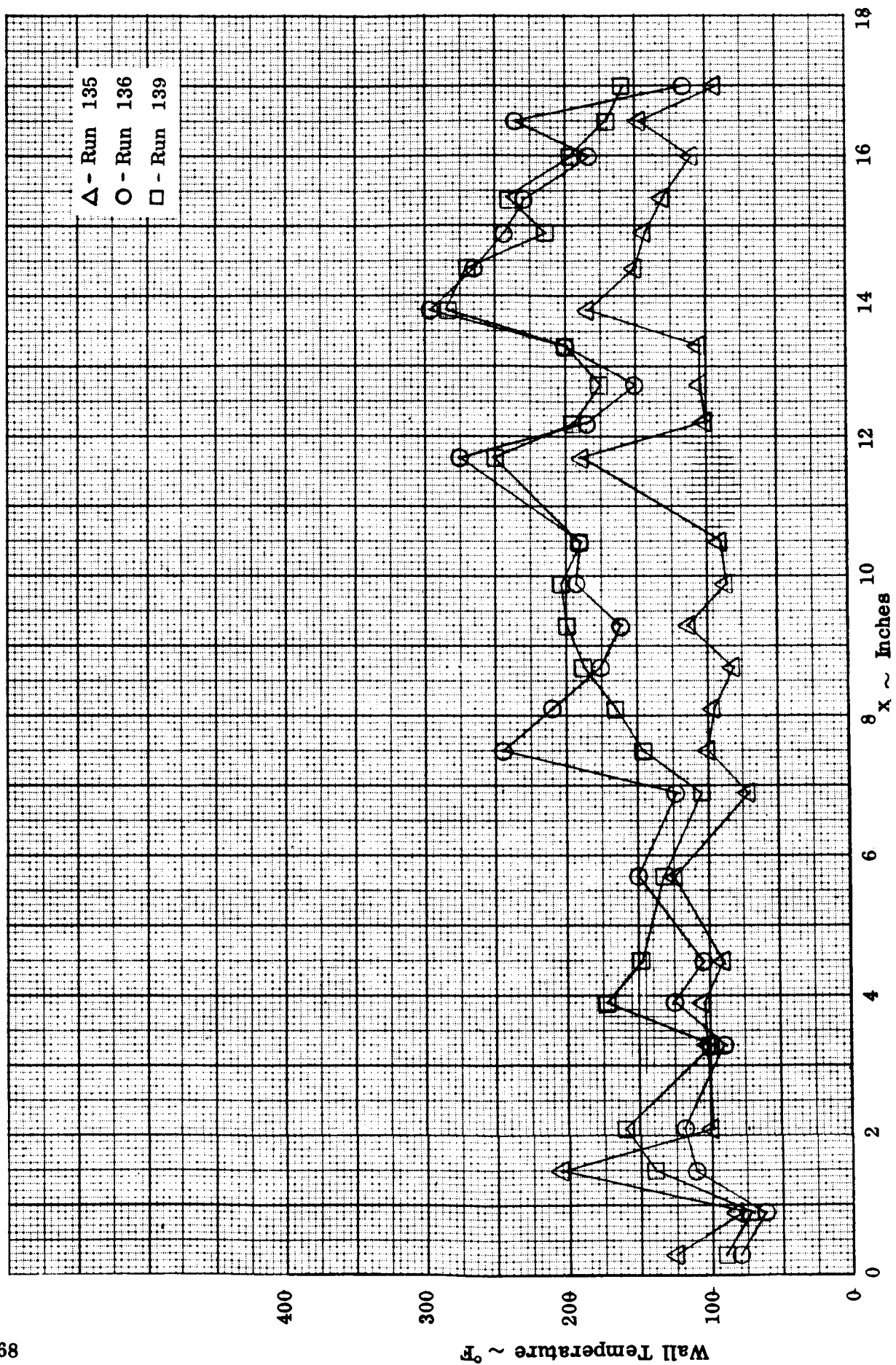


Figure 68. Wall Temperature Distributions for First Combustor Test Series

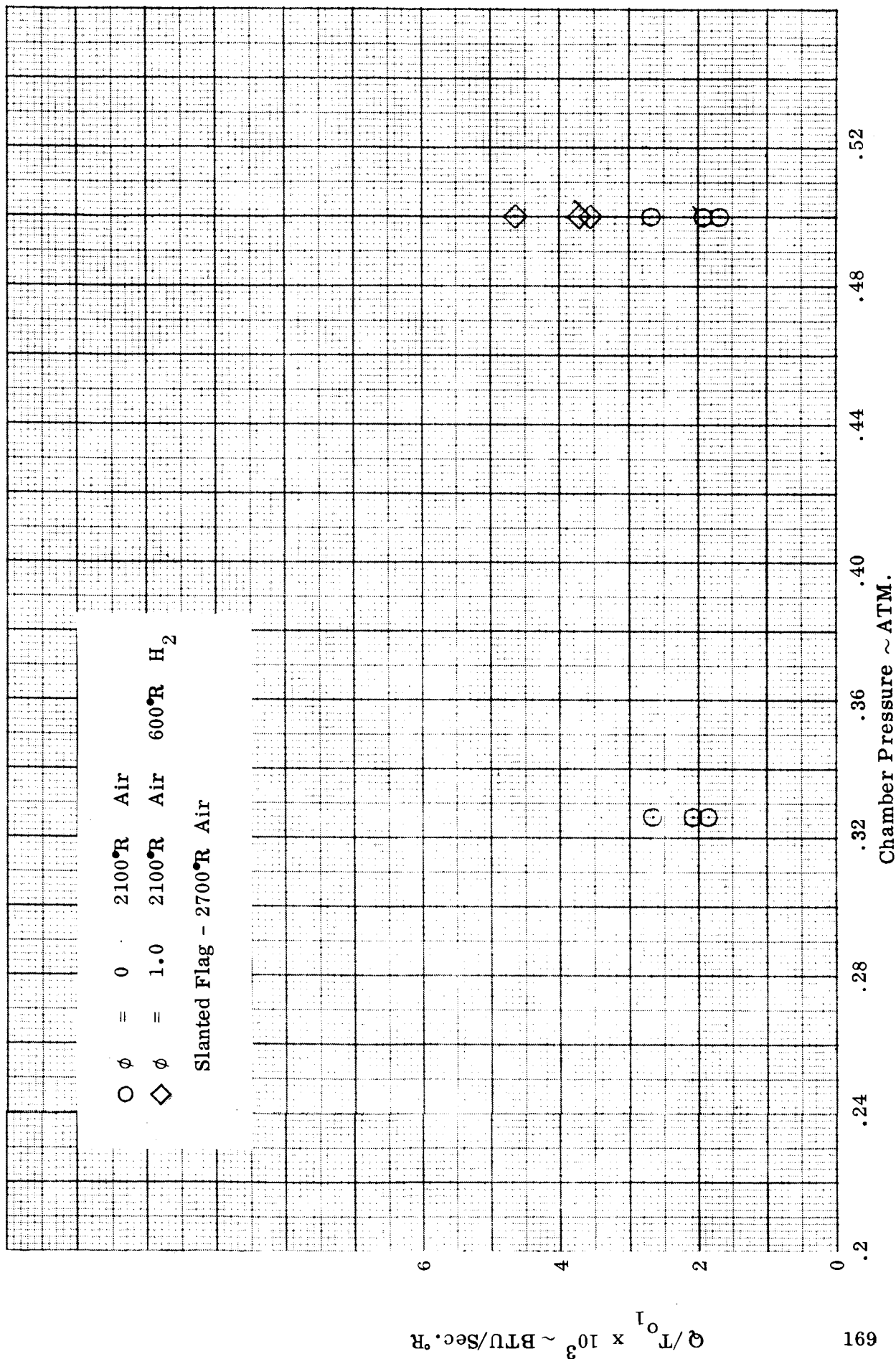


Figure 69 . 1 Segment Combustor Heat Rejection Rates - First Combustor

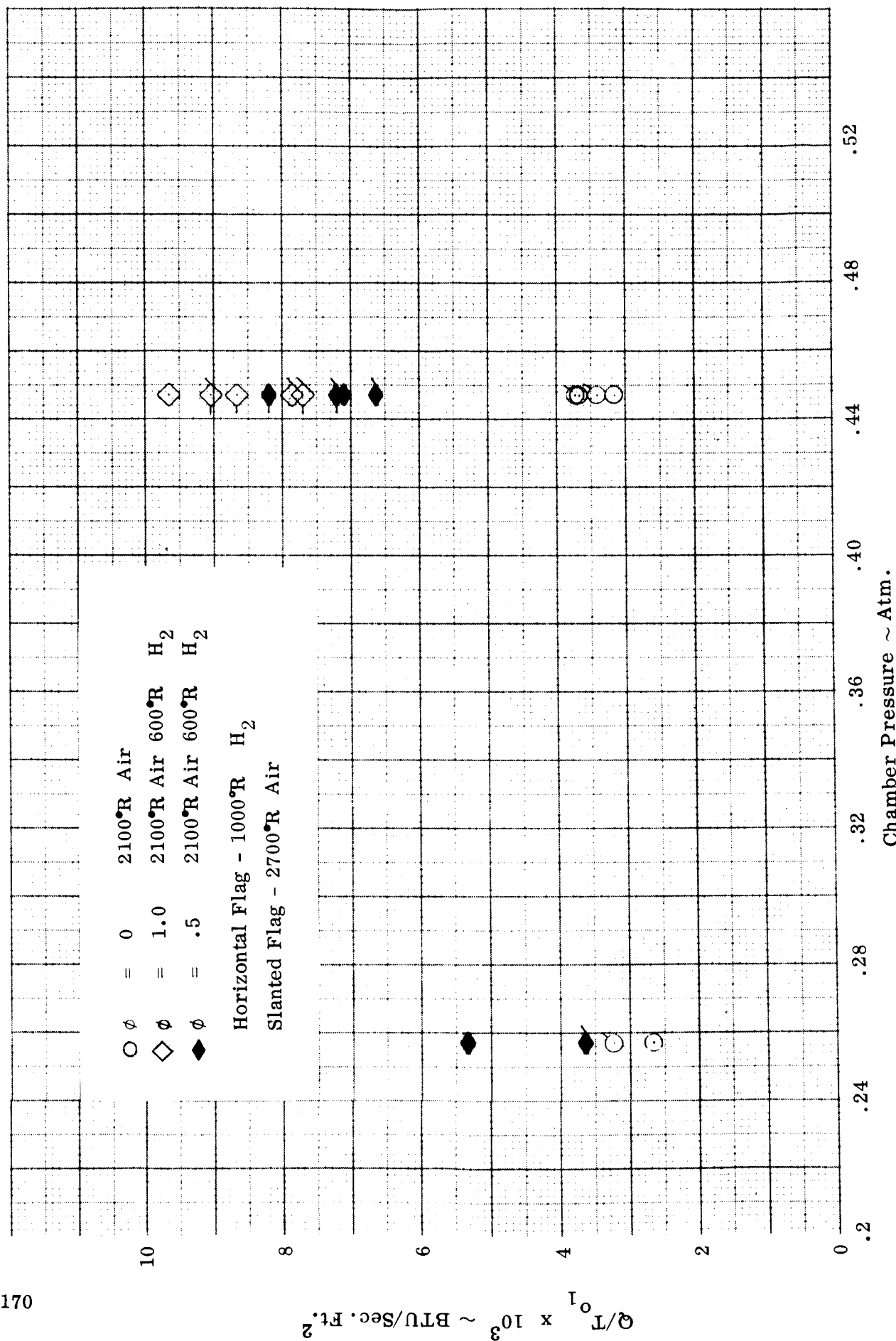


Figure 70. 2 Segment Combustor Heat Rejection Rates - First Combustor

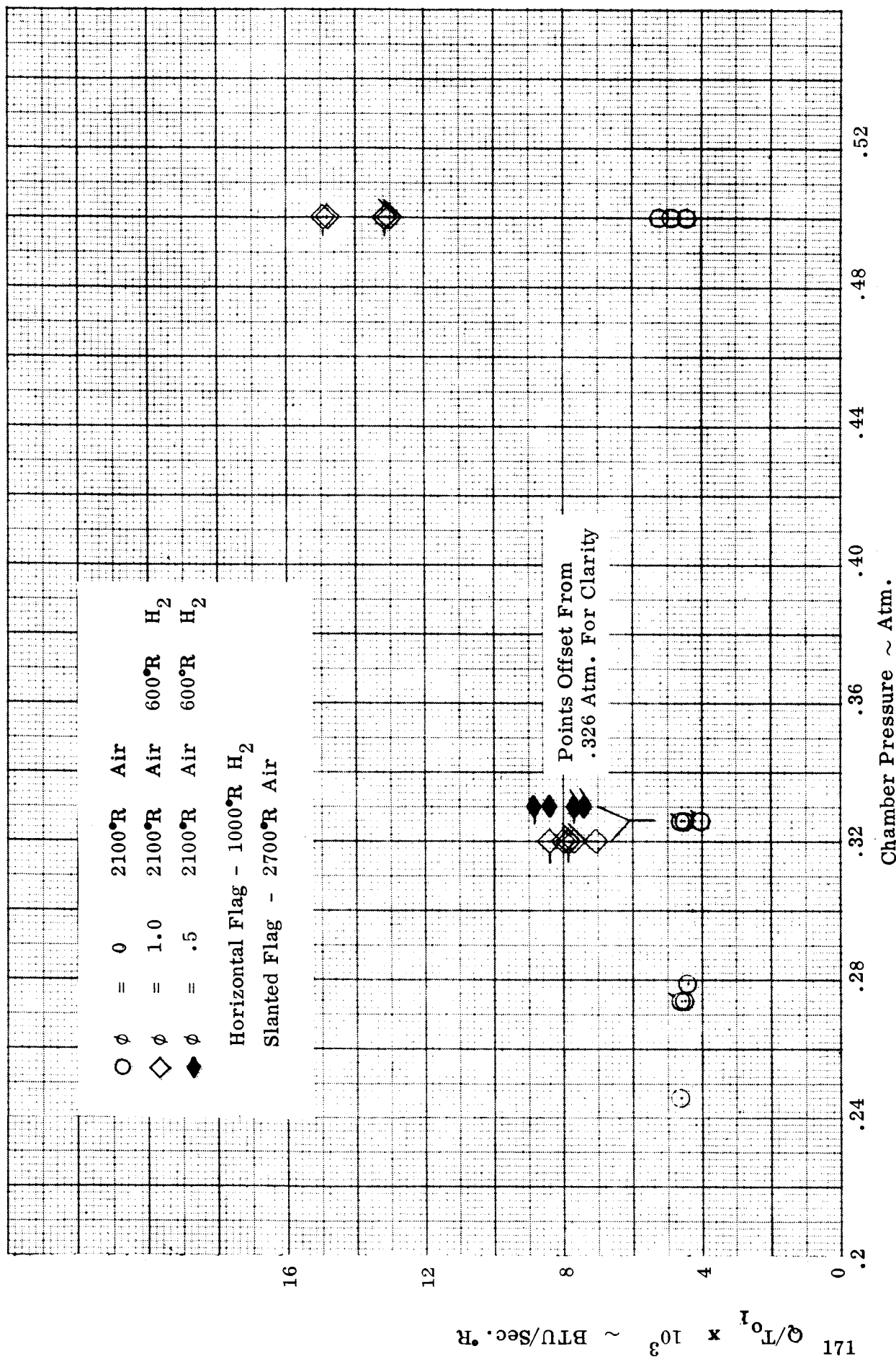


Figure 71.. 3 Segment Combustor Heat Rejection Rates - First Combustor

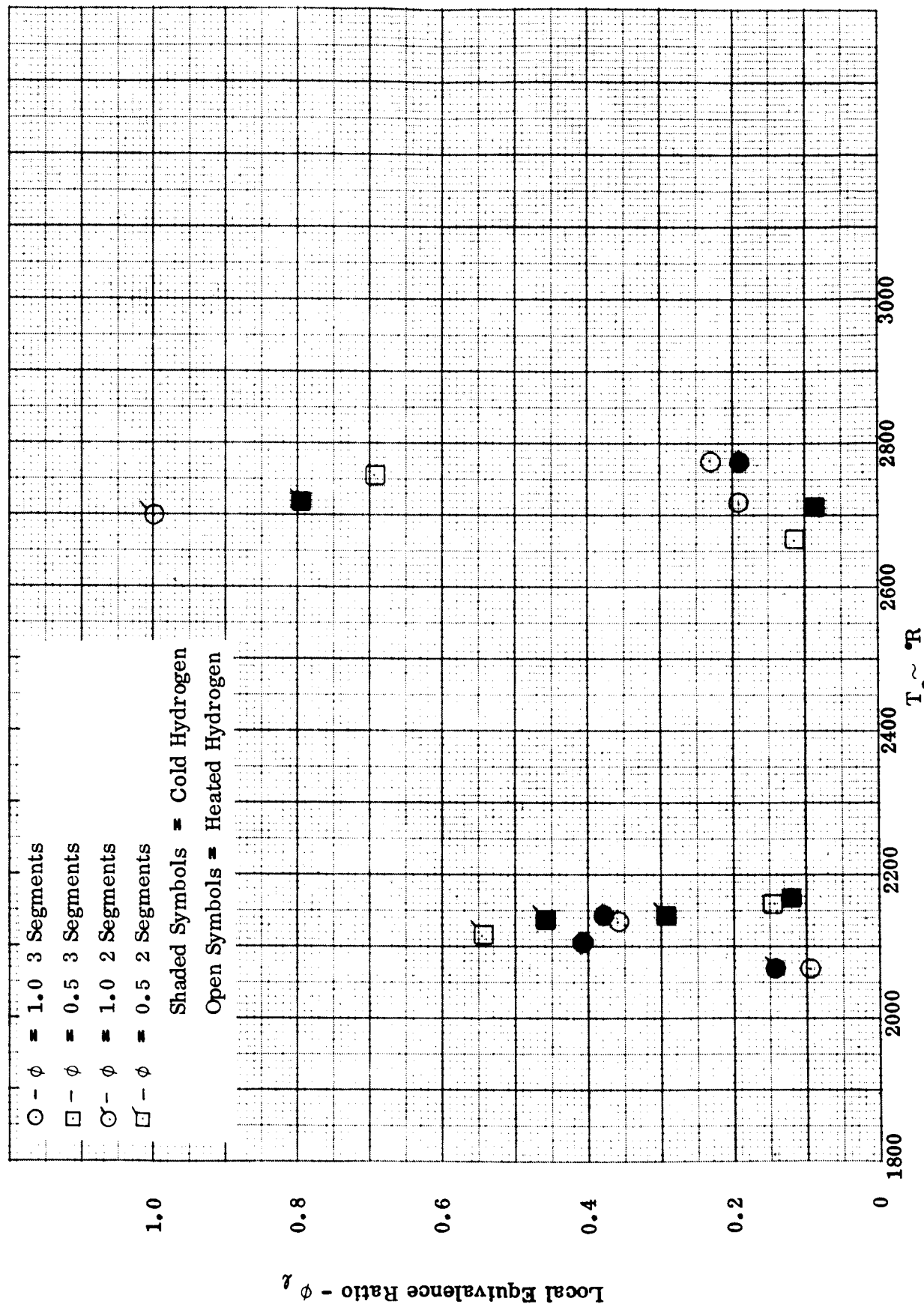


Figure 72. Local Equivalence Ratio vs  $T_a$  for the first Series of Combustor Tests



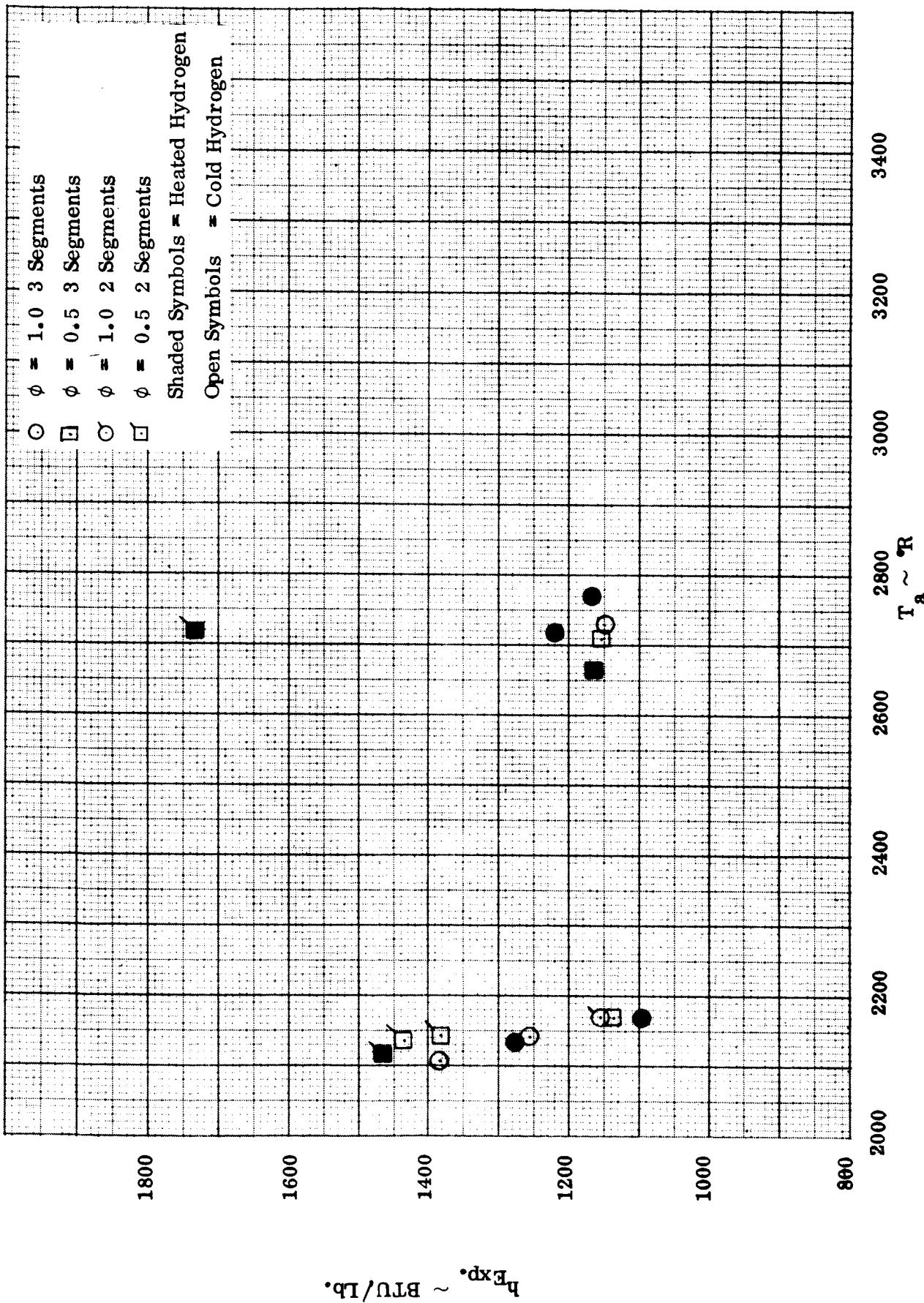


Figure 73. Experimental Static Enthalpies for the First Series of Combustor Tests

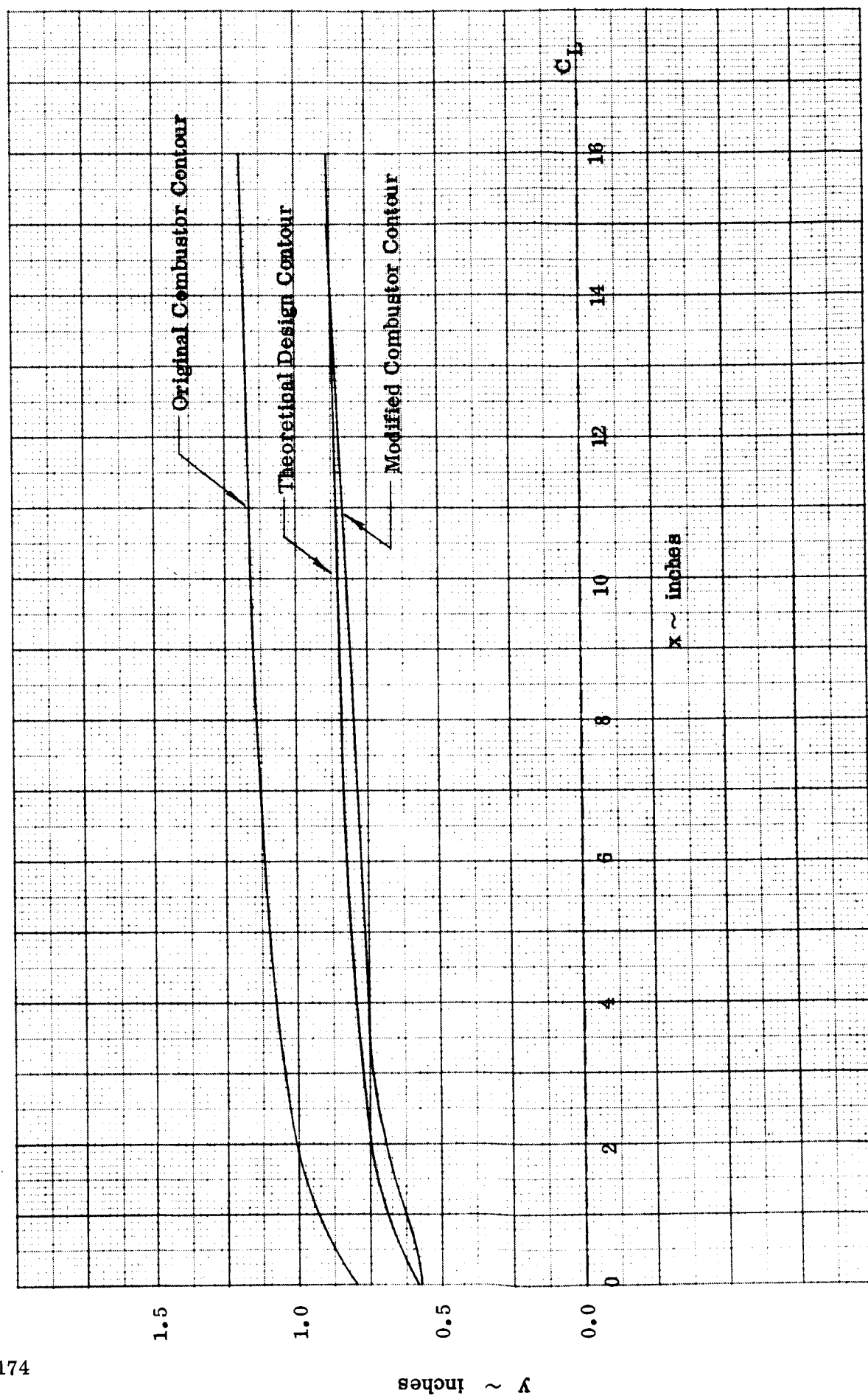


Figure 74. Comparison of Combustor Contours





**Figure 75. Modified Combustor Contour**

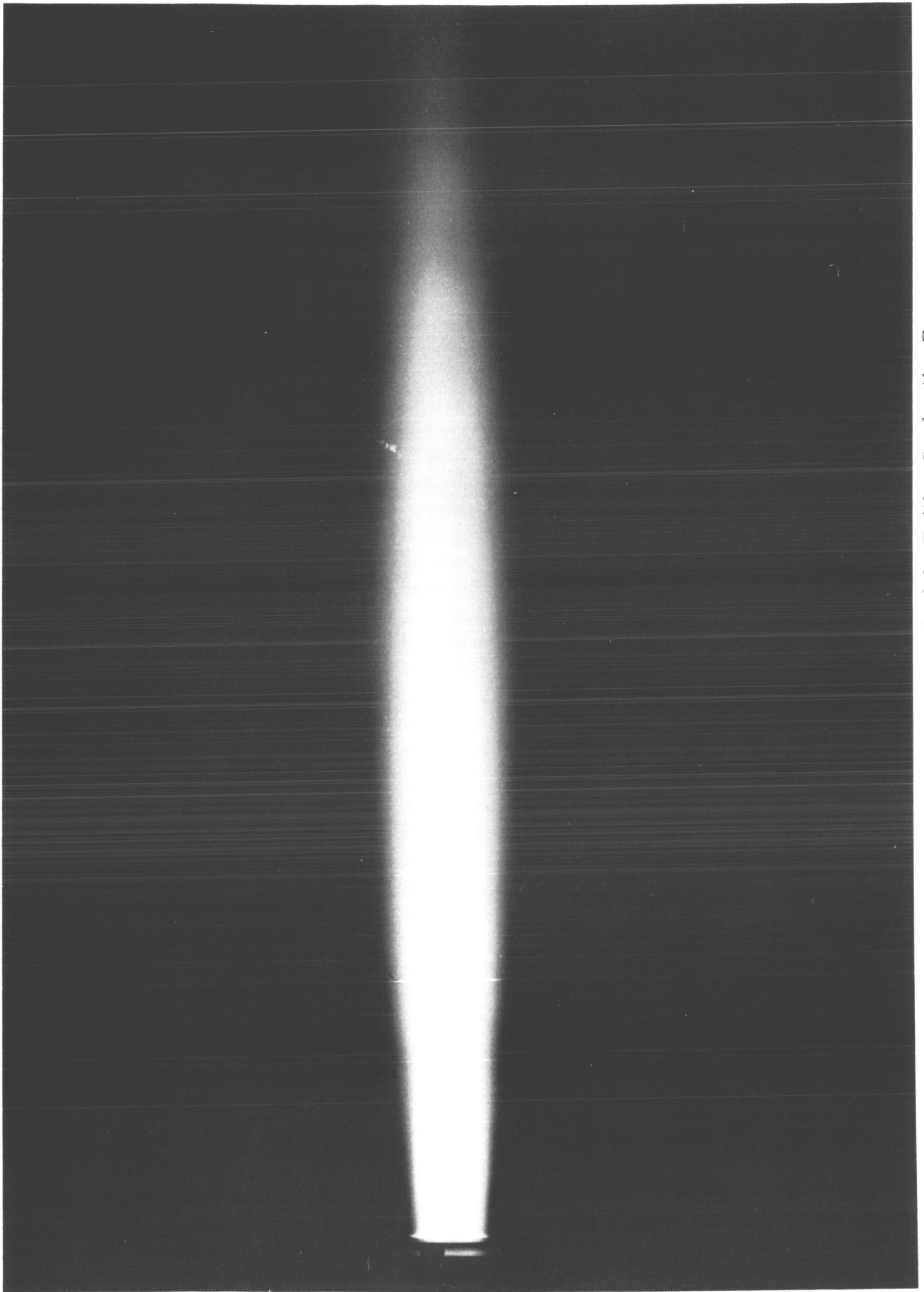


Figure 76. UV Photograph of the Exiting Combustion Zone  
 $T_a = 3105^\circ\text{R}$  - Cold Hydrogen -  $\phi = 1.0$

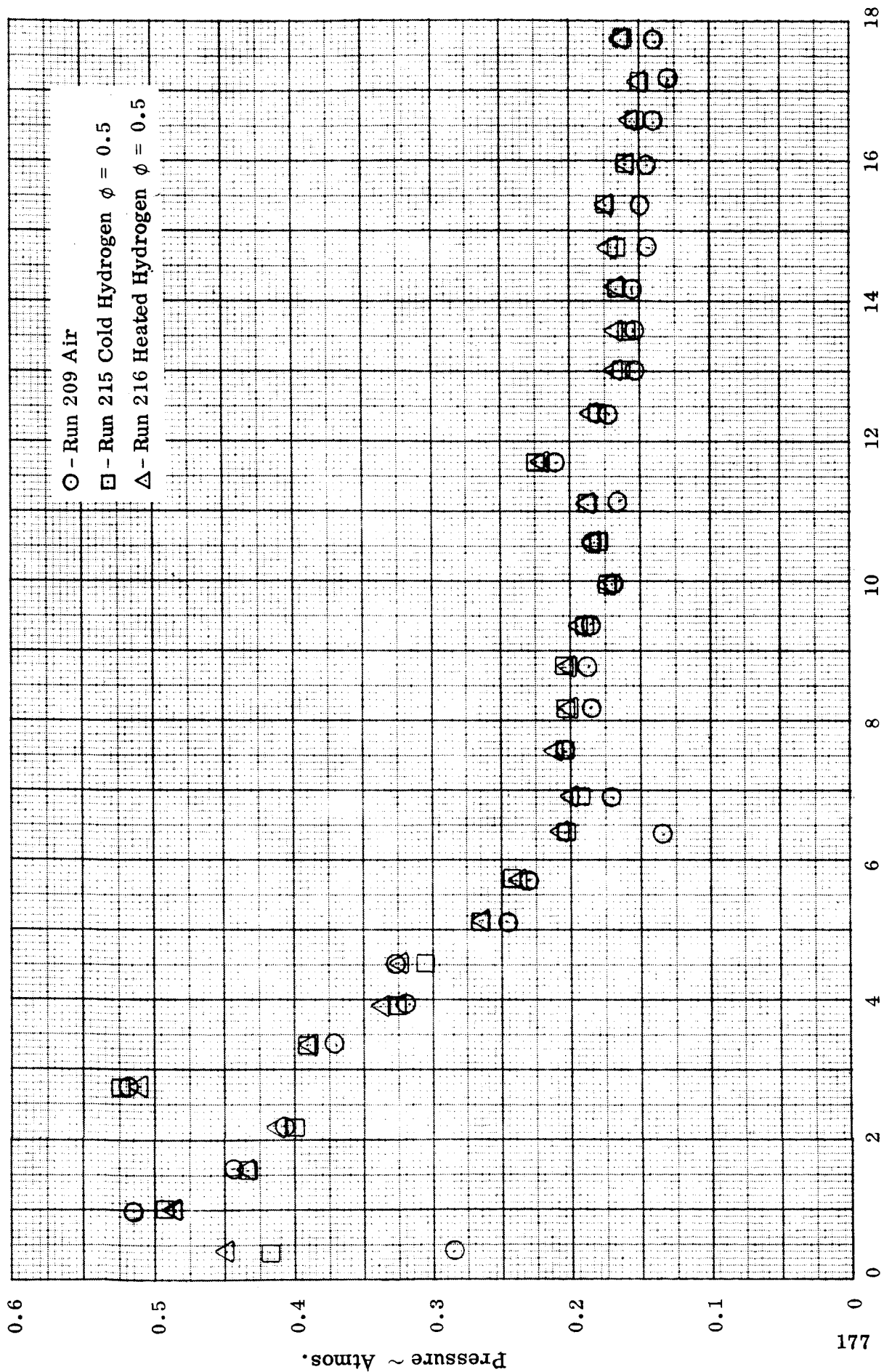


Figure 77. Pressure Distribution Inside Segmented Combustor - Air Temperature = 2700°R -  $\phi = 0.5$   
(Modified Combustor)

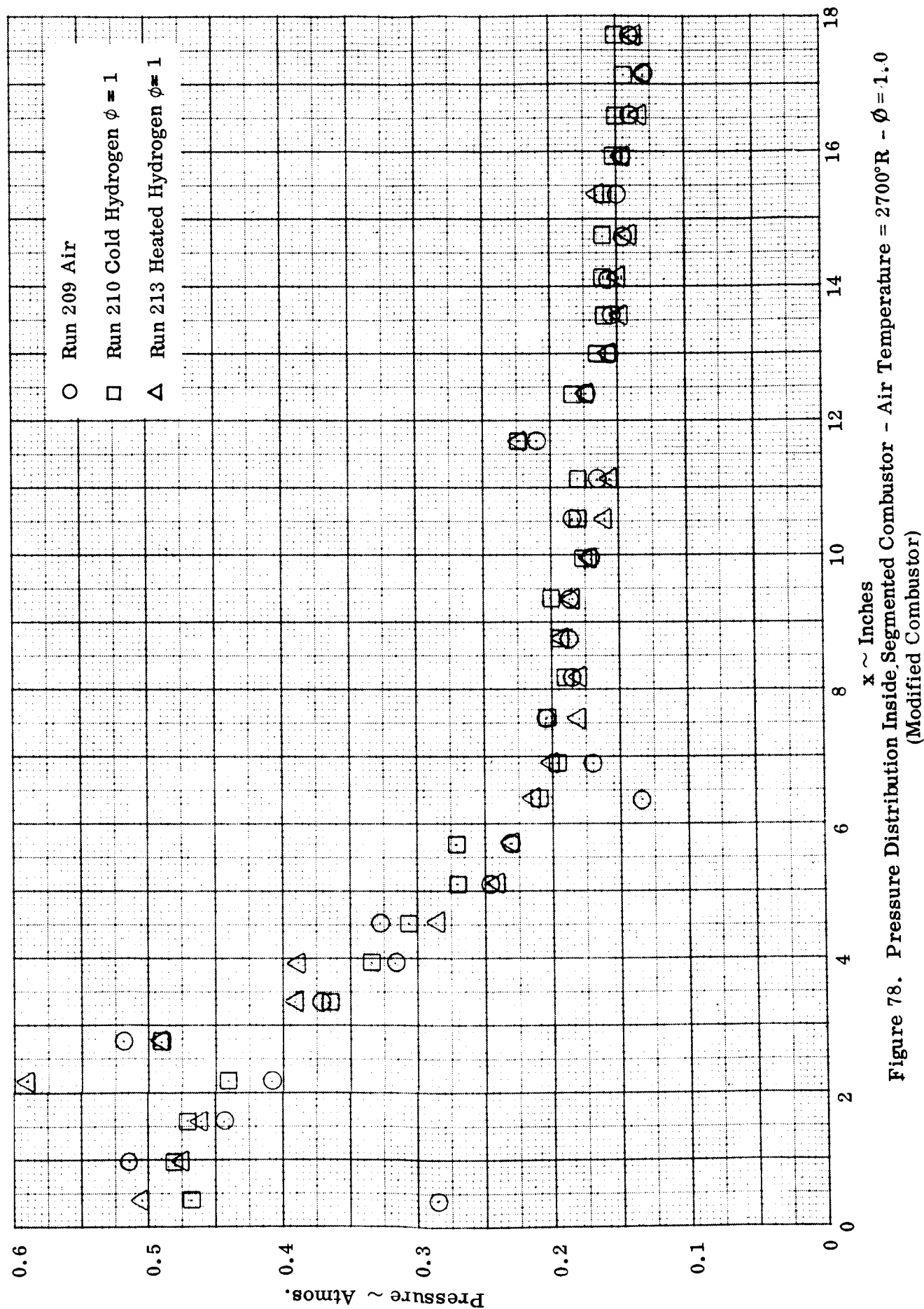


Figure 78. Pressure Distribution Inside Segmented Combustor - Air Temperature = 2700°R -  $\phi = 1.0$   
(Modified Combustor)

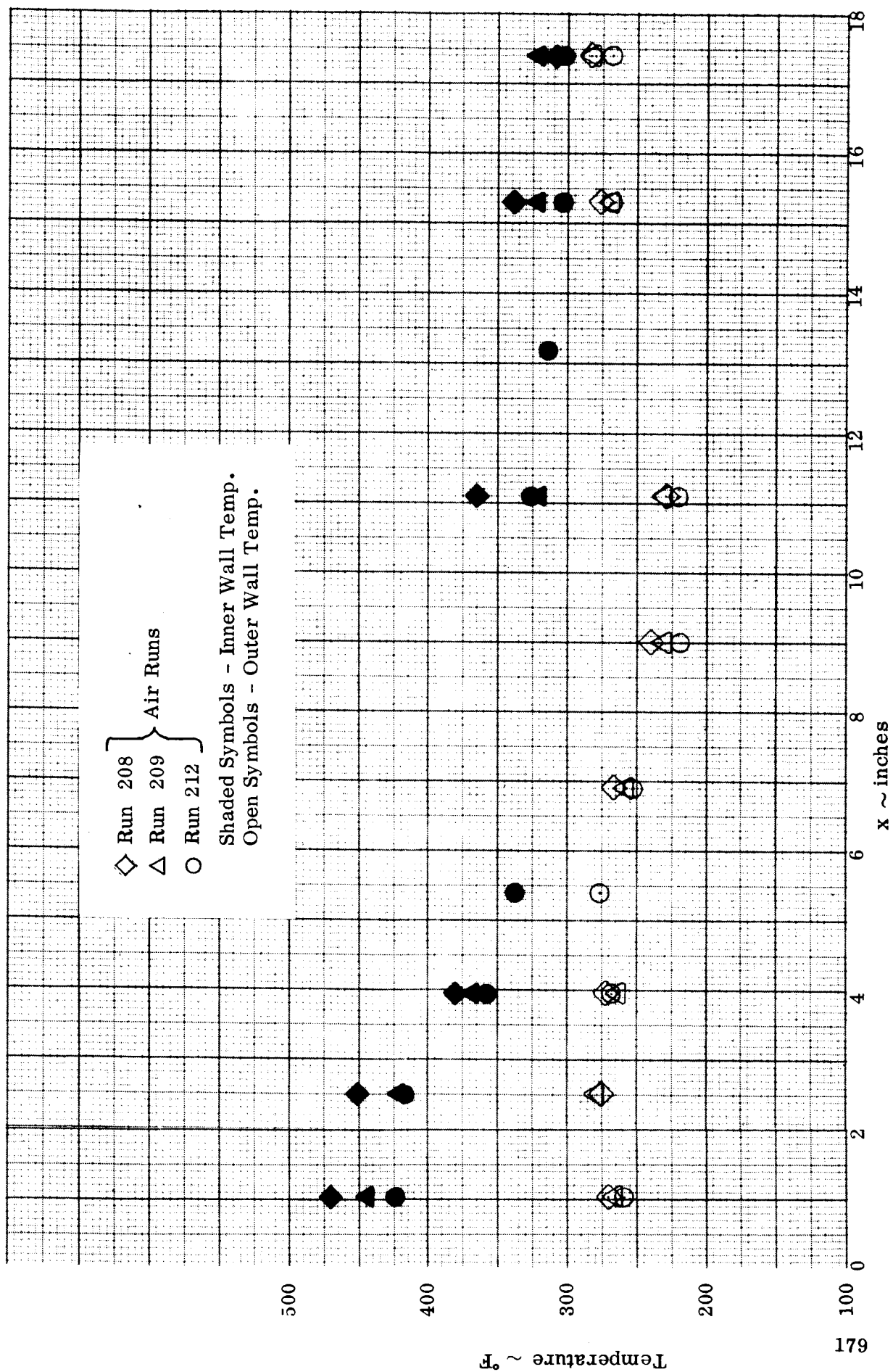


Figure 79. Temperature Distribution in Segmented Combustor - 2700°R Air Runs

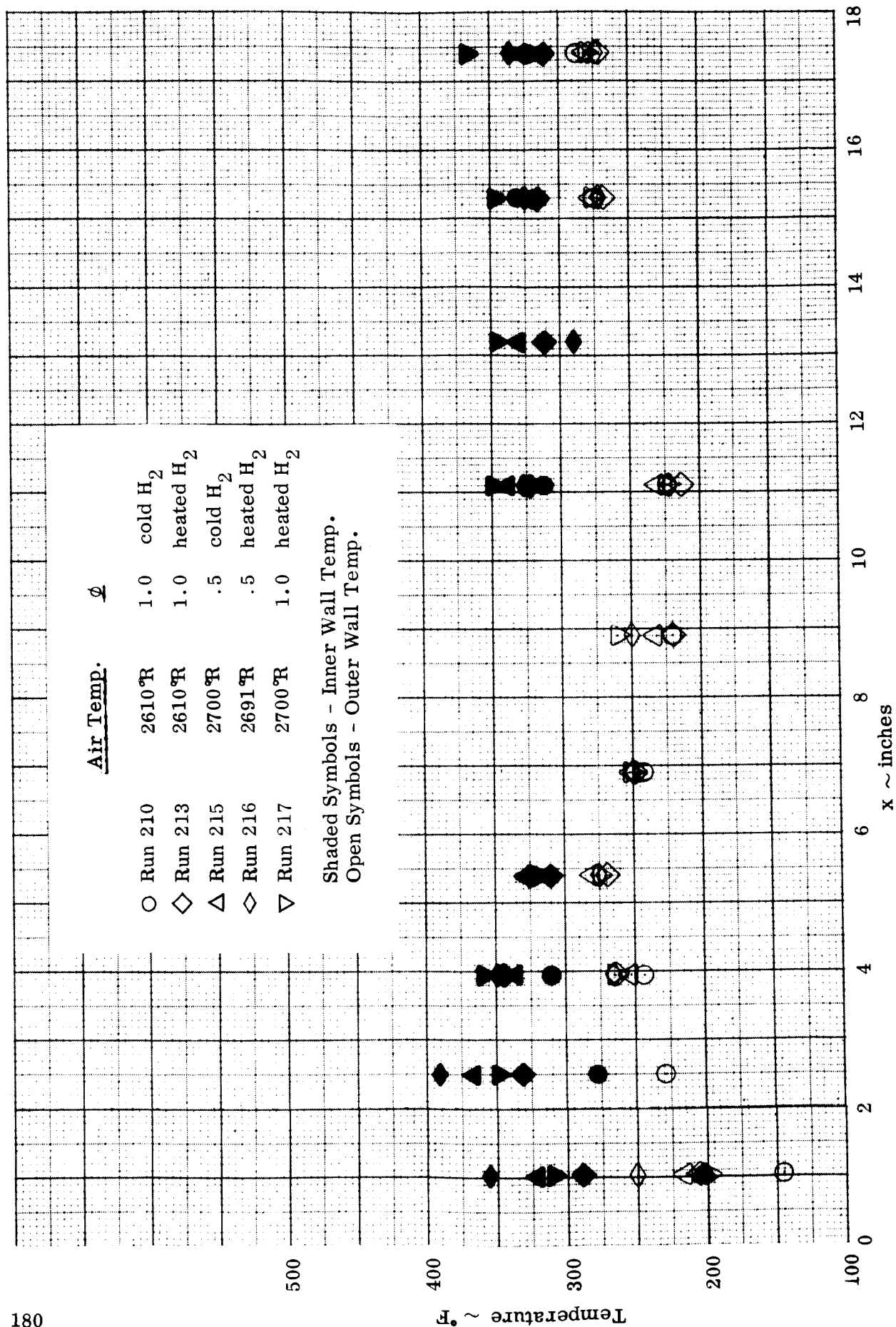


Figure 80. Temperature Distribution in Segmented Combustor - Hydrogen Runs

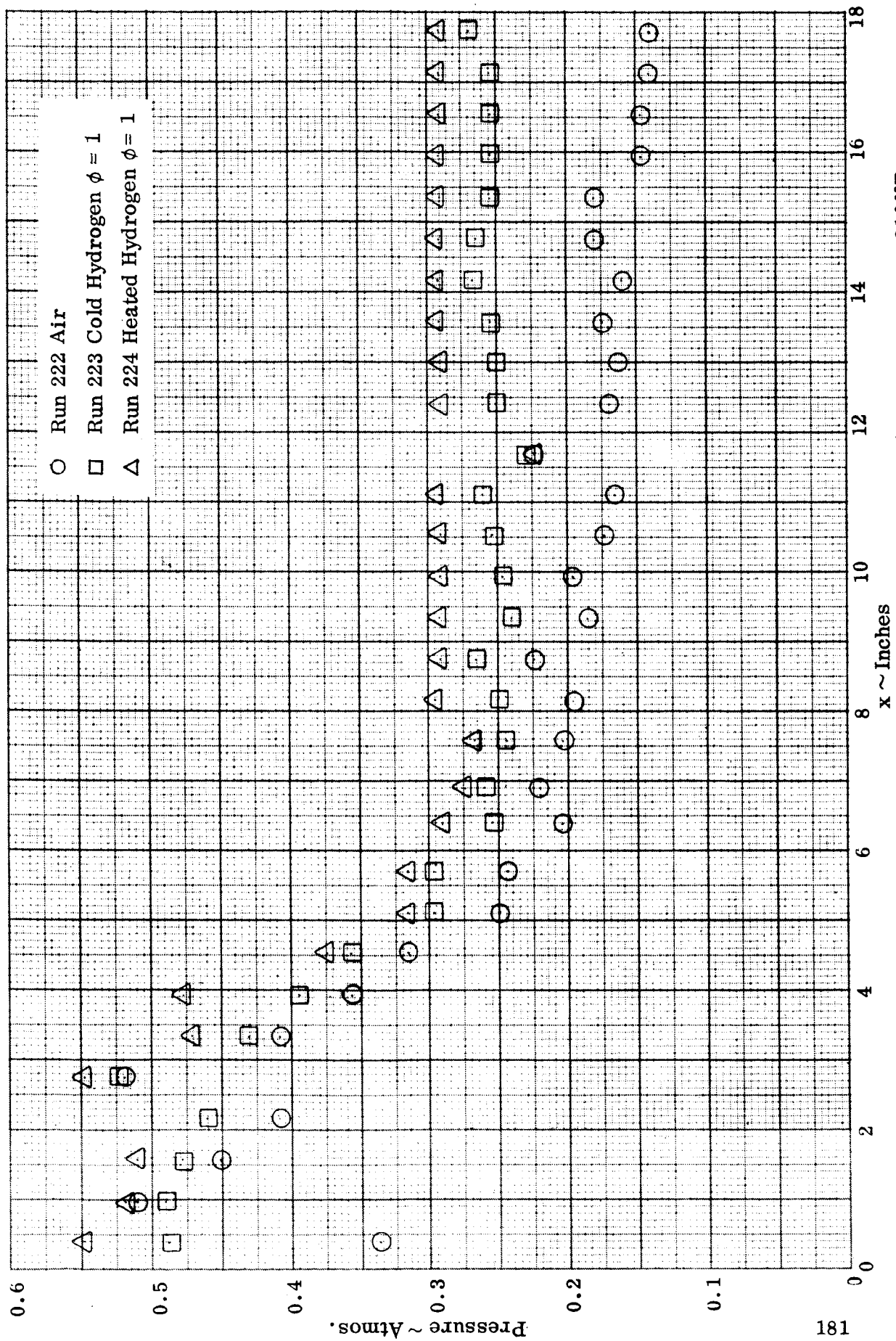


Figure 81. Pressure Distribution Inside Segmented Combustor - Air Temperature = 3100°R  
(Modified Combustor)

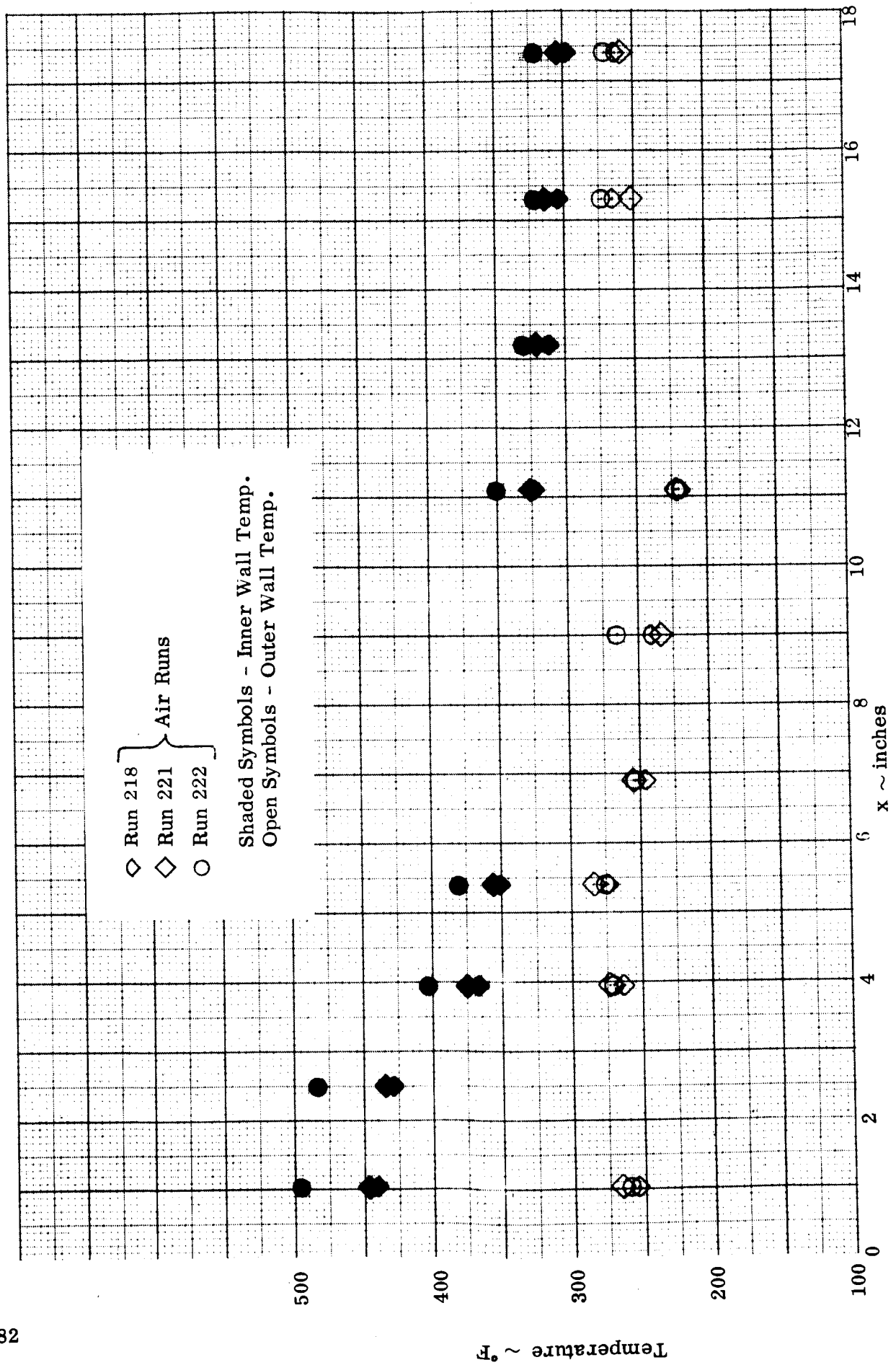


Figure 82. Temperature Distribution in Segmented Combustor - 3100°R Air Runs



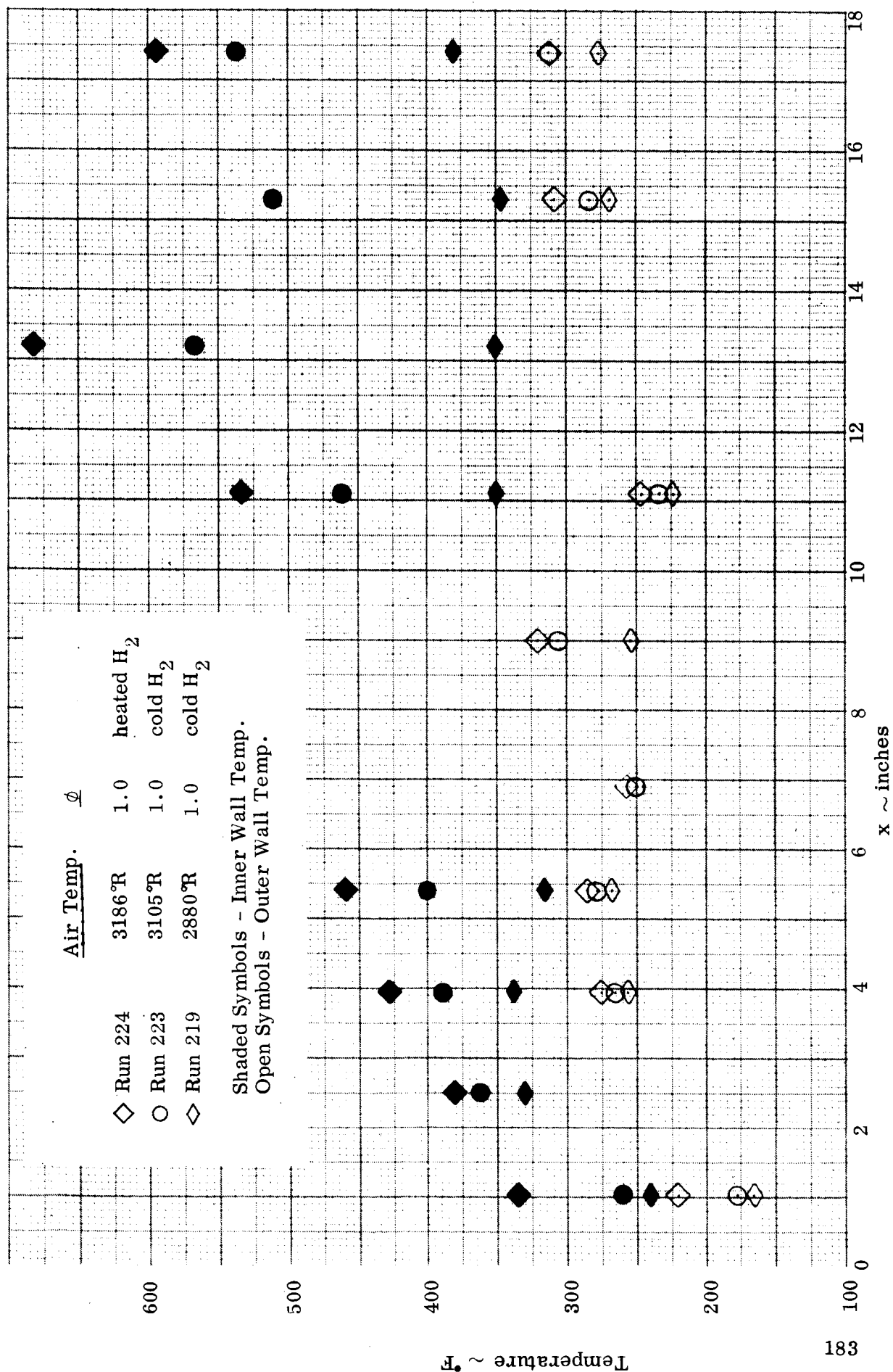


Figure 83. Temperature Distribution in Segmented Combustor - Hydrogen Runs

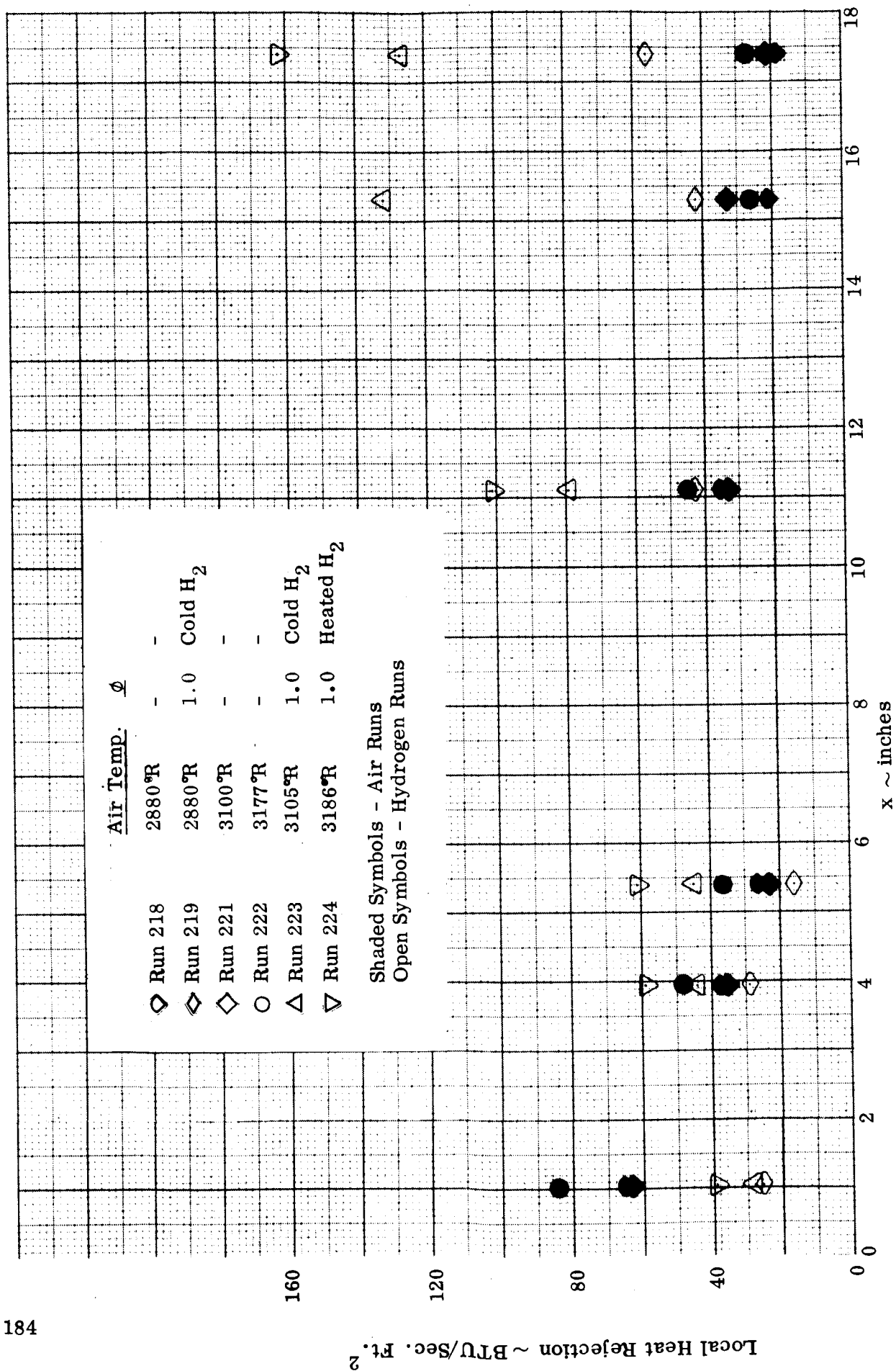


Figure 84.: Local Heat Rejection Distribution in Segmented Combustor - Second Combustor

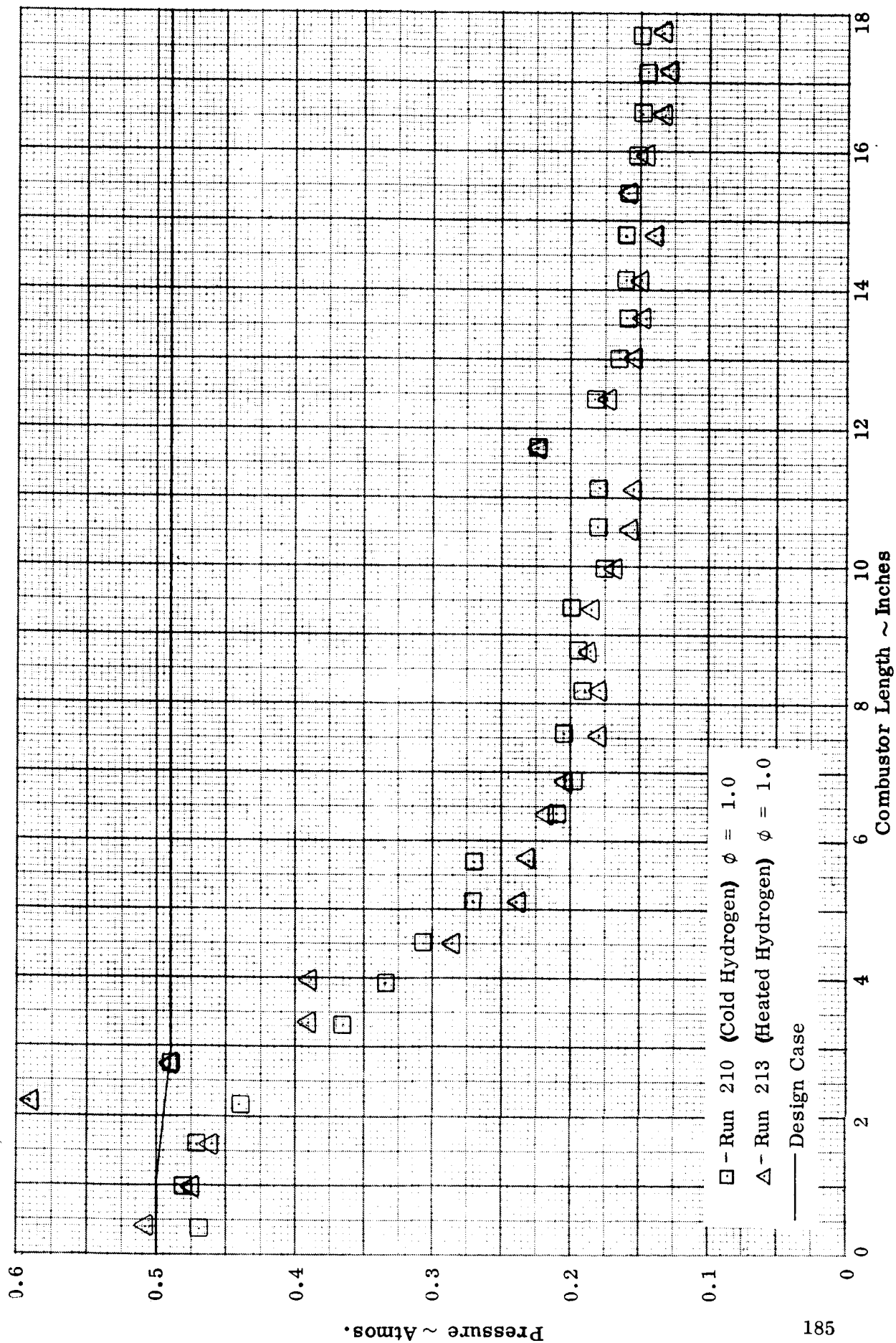


Figure 85. Comparison of Pressure Data for the 2700°R Modified Combustor Tests

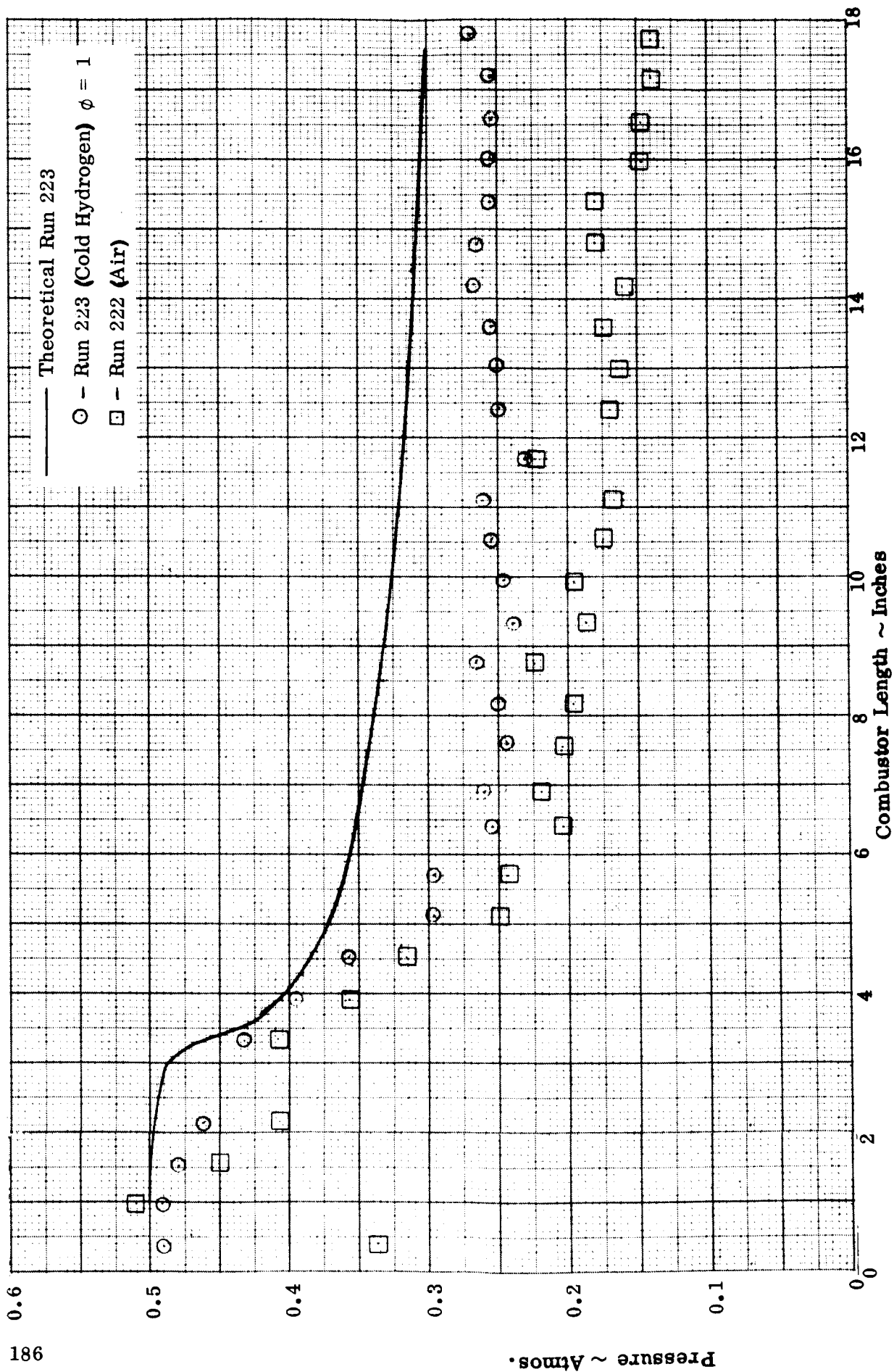


Figure 86.. Comparison of Pressure Data for the 3100°R Modified Combustor Tests (Cold Hydrogen)

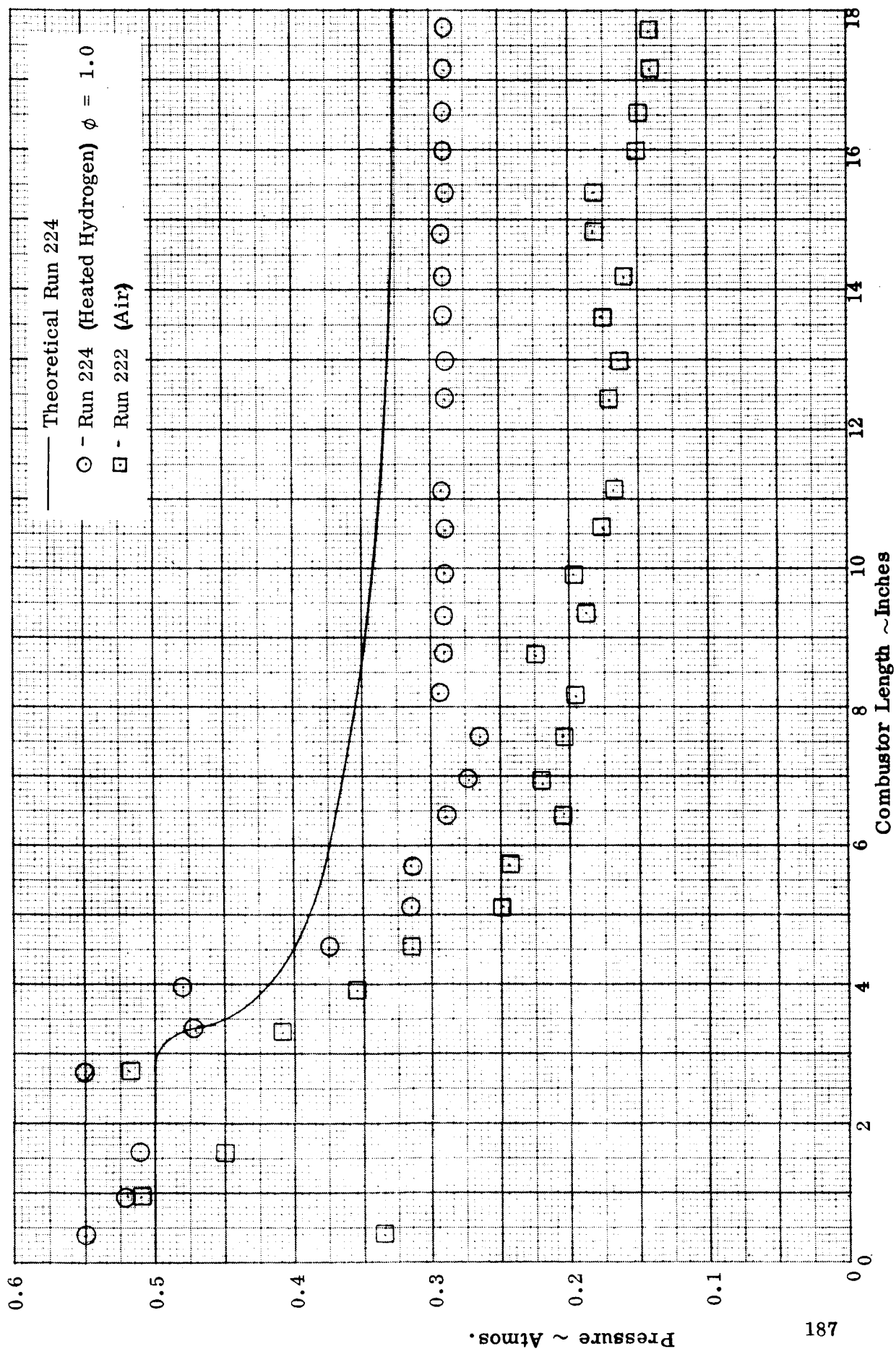


Figure 87. Comparison of Pressure Data for the 3100°R Modified Combustor Tests (Heated Hydrogen)

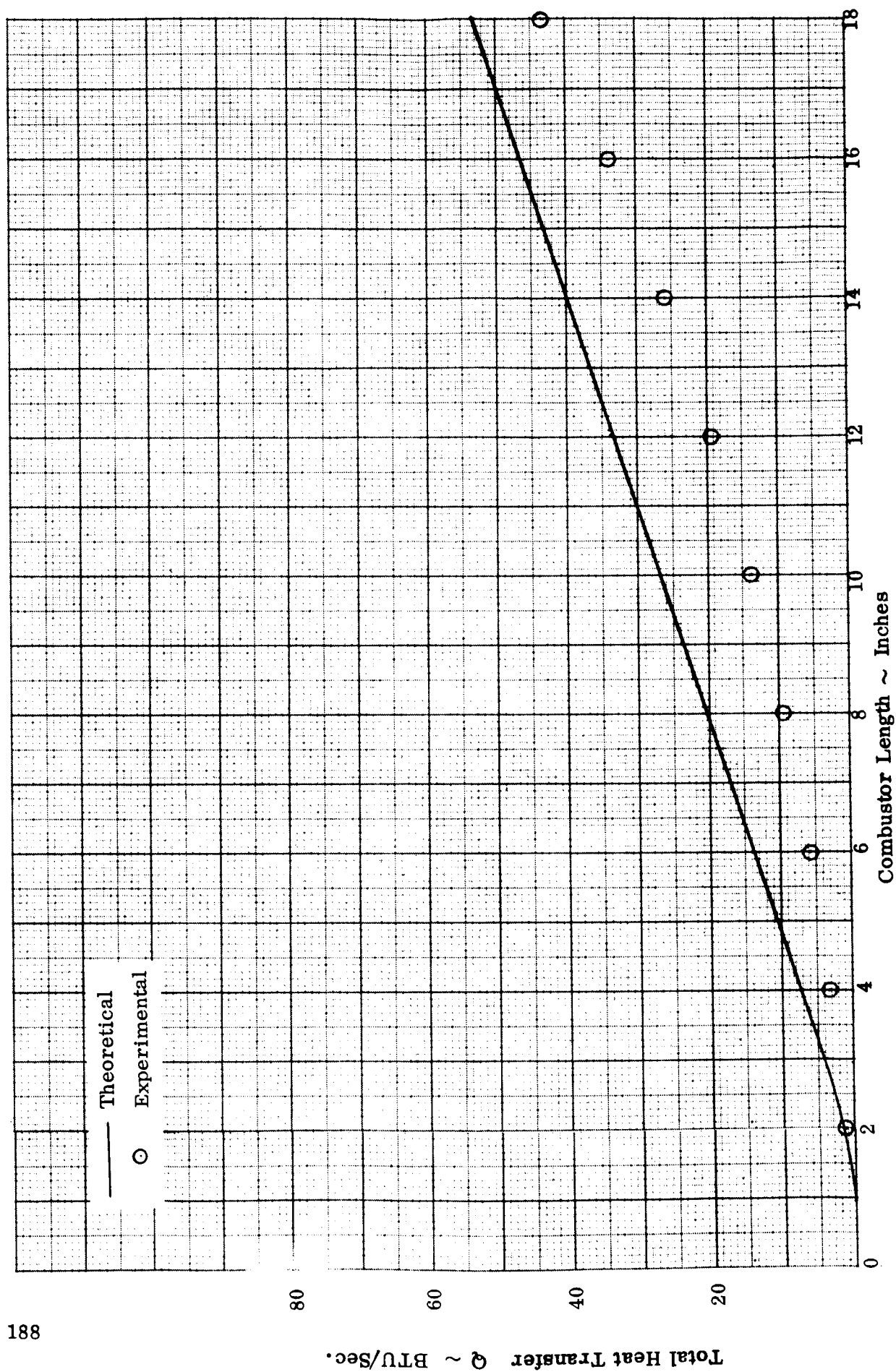


Figure 88. Comparison of Total Heat Transfer Data for a  $T_a = 3100^\circ\text{R}$ ,  $\phi = 1.0$ , Cold Hydrogen Test Run

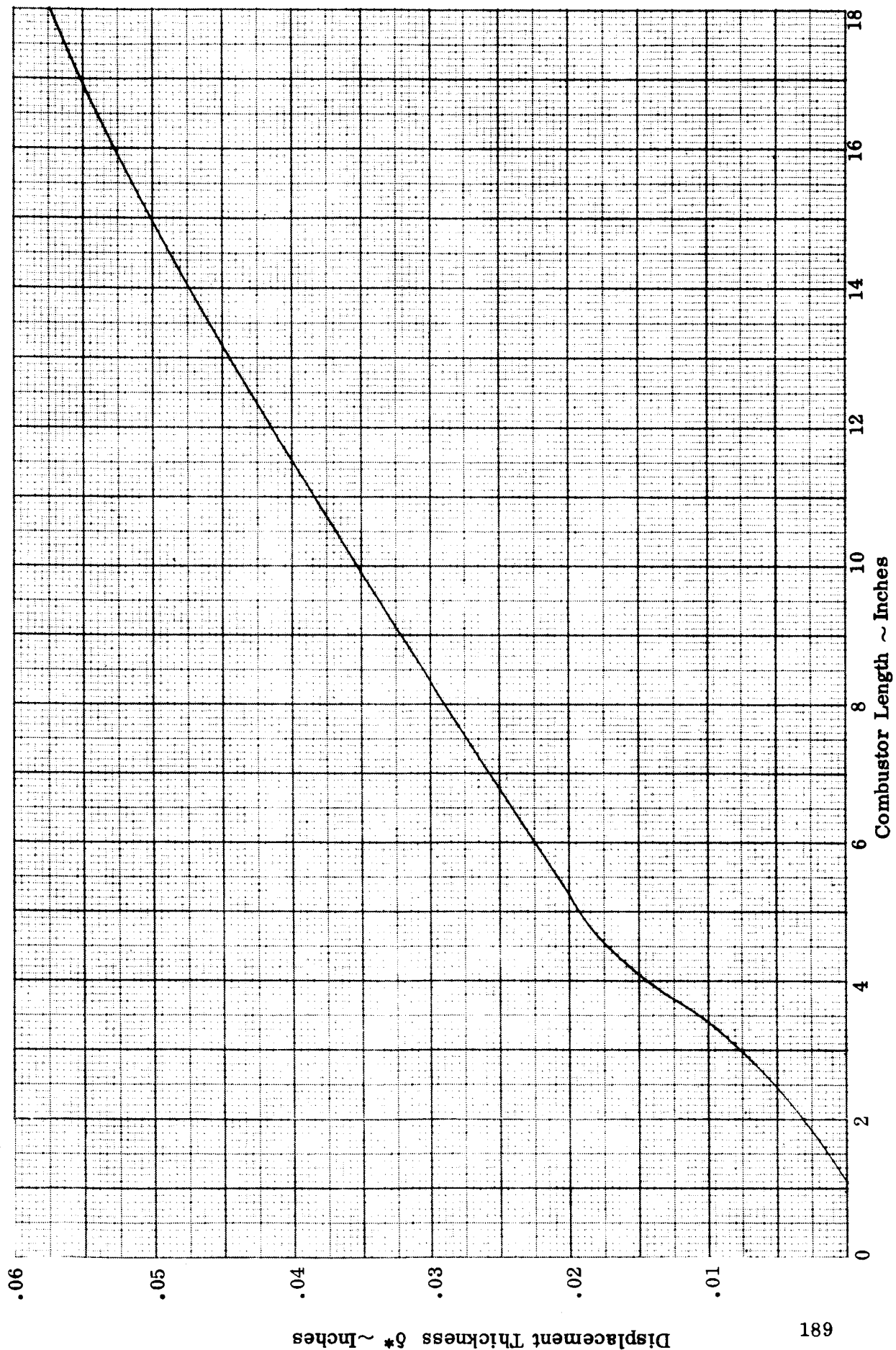


Figure 89. . Displacement Thickness Distribution for the Same Test as in Figure 88



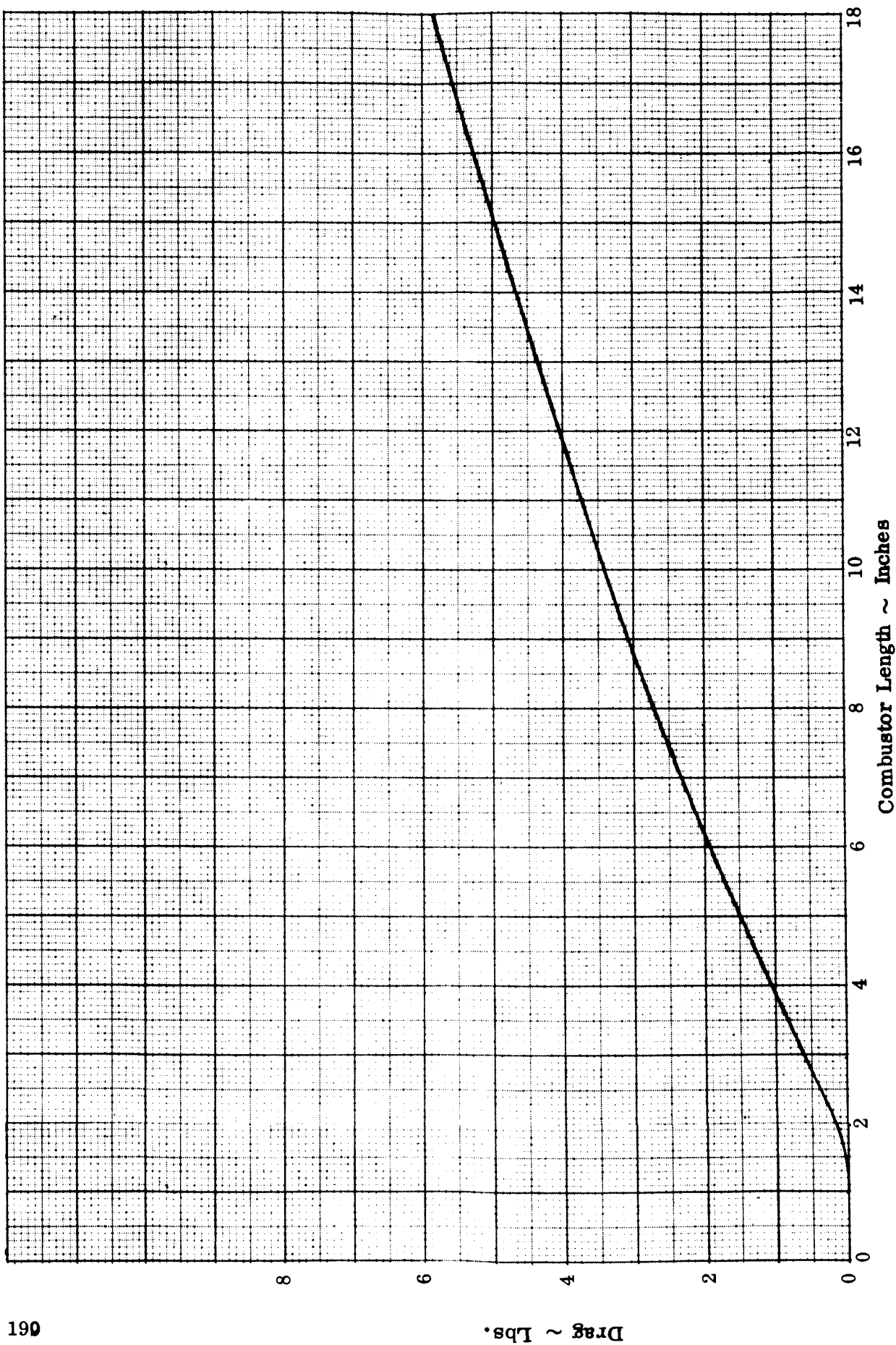


Figure 90. . Total Skin Friction Drag for the Same Test as in Figure 88



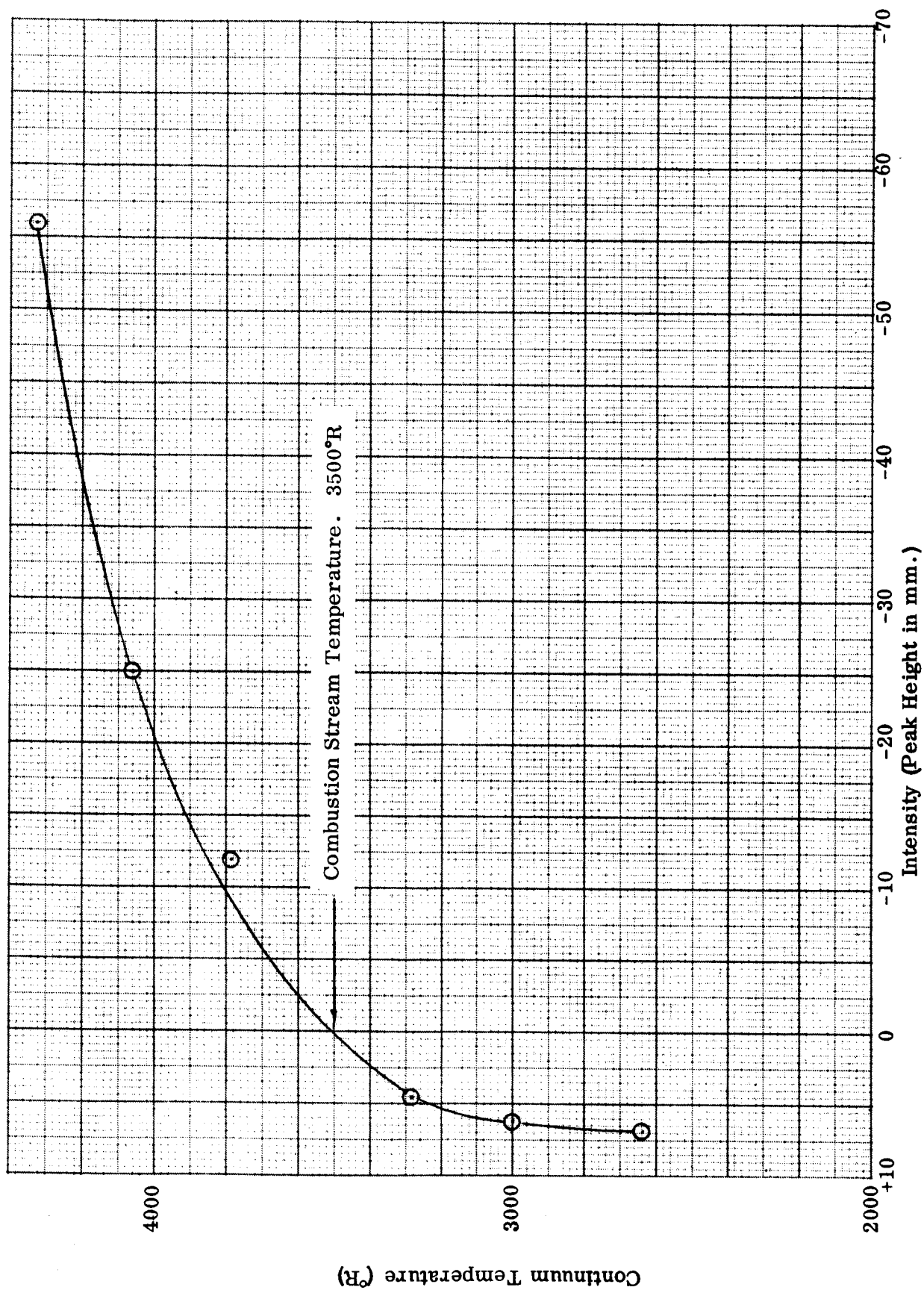


Figure 91. . Plot of Sodium Line Reversal Data for Temperature Determination

**APPENDIX F**  
**EXPERIMENTAL DATA**

A complete record of the experimental test data is presented in the following tables. This information has been included for completeness of presentation.

# EXPERIMENTAL DATA

PAGE 1  
REPORT NO. \_\_\_\_\_  
MODEL \_\_\_\_\_

PREPARED \_\_\_\_\_  
CHECKED \_\_\_\_\_  
REVISED \_\_\_\_\_



1	2	3	4	5	6	7	8	9	10	11	12	13	14	15	16	17	18	19	20	21
RUN#	MASS FLOW N <sub>2</sub>	MASS FLOW O <sub>2</sub>	H <sub>2</sub> OT	Ta	Totau	P <sub>0</sub>	P <sub>25V</sub>	P <sub>TRAC</sub>	MASS FLOW H <sub>2</sub>	T <sub>300V</sub>	P <sub>t</sub>	V <sub>1</sub> /V <sub>2</sub>	INJECT. CONFIG	PROBE POSITION	P <sub>PILOT</sub>	P <sub>BOTTLE</sub>	HEIGHT OF H <sub>2</sub> O	HEIGHT OF NO <sub>2</sub>		
	28/41V	28/41V	28/41V	28/41V	28/41V	28/41V	28/41V	28/41V	28/41V	28/41V	28/41V	28/41V	28/41V	28/41V	28/41V	28/41V	28/41V	28/41V	28/41V	28/41V
35	11.65	3.81	1307	2596	4350	1.50	0.92	0.50	0.102	0.00	0.601	0.4193	3 1/2" H <sub>2</sub>	1M	—	—	—	—	—	—
36	12.4	3.30	1207	2476	3771	0.50	0.95	0.50	0.102	0.00	0.598	0.4330	—	—	—	—	—	—	—	—
37	10.85	3.0	1353	2700	4602	0.50	0.95	0.50	0.102	0.00	0.614	0.4553	—	—	—	—	—	—	—	—
38B	11.4	3.65	1204	2245	4632	0.50	0.92	0.50	0.102	0.00	0.625	0.4605	—	—	—	—	—	—	—	—
39A	10.89	3.23	1322	2646	4054	0.50	0.92	0.50	0.102	0.00	0.630	0.4635	3 1/2" H <sub>2</sub>	40	—	0.414	—	—	—	—
40A	12.7	3.72	1046	2084	3778	0.50	0.92	0.50	0.102	0.00	—	—	3 1/2" H <sub>2</sub>	—	—	—	—	—	—	—
40B	12.7	3.72	1046	2084	3778	0.50	0.92	0.50	0.102	0.00	—	—	3 1/2" H <sub>2</sub>	—	—	—	—	—	—	—
40C	11.61	3.63	1225	2394	4320	0.50	0.92	0.50	0.102	0.00	0.605	0.4578	—	—	—	—	—	—	—	—
40D	11.61	3.77	1265	2502	4421	0.50	0.92	0.50	0.102	0.00	0.624	0.4603	—	—	—	—	—	—	—	—
40E	11.61	3.77	1342	2486	4356	0.50	0.92	0.50	0.102	0.00	—	—	—	—	—	—	—	—	—	—
41A	11.0	3.26	1391	2336	4788	0.50	0.92	0.50	0.102	0.00	—	—	—	—	—	—	—	—	—	—
41B	11.0	3.26	1407	2722	4806	0.50	0.92	0.50	0.102	0.00	0.610	0.4633	—	—	—	—	—	—	—	—
41C	11.61	3.69	1196	2340	4248	0.50	0.92	0.50	0.102	0.00	0.574	0.4603	—	—	—	—	—	—	—	—
42A	11.15	3.04	1341	2691	4635	0.50	0.92	0.50	0.102	0.00	—	—	—	—	—	—	—	—	—	—
42B	10.85	3.62	1350	2373	4626	0.50	0.92	0.50	0.102	0.00	0.588	0.4507	—	17 1/2	—	0.289	—	—	—	—
42C	11.62	3.64	1350	2373	4626	0.50	0.92	0.50	0.102	0.00	0.559	0.4360	—	—	—	—	—	—	—	—
43A	11.0	3.21	1346	2727	4700	0.50	0.92	0.50	0.102	0.00	—	—	—	—	—	—	—	—	—	—
43B	11.0	3.21	1346	2727	4700	0.50	0.92	0.50	0.102	0.00	0.574	0.4363	—	—	—	—	—	—	—	—
44A	10.2	2.82	1641	3222	5205	0.50	0.92	0.50	0.102	0.00	—	—	—	—	—	—	—	—	—	—
44B	10.2	2.82	1641	3222	5205	0.50	0.92	0.50	0.102	0.00	0.616	0.4578	—	17 1/2	—	—	—	—	—	—
45A	11.0	3.27	1368	2700	4635	0.50	0.92	0.50	0.102	0.00	—	—	—	—	—	—	—	—	—	—
45B	11.0	3.27	1368	2700	4635	0.50	0.92	0.50	0.102	0.00	0.598	0.4330	—	—	—	—	—	—	—	—
46	10.85	3.27	1411	2700	4779	0.50	0.92	0.50	0.102	0.00	0.616	0.4330	—	—	—	—	—	—	—	—
47	10.85	3.27	1411	2700	4779	0.50	0.92	0.50	0.102	0.00	—	—	—	—	—	—	—	—	—	—
48	—	—	—	—	—	—	—	—	—	—	—	—	—	—	—	—	—	—	—	—
49	10.85	3.48	1407	2700	4779	0.50	0.92	0.50	0.102	0.00	0.558	0.4175	—	—	—	—	—	—	—	—
50A	10.85	3.26	1430	2608	4760	0.50	0.92	0.50	0.102	0.00	—	—	—	—	—	—	—	—	—	—
50B	10.85	3.19	1407	2700	4779	0.50	0.92	0.50	0.102	0.00	0.554	0.4630	—	—	—	—	—	—	—	—
51	11.62	3.30	1202	2358	4248	0.50	0.92	0.50	0.102	0.00	0.554	0.4175	—	—	—	—	—	—	—	—

NOT 10W \*\* 34 10W

0.1732 1.04

PREPARED

CHECKED

REVISED



1	2	3	4	5	6	7	8	9	10	11	12	13	14	15	16	17	18	19	20	21
RUN #	(NO) RUN	$X_{H_2}$	$X_{O_2}$	$X_{H_2}$	THICK	LOCATION OF MEAS. STRAIN	$\bar{L}_0$	$\bar{A}_0$	STRESS TIME							REMARKS				
		(GAS SAMPLING DATA)																		
30					OP	IN	IN	IN	SEC.											
36							17.2	2.85	1											
37							18.10	3.31	10											
38							15.04	3.9	10											
39							18.6	3.2	5											
40							16.6	2.7	1											
41																				
42																				
43																				
44																				
45																				
46																				
47																				
48																				
49																				
50																				
51																				
52																				
53																				
54																				
55																				
56																				
57																				
58																				
59																				
60																				
61																				
62																				
63																				
64																				
65																				
66																				
67																				
68																				
69																				
70																				
71																				
72																				
73																				
74																				
75																				
76																				
77																				
78																				
79																				
80																				
81																				
82																				
83																				
84																				
85																				
86																				
87																				
88																				
89																				
90																				
91																				
92																				
93																				
94																				
95																				
96																				
97																				
98																				
99																				
100																				

HOT H<sub>2</sub> TOO LONG TO HEAT  
 WATER "H<sub>2</sub>O" REACTION PIECE  
 AFTER H<sub>2</sub> RUN - BEFORE H<sub>2</sub> RUN  
 H<sub>2</sub> WATER IN ANOMETER LINES



FAIRCHILD HILLER  
REPUBLIC AVIATION DIVISION  
10000 10000 10000 10000

PREPARED  
CHECKED  
REVISED

REPORT NO.  
MODEL

1	2	3	4	5	6	7	8	9	10	11	12	13	14	15	16	17	18	19	20	21
NUMBER	INSTRUMENT	$X_{H_2}$	$X_{O_2}$	$X_{H_2}$	TIME	ALTIMETER READING STATION	$L_p$	$L_d$	EXPOSURE TIME								REMARKS			
52					22	14.	14.	14.	SEC.								A.G. CATER LENA			
52A		0.047	0.117	0.130	—		16.95	3.78	10											
52B																				
52C																				
53							15.0	2.98	10											
54																				
55		—	0.140	0.150	—															
56		—	0.137	0.150	—		19.05	2.14	1.0											
57																				
↑																				
99																				
100																				
101		—	0.017	0.100	1200	13	21.7	5.75	1.0								MEASURED TEMP. MAY BE QUESTIONABLE			
102		—	0.115	0.165	2500	"	21.7	5.75	10								TEMPERATURE TO GAS COMPRESSOR 2500 BUREAU			
103A		—	0.145	0.150	3200	"											TEMP. MAY BE N.E.			
103B		—	—	—	2900	"											NO GAS ANALYSIS DUE TO TROUBLE IN 1030			
104A		—	—	—	2800	"	16.4	3.35	10								BOTTLE MAPPED C. CLOUTIER DUE TO NO GAS IN LINE			
104B		—	0.115	0.175	2910	"	17.25	3.6	10											
105A		—	0.138	0.133	2760	"	16.0	2.0	5											
105B		—	0.145	0.137	2380	"	16.11	1.89	5								MANUALLY RUGGED			
106A		—	—	—	—															
106B		—	0.015	0.120	—	16.5	16.30	2.41	1.0											
107		—	—	—	4250	"	16.27	2.5	1.0								NO GAS ANALYSIS			
101		—	0.160	0.152	3920	—	16.85	1.82	1.0											

FAIRCHILD HILLER  
AIRCRAFT CORPORATION  
AIRCRAFT DIVISION  
MEMPHIS, TENNESSEE, U.S.A.

PREPARED  
CHECKED  
REVISED

PAGE 5  
REPORT NO.  
MODEL

1	2	3	4	5	6	7	8	9	10	11	12	13	14	15	16	17	18	19	20	21
Run #	Mass Flow N <sub>2</sub>	Mass Flow O <sub>2</sub>	H <sub>2</sub> O	T <sub>0</sub>	T <sub>in</sub>	P <sub>0</sub>	P <sub>in</sub>	P <sub>stat</sub>	Mass Flow H <sub>2</sub>	T <sub>02</sub>	P <sub>02</sub>	V <sub>1/2</sub>	Wet. Comp.	Probe Position	P <sub>in</sub>	P <sub>stat</sub>	Weight of H <sub>2</sub> O	Weight of NO <sub>x</sub>		
	20/1000	20/1000	20/1000	"	"	ATMOS	ATMOS	ATMOS	20/1000	"	ATMOS	"	"	"	"	"	"	"	"	"
109	12.071	3.719	12.06	2023	3720	0.500	7.122	0.500	"	"	"	"	AIR	"	"	"	"	"	"	"
110A	11.043	3.334	12.16	2001	4520	"	6.918	"	0.1106	660	0.6068	"	AIR	16.5	"	"	"	"	"	"
110B	11.076	3.413	13.14	2635	4354	"	7.054	"	0.1112	1010	0.6333	"	"	"	"	"	"	"	"	"
111A	11.033	3.320	11.50	2046	4104	"	7.150	"	0.1436	570	0.6061	"	"	"	"	"	"	"	"	"
111B	12.082	3.105	11.59	2268	4050	"	"	"	"	1020	0.6701	"	"	"	"	"	"	"	"	"
112	11.045	3.538	12.48	2313	4122	0.444	6.578	"	"	"	"	"	AIR	"	"	"	"	"	"	"
113	12.032	3.191	8.89	1746	3916	0.500	6.646	"	0.1112	585	0.6025	0.318	AIR	16.5	"	0.50	14.5	0.552	"	"
114A	11.177	3.360	13.30	2054	4626	0.492	7.034	"	"	1045	0.6645	0.636	"	"	"	"	23.0	0.322	"	"
114B	11.212	3.607	12.93	2583	4545	0.494	"	"	0.1511	620	0.6011	0.4930	"	"	"	0.50	9.5	0.184	"	"
115A	11.054	3.475	10.70	2060	3818	0.500	6.626	"	0.1190	1020	0.6734	0.7341	"	"	"	"	43.0	0.46	"	"
115B	11.134	3.475	11.54	2304	4122	0.492	6.714	"	0.1190	570	0.6258	"	AIR	17.5	"	"	"	"	"	"
116	12.376	3.696	10.24	2043	3717	0.495	6.446	"	0.1992	570	0.6282	0.4644	"	"	"	0.50	26.5	0.23	"	"
117A	12.332	3.654	10.60	2115	3716	0.502	7.054	"	"	1030	0.6814	0.1034	"	"	"	0.50	15.6	0.276	"	"
117B	12.402	3.755	10.49	2070	3710	"	"	"	"	"	"	"	AIR	"	"	"	"	"	"	"
118A	11.034	3.316	13.38	2664	4644	0.497	"	"	0.1106	630	0.6077	0.3926	AIR	17.5	"	1.0	26.0	0.552	"	"
118B	11.076	3.459	13.59	2720	4610	"	"	"	0.1224	1040	0.6653	0.6444	"	"	"	1.0	23.0	0.69	"	"
111C	11.274	3.462	13.20	2646	4572	0.500	"	"	"	"	"	"	AIR	"	"	"	"	"	"	"
119	12.278	3.886	10.09	2043	3604	0.504	6.916	0.516	"	"	"	"	AIR	"	"	"	"	"	"	"
120	12.281	3.814	10.11	2019	3726	0.505	7.054	0.500	"	"	"	"	AIR	"	"	"	"	"	"	"
120A	12.303	3.834	9.70	1971	3564	0.503	"	"	0.2051	640	0.5396	0.2912	AIR	5" down screen	"	1.272	"	"	"	"
121	12.266	3.827	10.54	2106	3798	0.487	7.238	"	0.2022	1000	0.6122	0.4724	"	"	"	0.50	"	"	"	"
121A	10.887	3.227	14.00	2781	4506	0.500	7.054	"	"	"	"	"	AIR	"	"	"	"	"	"	"
121B	10.936	3.227	13.47	2681	4632	0.500	"	"	0.1102	660	"	"	"	"	"	0.50	"	"	"	"
121C	10.936	3.224	13.34	2664	4614	0.492	"	"	0.1112	1010	0.5578	0.3716	"	"	"	0.50	"	"	"	"
122	12.352	3.718	10.97	2115	3715	0.495	7.170	"	"	"	"	"	AIR	"	"	"	"	"	"	"

000-410-000-111-0000

## Revision

[illegible]



FAIRCHILD HILLER  
REPUBLIC AVIATION DIVISION  
LITTLE FALLS, IOWA 51041, 51042, 51043

REPORT NO.

MODEL

1	2	3	4	5	6	7	8	9	10	11	12	13	14	15	16	17	18	19	20	21
ITEM #	ITEM #	ITEM #	ITEM #	ITEM #	ITEM #	ITEM #	ITEM #	ITEM #	ITEM #	ITEM #	ITEM #	ITEM #	ITEM #	ITEM #	ITEM #	ITEM #	ITEM #	ITEM #	ITEM #	ITEM #
123	123	123	123	123	123	123	123	123	123	123	123	123	123	123	123	123	123	123	123	123
124	124	124	124	124	124	124	124	124	124	124	124	124	124	124	124	124	124	124	124	124
125	125	125	125	125	125	125	125	125	125	125	125	125	125	125	125	125	125	125	125	125
126	126	126	126	126	126	126	126	126	126	126	126	126	126	126	126	126	126	126	126	126
127	127	127	127	127	127	127	127	127	127	127	127	127	127	127	127	127	127	127	127	127
128	128	128	128	128	128	128	128	128	128	128	128	128	128	128	128	128	128	128	128	128
129	129	129	129	129	129	129	129	129	129	129	129	129	129	129	129	129	129	129	129	129
130	130	130	130	130	130	130	130	130	130	130	130	130	130	130	130	130	130	130	130	130
131	131	131	131	131	131	131	131	131	131	131	131	131	131	131	131	131	131	131	131	131
132	132	132	132	132	132	132	132	132	132	132	132	132	132	132	132	132	132	132	132	132
133	133	133	133	133	133	133	133	133	133	133	133	133	133	133	133	133	133	133	133	133
134	134	134	134	134	134	134	134	134	134	134	134	134	134	134	134	134	134	134	134	134
135	135	135	135	135	135	135	135	135	135	135	135	135	135	135	135	135	135	135	135	135
136	136	136	136	136	136	136	136	136	136	136	136	136	136	136	136	136	136	136	136	136
137	137	137	137	137	137	137	137	137	137	137	137	137	137	137	137	137	137	137	137	137
138	138	138	138	138	138	138	138	138	138	138	138	138	138	138	138	138	138	138	138	138
139	139	139	139	139	139	139	139	139	139	139	139	139	139	139	139	139	139	139	139	139
140	140	140	140	140	140	140	140	140	140	140	140	140	140	140	140	140	140	140	140	140
141	141	141	141	141	141	141	141	141	141	141	141	141	141	141	141	141	141	141	141	141
142	142	142	142	142	142	142	142	142	142	142	142	142	142	142	142	142	142	142	142	142
143	143	143	143	143	143	143	143	143	143	143	143	143	143	143	143	143	143	143	143	143
144	144	144	144	144	144	144	144	144	144	144	144	144	144	144	144	144	144	144	144	144
145	145	145	145	145	145	145	145	145	145	145	145	145	145	145	145	145	145	145	145	145
146	146	146	146	146	146	146	146	146	146	146	146	146	146	146	146	146	146	146	146	146
147	147	147	147	147	147	147	147	147	147	147	147	147	147	147	147	147	147	147	147	147





**FAIRCHILD HILLER**  
REPUBLIC AVIATION DIVISION  
1400 BOWLING GREEN BLVD., ST. LOUIS, MO. 63104

—  
—  
—

Run #	1	2	3	4	5	6	7	8	9	10	11	12	13	14	15	16	17	18	19	20	21
		Impedance	$X_{H_2}$	$X_{O_2}$	$X_{H_2}$	Thms	4. Critical W. or Heads Station														
																		REMARKS			
141			—	—	—	%	100														
149			—	0.120	0.150	3900	0.5"														
150			0.004	0.105	0.155	3160	0.5"														
151			—	—	—	—	—														
153			0.005	0.070	0.170	—	—											N/G. TEMPERATURE EXACTLY			
153			0.002	0.050	0.170	4030	0.5"											"	"	UNSTABLE	
154			—	—	—	—	—											N/G. TEMPERATURE EXACTLY			
155			—	—	—	—	—											N/G. TEMPERATURE EXACTLY			
156			—	—	—	—	—											N/G. TEMPERATURE EXACTLY			
157			—	—	—	—	—											N/G. TEMPERATURE EXACTLY			
158			—	—	—	—	—											N/G. TEMPERATURE EXACTLY			
159			—	0.110	0.105	—	0.5"											N/G. TEMPERATURE EXACTLY			
160			—	0.193	0.105	—	0.5"											N/G. TEMPERATURE EXACTLY			
161			—	—	—	—	—											N/G. TEMPERATURE EXACTLY			
162			—	—	—	—	—											N/G. TEMPERATURE EXACTLY			
163			—	—	—	—	—											N/G. TEMPERATURE EXACTLY			
164A			—	—	—	—	—											N/G. TEMPERATURE EXACTLY			
164B			—	—	—	—	—											N/G. TEMPERATURE EXACTLY			
165			—	—	—	—	—											N/G. TEMPERATURE EXACTLY			
166			—	—	—	—	—											N/G. TEMPERATURE EXACTLY			
167			—	0.140	0.150	3610	0.5"											N/G. TEMPERATURE EXACTLY			
168			—	—	—	—	—											N/G. TEMPERATURE EXACTLY			
169			—	—	—	—	—											N/G. TEMPERATURE EXACTLY			
170			—	—	—	—	—											N/G. TEMPERATURE EXACTLY			
171			—	0.110	0.110	3440	0.5"											N/G. TEMPERATURE EXACTLY			

1	2	3	4	5	6	7	8	9	10	11	12	13	14	15	16	17	18	19	20	21
RUN NO	WIND DIR	WIND SPEED	WIND DIR	WIND SPEED	WIND DIR	WIND SPEED	WIND DIR	WIND SPEED	WIND DIR	WIND SPEED	WIND DIR	WIND SPEED	WIND DIR	WIND SPEED	WIND DIR	WIND SPEED	WIND DIR	WIND SPEED	WIND DIR	WIND SPEED
1	11043	3403	1700	2745	4788	0.5711	7.18	0.3263	0.3263	6.25	0.4824	—	AIR	16.12	1.401	26.0	1.98	—	—	—
2	11048	3425	1734	2730	4780	0.5525	—	—	0.3260	6.25	0.4824	—	AIR	16.12	1.401	26.0	1.98	—	—	—
3	11054	3419	1731	2720	4781	—	—	—	0.3260	10.10	0.5576	—	AIR	—	—	13.10	2.10	1.66	—	—
4	11054	3421	1718	2718	4788	0.4987	7.22	—	—	—	—	—	AIR	—	—	—	—	—	—	—
5	11054	3421	1718	2718	4788	0.4987	7.22	—	—	—	—	—	AIR	—	—	—	—	—	—	—
6	11054	3421	1718	2718	4788	0.4987	7.22	—	—	—	—	—	AIR	—	—	—	—	—	—	—
7	11054	3421	1718	2718	4788	0.4987	7.22	—	—	—	—	—	AIR	—	—	—	—	—	—	—
8	11054	3421	1718	2718	4788	0.4987	7.22	—	—	—	—	—	AIR	—	—	—	—	—	—	—
9	11054	3421	1718	2718	4788	0.4987	7.22	—	—	—	—	—	AIR	—	—	—	—	—	—	—
10	11054	3421	1718	2718	4788	0.4987	7.22	—	—	—	—	—	AIR	—	—	—	—	—	—	—
11	11054	3421	1718	2718	4788	0.4987	7.22	—	—	—	—	—	AIR	—	—	—	—	—	—	—
12	11054	3421	1718	2718	4788	0.4987	7.22	—	—	—	—	—	AIR	—	—	—	—	—	—	—
13	11054	3421	1718	2718	4788	0.4987	7.22	—	—	—	—	—	AIR	—	—	—	—	—	—	—
14	11054	3421	1718	2718	4788	0.4987	7.22	—	—	—	—	—	AIR	—	—	—	—	—	—	—
15	11054	3421	1718	2718	4788	0.4987	7.22	—	—	—	—	—	AIR	—	—	—	—	—	—	—
16	11054	3421	1718	2718	4788	0.4987	7.22	—	—	—	—	—	AIR	—	—	—	—	—	—	—
17	11054	3421	1718	2718	4788	0.4987	7.22	—	—	—	—	—	AIR	—	—	—	—	—	—	—
18	11054	3421	1718	2718	4788	0.4987	7.22	—	—	—	—	—	AIR	—	—	—	—	—	—	—
19	11054	3421	1718	2718	4788	0.4987	7.22	—	—	—	—	—	AIR	—	—	—	—	—	—	—
20	11054	3421	1718	2718	4788	0.4987	7.22	—	—	—	—	—	AIR	—	—	—	—	—	—	—
21	11054	3421	1718	2718	4788	0.4987	7.22	—	—	—	—	—	AIR	—	—	—	—	—	—	—

4.5" x 10"

FAIRCHILD HILLER  
REPUBLIC AVIATION DIVISION  
"GARY" ALLY SYSTEMS, DIVISION

RECEIVED  
CREATED  
REVISED

1	2	3	4	5	6	7	8	9	10	11	12	13	14	15	16	17	18	19	20	21
NAME	INSTRUMENT	X <sub>1/2</sub>	X <sub>6</sub>	X <sub>4</sub>	TIME	ALTIMETER READING	L <sub>1</sub>	L <sub>2</sub>	EXPOSURE TIME							REMARKS				
171						IN	IN	IN	SEC.											
173						—	—	—	—											
174						0.110	0.117	3620	0.5											
175						0.170	0.122	3410	—											
176						—	—	—	—											
177						0.196	0.190	3460	0.5											
178						0.190	0.190	3350	0.5											
179						—	—	—	—											
180						0.187	0.185	3350	0.5											
181						0.193	0.190	3400	0.5											
182						—	—	—	—											
183						—	—	—	—											
184						—	—	—	—											
185						—	—	—	—											
186						—	—	—	—											
187						—	—	—	—											
188						0.185	0.185	3210	0.5											
189						—	—	—	—											
190						0.125	0.125	—	—											
191						0.100	0.100	3680	9											
192						0.116	0.069	0.810	3160	9										
193						—	—	—	—											
194						—	—	—	—											
195						0.100	0.110	0.295	—											
196						0.108	0.094	0.106	—											



1	2	3	4	5	6	7	8	9	10	11	12	13	14	15	16	17	18	19	20	21
NAME	INSTRUMENT	X <sub>1</sub>	X <sub>2</sub>	X <sub>3</sub>	T <sub>1</sub>	STATION	L <sub>1</sub>	L <sub>2</sub>	ELAPSED TIME							REMARKS				
197		0.025	0.013	0.128	3030	15	20.25	3.0	1.0											
198		0.035	0.015	0.115	3340	18	19.5	2.9	1.0											
199		0.020	0.070	0.112	3340	15	20.0	3.1	1.0							N/4 TANK SPARE, WERE, INSURE				
200		0.038	0.145	0.132	—	18	20.7	3.3	1.0							N/3				
201		0.065	0.085	0.120	—	15	—	—	—											
202		—	—	—	—	—	—	—	—											
203		—	—	—	—	—	—	—	—											
204		0.020	0.120	0.105	—	18	—	—	—							N/6 TANK SPARE, WERE, INSURE				
205		0.120	0.088	0.115	—	18	21.75	3.6	1.0							N/6				
206		0.046	0.110	0.108	—	18	—	—	—							N/6				
207		—	—	—	—	—	—	—	—							WATER LEAK AFTER DATA - ABORTED				
208		—	—	—	—	—	—	—	—											
209		—	—	—	—	—	—	—	—											
210		—	0.20	0.195	4285	0.5	—	—	—							N/6 RUN				
211		—	—	—	—	—	—	—	—											
212		—	—	—	—	—	—	—	—											
213		—	—	—	—	—	—	—	—							DID NOT TAKE 214 BECAUSE WAS RUN UNPAID				
214		—	0.210	0.195	4200	0.5	—	—	—											
215		—	0.201	0.103	4250	0.5	—	—	—											
216		—	0.210	0.105	4200	0.5	—	—	—											
217		—	0.203	0.110	4220	0.5	—	—	—											
218		—	—	—	—	—	—	—	—							WATER LEAK				
219		—	—	—	—	—	—	—	—											
220		—	—	—	—	—	—	—	—											
221		—	—	—	—	—	—	—	—							WATER LEAK				



1	2	3	4	5	6	7	8	9	10	11	12	13	14	15	16	17	18	19	20	21
AVG #	INLET FLOW $N_2$	INLET FLOW $O_2$	$H_{T1}$	$T_{T1}$	$P_{T1}$	$P_{T2}$	$P_{T3}$	Pressure	AVG FLOW $H_2$	Total	$P_2$	$V_1/V_2$	INLET CORRECTION	PROBE POSITION	$P_{T1}$	$P_{T2}$	HEIGHT OF $H_2O$	HEIGHT OF $N_2$		
2000	10.000	3.000	1605	3177	5310	0.2387	7.110	0.2037	—	—	—	—	AIR	IN	ATMOS	ATMOS	70.8			
2001	10.000	3.000	1579	3105	2238	0.2550	7.257	0.2303	0.3576	570	0.5140	0.5946	5.000	5.000	0.2923	0.467				
2002	10.000	3.000	1620	3116	5310	0.2556	7.257	0.2303	0.3576	1000	0.6655	0.9631	—	—	—	0.467				
2003	12.184	3.718	1138	2118	4012	0.3007	7.110	0.2037	—	—	—	—	AIR	18.5	—	0.467	8.0	0.07		
2004	12.305	3.747	1090	2004	3795	—	—	—	0.4000	570	0.6409	0.6508	—	—	—	1.272	14.0	0.07		
2005	12.305	3.747	1000	2020	3795	—	—	—	0.3824	960	0.7245	0.7225	—	—	—	—	—	—		
2006	12.305	3.747	1324	2673	4407	0.2006	7.054	—	—	—	—	—	AIR	—	—	0.330	12.0	0.164		
2007	12.305	3.747	1324	2592	4407	—	—	—	0.3462	600	0.4081	0.3743	—	—	—	0.100	14.0	0.495		
2008	11.005	3.450	1286	2619	4527	—	—	—	0.3462	940	0.5701	0.6259	—	—	—	—	—	—		
2009	10.249	2.871	1605	3177	5310	0.2053	7.054	—	0.3318	610	0.6007	0.3312	—	—	—	0.367	15.0	0.131		
2010	10.249	2.871	1593	3132	5274	0.2066	7.054	—	0.3364	940	0.6497	0.5017	—	—	—	0.339	14.0	0.15		
2011	10.249	3.001	1567	3078	5175	—	—	—	—	—	—	—	AIR	—	—	—	—	—		
2012	10.249	3.165	1587	3123	5247	0.2512	—	—	0.1688	570	0.5736	0.3272	—	—	—	0.433	6.0	0.122		
2013	10.249	3.126	1579	3105	5238	0.2518	7.122	—	0.1734	1060	0.5506	0.6136	—	—	—	1.272	12.0	0.145		
2014	10.249	3.304	1352	2700	4662	0.2020	—	—	—	—	—	—	AIR	11.5	—	—	—	—		
2015	10.249	3.383	1355	2720	4632	—	—	—	0.1848	610	0.5200	0.4415	—	—	—	0.433	15.0	0.15		
2016	11.201	3.457	1298	2619	4527	—	—	—	0.1878	1030	0.5314	0.7023	—	—	—	1.272	13.0	0.516		
2017	12.315	3.747	1112	2160	3998	—	—	—	—	—	—	—	—	—	—	—	—	—		
2018	12.346	3.747	1104	2142	3980	—	—	—	0.2112	640	0.5314	0.5531	—	—	—	0.433	10.0	0.146		
2019	12.346	3.736	1118	2160	3978	—	—	—	0.2024	560	0.5370	0.6207	—	—	—	0.433	13.0	0.146		

\* MODIFIED COMBUSTOR  
 \* SECOND SERIES OF RING INJECTION TESTS

FAIRCHILD HILLER  
REPUBLIC AVIATION DIVISION

DATE: \_\_\_\_\_  
CREATED: \_\_\_\_\_  
REVISED: \_\_\_\_\_

1	2	3	4	5	6	7	8	9	10	11	12	13	14	15	16	17	18	19	20	21
NUM	TIME	X <sub>1</sub>	X <sub>2</sub>	X <sub>3</sub>	TIME	TIME	TIME	TIME	TIME	TIME	TIME	TIME	TIME	TIME	TIME	TIME	TIME	TIME	TIME	TIME
202					08	14	14	14	14											
203																				
204																				
205																				
206																				
207																				
208																				
209																				
210																				
211																				
212																				
213																				
214																				
215																				
216																				
217																				
218																				
219																				
220																				
221																				
222																				
223																				
224																				
225																				
226																				
227																				
228																				
229																				
230																				
231																				
232																				
233																				
234																				
235																				
236																				
237																				
238																				
239																				
240																				
241																				
242																				
243																				
244																				
245																				
246																				
247																				
248																				
249																				
250																				
251																				
252																				
253																				
254																				
255																				
256																				
257																				
258																				
259																				
260																				
261																				
262																				
263																				
264																				
265																				
266																				
267																				
268																				
269																				
270																				
271																				
272																				
273																				
274																				
275																				
276																				
277																				
278																				
279																				
280																				
281																				
282																				
283																				
284																				
285																				
286																				
287																				
288																				
289																				
290																				
291																				
292																				
293																				
294																				
295																				
296																				
297																				
298																				
299																				
300																				